Structure, Electronic Structure and Electronic Spectra of Simple Materials at High Pressure

A dissertation submitted to the
College of Graduate and Postdoctoral Studies
in partial fulfillment of the requirements
for the degree of Doctor of Philosophy
in the Department of Physics and Engineering Physics
University of Saskatchewan
Saskatoon

By
Nnanna U. Ukoji

Permission to Use

In presenting this dissertation in partial fulfillment of the requirements for a Postgraduate degree from the University of Saskatchewan, I agree that the Libraries of this University may make it freely available for inspection. I further agree that permission for copying of this dissertation in any manner, in whole or in part, for scholarly purposes may be granted by the professor or professors who supervised my dissertation work or, in their absence, by the Head of the Department or the Dean of the College in which my dissertation work was done. It is understood that any copying or publication or use of this dissertation or parts thereof for financial gain shall not be allowed without my written permission. It is also understood that due recognition shall be given to me and to the University of Saskatchewan in any scholarly use which may be made of any material in my dissertation.

Disclaimer

Reference in this dissertation to any specific commercial products, process, or service by trade name, trademark, manufacturer, or otherwise, does not constitute or imply its endorsement, recommendation, or favoring by the University of Saskatchewan. The views and opinions of the author expressed herein do not state or reflect those of the University of Saskatchewan, and shall not be used for advertising or product endorsement purposes.

Requests for permission to copy or to make other uses of materials in this dissertation in whole or part should be addressed to:

Head of the Department of Physics and Engineering Physics
116 Science Place
University of Saskatchewan
Saskatoon,Saskatchewan S7N 5E2
Canada
OR
Dean College of Graduate and Postdoctoral Studies

University of Saskatchewan
116 Thorvaldson Building, 110 Science Place
Saskatoon, Saskatchewan S7N 5C9
Canada

Abstract

Under extreme conditions such as temperature and pressure, the chemical bonding, electronic structures and properties of materials undergo significant changes that leads to the discovery of new and unusual chemical species not obtainable at ambient conditions. Hence, chemical bonding plays a significant role in the description of systems in physics, solid state chemistry, material science etc. This makes the study and immense understanding of the structure and chemical bonding of solids significant and constitutes one of the main objectives of this thesis. The second part of this thesis employed state-of-the-art *ab initio* molecular dynamics simulation to reconstruct the phase transition in elemental Cs. Also, the Bethe-Salpeter Equation (BSE) was used to calculate the X-ray Absorption Spectra (XAS) and Non-Resonant Inelastic X-ray Scattering (NRIXS) spectra of crystalline ice Ih and compressed water.

In the first project, the structure and bonding analysis of K_2Ag and K_3Ag intermetallics were studied at 4.0GPa and 6.4GPa respectively by employing all available bonding analysis methods. Analysis of the K_2Ag reveal the K atom transfers electrons to the Ag atom and forms K-K, K-Ag and Ag-Ag closed shell interactions with the K-Ag being the strongest bond interaction present in the compound. Contrary to the K_2Ag, topological analysis of the K_3Ag yielded no Ag-Ag bond interaction. This is due to the very large bond length of the first nearest neighbour Ag-Ag interaction. All the plane wave and localized basis set dependent bond analysis methods employed gave consistent results. However, the projected density of state (PDOS) computed using the localized basis set method implemented in the LOBSTER code should always be checked against the PDOS calculated using a plane wave method before validating the crystal orbital overlap population (COOP) and crystal orbital Hamiltonian population (COHP) results from the LOBSTER code. In summary, the results from this study show that, all the bonding analysis techniques should be carefully applied when treating high pressure systems, due to the extensive modification of the electron density on application of pressure. Hence, a naive localized description is not appropriate and may lead to erroneous interpretation.

The second project focused on the analysis of bonding in the three phases of Na-Au intermetallics following the benchmark established in the first project. Analysis of the phase I Na_2Au structure at 0.83GPa revealed the presence of non-nuclear maximum (NNM) in the structure commonly known as electrides. The obtained NNMs were found to form off the Na atoms in agreement with the experimental maximum entropy method (MEM) analysis. The experimental structure of the Phase II Na_3Au intermetallics was found to have either a trigonal Cu_3As or hexagonal Cu_3P-type structure. The two structures could not be distinguished from experiment and DFT equations of state. However, through topological analysis of both structures, only the tetragonal structure does satisfy the Morse sum and is thus said to be the accurate phase II structure as it is topologically stable. Further analysis of the topologically stable phase II structure at 2GPa and the phase III Na_3Au at 51.7GPa yielded no NNMs. This implies the Na-Au intermetallics are stabilized by decreased localization of electrons at the interstitial sites at high pressure, contrary to elemental alkali metals that show increased localization of interstitial electrons at high pressure. Finally, Bader's quantum theory of atoms in molecule (QTAIM) revealed all the bond interactions present in the structures are closed shell interactions.

The third project reconstructs the phase transition paths of elemental Cs around the complex Cs-III in other to define the transition mechanism. In addition, topological properties of the Cs-II, Cs-III and Cs-IV structures were examined and the result show electrides in the three phases. The molecular dynamics results reveal the transition in the Cs-III $\rightarrow$ Cs-IV and Cs-II $\rightarrow$ Cs-III transformations are typical crystalline solid-solid transitions with no evidence of melting in the transition states. In addition, the transformation mechanism observed in the Cs-III $\rightarrow$ Cs-IV is not martensitic (i.e a transformation that occurs through a diffusionless cooperative motion of all the atoms in a transformation region) rather it occurs through nucleation and growth. The Cs-II $\rightarrow$ Cs-III transformation on the other hand was found to occur through a cooperative motion of all the atoms in the super cell. Also the results suggest existence of a very large activation barrier for the reverse transformation to Cs-II from a backward (i.e Cs-III $\rightarrow$ Cs-II) transition.

In the final project, BSE method was employed to calculate the XAS and NRIXS of crystalline ice Ih and compressed water at different momentum transfer values. Theoretical spectra computed using snapshots from the PICMD simulation performed here yield results in good agreement with experiment for both water and ice Ih. Further analysis of the trajectories revealed the water maintain approximate tetrahedral coordination and not dramatically different from crystalline ice. Also the results show dense water form interpenetrating hydrogen bonds by compressing the second nearest neighbour water molecules into the first coordination shell similar to the behaviour of high density ice.

Statement of Co-authorship

In this thesis, I present my contribution to this work. However, some part of the work are as a result of collaborations between the author, Ukoji Nnanna Ukpai, thesis supervisor Prof. John S. Tse of the Department of Physics and Engineering Physics at the University of Saskatchewan, Saskatoon and Dr. Jianbao Zhao, of the Canadian Light Source, Saskatoon. The contributions are described below.

Chapter 1 is a description of the underlying theory and computational tools employed in this thesis and it is solely written by Ukoji U. Nnanna.

Chapter 2 presents the structure and bonding analysis of K_2Ag and K_3Ag intermetallics. All the calculations were performed by Ukoji U. Nnanna while the result interpretation was collectively done by Nnanna U. Ukoji and Prof. John S. Tse. The chapter is solely written by Nnanna U. Ukoji.

Chapter 3 presents a detailed description of the bonding in the three phases of Na-Au intermetallics . Experimental data for this sodium gold project was supplied by Dr. Jianbao Zhao and Prof. Takemura. The theoretical calculations were carried out by Nnanna U. Ukoji while the analysis were done by Nnanna U. Ukoji and Prof. John S. Tse. The chapter is completely written by Nnanna U. Ukoji.

Chapter 4 presents the transition path, electronic structure and bonding of Cs-II to complex Cs-III and Cs-III to Cs-IV. All the calculations were performed by Ukoji U. Nnanna while the result interpretation was collectively done by Nnanna U. Ukoji and Prof. John S. Tse. The chapter is completely written by Nnanna U. Ukoji.

Chapter 5 presents the X-ray Absorption Spectra (XAS) and Non-resonant Inelastic X-ray Scattering (NRIXS) of Water and Ice Ih. All the calculations were performed by Ukoji U. Nnanna while the result interpretation was collectively done by Nnanna U. Ukoji and Prof. John S. Tse. Dr. X. Yong provided the program for the analysis of interpenetrating H-bond

network. The chapter is solely written by Nnanna U. Ukoji.

Chapter 6 is a general summary of the research projects in this thesis and it is fully written by Nnanna U. Ukoji.

Acknowledgements

My sincere gratitude first goes to the University of Saskatchewan, located on Treaty 6 Territory and the Homeland of the Metis.

I would like to express my profound appreciation to Prof. John S. Tse, for his immense support, care and encouragement as my thesis advisor; thank you so much for your impeccable patience and for sharing your vast knowledge of expertise. I also appreciate the highly supportive role of my advisory committee members: Prof. Alexander Moewes, Prof. Yansun Yao, Prof. Richard Bowels and Prof. Rainer Dick: their consistent and enormous support made my PhD program successful. I also want to thank Dr. Jianbao Zhao and Dr. Yong Xue for their help.

I am very grateful to the Ruth and Eber Pollard Graduate Scholarship for finding me worthy to be the first graduate student to receive the scholarship. I also appreciate the financial support of Canadian Natural Sciences and Engineering Research Council (NSERC) and the Department of Physics and Engineering Physics. I acknowledge access to high performance computers: Compute Canada (Westgrid), Plato at the University of Saskatchewan on which most of the research reported in this thesis were performed.

Without the immense support, patience, ceaseless understanding and unconditional love of my beautiful wife; Mrs. Ima-obong Ukoji, my siblings; Obasi Ukoji, Okechukwu Ukoji, Adaoma Ukoji, my beloved mother; Mrs. Cecilia Ukoji, my loving uncles; Eng. Awa Osonwa, Mr. Ibe Mba, Barr. John Awa Kalu and every other member of my family none of these would have been possible, I am forever grateful to you all for your unwavering love. Also, I want to say a big thank you to my friends Dr. Adebayo Adeniyi and Dr. Hammed Ejalonibu for being overly supportive. Finally, I will also like to express my profound gratitude to everyone that have been a part of my PhD journey thus far. You are all part of this success and I want to say a very big thanks to you all.

Dedication

To the Loving Memory of my Father, Late Chief Daniel Ukpai Mba Ukoji.

Contents

List of Tables

List of Figures

List of Abbreviations

1D	One Dimension
2D	Two Dimension
3D	Three Dimension
AdNDP	Adaptive Natural Density Partitioning
AIMD	*Ab initio* Molecular Dynamics
AO	Atomic Orbital
ASE	Atomic Simulation Environment
BCC	Body Centered Cubic
BCPs	Bond Critical Points
BZ	Brillouin Zone
CCP	Cage Critical Point
COHP	Crystal Orbital Hamiltonian Population
COOP	Crystal Orbital Overlap Population
DAC	Diamond Anvil Cell
DFT	Density Functional Theory
DOS	Density of States
EOS	Equation of States
ELF	Electron Localization Function
FCC	Face Centered Cubic
GGA	Generalized Gradient Approximation
KS	Kohn Sham
LDA	Local Density Approximation
LOBSTER	Local Orbital Basis Suit Towards Electronic Reconstruction
MLWF	Maximally Localized Wannier Functions
MD	Molecular Dynamics
NAO	Natural Atomic Orbital
NBO	Natural Bond Orbital

NCP	Nuclear Critical Point
NNM	Non-nuclear Maximum
NRIXS	Non-Resonant Inelastic X-ray Scattering
ON	Occupation Number
PAW	Projector Augmented Wave
PBE	Perdew-Burke-Ernzerhof
PBC	Periodic Boundary Conditions
PICMD	Path-Integral Centroid Molecular Dynamics
PW	Plane Wave
QTAIM	Quantum Theory of Atoms in Molecule
RCP	Ring Critical Point
SSAdNDP	Solid State Adaptive Natural Density Partitioning
VASP	Vienna Ab-initio Simulation Package
VESTA	Visualization for Electronic Structure Analysis
XAS	X-ray Absorption Spectra

Chapter 1

INTRODUCTION AND THEORETICAL METHODS

Materials under extreme conditions such as high temperature and high pressure undergo significant changes in their chemical bonding, electronic structures and properties which leads to discovery of unusual chemical species not obtainable at ambient conditions. Over the last decades, high pressure research have enormously advanced, thanks to the development of various experimental pressure devices such as diamond anvil cell (DAC) [12, 13, 14, 15, 16, 17] and progress in many essential techniques such as X-ray and neutron scattering, infrared and Raman spectroscopy, needed to characterize new compounds. Contrary to experiments where high pressure is not easy to reach and control in a DAC, numerical simulations are fast, of low-cost and adjusting pressure can be straightforwardly achieved by varying the unit cell size. Recent software advancements and increased computational power have put numerical simulations at the forefront of the exploration of physics, chemistry, material science etc. under high pressure. First principle computer simulation methods have over the years played a key role in the exploration and guiding of experiments under pressure with tremendous increase in the accuracy of predicted physical properties and complexity of materials able to be studied. High pressure materials studies involves decrease in atomic volume and increase in the electronic density thus changing the structure and chemical bonding of the system which plays a significant role in the description of systems in physics, solid state chemistry, material science etc. This makes the study and immense understanding of the structure and chemical bonding of solids significant and constitutes one of the main objectives of this thesis.

In the well known molecular orbital (MO) theory, atomic orbitals of comparable energy and identical symmetry overlap to form molecular orbitals. For two atomic orbitals, the

orbital overlap can occur in two ways depending on the phase relationship of the atomic orbitals, where an orbital's phase is a direct consequence of the wave-like properties of electrons [18]. The orbital phase can be denoted by a plus or minus sign (the signs does not have any physical meaning by itself except when overlapping orbitals to form a molecular orbital). During atomic orbital overlap, same-sign orbitals overlap constructively to form a bonding orbital while a destructive overlap (formed by orbitals of different sign) constitute the antibonding orbital. Figure 1.1 is a molecular orbital diagram of the H_2 molecule and show the electrons from each hydrogen atom constructively overlap to form a lower energy molecular orbital known as a σ bond (in wave function representation $\psi_\sigma = c_1\psi_{1s}^a + c_2\psi_{1s}^b$ is the wavefunction of the bonding orbital where c_1 and c_2 are positive expansion coefficients of each atomic wavefunction ψ_{1s}^a and ψ_{1s}^b respectively). On the other hand, the higher energy σ^* is the antibonding orbital with $\psi_{\sigma^*} = c_1\psi_{1s}^a - c_2\psi_{1s}^b$. Also the bond order (BO) is simply the difference between bonding electrons and antibonding electrons divided by two because a bond consist of two electrons i.e BO = ((number of bonding electrons) - (number of antibonding electrons))/2. At high pressure, bonding description is not as trivial as the simple H_2 molecular orbital description. This is mostly due to the modification of atomic orbital by application of pressure and thus electrons are widely delocalized.

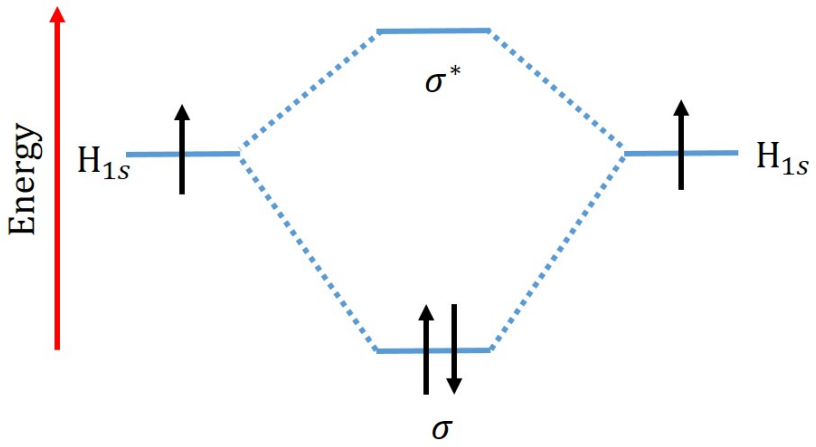

Figure 1.1: Schematic of the molecular orbital of H_2. The black arrows represents the electrons while σ and σ^* are bonding and antibonding molecular orbitals respectively.

However, there are currently several computational approach to analyze the structure and bonding in periodic solid state systems, some of which include, Electron Localization function (ELF) based on Density Functional Theory (DFT), Natural Bond Orbital (NBO) analysis [19, 20, 21, 22, 23], Solid State Adaptive Natural Density Partitioning (SSAdNDP) [24], Maximally Localized Wannier Functions (MLWF) [25], Crystal Orbital Hamiltonian Population (COHP) analysis [26] and Quantum Theory of Atoms in Molecules (QTAIM) [27, 28, 29, 30]. The aforementioned methods have been employed in this thesis and are described in the preceding sections. The atom which is made up of electrons and nuclei holds the underlying science while studying any material. A system of electrons and nuclei is governed by the Schrödinger equation postulated by Erwin Schrödinger in 1925 and is represented mathematically as

$$\hat{H}(r,R)\Psi(r,R) = E\Psi(r,R) \tag{1.1}$$

where r and R are the electronic and nuclear coordinates respectively, $\hat{H}$ is the Hamiltonian of the system, E the energy and Ψ the many-particle wave function. Hence one can obtain the electronic structure of the system by solving the Schrödinger equation associated with the electronic molecular Hamiltonian defined in Eq.1.1. The dynamics of the system obey the time-dependent Schrödinger equation which has the form:

$$\hat{H}(r,R,t)\Psi(r,R,t) = i\hbar\frac{\partial}{\partial t}\Psi(r,R,t) \tag{1.2}$$

The general Hamiltonian of the system in atomic units is given by Eq.1.3

$$\begin{aligned}\hat{H} = &-\frac{1}{2}\sum_{I=1}^{N_n}\nabla_I^2 + \sum_{I=1}^{N_n}\sum_{J>I}^{N_n} Z_I Z_J \frac{1}{|R_I - R_J|} \\ &-\frac{1}{2}\sum_{i=1}^{N_e}\nabla_i^2 + \sum_{i=1}^{N_e}\sum_{j>i}^{N_e}\frac{1}{|r_i - r_j|} - \sum_{i=1}^{N_e}\sum_{J=1}^{N_n} Z_J \frac{1}{|r_i - R_J|}\end{aligned} \tag{1.3}$$

where R and r are the nuclear and electronic coordinates respectively, N_n and N_e are the number of nuclei and electrons, and Z is the atomic number. The first term in Eq.1.3 is the

nuclear kinetic energy (T_n), the second term is the nuclei-nuclei Coulomb repulsion (V_{nn}), the third term is the electron kinetic energy (T_e), the fourth term is the electron-electron Coulomb repulsion (V_{ee}) and finally the last term represents the nuclei-electron potential (V_{ne}).

This Schrödinger equation is a second order differential equation in $3N_n$ and $3N_e$ coordinates, hence it is difficult to solve analytically except for some special cases such as particle in a box, harmonic oscillator and hydrogen atom. Certain approximations have to be made in order to solve it for a system of N_e electrons and N_n nuclei. One of the first approximations made was the Born-Oppenheimer (BO) approximation which was introduced by Max Born and J. Robert Oppenheimer in 1927 [31]. The central claim of this approximation was that given a system of N_n nuclei and N_e electrons, the movement of the electrons and nuclei can be separated because the mass of the electrons is very much smaller than that of the nuclei and their velocities are consequently much larger than that of the nuclei. Hence, as a consequence of their approximation, one can thereby describe the electronic structure independent of the nuclei and allow the electrons to relax to optimal eigenstates even before the nuclei move to the next arrangement. The Hamiltonian in Eq. 1.3 reduces to an electronic Hamilonian of the form:

$$\hat{H}_e = -\frac{1}{2}\sum_{i=1}^{N_e}\nabla_i^2 - \sum_{i=1}^{N_e}\sum_{J=1}^{N_n} Z_J \frac{1}{|r_i - R_J|} + \sum_{i=1}^{N_e}\sum_{j>i}^{N_e}\frac{1}{|r_i - r_j|} \tag{1.4}$$

The kinetic energy of the nuclear Coulomb potential can now be considered to be constant for a given nuclear configuration within the Born-Oppenheimer approximation. Also, the electronic motion in an external potential are said to be due to Coulomb interactions between the electrons and the nuclei. Hence, the simplified electronic Hamiltonian presented in Eq.1.4 depends only parametrically on the nuclear coordinates. Following the advent of the Born-Oppenheimer approximation, several methods have been developed to solve the electronic Schrodinger equation and some of the methods which make different approximations to solve this N_e electrons and N_n nuclei system include: the Density based methods such as Density Functional Theory etc.

1.1 Density Functional Theory (DFT)

In DFT, the problem is redefined in a computationally different manner. Instead of the wave function , density functional theory allows us to express the properties of an atom or molecule in terms of the electron density which is a much simpler object than the wavefunction. The equations for determining the orbitals are called the Kohn-Sham equations:

$$[-\frac{1}{2}\nabla^2 - \sum_A Z_A \frac{1}{\mid r - R_A \mid} + \int \rho(r') \frac{1}{\mid r - r' \mid} dr' + U_{xc}(r)]\phi_i = \varepsilon_i \phi_i \tag{1.5}$$

Where the exchange potential and the electron correlation are embedded in $U_{xc}(r)$. The theorem of Hohenberg-Kohn is the basic foundation of the density functional theory [32].

1.1.1 Hohenberg-Kohn Theorem

The theorem states that the external potential $v(\boldsymbol{r})$ in an N-electron system is a unique functional of the ground state electron density $\rho(\boldsymbol{r})$ apart from a trivial additive constant [32]. In other words the density determines everything about the system. The proof that $v(\boldsymbol{r})$ is a unique functional of $\rho(\boldsymbol{r})$ apart from a trivial additive constant was shown by Hohenberg-Kohn [32] as follows:
let the Hamiltonian of an N electron system subject to an external potential $v(\boldsymbol{r})$ and Coulomb repulsion be written as

$$H = T + V + U \tag{1.6}$$

where,
$T \equiv \frac{1}{2}\int \nabla\psi^*(\boldsymbol{r})\nabla\psi(\boldsymbol{r})d\boldsymbol{r}, \quad V \equiv \int v(\boldsymbol{r})\rho(\boldsymbol{r})d\boldsymbol{r}$ and $U = \frac{1}{2}\int \frac{\rho(\boldsymbol{r})\rho(\boldsymbol{r'})}{|\boldsymbol{r}-\boldsymbol{r'}|} d\boldsymbol{r}d\boldsymbol{r'}$
The electronic density $\rho(\boldsymbol{r})$ in the ground state Ψ is given by

$$\rho(\boldsymbol{r}) = \sum_i |\Psi_i(\boldsymbol{r})|^2 \tag{1.7}$$

Assume there are two distinct potentials $v(\boldsymbol{r})$ and $v'(\boldsymbol{r})$ with distinct Hamiltonians H and H' but having the same density $\rho(\boldsymbol{r})$, with ground state energies and wavefunctions given by E_0, $\psi(\boldsymbol{r})$ and E_0', $\psi'(\boldsymbol{r})$ respectively. From the Schrödinger equation

$$H' \left|\Psi'\right\rangle = E_0' \left|\Psi'\right\rangle \tag{1.8}$$

applying $\langle\Psi'|$ to the above equation yields

$$\left\langle\Psi'\right| H' \left|\Psi'\right\rangle = E_0' \left\langle\Psi'\right| \left|\Psi'\right\rangle \tag{1.9}$$

by orthornormality of the wavefunction $\langle\Psi'| \left|\Psi'\right\rangle = 1$

$$\Rightarrow E_0' = \left\langle\Psi'\right| H' \left|\Psi'\right\rangle \tag{1.10}$$

Similarly,

$$E_0 = \left\langle\Psi\right| H \left|\Psi\right\rangle \tag{1.11}$$

$$\Rightarrow E_0' = \left\langle\Psi'\right| H' \left|\Psi'\right\rangle \tag{1.12}$$

by the minimal property of the ground state we have that;

$$E_0' = \left\langle\Psi'\right| H' \left|\Psi'\right\rangle < \left\langle\Psi\right| H' \left|\Psi\right\rangle \tag{1.13}$$

rewriting Eq.1.6 in terms of H' and subtracting the two we have

$$H' = H + V' - V \tag{1.14}$$

substituting the above equation for H' in Eq.1.13 we have;

$$E_0' < \left\langle\Psi\right| H + V' - V \left|\Psi\right\rangle \tag{1.15}$$

so that,

$$E_0' < E_0 + \int [v'(\boldsymbol{r}) - v(\boldsymbol{r})]\rho(\boldsymbol{r})d\boldsymbol{r} \tag{1.16}$$

interchanging primed and unprimed quantities we find in exactly the same way that

$$E_0 < E_0' + \int [v(\boldsymbol{r}) - v'(\boldsymbol{r})]\rho(\boldsymbol{r})d\boldsymbol{r} \tag{1.17}$$

Adding these two equations (Eq.1.16 and Eq.1.17) gives:

$$E_0 + E_0' < E_0 + E_0' \tag{1.18}$$

which is a contradiction. Thus two distinct potentials cannot give the same electron density and the same number of electrons. This implies that $\rho(r)$ determines N and a unique V and hence determines the Hamiltonian and therefore all the wavefunctions and all the energies.

1.1.2 Kohn-Sham Formalism

Here, the total energy is expressed as a functional of the density:

$$E[\rho] = T_s[\rho] + \int v_{ext}\rho(r)dr + E_H[\rho] + E_{xc}[\rho] \tag{1.19}$$

where T_s is the kinetic energy that can be written in terms of the Kohn-Sham orbitals as:

$$T_s[\rho] = \sum_{i=1}^{N} \int dr \phi_i^*(-\frac{1}{2}\nabla^2)\phi_i(r) \tag{1.20}$$

v_{ext} is the external potential on the system and E_H is the Coulumb (or Hartree) energy:

$$E_H = \frac{1}{2}\int dr \int dr' \frac{\rho(r)\rho(r')}{\mid r - r' \mid} \tag{1.21}$$

E_{xc} is the exchange-correlation energy. Kohn-Sham equations are obtained by the variation

of the total energy with respect to a set of orbitals to give the Kohn-Sham potential [33],

$$v_{eff}(r) = v_{ext}(r) + \int \frac{\rho(r')}{\mid r - r' \mid} dr' + \frac{\delta E_{xc}[\rho]}{\delta \rho(r)}, \tag{1.22}$$

where $v_{xc}(r) = \frac{\delta E_{xc}(r)}{\delta \rho(r)}$ is the exchange-correlation potential. Thus the equation satisfied by the system can be written as:

$$(-\frac{1}{2}\nabla^2 + v_{eff}(r))\phi_i(r) = \varepsilon_i \phi_i(r). \tag{1.23}$$

In contrast to the first three terms on the right hand side of equation (1.28) for which the exact analytic dependence on ρ could be determined, the analytic form of the ρ dependence of $E_{xc}[\rho]$ is not known. In practice, certain approximations are used for the expression of $E_{xc}[\rho]$. It is important to note that orbitals are still used in DFT calculations because there is no good kinetic functional.

1.2 Exchange-Correlation Approximations

As previously noted above, lack of knowledge on the exact value of the exchange-correlation functional is one of the main challenges faced in the application of density functional theory. However, several approximations have been developed to represent the exchange-correlation, hence, a concise discussion of the most widely used; Local Density Approximation (LDA) [34] and Generalized Gradient Approximation (GGA) [35, 36] is presented here. The local density approximation is the simplest approach used to represent the exchange-correlation energy in density functional approximation. In the LDA approximation, the homogeneous density ρ_0 in the exchange-correlation energy density of the homogeneous electron gas $\epsilon_{xc}^{hom}(\rho_0)$ is replaced by the inhomogeneous density $\rho(r)$:

$$\epsilon_{xc}^{LDA}(\rho(r)) = \epsilon_{xc}^{hom}(\rho_0) \mid_{\rho_0 = \rho(r)} . \tag{1.24}$$

Thus the exchange-correlation energy functional now has the form;

$$E_{xc}^{LDA}[\rho(r)] = \int \epsilon_{xc}^{LDA}\rho(r)d^3r. \tag{1.25}$$

Due to the fact that the LDA approximation was derived from the uniform electron gas model, it was saddled with some limitations mostly for covalent materials with rapidly varying electron densities.

$$E_{xc}^{GGA}[\rho_\uparrow, \rho_\downarrow] = \int \epsilon_{xc}(\rho_\uparrow, \rho_\downarrow, \nabla_{\rho_\uparrow}, \nabla_{\rho_\downarrow})\rho(r)d^3r \tag{1.26}$$

Hence, since real materials have a strong varying density, the generalized gradient approximation functional was introduced and is written as a combination of the local electron density and the spatial variation in the electron density which is expressed as the density gradient [35, 36]. The general form of the functional is given in equation 1.26. The Perdew–Burke–Ernzerhof (PBE) [37] formalism of the GGA have been used in all the calculations performed here.

1.3 Natural Bonding Orbital (NBO) and Adaptive Natural Density Partitioning (AdNDP)

The natural bonding orbital (NBO) analysis by Weinhold [19] constructs the Lewis structure of a given molecule in an *a priori* manner and being extremely computationally efficient, the method is the first choice in dealing with the widest range of systems [38]. NBOs are important because they provide a valence bond-type description of the wavefunction in relation to the classical Lewis structure concepts [19]. Lots of literature [39, 40, 41, 42] have shown that combination of the localized and delocalized (aromatic/antiaromatic) description can consistently explain structures and properties of the main group element and transition metal clusters. From a computational point of view, the adaptive natural density partitioning (AdNDP) is a generalization of Wenhold's NBO analysis.

If the first order density operator is given by

$$\gamma(1|1') = N \int \psi(1, 2, \ldots, N)\psi^*(1', 2, \ldots, N)d2 \ldots dN \tag{1.27}$$

where 1 and $1'$ are abbreviations for $\boldsymbol{x_1}$ and $\boldsymbol{x_1}'$ and the matrix element (expectation value) of Eq.1.27 is

$$P_{kl} = \int \chi_k^*(1)\gamma(1|1')\chi_l(1')d1d1' \tag{1.28}$$

then $\gamma(1|1')$ can be expanded in a complete orthonormal basis set of atomic orbitals $\{\chi_k\}$ as follows

$$\gamma(1|1') = \sum_{kl} P_{kl}\chi_k(1)\chi_l^*(1') \tag{1.29}$$

The set of atomic hybrids which form bond orbitals χ_k with maximum occupancy should be considered optimal because approximate wavefunctions constructed from the found χ_k will best overlap the original wavefunction [38].

Based on the condition of maximum occupancy, the search for maximum occupancy hybrids can be performed numerically but it's a computationally expensive procedure, so an alternative approach is used.

The density matrix is represented in the block form

$$\boldsymbol{P} = \begin{vmatrix} \boldsymbol{P}_{11} & \boldsymbol{P}_{12} & \ldots & \boldsymbol{P}_{1N} \\ \boldsymbol{P}_{21} & \boldsymbol{P}_{22} & \ldots & \boldsymbol{P}_{2N} \\ \ldots & \ldots & \ldots & \ldots \\ \boldsymbol{P}_{i1} & \boldsymbol{P}_{i2} & \ldots & \boldsymbol{P}_{iN} \\ \ldots & \ldots & \ldots & \ldots \\ \boldsymbol{P}_{N1} & \boldsymbol{P}_{N2} & \ldots & \boldsymbol{P}_{NN} \end{vmatrix} \tag{1.30}$$

where block P_{jj} corresponds to the jth atomic block. If we consider the density due to the valence electrons, the eigenvalue problem of the form

$$P_{jj}h_l^{(j)} = n_l^{(j)}S_{jj}h_l^{(j)} \tag{1.31}$$

gives $n_l^{(j)}$ close to 2, hence the eigenvector $h_l^{(j)}$ can be seen as describing a lone pair on center j. Note P_{jj} is the density matrix sub-block on the jth center, S_{jj} is overlap matrix, $h_l^{(j)}$ and $n_l^{(j)}$ are the lth eigenvector and eigenvalue of P_{jj} respectively. Vectors available for bonding with other centers are identified by their eigenvalues which are significantly less than 2.By diagonalizing the matrix sub-blocks, including the centers of interest and corresponding off diagonal blocks, these vectors can be recovered i.e 2 $\times$ 2 sub-blocks of the form

$$\boldsymbol{P}^{(ij)} = \begin{bmatrix} \boldsymbol{P}_{ii} & \boldsymbol{P}_{ij} \\ \boldsymbol{P}_{ji} & \boldsymbol{P}_{jj} \end{bmatrix} \tag{1.32}$$

can reveal 2c-2e bonds between centers i and j (eigenvectors $h_l^{(ij)}$ with eigenvalues $n_i^{(ij)}$ close to 2), 3 $\times$ 3 sub-blocks

$$\boldsymbol{P}^{(ijk)} = \begin{bmatrix} \boldsymbol{P}_{ii} & \boldsymbol{P}_{ij} & \boldsymbol{P}_{ik} \\ \boldsymbol{P}_{ji} & \boldsymbol{P}_{jj} & \boldsymbol{P}_{jk} \\ \boldsymbol{P}_{ki} & \boldsymbol{P}_{kj} & \boldsymbol{P}_{kk} \end{bmatrix} \tag{1.33}$$

can reveal 3c-2e bonds between centers i, j and k and so on.

After n-center eigenvectors (on the centers i, j, ... k-total n) are obtained, there is need to deplete the full density matrix P from the density associated with the found bonding objects (n centers eigenvectors with eigenvalues close to 2)

$$\tilde{\boldsymbol{P}} \equiv \boldsymbol{P} - n_l^{(ij\ldots k)} \boldsymbol{h}_l^{(ij\ldots k)} \boldsymbol{h}_l^{(ij\ldots k)} \tag{1.34}$$

After depletion the search for (n + 1)-center occurs without mixing near degenerate n- and (n + 1)-center eigenvectors.

So, NBOs are obtained as local block eigenfunctions of the one-electron density matrix and have optimal convergence properties for describing the electron density. The implementation of the algorithm for the search of n-center 2-electron bonding objects is called adaptive natural density partitioning. AdNDP is based on the diagonalization of the n-atomic sub-block of the density matrix (full or depleted) of N-atomic molecular system in the basis of natural atomic orbitals (NAO) [38]. These NAOs are localized 1-center orbitals that can be described as the effective natural orbitals of an atom in its molecular environment.

1.4 Bloch Functions and Wannier Functions

Periodic boundary conditions are often used in electronic structure calculations. The one particle effective Hamiltonian H then commutes with the lattice translation operator $T_{\boldsymbol{R}}$, allowing one to choose as common eigenstates the Bloch orbitals $|\psi_n \boldsymbol{k}\rangle$:

$$[H, T_{\boldsymbol{R}}] = 0 \Rightarrow \psi_{n\boldsymbol{k}}(\boldsymbol{r}) = u_{n\boldsymbol{k}}(\boldsymbol{r}) e^{i\boldsymbol{k}\cdot\boldsymbol{r}} \tag{1.35}$$

where $u_{n\boldsymbol{k}}(\boldsymbol{r})$ has the periodicity of the Hamiltonian and $\psi_{n\boldsymbol{k}}(\boldsymbol{r})$ is called the Bloch wave function[25].

To get a localized wave packet in real space requires the use of a very broad superposition in **K** space. But **K** lives in the periodic Brillouin zone, so the best we can do is to choose equal amplitudes all across the Brillouin zone. Thus, we can construct

$$w_0(\boldsymbol{r}) = \frac{V}{(2\pi)^3} \int_{BZ} d\boldsymbol{K} \psi_{n\boldsymbol{k}}(\boldsymbol{r}) \tag{1.36}$$

where V is the real-space cell volume and the integral is carried over the BZ. The above Eq.1.36 can be interpreted as the Wannier functions (WFs) located in the home unit cell. We can insert a phase factor $e^{i\boldsymbol{k}\cdot\boldsymbol{R}}$ into the integrand in Eq.1.36, where $\boldsymbol{R}$ is a real-space lattice vector. Hence in Dirac Bra-Ket notation we can write,

$$|\boldsymbol{R}_n\rangle = \frac{V}{(2\pi)^3} \int_{BZ} d\boldsymbol{K} e^{-i\boldsymbol{k}\cdot\boldsymbol{R}} |\psi_{n\boldsymbol{k}}\rangle \,, \tag{1.37}$$

where $\boldsymbol{R}_n$ is the WF in cell $\boldsymbol{R}$ associated with band n. The inverse transform of Eq.1.37 reads

$$|\psi_{n\boldsymbol{k}}\rangle = \sum_{\boldsymbol{R}} e^{i\boldsymbol{k}\cdot\boldsymbol{R}} |\boldsymbol{R}_n\rangle \tag{1.38}$$

The transformations of Eqs. 1.36 and 1.37 constitute a unitary transformation between Bloch and Wannier states. Hence we can define the Wannier function as unitary transformation of Bloch function [43].

1.4.1 Gauge Freedom

The presence of a "gauge freedom" that exists in the definition of the $\psi_{n\boldsymbol{k}}$ makes the theory of Wannier functions more complex. Thus, we can replace

$$|\tilde{\psi}_{n\boldsymbol{k}}\rangle = e^{i\phi_n(\boldsymbol{k})}\,|\psi_{n\boldsymbol{k}}\rangle \tag{1.39}$$

Which in general can be written as

$$|\tilde{\psi}_{n\boldsymbol{k}}\rangle = \sum_{m=1}^{J} U_{mn}^{(\boldsymbol{k})}\,|\psi_{m\boldsymbol{k}}\rangle \tag{1.40}$$

Here $U_{mn}^{(\boldsymbol{k})}$ is a unitary matrix of dimension J that is periodic in $\boldsymbol{k}$ (it mixes the Bloch states at each $\boldsymbol{k}$).

1.4.2 Wannier Functions via Projection

A simple yet often effective approach for constructing a smooth gauge in k, and a corresponding set of well-localized WFs, is by projection [25]. One starts from a set of J localized trial orbitals $g_n(\boldsymbol{r})$ corresponding to some rough guess for the WFs in the home unit cell and are projected onto the Bloch manifold at wave vector $\boldsymbol{k}$ to obtain;

$$|\phi_{n\boldsymbol{k}}\rangle = \sum_{m=1}^{J} |\psi_{m\boldsymbol{k}}\rangle\,\langle\psi_{m\boldsymbol{k}}|\,|g_n\rangle\,, \tag{1.41}$$

which are typically smooth in k space.

The overlap matrix $(S_{\boldsymbol{k}})_{mn} = \langle\phi_{m\boldsymbol{k}}|\,|\phi_{n\boldsymbol{k}}\rangle_V = (A_{\boldsymbol{k}}^{\dagger}A_{\boldsymbol{k}})_{mn}$ is then computed and used to construct the Löwdin-orthonormalized Bloch-like states which now have a smooth gauge in $\boldsymbol{k}$. In addition, the projection window has to be chosen appropriately. One point to consider while making a choice of energy window is the total number of initial projection orbitals. For example, if the initial guess orbital is "s, p" for a two atom system, then the total number of wannier orbitals is eight based on the chosen projection orbitals. Hence, the chosen energy

window should contain at least eight bands to ensure accurate wannier orbitals are produced.

$$|\tilde{\psi}_{n\boldsymbol{k}}\rangle = \sum_{m=1}^{J} |\phi_{m\boldsymbol{k}}\rangle \, (S_{\boldsymbol{k}}^{1/2})_{mn}$$

1.5 Crystal Orbital Hamiltonian Population (COHP)

Following Mulliken's pioneering work [30] on electron assignment to bonds and to atom centers, several methods for electron partitioning in molecules have evolved. Within non-variational extended Huckel theory, Hughbanks and Hoffmann introduced a tight binding method with overlap which they called the Crystal Orbital Overlap Population (COOP) [44, 45]. In the COOP method, having calculated the band structure, the Mulliken's overlap population technique is then applied to a crystal measuring the bonding by $c_\mu^* c_\nu S_{\mu\nu}$ where c_ν is the coefficient and $S_{\mu\nu}$ is the overlap integral with positive, zero and negative overlaps implying bonding, nonbonding and antibonding respectively [46, 26]. The dependence of the COOP method on the basis set makes it not ideal for bonding description within first principle Density Functional Theory (DFT) [26]. Hence, the need for a bonding descriptor within first principles DFT led to the development of Crystal Orbital Hamiltonian Population (COHP) [26] method, which partitions the energy other than electrons but then similar to the COOP method since it also extracts information on the chemical interaction in a system from the band structure. A comprehensive review of the various applications of the COHP method can be found in ref.[47].

1.6 Quantum Theory of Atoms in Molecules (QTAIM)

Baders Quantum theory of Atoms in Molecules (QTAIM) have made quantum mechanical description of molecular structures possible [27, 28, 29, 30]. QTAIM extracts bonding information from the electron density of the molecular system. Both theoretical and experimental electron densities have been shown to give information on the chemical bonding in molecular systems [48, 49, 50, 51]. QTAIM identifies where the gradient of the electron density vanishes i.e. $\nabla\rho(r_c) = 0$. These special points r_c are called critical points (CPs) and are characterized

by their rank and signature labelled as (ω, σ). The rank of a CP corresponds to the number of non-zero curvatures (eigenvalues of the Hessian matrix) of $\rho(r_c)$ at the CP, while the sum of the signs of the curvatures of $\rho(r_c)$ at the CP denotes its signature. CPs of rank three are topologically stable and have four possibilities, which are (3, -3), (3,-1), (3, +1) and (3, +3) [27]. The (3, -3) CP is a local maximum with all curvatures negative and is called a nuclear CP. For (3, -1), the density parallel and perpendicular to a plane is a maximum and minimum respectively and is called a bond CP. On the other hand, for (3, +1) CP, density parallel and perpendicular to a plane is a minimum and maximum respectively and is called a ring CP. The (3, +3) CP is a cage CP with all curvatures positive. The different criteria for use of other important topological parameters at the critical point such as density (ρ), Laplacian ($\nabla^2\rho$), potential energy (V), kinetic energy (G), and the local energy densities (H) for bonding description have been summarized in previous reports [52, 53] and are defined as:

$$V(r) = \frac{\hbar^2}{4m}\nabla^2\rho(r) - 2G(r) \tag{1.42}$$

where

$$G(r) = \frac{3}{10}(3\pi^2)^{2/3}\rho^{5/3}(r) + \frac{1}{6}\nabla^2\rho(r) \tag{1.43}$$

and

$$H(r) = V(r) + G(r) \tag{1.44}$$

The signs and magnitude of the aforementioned topological parameters collectively give an insight on the nature and type of bond interaction present in the compound been studied. For example, typical shared interactions are indicated by a large density ($\rho > 0.1$), negative laplacian ($\nabla^2\rho < 0$) and negative local energy density (H < 0) at the bond critical point. On the other hand, closed shell interactions are defined by small density ($\rho < 0.2$), positive laplacian ($\nabla^2\rho > 0$) and positive local energy density (H > 0) at the bond critical point. The kinetic and potential energies at the bond critical points are always positive and negative respectively.

1.7 Green Function Based Methods

Excited state properties and spectroscopic experimental results are accurately studied and interpreted respectively using the Greens function theory [54].
In the Lehman representation, the Green function is given by

$$G(\mathbf{r}, \mathbf{r\prime}, \omega) = \sum_i \frac{f_i(\mathbf{r}) f_i^*(\mathbf{r\prime})}{\omega - \epsilon_i - i\eta} - \sum_a \frac{f_a(\mathbf{r}) f_a^*(\mathbf{r\prime})}{\omega - \epsilon_a + i\eta} \tag{1.45}$$

where η is a positive infinitesimal.
The poles of the Green function $\epsilon_a = E(N+1, a) - E(N, 0)$ and $\epsilon_i = E(N, 0) - E(N-1, i)$ are the electron addition and electron removal energies i.e energy levels for the unoccupied and occupied states respectively. Where $E(N+1, a)$, $E(N-1, i)$ and $E(N, 0)$ represents the total energies of the (N+1)-electron system in it's ath quantum state, (N-1)-electron system in it's ith quantum state and N-electron system in it's ground state respectively.
Single particle like framework is achieved in practical applications by the introduction of the concept of Quasiparticle (QP).The self energy operator Σ includes electron correlation and relaxation effect. The self energy distinguishes the QPs from bare particles (subject to only Hartree potential). The QP equation which has a Schrodinger like form reads

$$H_0(r) f_n(\mathbf{r}, \omega) + \int \Sigma(\mathbf{r}, \mathbf{r\prime}, \omega) f_n(\mathbf{r\prime}, \omega) d\mathbf{r\prime} = E_n(\omega) f_n(\mathbf{r}, \omega) \tag{1.46}$$

1.7.1 GW Approximation

The many-body perturbation theory gives access to the excited state properties not obtainable from the ground state electron density. The central variable of this theory is the time ordered Green function $G(\boldsymbol{r}t, \boldsymbol{r}'t')$ which contains the excitation energies and lifetimes. Observeables measured from the ground state electron density can be extracted from the Green function in addition to the excited state properties, though the complex nature of the Green function makes its application to calculate ground state properties very rare [55]. The acronym 'GW' represents an approximation to the self energy, where G describe the evolution of a particle in an interacting system and is called the one body Greens function and W

stands for the linear response dynamically screened Coulomb interaction. One can simply describe the GW as an approximation to the self energy. To find an accurate expression for the self energy operator (Σ), Hedin [56, 57] proposed a set of five equations which can be solved iteratively as shown in fig.1.2.

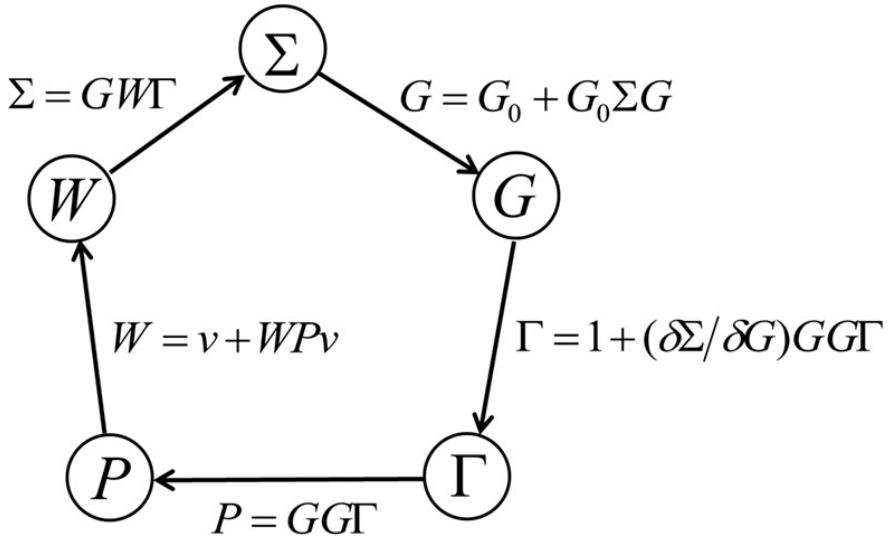

Figure 1.2: Schematic of the iteration using Hedin's equations and Dyson's equation. Adapted from Ref. [1]

With the vertex evaluated at a single point ($\Gamma = \delta\delta$) only we have

$$G = G_0 + G_0 \Sigma G \tag{1.47}$$

$$W = \nu + \nu P W \tag{1.48}$$

$$\Sigma = iGW \tag{1.49}$$

$$P = -iGG \tag{1.50}$$

$$\Gamma = \delta\delta \tag{1.51}$$

Where G is the one-body Green's function, P is the polarization operator, W is the dynamically screened Coulomb interaction and Γ is the vertx function. From the first iteration of the Hedins equations, the self energy becomes the GW. The Equation 1.49 to 1.51 is the GW approximation.

1.7.2 Bethe-Salpeter equation

Inclusion of vertex corrections becomes very important to account for electron hole interaction when considering absorption spectra [54]. To achieve this, the Hedin's equation has to be iterated for the second time.
Starting from $\Sigma = iGW$ and the vertex equation

$$\Gamma = 1 + \frac{\delta\Sigma}{\delta G} GG\Gamma \tag{1.52}$$

where

$$\frac{\delta\Sigma}{\delta G} = iW + iG0\frac{\delta W}{\delta G} \simeq iW \tag{1.53}$$

Hence the vertex equation becomes

$$\Gamma \simeq 1 + iWGG\Gamma \tag{1.54}$$

introducing 4 point equations i.e ${}^4P(1234)$, ${}^4W(1234) = W(12)\delta(13)\delta(24)$ and ${}^4P_0(1234) = P_0(12)\delta(13)\delta(24)$, the Bethe-Salpeter equation for the polarizability can be derived and yields

$${}^4P = {}^4P_0 + {}^4P_0K\ {}^4P \tag{1.55}$$

where the Kernel K is composed of the screened potential W and bare potential V electron hole attraction and exchange terms respectively represented as

$$K(1234) = \delta(12)\delta(34)V(13) - \delta(13)\delta(24)W(12) \tag{1.56}$$

In practical calculations, the eigenfunctions and eigenvalues of an effective two-particle excitonic Hamiltonian constitutes the absorption spectrum [54]. Details of the derivation can be

found in ref.[58].

1.8 X-ray absorption spectroscopy (XAS) and X-ray Raman Scattering (XRS)

X-ray absorption spectroscopy (XAS) is an element specific method which probes the density of unoccupied electronic states of a material by exciting an electron from the occupied to empty state as shown in fig.1.3 using energy tunable high intensity photon source such a synchrotron radiation [59]. The electron excitation requires absorption of a photon with energy higher than or equal to the binding energy of the electron. The X-ray Absorption Fine Structure (XAFS) spectra is composed of two regions at lower and higher energies referred to as X-ray Absorption Near Edge Structure (XANES) and Extended X-ray Absorption Fine Structure (EXAFS) respectively. The XANES and EXAFS provide electronic properties and structural information respectively [60]. XANES absorption cross section for transition from the initial to the final state of a system is given by the Fermi golden rule as

$$\sigma(\omega) \propto \sum_f |M_{i\rightarrow f}|^2 \delta(E_i - E_f + \omega) \tag{1.57}$$

and satisfy the dipole selection rule $\Delta l = \pm 1$ with the spin conserved ($\Delta S = 0$). $M_{i\rightarrow f}$ in equation1.57 is the matrix element of the transition between the initial and final states. For XAS it's a dipole of the form

$$M_{i\rightarrow f} = \langle \psi_f | \hat{\epsilon} \cdot \mathbf{R} | \psi_i \rangle \tag{1.58}$$

where $\hat{\epsilon}$ and $\mathbf{R}$ are the polarization direction and position operator respectively.

Unlike XAS, X-ray Raman Scattering (XRS) is a non resonant inelastic x-ray scattering (NRIXS) process of core electron excitation. In XRS, an inelastically scattered photon of energy ω_1 resulting from the interaction of an incident photon of energy ω_0 with the electrons of a sample, transfers $\omega = \omega_0 - \omega_1$ and $\mathbf{q} = \mathbf{k}_0 - \mathbf{k}_1$ energy and momentum respectively to the sample. Where $\mathbf{k}_0$ and $\mathbf{k}_1$ are incident and scattered photon momenta respectively. A measure of the inelastically scattered particle is the doubly differential cross-section (DDCS)

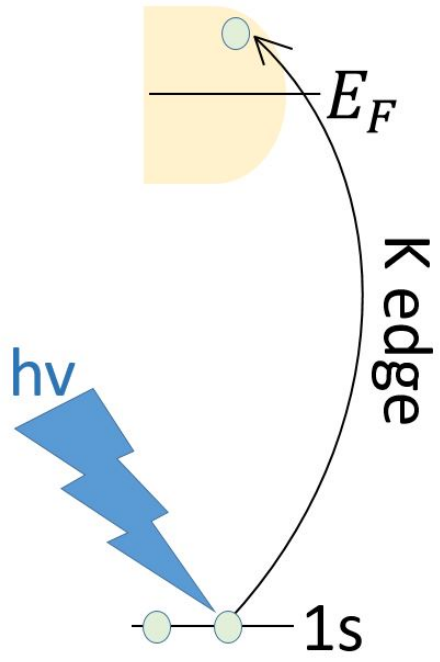

Figure 1.3: Schematic of X-ray Absorption Spectroscopy. The incoming photon (hv) excites the the core electron to the unoccupied state.

given by

$$\frac{d^2\sigma}{d\Omega d\omega_1} = \left(\frac{d\sigma}{d\Omega}\right)_{Th} S(\mathbf{q},\omega) \tag{1.59}$$

where $\left(\frac{d\sigma}{d\Omega}\right)_{Th}$ is the thompson scattering cross section and $S(\mathbf{q},\omega)$ is a property of the many body system known as the dynamical structure factor which is independent of the external probe and contains information on the excitation spectrum of the system. From the Fermi's golden rule, excitation of a many body particle ground state $|i>$ into all final states $|f>$ reads

$$S(\mathbf{q},\omega) = \sum_{i,f} P_i |<f| \sum_j \exp(i\mathbf{q}\cdot\mathbf{r_j})|i>|^2 \delta(E_i - E_f + \omega) \tag{1.60}$$

where P_i is the probability of finding the system in the initial state $|i>$ and the energy conservation is ensured by the delta function. The transition in Eq.1.60 can be Taylor expanded to yield

$$\exp(i\mathbf{q}\cdot\mathbf{r}) \approx 1 + i\mathbf{q}\cdot\mathbf{r} - \frac{(\mathbf{q}\cdot\mathbf{r})^2}{2} + \ldots \tag{1.61}$$

The first term in Eq.1.61 is always zero and at low $\mathbf{q}$ it's evident that Eq.1.61 approximates as a dipole only (the second term) and the XRS becomes equivalent to XAS. As $\mathbf{q}$ increases,

the quadrupole term becomes important because the XRS spectra depends on all the angular momentum projections of the density of state. For example, for the case of oxygen K-edge in H_2O, only the s and p-type density of state significantly contribute to the XRS spectra [9].

1.9 Molecular Dynamics

Molecular Dynamics (MD) technique which was pioneered in the 1950s by Alder and Wainwright [61, 62] and Rahman [63] has become a great tool in the simulation of matter and its dynamics. The understanding and prediction of structure, dynamical properties and function of molecular systems to date are owing to this great simulation technique which is a key tool as we also seek to enable predictive molecular design. The structure and dynamics of systems impossible to solve analytically can be greatly studied using simulation methods whose results help to interpret experimental data in terms of molecular motions. Just like in real experiments, the first step in an MD simulation is sample preparation which in this case is the electronic structure of the system under consideration with initial conditions set. This is followed by an equilibration run and finally the production run where the measurements of the desired physical quantities are taken. The MD method involves numerically solving the Newtonian equations of motion of a set of N particles in volume V. MD was originally formulated in the microcanonical "NVE" ensemble i.e an ensemble in which the number of particles N, the volume V and the total energy E of the system remains constant over time. Subsequently, attempts to correctly generate other ensembles such as the NVT ensemble (where the simulation temperature T remains constant, in place of the original constant energy formulation of MD) during MD simulations were made, with the first successful attempt made by Andersen in his 1980 seminal paper [64]. Prior to Anderson's seminal work, constant temperature MD simulation was obtained by Woodcock through an *ad hoc* manner scaling of the particle velocity [65]. Broughton et al.[66] evaluated the effect of this average temperature driven *ad hoc* velocity rescaling at regular intervals and showed that this method breaks the energy conservation in a system and contains discontinuous changes at the scaling intervals. Following the advent of Langevin dynamics, another pre-1980 attempt at the MD temperature control was made [67], here the particles were assumed to undergo a

collision with much lighter ones, which represents the heat bath, with the collisions described by a friction term and a random force added to the classical equation of motion. This dynamics gives a canonical distribution without conserving energy due to the contact between the heat bath and the system Hamiltonian [67]. The friction coefficients using this method can be really large which leads to unreliable dynamics [68]. Andersen's thermostat which accurately generates the NVT ensemble also uses a stochastic heat bath with the velocities of randomly selected colliding particles (i.e particles colliding with the heat bath) sampled from the Maxwell-Boltzmann distribution according to certain probability [64]. The thermostat reported in 1984 by Berendsen et al. [69] which uses the weak-coupling method is another common choice. This scheme does not follow a well defined ensemble and may lead to problems such as flying-ice-cube effect which violates the equipartition of energy [70]. The introduction of an extended Lagrangian by Nosé [71] subsequently refined by Hoover [72] correctly yields the canonical ensemble which makes it a more reliable method for simulating the NVT ensemble. The Nosé-Hoover method was faced with the problem of ergodicity at some difficult cases, such as harmonic systems. In other to overcome this problem of ergodicity, several extensions were made to the Nosé-Hoover method with the most notable one by Martyna et al. [73] where they coupled each thermostat to one or more additional thermostats which they called the Nosé–Hoover chains (NHCs). The NHCs addresses the ergodicity problem at an increased complexity in the algorithm. Here we focus the discussion on the velocity rescaling, Langevin, Andersen, Berendsen and NHC thermostat approaches which are commonly used presently.

1.10 Thermostat algorithms

The movement of particles in a system of N particles of fixed volume V is governed by the Newton's equations.

$$m_i \frac{d^2 \boldsymbol{q}_i}{dt^2} = \boldsymbol{F}_i = -\frac{\partial \boldsymbol{\Phi}}{\partial \boldsymbol{q}_i} \tag{1.62}$$

where $\boldsymbol{q}_i$ is a coordinate of particle i, $\boldsymbol{F}_i$ is the force on particle i and $\boldsymbol{\Phi}$ is the potential. This equation can be written in a canonical form using coordinate $\boldsymbol{q}_i$ and momentum, $\boldsymbol{p}_i$ in

the form

$$\frac{d\boldsymbol{q}_i}{dt} = \frac{\boldsymbol{p}_i}{m_i} \qquad\qquad \frac{d\boldsymbol{p}_i}{dt} = \boldsymbol{F}_i = -\frac{\partial \boldsymbol{\Phi}}{\partial \boldsymbol{q}_i} \tag{1.63}$$

These equations are numerically solved following the trajectory of every particle in the system using computers. All the thermodynamic and structural information of the system of N particles are then extracted from this trajectory. Dynamical information can also be obtained from the MD simulation.

The equation of motion in both forms 1.62 and 1.63 conserve the total energy of a system. Thus, MD formulation is by default in the microcanonical ensemble. Direct comparison of MD in the NVE ensemble with experiment is difficult because laboratory experiments are performed at constant temperature and pressure which is not possible in the NVE ensemble since we can't know the temperature until the simulation is done. We relate the temperature T to the mean kinetic energy (KE) from the equipartition theorem as

$$\left\langle \sum_i \frac{\boldsymbol{p}_i^2}{2m_i} \right\rangle = \frac{3}{2} NkT. \tag{1.64}$$

From Eq. 1.64, the temperature T is obtained only after we calculate the mean KE at the end of the simulation. To overcome these limitations, we resort to constant temperature simulations. Over the years, several modifications have been made to the equation of motion in a bid to correctly achieve a constant temperature MD simulation, we briefly review these methods and their algorithms.

1.10.1 Velocity rescaling

The first constant temperature algorithm proposed by Woodcock [65] used a velocity scaling method. Here, the KE is scaled to the desired value by multiplying the particle velocity with a common factor at every time step of the simulation. Using the leap frog algorithm [74], the coordinate $\boldsymbol{q}_i(t + \Delta t)$ and momentum $\boldsymbol{p}_i(t + \frac{\Delta t}{2})$ at times $t + \Delta t$ and $t + \frac{\Delta t}{2}$ respectively can be obtained from the knowledge of the coordinate $\boldsymbol{q}_i(t)$ and momentum $\boldsymbol{p}_i(t - \frac{\Delta t}{2})$ at times t and $t - \frac{\Delta t}{2}$ respectively. Where Δt is the time step with the force $\boldsymbol{F_i}$ calculated at time t.

The updated coordinates and velocities now reads

$$\boldsymbol{v}_i\left(t+\frac{\Delta t}{2}\right)=\boldsymbol{v}_i\left(t-\frac{\Delta t}{2}\right)+\left(\frac{\boldsymbol{F_i}(t)}{m_i}\right)\Delta t \tag{1.65}$$

$$\boldsymbol{q}_i\left(t+\Delta t\right)=\boldsymbol{q}_i\left(t\right)+\boldsymbol{v}_i\left(t+\frac{\Delta t}{2}\right)\Delta t \tag{1.66}$$

From Eq. 1.65 and 1.66, we still obtain the equation of motion

$$\frac{d\boldsymbol{v}_i}{dt}=\frac{\boldsymbol{F}_i}{m_i} \tag{1.67}$$

$$\frac{d\boldsymbol{q}_i}{dt}=\boldsymbol{v}_i \tag{1.68}$$

Woodcock corrected the estimated velocity at time $t+\frac{\Delta t}{2}$ to satisfy a constraint of the constant kinetic energy,

$$\boldsymbol{v}_i^*\left(t+\frac{\Delta t}{2}\right)=s\boldsymbol{v}_i\left(t+\frac{\Delta t}{2}\right) \tag{1.69}$$

where s is the scaling factor which can be obtained from

$$\sum_i\frac{m_i}{2}(\boldsymbol{v}_i{}^*\left(t+\frac{\Delta t}{2}\right))^2=s^2\sum_i\frac{m_i}{2}(\boldsymbol{v}_i\left(t+\frac{\Delta t}{2}\right))^2=\frac{g}{2}kT \tag{1.70}$$

The parameter g is essentially equal to the number of degree of freedom of the physical system.

Hence,

$$s=\left[\frac{gkT}{\sum_i m_i\left(\boldsymbol{v}_i\left(t+\frac{\Delta t}{2}\right)\right)^2}\right]^{\frac{1}{2}} \tag{1.71}$$

The updated coordinate at $t+\Delta t$ now has the form

$$\boldsymbol{q}_i\left(t+\Delta t\right)=\boldsymbol{q}_i\left(t\right)+\boldsymbol{v}_i{}^*\left(t+\frac{\Delta t}{2}\right)\Delta t \tag{1.72}$$

This velocity scaling method was shown to yield discontinuous trajectories in phase space at the scaling interval [66]. It only yields the correct coordinate space canonical distribution

when the scaling is performed at every time step and has an accuracy of order Δt [75].

1.10.2 Langevin

In the Langevin dynamics [67], a canonical ensemble is achieved by assuming the particles collide with much lighter particles which represents the heat bath. A friction $-\gamma_i p_i$ and a random force $\eta_i(t)$ which describe these collisions is added to the equation of motion which are coupled Langevin equations

$$m_i \frac{d^2 \boldsymbol{q_i}}{dt^2} = -\frac{\partial \mathscr{H}}{\partial \boldsymbol{q_i}} - m_i \gamma_i \frac{d\boldsymbol{q_i}}{dt} + \eta_i(t) \tag{1.73}$$

Where the first, second and third terms of Eq.1.73 correspond to the standard interaction term calculated during the simulation, the damping used to tune the viscosity of the bath and Gaussian random variable with zero mean. The magnitude of this random variable is given by

$$\left\langle \eta_i(t)\eta_{i'}(t') \right\rangle = 2m_i\gamma_i k_B T \delta_{ii'}\delta(t-t') \tag{1.74}$$

The coupling strength of the physical system to the heat bath is given by the damping constant γ_i and T represents the temperature of the bath. Careful considerations are to be made when choosing the damping constant. Schneider and Stoll [67] require the choice of damping constant satisfy

$$\tau_{ch} >> \frac{1}{\gamma_i} >> \tau_c \tag{1.75}$$

this is necessary to nearly realize energy conservation using the Langevin dynamics. Where τ_{ch} is the equilibrium chain lenght and τ_c is the characteristic times of the dynamics.
It is important to note that the Langevin thermostat was combined with the Parrinello-Rahman [76, 77] method to generate the isobaric isothermal (NPT) ensemble used for the molecular dynamics simulation performed in this work. The equations of motion for the ionic and lattice degrees of freedom in the Parrinello and Rahman method are derived from the

Lagrangian in Eq. 1.76.

$$\mathscr{L}\left(s,h,\dot{s},\dot{h}\right)=\frac{1}{2}\sum_{i=1}^{N}m_i\dot{s}_i^{\dagger}G\dot{s}_i-V\left(s,h\right)+\frac{1}{2}WTr(\dot{h}^{\dagger}\dot{h})-p_{ext}\Omega \tag{1.76}$$

where $\boldsymbol{s}_i$ is a position vector of atom i in fractional coordinates, h is the matrix formed by lattice vectors, p_{ext} is the external pressure, Ω represents the cell volume, G can be defined as G = $h^t h$ and W is a constant with the dimensionality of mass.

1.10.3 Andersen

In the formulation of Anderson thermostat [64], he introduced a stochastic force to the Hamiltonian equation of motion which causes a random collision of the atoms with an imaginary heat bath at the desired temperature. The Hamiltonian equations of the N particles in volume V are given by;

$$\frac{d\boldsymbol{q_i}}{dt}=\frac{\partial\mathscr{H}}{\partial\boldsymbol{p_i}}=\frac{\boldsymbol{p_i}}{m} \tag{1.77}$$

$$\frac{d\boldsymbol{p_i}}{dt}=-\frac{\partial\mathscr{H}}{\partial\boldsymbol{q_i}} \tag{1.78}$$

with the stochastic collision term added to the $\frac{d\boldsymbol{p_i}}{dt}$ equation. It's important to note each instantaneous collision term only affects the momentum of one particle. The time evolution of the state of the system between successive stochastic collisions follow Eq.1.77 and 1.78. The collision times are usually chosen before the simulations by generating intervals between successive particle collisions or choosing which particles undergo a collision within a small interval of time using random numbers in both cases. The momentum of the colliding particle after collision is randomly and instantaneously chosen from a Maxwell-Boltzmann distribution at the desired temperature T. Due to the instantaneous collision, the Anderson's thermostat can greatly affect dynamical properties, hence, it's mainly recommended to use only when interested in structural properties of the system under consideration [78].

1.10.4 Berendsen

This thermostat which is also known as weak coupling thermostat was introduced by Berendsen [69]. It's very similar to the velocity rescaling method of Woodcock [65]. Unlike Woodcock's method which abruptly rescales the velocity to the target kinetic energy, the Berendsen method includes a relaxation time to slowly equilibrate the system to the target temperature. Berendsen assumed a weak coupling of the system to a heat bath with a heat transfer coupling constant or time scale τ related to the velocity rescaling factor s as

$$s^2 = 1 + \frac{\delta t}{\tau}\left(\frac{T}{T_{inst}} - 1\right) \tag{1.79}$$

Where, δt is the simulation time step and τ ranges from 0.1 to 0.4ps for $\delta t = 1fs$. Similar to the velocty rescaling method, energy fluctuations are not correctly captured in the Berendsen thermostat. It does not also yield accurate canonical ensemble and is known to lead to problems such as flying-ice-cube effect which violates the equipartition of energy [70], so it is not recommended.

1.10.5 Nosé-Hover chains (NHCs)

At constant temperature, energy fluctuation is allowed in other to correctly simulate the system. Nose [71] used the idea of extendend Lagrangian to achieve constant temperature formulation. Andersen [64] in his constant temperature formalism first introduced this method of extended Lagrangian. The idea here is to extend a physical system to a single system consisting of a physical system and an external system, the external system is very small unlike the macroscopic reservoir. The extended system still follow the conservation laws but the total energy of the physical system fluctuates [75]. Nose introduced a degree of freedom s to the physical system of time, coordinates and momentum $\boldsymbol{t}^{'}$, $\boldsymbol{q}_{\boldsymbol{i}}^{'}$ and $\boldsymbol{p}_{\boldsymbol{i}}^{'}$ respectively. He also introduced virtual variables $\boldsymbol{t}$, $\boldsymbol{q_i}$ and $\boldsymbol{p_i}$ related to the real (primed) time, coordinate and momentum by

$$\boldsymbol{q}_{\boldsymbol{i}}^{'} = \boldsymbol{q_i} \tag{1.80}$$

$$\boldsymbol{p_i^{'}} = \frac{\boldsymbol{p_i}}{s} \tag{1.81}$$

$$\boldsymbol{t}^{'} = \int \frac{dt}{s} \tag{1.82}$$

the real velocity $\boldsymbol{v_i^{'}}$ of particle i is obtained by multiplying a scaling factor s to a virtual velocity $\boldsymbol{v_i}$,

$$\boldsymbol{v_i^{'}} = s\boldsymbol{v_i} \tag{1.83}$$

These transformations can be basically thought of as an infinitesimal time scaling of the form.

$$dt^{'} = \frac{dt}{s} \tag{1.84}$$

An extended system of N particles and degree of freedom s has a Lagragian in terms of the virtual variables of the form

$$\mathscr{L}_N = \sum_{i=1}^{N} \frac{m_i}{2} s^2 \dot{\boldsymbol{q}}_{\boldsymbol{i}}^{\boldsymbol{2}} - \phi(\boldsymbol{q}) + \frac{Q}{2}\dot{s}^2 - gkT \ln s \tag{1.85}$$

where m_i is the mass of the real system, g is the degree of freedom of the physical system, However, its exact value will be chosen to satisfy the equilibrium of a canonical distribution. T is the temperature of the heat bath and Q is an effective mass associated with s. The conjugate momenta corresponding to $\boldsymbol{q_i}$ and s are given by

$$\boldsymbol{p_i} = \frac{\partial \mathscr{L}_N}{\partial \dot{\boldsymbol{q}}_i} = m_i s^2 \dot{\boldsymbol{q}}_i \tag{1.86}$$

$$p_s = \frac{\partial \mathscr{L}_N}{\partial \dot{s}} = Q\dot{s} \tag{1.87}$$

from which the extended system Hamiltonian can be written as

$$\mathscr{H}_N = \sum_{i=1}^{N} \frac{\boldsymbol{p}_i^2}{2m_i s^2} + \phi(\boldsymbol{q}) + \frac{p_s^2}{2Q} + gkT \ln s \tag{1.88}$$

The first and second terms in Eq.1.88 corresponds to the kinetic energy and the potential energy of the physical system of interest. The third and last terms correspond to an added degree of freedom, where p_s is a conjugate momentum of s. We've replaced the momentum $\boldsymbol{p}_i$ with a real momentum $\boldsymbol{p}_i^{'} = \boldsymbol{p}_i/s$ everywhere it's expected to appear. The total Hamiltonian in Eq.1.88 remains conserved in the total extended system, but that of the physical system Eq.1.89 can fluctuate and the energy distribution follow the canonical distribution.

$$\mathscr{H}_0 = \sum_{i=1}^{N} \frac{\boldsymbol{p}_i^{'2}}{2m_i} + \phi(\boldsymbol{q}^{'}) \tag{1.89}$$

By using the extended Hamiltonian, the equations of motion are obtained via canonical equations as

$$\frac{d\boldsymbol{q}_i}{dt} = \frac{\partial \mathscr{H}_N}{\partial \boldsymbol{p}_i} = \frac{\boldsymbol{p}_i}{m_i s^2} \tag{1.90}$$

$$\frac{d\boldsymbol{p}_i}{dt} = -\frac{\partial \mathscr{H}_N}{\partial \boldsymbol{q}_i} = -\frac{\partial \phi}{\partial \boldsymbol{q}_i} \tag{1.91}$$

$$\frac{ds}{dt} = \frac{\partial \mathscr{H}_N}{\partial p_s} = \frac{p_s}{Q} \tag{1.92}$$

$$\frac{dp_s}{dt} = -\frac{\partial \mathscr{H}_N}{\partial s} = \frac{\sum \frac{\boldsymbol{p}_i^2}{m_i s^2} - gkT}{s} \tag{1.93}$$

For more convenient application to simulations, the equations of motion Eq.1.90 to Eq.1.93 can be transformed to equations with the real variables [71], using the basic relations Eq.1.80 to Eq.1.82 between the real and virtual variables and introducing an additional relation

$$p_s^{'} = \frac{p_s}{s} \tag{1.94}$$

the transformed equations with the real variables reads

$$\frac{d\boldsymbol{q}_i^{'}}{dt^{'}} = s\frac{d\boldsymbol{q}_i^{'}}{dt} = s\frac{d\boldsymbol{q}_i}{dt} = \frac{\boldsymbol{p}_i}{m_i s} = \frac{\boldsymbol{p}_i^{'}}{m_i} \tag{1.95}$$

$$\frac{d\boldsymbol{p}_i^{'}}{dt^{'}} = s\frac{d}{dt}\left(\frac{\boldsymbol{p}_i}{s}\right) = \frac{d\boldsymbol{p}_i}{dt} - \frac{1}{s}\frac{ds}{dt}\boldsymbol{p}_i = -\frac{\partial\phi}{\partial\boldsymbol{q}_i^{'}} - \frac{1}{s}\frac{ds}{dt^{'}}\boldsymbol{p}_i^{'} \tag{1.96}$$

$$\frac{ds^{'}}{dt^{'}} = s\frac{ds^{'}}{dt} = s\frac{ds}{dt} = s^{'2}\frac{p_s^{'}}{Q} \tag{1.97}$$

$$\frac{dp_s^{'}}{dt^{'}} = s\frac{d}{dt}\left(\frac{p_s}{s}\right) = \frac{dp_s}{dt} - \frac{1}{s}\frac{ds}{dt}p_s = \frac{\left(\sum_i \frac{\boldsymbol{p}_i^{'2}}{m_i} - gkT\right)}{s} - \frac{1}{s}\frac{ds}{dt^{'}}p_s^{'} \tag{1.98}$$

Hoover [72] noted that introduction of a new variable

$$\zeta = \frac{1}{s}\frac{ds}{dt^{'}} = s\frac{p_s^{'}}{Q} \tag{1.99}$$

simplifies the transformed equations of motion to

$$\frac{d\boldsymbol{q}_i^{'}}{dt^{'}} = \frac{\boldsymbol{p}_i^{'}}{m_i} \tag{1.100}$$

$$\frac{d\boldsymbol{p}_i^{'}}{dt^{'}} = -\frac{\partial\phi}{\partial\boldsymbol{q}_i^{'}} - \zeta\boldsymbol{p}_i^{'} \tag{1.101}$$

$$\frac{d\ln s^{'}}{dt^{'}} = \zeta \tag{1.102}$$

$$\frac{d\zeta}{dt^{'}} = \frac{\left(\sum_i \frac{\boldsymbol{p}_i^{'2}}{m_i} - gkT\right)}{Q} \tag{1.103}$$

This simplified form is commonly known as the Nose-Hoover thermostat [79]. Eq.1.100 and Eq.1.101 are similar to the equations of motion of a body with a frictional force ζ, but the frictional force in this case can either be positive or negative hence, it is not a constant. This thermostat is one of the most commonly used and widely implemented thermostat. However, it sometimes yields ergodicity problem for smaller systems [78]. This ergodicity problem was addressed by the method of Martyna et al. [73] which involves chaining the thermostats. Hence, most of the implementation of this thermostat now use the Nose-Hover

chains (NHCs).

1.11 Path integral Molecular Dynamics

The Feynman's imaginary time path integral theory which maps a quantum system into P copies of a classical subsystem called beads that interact with each other through harmonic springs, forms the bedrock of path integral (PI) simulations. Path integral Molecular Dynamics (PIMD) is one of the PI simulation technique where statistical averages are computed by using molecular dynamics as the sampling technique. The need to accurately account for the quantum nature of nuclear motions, which greatly describes the structure, stability and thermodynamic properties of condensed matter systems led to PIMD [2]. Given a quantum system, all we do in PI simulation is to first make a replicated necklace-like classical copies of the quantum system with identical statistical behaviours. Then molecular dynamics is employed to compute the statistical averages of the classical system which corresponds to the statistical averages of the original quantum system. The path integral representation of the partition function of an N particle system is given by

$$Z_{\mathscr{P}} = \prod_{I=1}^{N} \left[\left(\frac{M_I \mathscr{P}}{2\pi\beta\hbar^2} \right)^{\frac{3\mathscr{P}}{2}} \int d\boldsymbol{R_I^{(1)}} \cdots \int d\boldsymbol{R_I^{(\mathscr{P})}} \right] \exp -\beta W \tag{1.104}$$

with

$$W = \sum_{s=1}^{\mathscr{P}} \sum_{I=1}^{N} \frac{M_I}{2} \omega_{\mathscr{P}}^2 \left(\boldsymbol{R_I}^{(s)} - \boldsymbol{R_I}^{(s-1)} \right)^2 + \sum_{s=1}^{\mathscr{P}} \frac{1}{\mathscr{P}} V \left(\boldsymbol{R_I}^{(s)}, \ldots, \boldsymbol{R_N}^{(s)} \right) \tag{1.105}$$

where $\boldsymbol{R_N}^{(s)}$ represents the nuclear coordinate of particle I at time s, V(R) represents the interatomic interaction and the chain frequency $\omega_{\mathscr{P}} = \sqrt{\mathscr{P}}/\beta\hbar$. It is important to note that the path periodicity $R^{(0)} = R^{(\mathscr{P})}$ is maintained. By close observation, one can tell Equation 1.104 has the same form as the partition function of a classical system of $N\mathscr{P}$ particles with an effective potential of W defined above. Hence, a quantum ensemble of N particles is similar to a classical ensemble of $N\mathscr{P}$ particles with interactions defined by Equation 1.105 and they become identical as $\mathscr{P} \to \infty$. This classical isomorphism makes it possible for us to perform

constant temperature molecular simulation of the $N\mathscr{P}$ particle system with sufficiently large $\mathscr{P}$ value, and the obtained ensemble belongs to the original N particle quantum system. Details of the theoretical formulation of PI simulations can be found in ref. [2, 80].

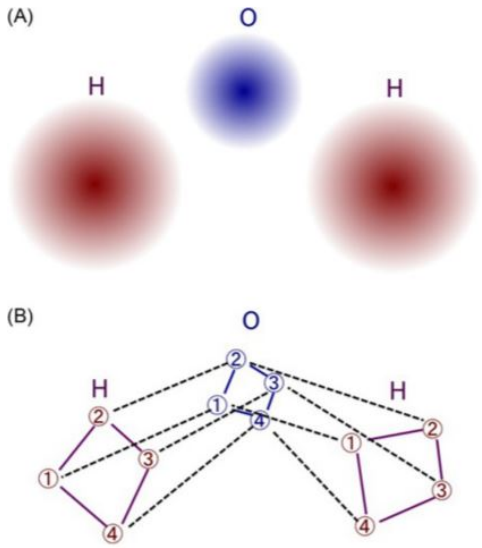

Figure 1.4: Schematic illustration of the translation of a (A) wavefunction representation to the corresponding (B) path integral representation for a water molecule. The number of beads for the path integral representation is four i.e $\mathscr{P} = 4$. Adapted from ref. [2]

A schematic representation of the path integral of a water molecule using four beads ($\mathscr{P} = 4$) is shown in Figure 1.4. Each atom is represented by beads one to four, the solid lines indicate the physical interactions of an atom within the same beads while the dashed lines indicate the harmonic nearest neighbour bead interaction [2].

In this thesis, the path integral centroid molecular dynamics (PICMD) approach developed by Cao and Voth [81] have been employed. The centroid variable q_0 [82] of the path represents the imaginary time average of a particular closed Feynman path q(τ), and is simply the zero frequency Fourier mode of that path, i.e.,

$$q_0 = \frac{1}{\hbar\beta}\int_0^{\hbar\beta} d\tau q(\tau) \tag{1.106}$$

The corresponding quantum mechanical centroid density $\rho_c(q_c)$, can be defined for the path centroid variable q_c. Where q_c is the path sum over all paths having their centroids fixed

at a point in space [82]. Hence, the formal imaginary time path integral expression for the centroid density in one dimension is given by;

$$\rho_c(q_c) = \int \cdots \int \mathscr{D}q(\tau)\delta(q_c - q_0)\exp\{-S[q(\tau)]/\hbar\} \tag{1.107}$$

Where S[q(τ)] is the imaginary time action functional and the quantum partition function is then obtained by the integration of the centroid density over all possible positions of the centroid as shown in Eq. 1.108.

$$Z = \int dq_c \rho_c(q_c) \tag{1.108}$$

It is important to note that the particle (or coordinate) density is different from the centroid density, the former is the diagonal element of equilibrium density matrix in the coordinate representation, while the later does not have a similar physical interpretation. However, both densities yield the the quantum partition function when integrated [81, 83, 84].

1.12 Software Used in This Thesis

The objective of this thesis is to interpret the electronic structure and detailed bonding properties of simple materials by employing all the available theoretical bonding analysis methods. The first principle calculations involving DFT were performed using the VASP code [85]. In addition, local structure probing using X-ray absorption spectroscopy and X-ray emission spectroscopy were performed using the OCEAN code [86]. The SSAdNDP code [24] was used to search for localized and delocalized n center 2 electron (nc-2e) bonds. The wannier90 code [87] interfaced with VASP was used to obtain the band structure from a GW [88] calculation, disentangle the various bands and generate the Wannier orbitals corresponding to the disentangled bands. Further bonding information was obtained from the energy band structure by calculating the COHP as implemented in the Local Orbital Basis Suite Towards Electronic Reconstruction (LOBSTER) program [89]. The topological analysis, evaluation of crystal voids with procrystal density [90] and search for non-nuclear maxima (NNM) were performed using the Critic2 program [91] and bond orders were obtained using Chargemol programs [92].

1.12.1 VASP

VASP stands for Vienna Ab-initio Simulation Package, is a first-principle simulation package designed for atomic scale materials modelling such as electronic structure calculations and quantum-mechanical molecular dynamics. Determination of the electronic ground state in VASP is done through an iterative matrix diagonalization schemes coupled to highly efficient Broyden and Pulay density mixing schemes in other to speed up the self-consistency cycle. Plane wave basis sets are used for materials modelling in VASP. The Blochl's projector augumented-wave (PAW) method which is a frozen core electronic method is also implemented in VASP [93].

1.12.2 Wannier90

The Wannier90 code is primarily used to construct Maximally Localized Wannier Functions (MLWFs) from a set of Bloch energy bands that may or may not be mixed with other bands [43]. The local environments of these MLWFs can be exploited to compute band-structure, density of state and Fermi surfaces at reasonable computational cost. These MLWFs are constructed by minimizing it's total spread which is done in the real space of unitary matrices that describe rotations of the Bloch bands at each k-point. This MLWFs construction mechanism makes wannier90 code independent of the basis set used in the underlying calculation from which the Bloch states were obtained and hence, it can be directly linked to any electronic structure code.

1.12.3 Critic2

The critic2 code [91] provides an interface to many solid-state electronic structure programs is primarily designed for the analysis and representation of solid-state electron densities based on Bader's Quantum Theory of Atoms in Molecules (QTAIM) . This program integrates atomic basins of the electron density and searches for special points called critical points where derivatives of the electron density is zero. Critic2 is not limited to QTAIM analysis, it can also extract non-covalent interaction (NCI) plot, Hirshfeld charges etc. It also serves as a handy tool for arithmetic manipulations on fields defined in real space and to inter-convert between crystal structure and field file formats.

1.12.4 NBO

The natural bond orbital (NBO) code utilizes the first-order reduced density matrix of the wavefunction, and transforms it into localized one-center ("lone pair") and two-center ("bond") elements of the Lewis bonding picture [19]. The program first determines the natural atomic orbitals (NAOs), natural hybrid orbitals (NHOs), natural bond orbitals (NBOs), and natural localized molecular orbitals (NLMOs), and then uses these to perform natural population analysis (NPA) and so on. The NBOs are eigenfunctions of the density matrix, and are said to be "natural" in the sense of Löwdin, because they have optimal convergence

properties for describing the electron density [94].

1.12.5 SSAdNDP

The solid state adaptive natural density partitioning (SSAdNDP) is an extension of the AdNDP to periodic systems. The electronic structure of periodic systems are mostly described in the reciprocal space [95], hence orbitals from an electronic structure calculation of a periodic system are represented on a grid of points spanning the Brillouin zone (reciprocal space equivalent of the unit cell), known as k-space, yielding a set of density matrices $P^{k,AO}$. In SSAdNDP, the set of $P^{k,AO}$ are transformed to their corresponding natural atomic orbital basis $P^{k,NAO}$ [96]. The new $P^{k,NAO}$ is now Fourier transformed to it's corresponding basis in real space $P^{0s,AO}$ which is now used as the starting density to search for localised bonding orbitals as explained in section 1.3.

It is necessary to note that SSAdNDP is aimed at accounting for all electrons within the central unit cell, this is necessary to account for the symmetrically equivalent bond between atom i in unit cell $-s$ and atom j in unit cell 0. Hence Identifying both bonds leads to double counting, but the contribution of both hybrids in the central unit cell must be depleted to prevent inclusion of either in an $n+1$-center bond [24].

1.12.6 LOBSTER

The Local Orbital Basis Suite Towards Electronic Reconstruction (LOBSTER) program is designed to extract bonding information from the energy band structure of solids by means of density functional electronic structure calculations. This energy resolved method is known as the Crystal Orbital Hamiltonian Population (COHP) [26]. The COHP analysis is a theoretical bond detecting tool for solids which partitions the band structure energy into orbital-pair interactions. The COHP diagram shows region of bonding, non-bonding and anti-bonding within a specific energy range.

1.12.7 PICMD

The Path Integral Centroid Molecular Dynamics (PICMD) simulations carried out in this work were performed using an in-house, parallelised MD code that employed the Thole-type interaction potential for water (TTM2.1-F) model simulated in an NVT ensemble. PICMD replaces each quantum particle with a p-harmonic-beads ring-polymers ($p \geq 16$) and formulates the equation of motion with the centroid of the harmonic ring [97]. In this work, 16 beads were used to mimic the quantum nature of each hydrogen and oxygen atom. The code was originally written by Dr. Burnham and modified to run on MPI by Dr. Yong Xue.

1.12.8 OCEAN

The OCEAN (Obtaining Core Excitations from *Ab initio* electronic structure and NBSE) code where NBSE refers to the NIST BSE solver, is a first-principles code based on both DFT and BSE. It calculates core level excitation by solving the BSE numerically [86]. It first sets up and parses the input files, then it performs an atomic calculation to construct optimal projector functions (OPFs) similar to the PAW method which orthorgonalizes the valence and core states, followed by a DFT calculation.

Unlike other current codes where the frozen core hole approximation is made, the OCEAN code considers both electron-electron correlation (GW approximation) and electron-hole interactions (BSE) which is expensive to compute, but the code reduces the time required to calculate the screening response to the core hole by treating it as an atomic problem since the screening is highly localized around the excited atom. The electron-electron problem is limited by the range, so one select a cutoff to eliminate numerous small excitations. Hence the electron hole attraction is screened using the Random Phase Approximation (RPA) $\chi_0 = iGG$, where χ_0 is the response function which is unique to each atomic site. The screening method implemented in the OCEAN code makes it an excellent choice for computing core excitation spectra (XAS and XRS) using all the atoms in the model. Finally it solves the BSE in a CNBSE directory.

Chapter 2

Structure and Bonding Analysis of K_2Ag and K_3Ag

2.1 Introduction

In solid-state science, one of the main goals is to design and create materials with desired electronic and structural properties. These properties often change in response to variations in external conditions such as temperature and pressure. Hence, it is essential to have an immense understanding of the structure of solids and the chemical bonding which favours the aggregation of atoms into structures. Atomic orbital hybridization and the number of valence orbitals available for bonding formulates the concept of directional chemical bonds and structural prediction of elemental solids [98]. A recent review on the high pressure crystal structures and properties from a chemical perspective can be found in Ref.[99]. The development of diamond anvil cell (DAC) techniques have made high pressure attainable experimentally up to 1,000GPa [12, 13, 14, 15, 16, 17]. Theory on the other hand is able to probe pressure ranges beyond present experimental capabilities, thanks to several computer simulation methods such as DFT [32]. This possibility of attaining high pressure theoretically and experimentally has driven research into several vast areas, one of such research areas which is of immense interest is the development and synthesis of unusual compounds that have atypical stoichiometries different from common textbook stoichiometries and not also obtainable at ambient conditions. For instance, rather than forming H_2S, hydrogen and sulphur have been found to form an atypical H_3S stoichiometry under pressure and this H_3S was found to be superconducting with a critical temperature, T_C as high as 203K [100, 101]. Similarly, a large variety of unusual compounds have been predicted or synthesized under high

pressure and have been summarized in the recent review paper of Miao *et. al* [13]. Following the discovery of several unusual compounds with non-intuitive structural modifications, it is obvious how greatly pressure can modify and enrich chemistry. These enormous progress in the synthesis and discovery of high pressure compounds by experiment and theory have called for great advancement of conceptual frameworks which includes our understanding of the chemical bonding, related to the orbital hybridization and modification of matter under pressure [99, 13]. Under compression, the size and electron concentration of alkali metals change enormously. This unique property results in the significant change of the solid sate chemistry of these elements, which in turn favours the formation of alkali-metal transition metal alloys at elevated pressures. The relative accessibility of intermetallic compounds made them gain practical use long before they got recognized as chemical objects. These set of intermetallic compounds follow the usual valence rules and are formed by elements around the Zintl line (the line between group 13 and 14) on the periodic table or left of it i.e down to group one [102]. In the early 1930s, Eduard Zintl [103] first discovered phases with a crystal structure of the NaTi type that constitute a special group of intermetallic compounds which F. Laves [104] called Zintl phases [105]. These Zintl phases are special intermetallic compounds because they can simply be understood by recognized valence rule known as the Zintl-Klemn concept [106]. Zintl noted that the structure of these Zintl phases were characterized by total electron transfer to the more electronegative element in the structure and hence form ionic structures. Contrary to the Zintl phases, the definition of Lave phases (classified by AB_2 intermetallics) follow the general Pearson rule which defines the number of homonuclear bonds per atom within the anionic part of a crystal structure [107]. A recent review of the functional and structural applications of Lave phases is summarized in Ref. [108]. Elemental potassium have been reported to undergo up to 6.7 times change in the volume when compressed from ambient pressure to 112GPa [109]. This large compressibility of K is accompanied by electronic structure changes. Miedema's rule [110, 111] which govern the formation of intermetallic phases states that elements of similar valence electron density and a large electronegativity difference ($\Delta\chi$) are more likely to form thermodynamically stable alloys. Hence, intermetallics involving alkali metals such as K, Rb, Cs and transition metal such as Ag, and Ni are not obtainable at ambient conditions because they possess

much smaller charge densities relative to transition metals. However, it has been shown that these alkali metals of K, Rb, Cs can assume transition metal characteristics as a consequence of their pressure induced $s \rightarrow d$ hybridization [112, 113]. Occupation of the d band of these alkali metals at elevated pressures enable the formation of complex intermetallic phases.

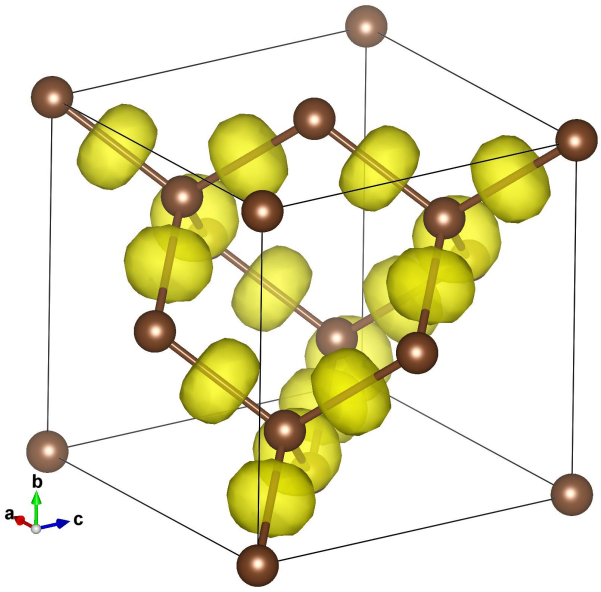

Figure 2.1: A typical electron localization function of Fd-3m diamond at 0.8 isovalue.

For example, Atou et. al. [114] reported the formation of two alkali metal-transition metal compounds, K_3Ag and K_2Ag. These compounds were reported to rapidly form at room temperature upon compression of stoichiometric mixtures of the elements at 6.1GPa - a pressure far less than the 26GPa required for the s to d transition in elemental alkali metals. Hence, the aim of this work is to provide a chemical interpretation of the potassium silver intermetallics while also benchmarking accurate high pressure description of bonding by employing all the known bonding analysis methods. It may be of interest to know that at ambient pressure, bonding analysis is pretty straightforward because the electrons can be easily localized to create a bonding picture. Let's take for instance, the simple case of the structure of diamond which has a face centered cubic structure with Fd-3m space group. The crystal structure of diamond is well understood with the carbon atoms forming tetrahedral co-ordinations as can be seen in Figure 2.1. The C atoms are said to be covalently bonded as evident from the electron localization function (ELF) with the electrons localized

along the C-C bonds at 0.8 isovalue. On the other hand, as pressure increases, the structure, bonding features and electronic states of matter also changes which makes structural description from a bonding perspective non-trivial. Following laid down rules used to rationalize the aforementioned pressure induced modifications, several previously discovered structures from experiments or computations were found to agree with expectations of close-packing and homogeneity [115, 116, 117]. That is, a wide variety of the known compounds greatly becomes more homogeneous in response to pressure while also exhibiting several features which includes the compression of longer and weaker bonds to a greater extent, increased coordination number, adoption of close-packed structures, attaining higher symmetries and in addition show insulator-metal transition due to the delolalization of their electrons at elevated pressure [115, 116, 117]. However, several stoichiometric compounds whose structure and bonding cannot be intuitively understood have been observed, one of such compounds are the K_3Ag and K_2Ag stoichiometric mixtures of potassium and silver which have been studied in this chapter. More also, it is important to point out that not all matter becomes more homogeneous under pressure. For instance, it has been shown that many metals, such as Li and Na, assume complex open structures which exhibit a decrease in conductivity under high pressure [118, 119]. Recent experimental and theoretical studies are beginning to remarkably show that the geometries and properties of observed stoichiometric compounds are impacted profoundly, much more than could have been previously anticipated. Some of the said compounds often take up really surprising and non ideal structural and bonding schemes. A typical example is a classes of compounds composed of electrides i.e compounds where electrons are so localized that they even detach from all atoms and accumulate in the interstitial sites [120, 121]. Thus, there are large variety of stoichiometric structural compositions with unpredictable properties found at high pressure which makes high pressure chemistry complex. Hence, there is need for a benchmark of bonding and structural description of high pressure stoichiometric compounds which motivated this study of unmixable K and Ag that forms K_3Ag and K_2Ag compounds on the application of pressure.

This chapter discussed the common bonding analysis methods applied to interpret the electronic structure and bonding of the K_3Ag and K_2Ag alloys reported by Atou et. al. [114]. The methods employed are based on two approaches, first the plane wave basis set methods

(Quantum theory of Atoms in Molecules (QTAIM) and wannier orbitals) and the localized basis set dependent methods (Natural Bond Orbital Analysis (NBO), Solid State Adaptive Natural Density Partitioning (SSAdNDP), Crystal Orbital Overlap Population (COOP) and the Crystal Orbital Hamiltonian population (COHP)). As already established above, the need for a complete description of the electron transfer which favours the K_3Ag and K_2Ag intermetallic formation stems from the fact that at ambient pressure K and Ag are immiscible, however, they form compounds on the application of pressure. We found that these bonding analysis techniques must be applied with care due to the extensive modification of the electron density on application of pressure. Hence, a naive localized description is not appropriate and may lead to erroneous interpretation.

2.2 Computational Details

All structural optimizations, charge densities and electronic band structures were calculated using the Vienna *ab initio* Simulation (VASP) code [85] and Projector Augmented plane Waves (PAW) potential [93]. The K potential employed $3p^6$ $4s^1$ as valence states while the Au potential employed $4d^{10}$ $5s^1$ as valence states, with the Perdew-Burke-Ernzerhof (PBE) exchange correlation functional [37]. In other to get a real space description of the bonding, the plane wave calculations were projected into a localized atomic orbital picture. Search for localized and delocalized multicenter (n center 2 electron) bonds were done using the Solid State Adaptive Natural Density Partitioning (SSAdNDP) code [24]. The Gaussian type atom centered basis set used for the projections included many empty and diffuse orbital with exponents less than 0.1 in other to ensure that the density matrix used in the search for multi-center bonds accurately mimics the plane wave results. The wannier90 code [87] interfaced with VASP was used to obtain the band structure from a GW [88] calculation, disentangle the various bands and generate the Wannier orbitals corresponding to the disentangled bands. Further bonding information was obtained from the energy band structure by calculating the COOP and COHP as implemented in the Local Orbital Basis Suite Towards Electronic Reconstruction (LOBSTER) program [89]. The topological analysis were performed using the Critic2 program to obtain all the bond critical points (BCPs) and the topological properties at the found BCPs [91]. In addition, the bond orders were obtained using the density derived electrostatic and chemical (DDEC6) method implemented in the Chargemol programs [92]. All visualizations were done using Visualization for Electronic Structure Analysis (VESTA) [122].

2.3 Results and Discussion

2.3.1 Hexagonal P6/mmm K_2Ag

We start with a description of the K_2Ag which has a hexagonal P6/mmm structure. This structure has a first nearest neighbour distance of 3.44Å between the Ag atoms at 4.0GPa

and form layered chains stacked along the crystallographic **a** axis as shown in Figure.2.2a. The second nearest neighbour distance at the same pressure has an Ag-Ag distance of 5.54Å and form hexagonal planes of Ag atoms stacked along the crystallographic **c** axis with an interlayer spacing of 3.77Å evident in Figure.2.2b. Similarly, the K atom in this structure form graphitelike sheets intercalated between the Ag hexagonal sheets. Having understood the atomic arrangements in the structure, further analysis were performed to interpret the chemical bonding by employing all available bonding analysis methods.

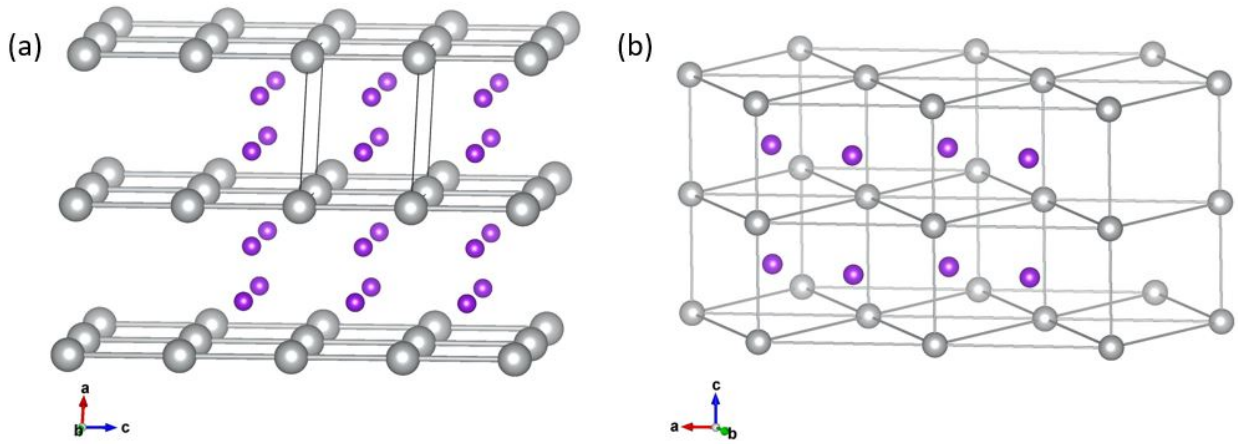

Figure 2.2: Crystal structure of hexagonal P6/mmm K_2Ag with the K atoms in purple and Ag atoms in silver

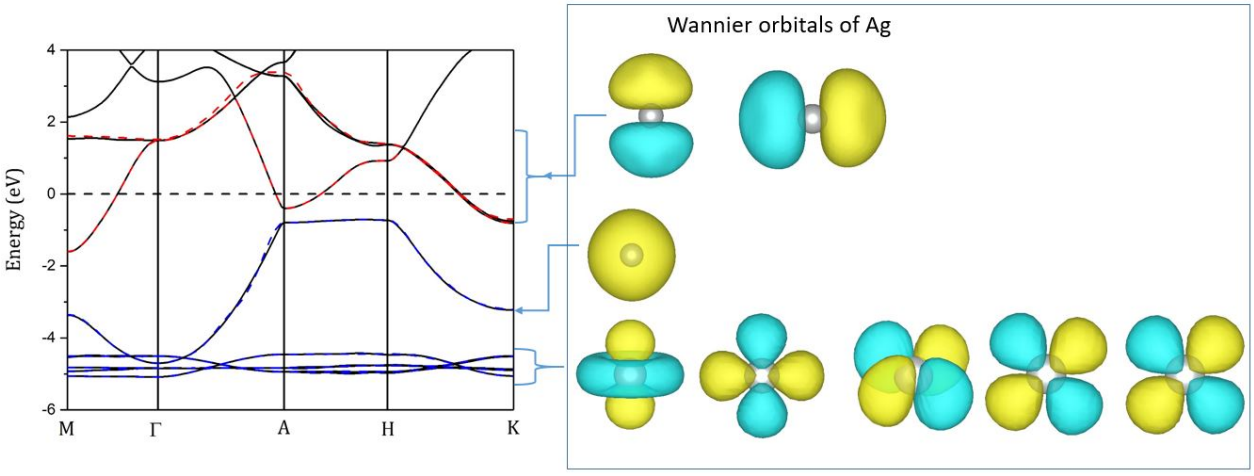

Figure 2.3: Disentangled band structure and corresponding Wannier orbitals of hexagonal P6/mmm K_2Ag centered on the Ag atom.

Previous report by Tse. et. al. [123] have investigated the role or individual contributions of the Ag and K atoms to the total band structure. By comparing the band structure of the total K_2Ag and corresponding hypothetical $\square_2Ag$ with the K atoms removed, the authors reported that the K atoms do not appreciably contribute to the occupied energy levels and fairly contribute to the bonding. Hence, to determine if the K atoms are truly spectators in the K_2Ag intermetallics, the K_2Ag have been extensively studied here. The disentangled band structure and corresponding wannier function of the K_2Ag at 4.0GPa is shown in Figure 2.3. From the energy corrected band structure, we notice some band mixing on the Γ point and we can also tell the structure is metallic with the band crossing at the fermi level (0eV). To accurately disentangle the bands in the lower valence state, we employ a projection based method with the inner and outer disentanglement energy windows set to -6eV and 0eV respectively. As can be seen in Figure 2.3, the obtained wannier orbital from this disentanglement shows that the band mixing are primarily due to s and d orbitals of Ag atom. The localized bands between -4eV and -5.2eV corresponds to the 5d orbitals of the Ag atoms which are lone pairs and do not contribute to the bonding in the structure. Similarly, we proceed to disentangle the bands around the Fermi level by freezing states up to the Fermi level, with the inner and outer energy window in this case set to -2eV and 4eV. It is important to note that the choice of disesntanglement window greatly determines the projection quality. We explored several energy windows and ensured the chosen inner and outer windows contains the total number of desired wannier functions. The obtained wannier functions around the Fermi level are mostly p-orbitals centered on the Ag atom as shown in Figure 2.3. Hence, from the obtained wannier orbitals, we can tell the band structure of the K_2Ag is primarily dominated by s p and d orbitals of the Ag atom with very minimal contributions from the K atom. This finding, corroborates with previous reports but still insufficient to completely answer the question "what is the role of K and bonding nature of K_2Ag?". To further answer the aforementioned question, the Natural Bond Orbital (NBO) and Solid State Adaptive Natural Density Partitioning (SSAdNDP) methods were employed to probe the existence of Ag-Ag, K-Ag and K-K bond interactions in the hexagonal K_2Ag intermetallics. It is important to first note that NBO's are localized few-center orbitals (i.e typically one or two center, but occasionally more) which truly presents a compact description of the Lewis-like

molecular bonding pattern of an electron pair [19]. This method is a basis set dependent method which require an optimal choice of the basis set to accurately project results from a plane wave calculation into a localized orbital picture. For this reason, several tests were performed on the potassium silver intermetallics to find an optimal basis set that accurately projects the plane wave result with minimal spread. Occasionally, manual modifications had to be made to the Gaussian basis set parameters in other to include diffuse orbital but still tight and make it more flexible in other to accurately and completely reproduce the results from the plane wave calculation. Plane wave DFT calculation was first performed on the hexagonal P6/mmm K_2Ag structure at 4.0GPa, then a quadruple-zeta Atomic Orbital (AO) basis set such as the def2-QZVP [124, 125, 126] was used to represent the projected plane wave density into Natural Atomic Orbital (NAO) basis with a projection spillover of the order 10^{-2}. The NBO hybridization for the s, p and d orbitals of Ag are 1.64, 0.64 and 10 electrons respectively while that of the K atom are 0.29, 0.24 and 0.02 electrons for the s, p and d orbitals respectively. It is evident from the NBO hybridization of the K and Ag atoms that there is indeed an electron transfer from the K atoms to the Ag atoms. However, the electrons donated by the K atom does not go to the p orbital of Ag alone, rather it fills the s orbital of Ag as well. Having obtained the orbital occupancy from the NBO analysis, the resulting density matrix from the projection of the plane wave result to NAO basis was further analyzed by using the SSAdNDP to search for muti-center two electron bonds (i.e nc - $2e^-$ bonds) where number of centers can be 1,2,3. . . ,n. The 2c - $2e^-$ bond search recovers the Ag-Ag, K-Ag and K-K bonds with occupation numbers way less than two electrons as shown in table 2.1. The low occupation number makes sense since the K_2Ag binary is metallic and at elevated pressure with the electrons more delocalized.

2c-2e^- Bond	Occupation Number (ON)
Ag-Ag	0.96
K-Ag	0.94
K-K	0.62

Table 2.1: Solid State Adaptive Natural Density Partitioning (SSAdNDP) analysis of K_2Ag .

Atom	Bader Charge	NBO Charge	DDEC6 Charge
Ag	-1.171	-0.961	-1.018
K	+0.585	+ 0.480	+0.509

Table 2.2: Bader, natural bond orbital (NBO) and density derived electrostatic and chemical (DDEC6) charge analysis of K_2Ag.

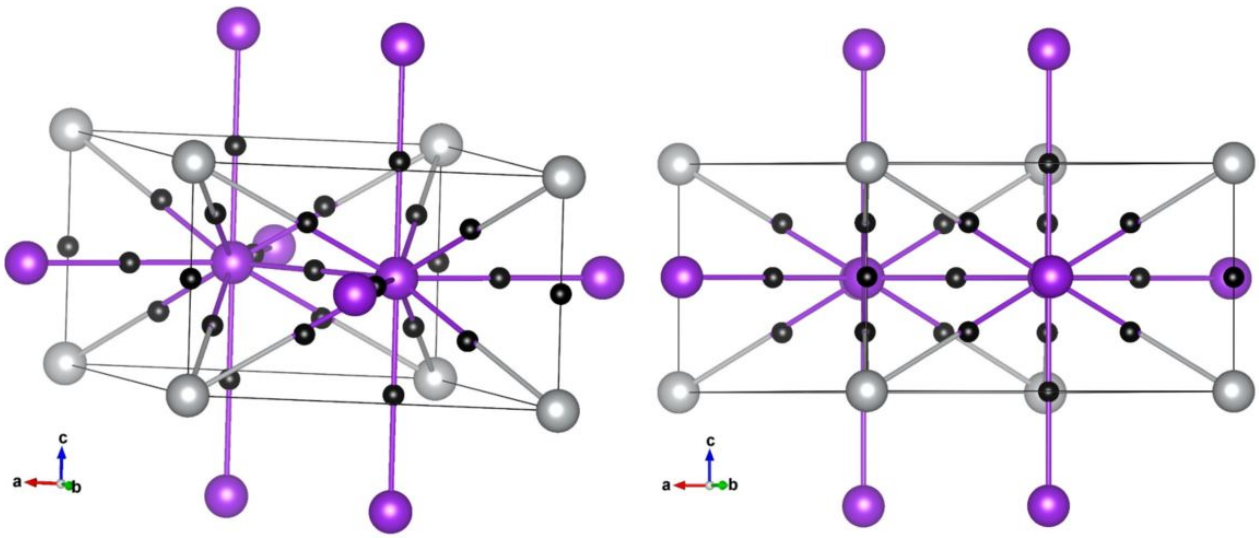

Figure 2.4: Bond critical points of hexagonal P6/mmm K_2Ag. Colour code; Purple=K atom, Silver=Ag atom and Black=Bonds critical point.

In other to account for the electron sharing, we computed the Bader charges on the Ag and K atoms summarized in table 2.2. Due to the higher electronegativity of silver, it is expected that the potassium atoms donate electrons to the silver as in this case each K donates about +0.585 electrons to the Ag atom. The Bader charges indicate electrons have been transferred from K to Ag in the K_2Ag intermetallics, this supports the already recovered bonding interactions using the SSAdNDP. Other charge analysis methods such as the NBO and the density derived electrostatic and chemical (DDEC6) [92] were also employed to extract the atomic charges of K and Ag in the K_2Ag as shown in table 2.2. The DDEC6 have been employed in this work because, in addition to atomic charges, it also gives a comprehensive description of the bond order which is an indicator of the bond strength. The magnitude of the obtained atomic charges from all three charge analysis methods slightly differ from each other, however this is not a problem because the charges are partitioned

differently in NBO, Bader and DDEC6 methods, hence the important thing to check is the trend of the obtained charges which has to be consistent. As can be seen in table 2.2, the Bader, NBO and DDEC6 charges reveal the K atom is the electron donor while Ag is the electron acceptor, hence there is a consistent trend in the charge transfer from all methods. Quantum mechanical description of molecular structures have been simplified by the Baders Quantum theory of Atoms in Molecules (QTAIM) [27, 28, 29], which we have introduced in chapter one. QTAIM identifies points where the gradient of the electron density vanishes i.e. $\nabla\rho(r_c) = 0$, these special points r_c are called critical points (CPs) and are characterized by their rank and signature labelled as (ω, σ). The rank of a CP corresponds to the number of non-zero curvatures (eigenvalues of the Hessian matrix) of $\rho(r_c)$ at the CP, while the sum of the signs of the curvatures of $\rho(r_c)$ at the CP denotes its signature. The charge density at the critical point ($\rho(r_{BCP})$) and its Laplacian ($\nabla^2\rho(r_{BCP})$) are valuable pieces to reveal essential information about the strength and type of interaction. The absolute magnitude of the charge density at the bond critical point indicates the relative strength of the bond while its Laplacian characterizes the nature of interatomic interaction between the bonding atoms. A negative Laplacian at the bond critical point is an indicator of a covalent bonding interaction while a positive Laplacian may be attributed to a closed shell interaction. Several other topological parameters such as the potential energy density ($V(r_{BCP})$), kinetic energy density ($G(r_{BCP})$) and total energy density ($H(r_{BCP})$) at the bond critical points are also essential quantities in the characterization of the bonding strength and type. In other to visualize the bonds in the K_2Ag intermetallics, there is need for topological analysis from QTAIM to obtain the bond critical points. From the critical point analysis, we obtained three non-equivalent bond critical points with the critical point list and bond orders shown in table 2.3. The obtained critical points satisfy the Morse sum (nuclear - bond + ring - cage = 0) and the topological distribution is valid [127]. The densities ($\rho(r_{BCP})$ at the bond critical point are relatively small with all the Laplacian ($\nabla^2\rho(r_{BCP})$) at the bond critical points being positive which indicate charge depletion in the bond critical point and suggest a closed shell interaction between the atoms. A visual representation of the bond critical points (black colour) in the unit cell is shown in Figure 2.4. The corresponding bond orders for the Ag-Ag, Ag-K and K-K bonds are summarized in table 2.3. From the computed bond order

using the DDEC6 method, the Ag-Ag bond has the largest bond order which is almost twice that of the Ag-K interaction. The density at the bond critical point ($\rho(r_{BCP})$ which is also an indicator of bond strength can be seen to follow the same trend as the actual calculated bond order.

Bond	d(Å)	Bond Order	$\rho(r_{BCP})$ (ea_0^{-3})	$\nabla^2(r_{BCP})$ (ea_0^{-5})	V (E_h)	G (E_h)	H (E_h)	G/ρ $(E_h e^{-1} a_0^3)$
Ag-Ag	3.437	0.296	0.015	0.017	-0.007	0.006	-0.001	0.366
Ag-K	3.626	0.106	0.008	0.018	-0.004	0.004	0.001	0.476
K-K	3.191	0.072	0.007	0.032	-0.004	0.006	0.002	0.847

Table 2.3: Characterization of atomic interaction in K_2Ag from QTAIM. Where a_0 and E_h are bohr and hartree units respectively.

The Crystal orbital Hamiltonian population analysis (COHP) method was employed to identify the orbital contributions to the bonds from a localised basis set picture. The COHP is a local basis set method which partitions the bands-structure energy in terms of orbital pair contribution by projecting the results from a plane wave calculation into linear combination of atomic orbitals (LCAO) [89]. Thus, one can easily identify regions of bonding and antibonding from an energy-resolved COHP(E) plot. Given that this method have been previously applied to partition band structure of solid state systems [128], we apply it to further extract bonding information from the bandstructure of the K_2Ag. Having obtained an $\approx 99\%$ overall projection of the plane wave orbitals to localized orbitals using the projection scheme defined in ref.[128] as implemented in the LOBSTER code [89]. A comparison of the plane wave and LCAO orbital decomposed density of state from VASP and LOBSTER respectively is necessary to ensure the true valence orbitals of the K and Ag atoms are completely reproduced. In addition, it is also important to check the individual band overlaps at each K-point to ensure the diagonals are approximately one. This band overlap check was done for all the K-points for each of the atoms in the K_2Ag intermetallics. Figure 2.5 shows the projected desity of state (PDOS) of the K atom using a plane wave method (VASP) and basis set method (LOBSTER). The PDOS from the plane wave method show

very little d contribution of K around the Fermi level, this d orbitals were missing from the LOBSTER PDOS due to the fact that the default basis set programmed into the code for K does not contain d orbitals of K and LOBSTER has a fixed basis set which can't be modified by the user. Also, the 3p DOS from the basis set method is extremely small compared to the plane wave method. However, the s DOS profiles from both methods are qualitatively similar. Similar check for DOS reproducibility of the Ag with a basis set that employed 4d 5p 5s orbitals as the projection orbitals was performed as shown in Figure 2.6. The s p and d orbitals in the valence state agree qualitatively as well.

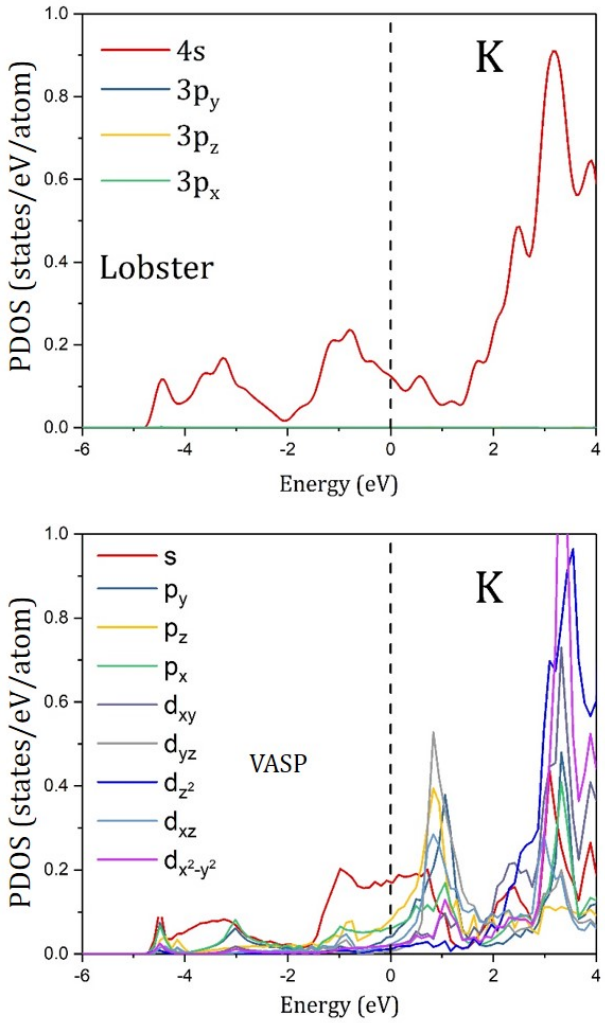

Figure 2.5: Projected density of state (PDOS) of K in the hexagonal P6/mmm K_2Ag using LOBSTER and VASP

Irrespective of the slight variations in the orbital decomposed DOS of the K and Ag using the localized basis set method compared with the plane wave method, a comparison of the total density of state using both methods agree qualitatively and quantitatively up to the Fermi level as shown Figure 2.7. This stunning agreement prompt the question "when can the LOBSTER results be trusted?".

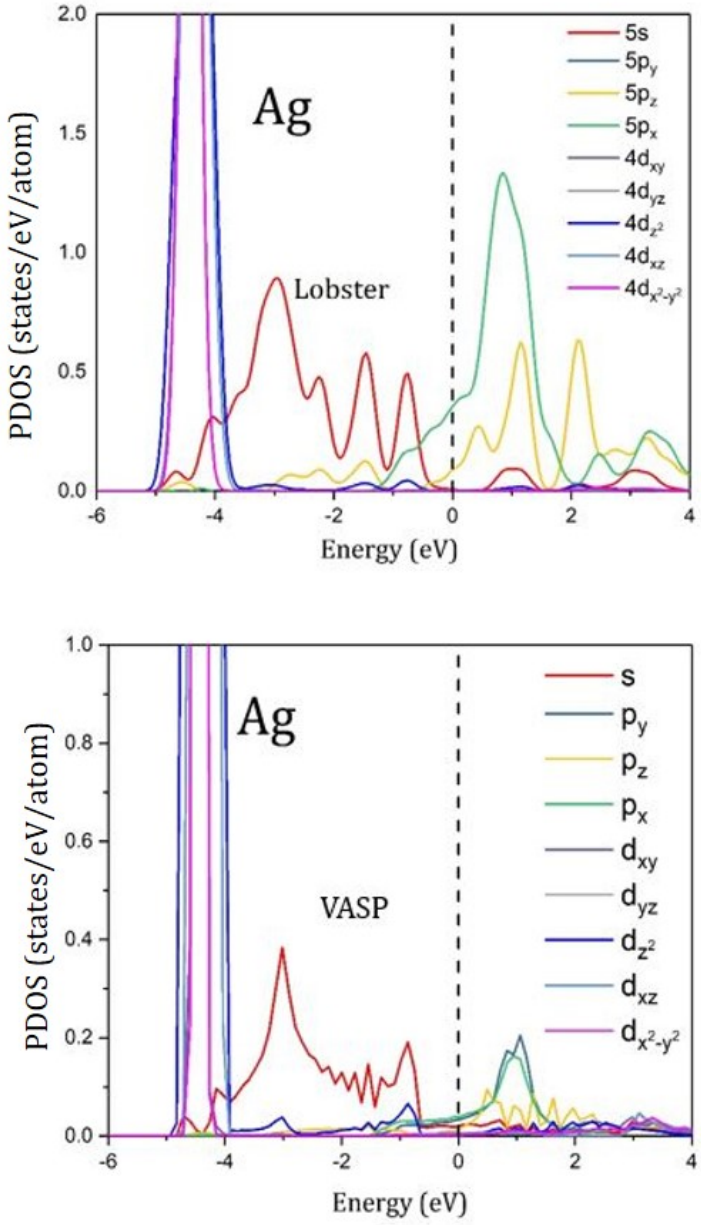

Figure 2.6: Projected density of state (PDOS) of Ag in the hexagonal P6/mmm K_2Ag using LOBSTER and VASP

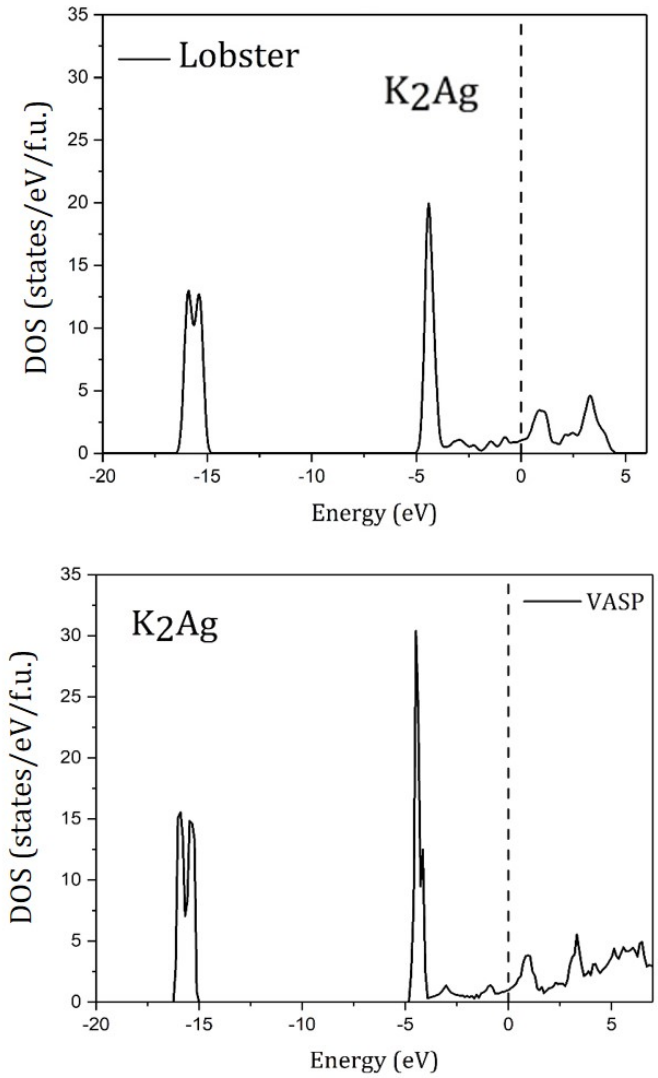

Figure 2.7: Total density of state (PDOS) of the hexagonal P6/mmm K_2Ag using LOBSTER and VASP

Having performed several checks and tests summarized in Appendix A, the recommendation derived is that, irrespective of the projection accuracy from plane wave to LCAO, the accurate way to validate the projected localized orbitals is by comparing the orbital decomposed density of state which gives a quantitative description of how the projected orbitals mimics the original Bloch orbitals. The refine energy resolved -COHP plots of the Ag-Ag, Ag-K and K-K interactions were calculated and shown in Figure 2.8. The positive and negative -COHP axis denotes bonding and anti-bonding regions respectively.

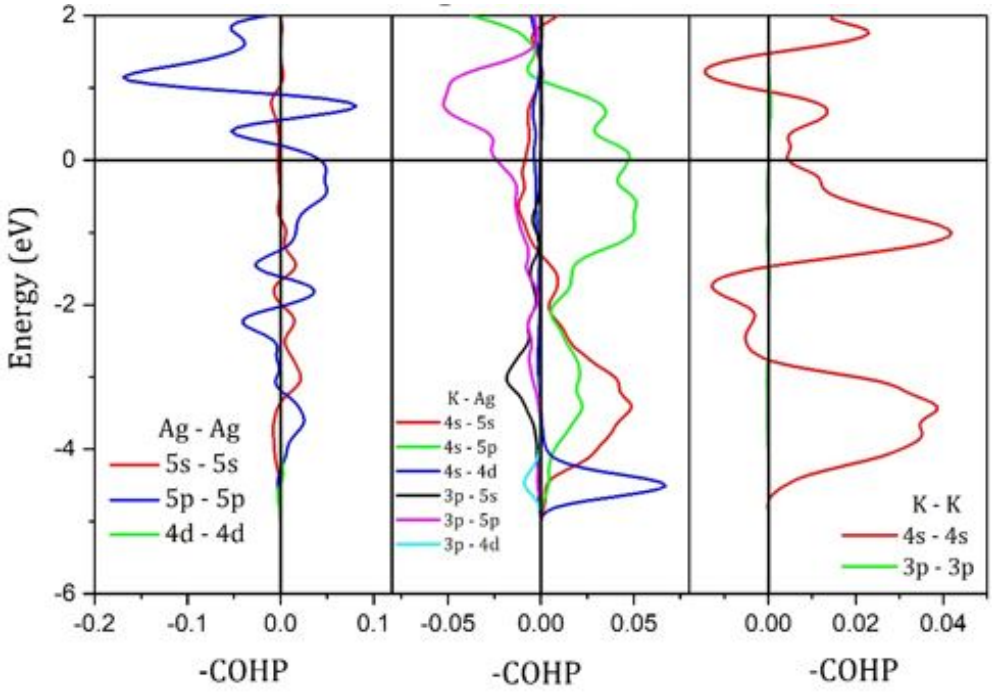

Figure 2.8: Crystal orbital Hamiltonian Population (COHP) of hexagonal P6/mmm K_2Ag. The positive and negative -COHP axis denotes bonding and ant-bonding regions respectively.

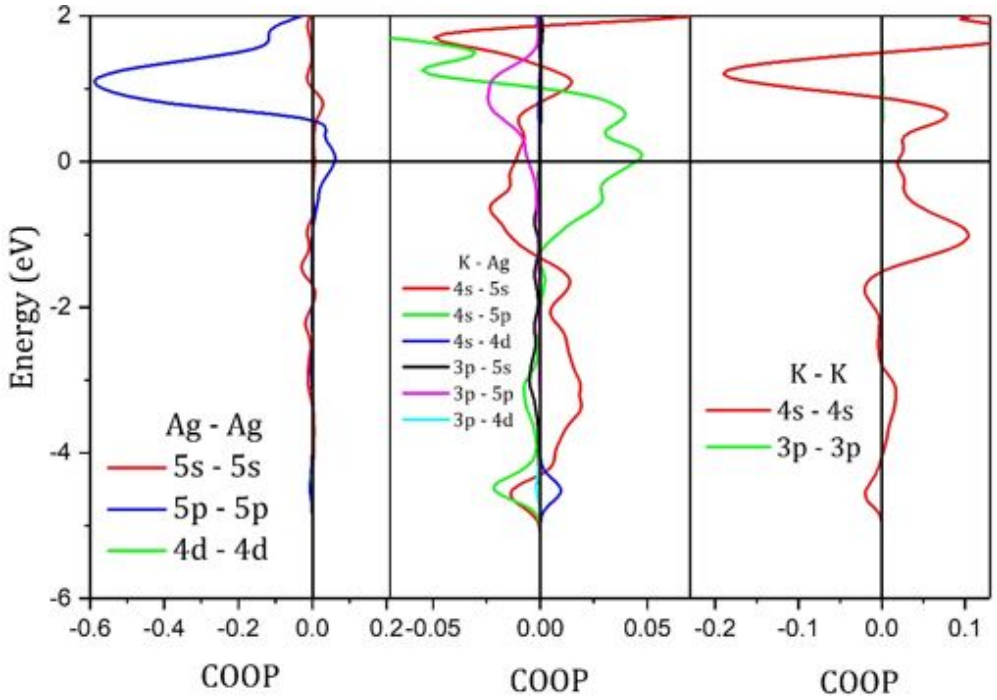

Figure 2.9: Crystal orbital overlap Population (COOP) of hexagonal P6/mmm K_2Ag. The positive and negative COOP axis denotes bonding and ant-bonding regions respectively.

For the Ag-Ag interaction, the 4d orbitals of Ag are non-bonding as they constitutes bonding and anti-bonding states between -3.8eV and 5.8eV. The Ag-Ag bonding interaction is mostly due to silver 5p orbitals. A similar analysis show the K-Ag bond interaction is primarily formed by the 4s and 5p orbitals of K and Ag respectively, where a combinations of all the Ag projected orbitals with the 3p orbital of K constitute the anti-bonding states. Also Figure 2.8 shows that the bonding interaction between the K atoms is mostly formed by the 4s orbitals of K. The 3p-3p contribution can be seen to be nearly zero similar to the 3p projected density of state for the K atom using the basis set method. The obtained results here suggest that the K atoms significantly contribute to the bonding and stability of the K_2Ag. It is important to note that the integrated crystal orbital Hamiltonian population (ICOHP) can provide information on the bond strength but cannot be regarded or treated as the actual bond order. Hence, the bond orders presented in table 2.3 reveal that the Ag-Ag is the strongest bond in the P6/mmm K_2Ag intermetallics followed by the K-Ag bond. Similar to the COHP method, the COOP is able to also extract bonding information from the overlap population by partitioning the electron number. The positive and negative COOP regions corresponds to the bonding and anti-bonding regions respectively. Hence, the calculated COOP for the K_2Ag is plotted in Figure 2.9 and the COOP plot also shows that the Ag-Ag interaction is mostly due to the 5p orbitals of Ag while the K-Ag interaction is formed by the 4s and 5p orbitals of K and Ag respectively. Some K-K bonding interaction is also observed around the Fermi level similar to the COHP result. Therefore, the COOP also emphasizes that the K atoms play a significant role in the structure. Hence, the NBO, SSAdNDP, COOP, COHP and QTAIM methods employed to interprete the K_2Ag structure all suggest that the K atom significantly contribute to the bonding of the intermetallics and are thus not spectators in the structure as suggested by the previous report [123]. Similar analysis have also been employed to interpret the higher pressure cubic structure (K_3Ag) of the potassium silver intermetallics at 6.4GPa.

2.3.2 Cubic Fm-3m K_3Ag

Unlike the low pressure hexagonal structure, at 6.4GPa K_3Ag crystallizes in the BiF_3 structure type with Fm-3m space group. In the FCC sublattice the K atoms occupy the octahedral and tetrahedral sites as shown in Figure 2.10. The nearest neighbour Ag-Ag distance here has an exceptionally long length of 5.4Å but similar to the second nearest neighbour Ag-Ag distance of the K_2Ag at 4.0GPa. The first nearest neighbour K-K separation of 3.39Å in the K_3Ag at 6.4GPa is 10% shorter than the K-K separation found in elemental K at the same pressure [114]. These unusual features of the K_3Ag prompts the need for a detailed study of its electronic structure and bonding pattern.

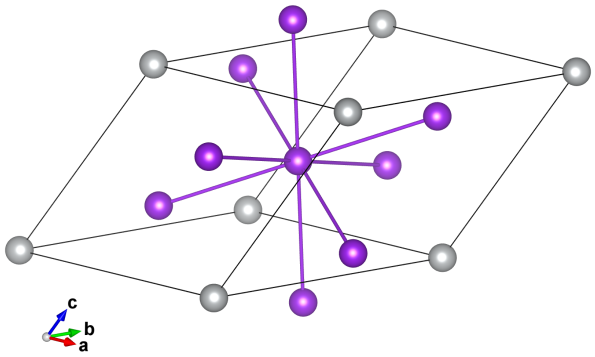

Figure 2.10: Crystal structure of primitive Fm-3m K_3Ag with the K atoms in purple and Ag atoms in silver

Figure 2.11 shows the disentangled band structure and corresponding wannier orbitals of the cubic K_3Ag at 6.4GPa. The lower non-dispersive bands between -4.5eV and -5eV corresponds to the doubly degenerate (e_g) and triply degenerate (t_{2g}) 4d orbitals of the Ag which do not contribute to the bond. Unlike K_2Ag where we noticed an s and d orbital mixing in the lower valence states, the Ag s orbital of the K_3Ag is completely isolated from the d band of Ag with an energy separation of about 1eV. So far, the extracted wannier orbitals in the lower valence level of the K_3Ag reveals the band structure of this cubic phase of the potassium silver intermetallics is dominated by orbital contributions from the Ag atom. This may indicate that the K atoms are insignificant to stabilize the structure. However, using an

inner and outer energy windows of -1eV and 2eV respectively, with the frozen state set to the Fermi level (i.e only states up to the Fermi level are included in the wannierization), the wannier orbitals extracted from the upper valence state and lower conduction bands reveal significant contribution of the K atoms to the bonding states with the obtained wannier orbitals showing a possible s, p and d hybrid orbitals of K formed by the d_{z^2} and $d_{x^2-y^2}$ orbitals of the potassium atom.

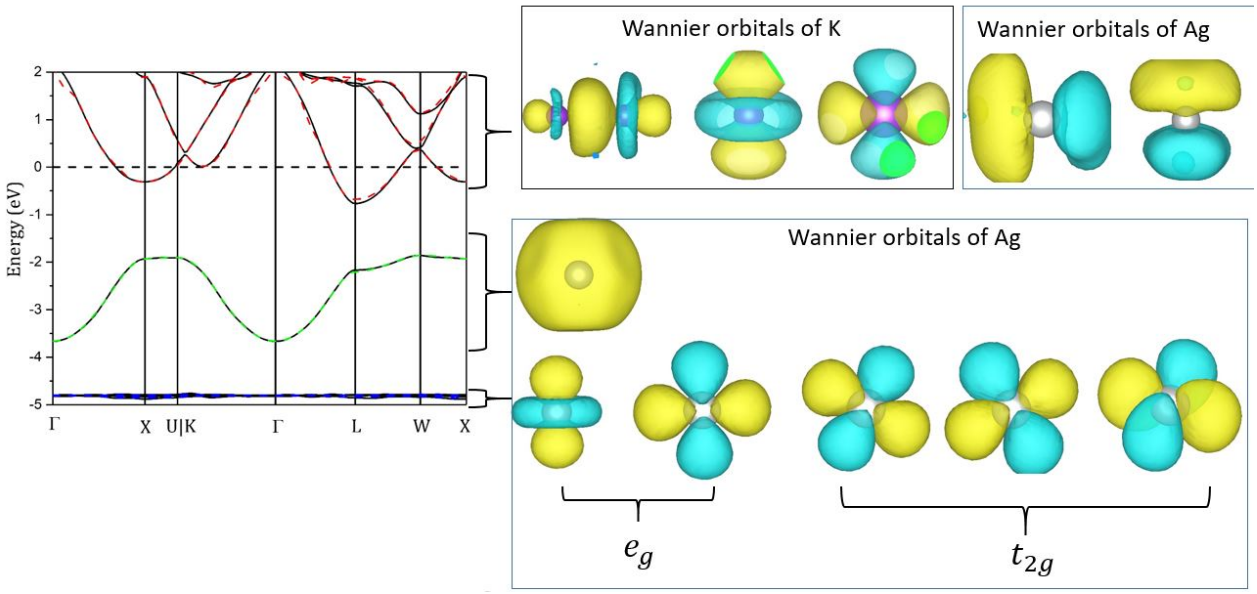

Figure 2.11: Disentangled band structure and corresponding Wannier orbitals of cubic Fm-3m K_3Ag

The character of Wannier functions have been previously reported to relate to the degree of s-p(-d) hybridization and reflect possible muti-center bonds in solids [129]. In addition to the obtained wannier orbitals of K, the upper valence and lower conduction states of the K_3Ag also contains p orbitals of Ag. Unlike the K_2Ag where primarily p orbitals of Ag dominated the bonding state, the K_3Ag in addition shows significant contributions from the K atom as well. Having revealed the character of wannier orbitals corresponding to the various bands in the band structure, an orbital decomposed bonding description is necessary to ascertain the validity of the extracted wannier orbitals. Using a quadruple-zeta Atomic Orbital (AO) basis set, PW density results of the cubic K_3Ag structure were projected into Natural Atomic Orbital (NAO) basis with a projection spillover of the order 10^{-2}. The calculated NBO orbital hybridization for the s, p and d orbitals of Au are 1.55, 0.11 and 10

electrons respectively while that of the K atom are 0.22, 0.29 and 0.02 electrons for the s, p and d orbitals respectively. Following the recovery of the orbital occupancy from the NBO analysis, the SSAdNDP was employed to search for muti-center two electron bonds (i.e nc - $2e^-$ bonds) using the resulting density matrix from the projection. The SSAdNDP bond search recovers the Ag-K2, Ag-K1 and K2-K1 which are 2c - $2e^-$ bonds with occupation numbers way less than two electrons as shown in table 2.4, where K1 and K2 are the two unique K atoms occupying the O_h and T_d point groups respectively. No Ag-Ag bond was found from the SSAdNDP search.

2c-2e^- Bond	Occupation Number (ON)
K2-Ag	1.00
K1-Ag	0.94
K1-K2	0.67

Table 2.4: Solid State Adaptive Natural Density Partitioning (SSAdNDP) analysis of K_3Ag .

Bader charge analysis shown in table 2.5 for the K_3Ag intermetallics at 6.4GPa reveals electron transfer from the electropositive K atoms to the more electronegative Ag. Each K atom contributes approximately $+0.5e^-$ to the silver atoms. A comparison of the Bader charges obtained from the low pressure K_2Ag and higher pressure K_3Ag reveals an $\approx 13\%$ decrease in the Bader charge of each K atom and an $\approx 30\%$ increase in the Bader charge of Ag as the pressure increased from 4.0GPa in K_2Ag to 6.4GPa in the K_3Ag intermetallics. Atomic charges from NBO and DDEC6 analysis are also presented in table 2.5. Though the magnitude of the charges from all three methods slightly vary, they all follow the same charge transfer trend and collectively reveal significant charge transfer from the K atom to the Ag atom as also observed in the lower pressure K_2Ag structure. The observed charge transfer trends for both cases are consistent with the electronegativity difference of the K and Ag atoms.

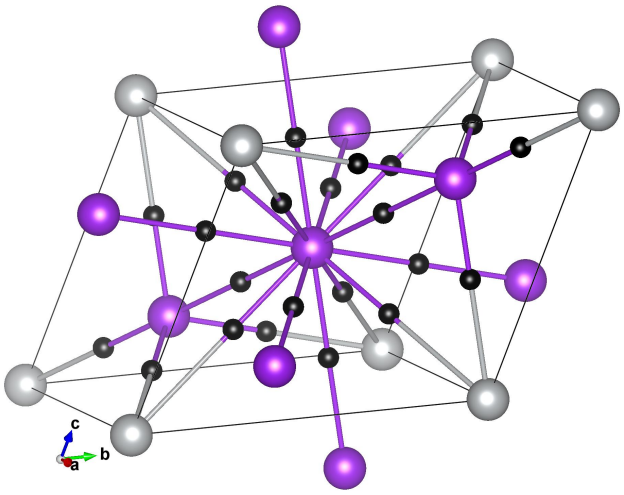

Figure 2.12: Bond critical points of cubic Fm3m K_3Ag. Colour code; Purple=K atom, Silver=Ag atom and Black=Bonds critical point.

Atom	Bader Charge	NBO Charge	DDEC6 Charge
Ag	-1.531	-1.311	-1.361
K1	+0.519	+ 0.451	+0.411
K2	+0.506	+0.430	+0.474

Table 2.5: Bader, NBO and DDEC6 charge analysis of K_3Ag intermetallics.

Bond	d(Å)	Bond Order	$\rho(r_{BCP})$ (ea_0^{-3})	$\nabla^2(r_{BCP})$ (ea_0^{-5})	V (E_h)	G (E_h)	H (E_h)	G/ρ $(E_h e^{-1} a_0^3)$
Ag-K2	3.393	0.195	0.012	0.025	-0.006	0.006	0.000	0.513
Ag-K1	3.918	0.070	0.008	0.009	-0.002	0.002	0.000	0.307
K2-K1	3.393	0.076	0.006	0.018	-0.003	0.004	0.001	0.590

Table 2.6: Characterization of atomic interaction in K_3Ag from QTAIM. where K1 and K2 are the two unique K atoms occupying the Oh and Td point groups respectively

Using the Quantum theory of atoms in molecule (QTAIM) method of Bader [27, 28, 29] for the topological analysis of K_3Ag, we obtained a set of complete critical point list that satisfy the Morse sum (nuclear - bond + ring - cage = 0) for periodic crystals [127]. Three of the

critical points are bond critical points which have been tabulated in table 2.6 along side the bond orders and topological parameters. The densities ($\rho(r_{BCP})$ at the bond critical point are fairly small for the second nearest neighbour Ag-K1 distance as well as the K2-K1 bond interaction. This density at the bond critical point ($\rho(r_{BCP})$ is also an indicator of bond strength and can be seen to follow the same trend as the actual calculated bond order given in table 2.6. From the computed bond order, the Ag-K2 bond has the largest bond order which is over twice that of the Ag-K1 and K2-K1 interactions. All the Laplacian ($\nabla^2\rho(r_{BCP})$) at the bond critical points given in table 2.6 are positive which indicate charge depletion in the bond critical point and suggest a closed shell interaction between the bonding atoms. A plot of the bond critical points (black colour) in the unit cell of the K_3Ag is shown in Figure2.12. The corresponding bond orders calculated using DDEC6 for Ag-K2, Ag-K1 and K2-K1 bonds are shown in table 2.6. It is important to note that topological analysis show no evidence of a covalent Ag-Ag bond interaction in the K_3Ag intermetallics at 6.4GPa. In other to obtain an orbital decomposed description of the bond interactions present in the K_3Ag structure, the COOP and COHP methods have been employed to define which orbitals are responsible for the bonding and anti-bonding states in the K_3Ag intermetallics. The 3p 4s and 4d 5p 5s orbitals of K and Ag atoms respectively were used as projection orbitals to represent the plane wave result in the form of an LCAO as incorporated in the LOBSTER program [89]. As already established from the K_2Ag studies, it is important to compare the PDOS of the individual atoms using the plane wave and LCAO method in other to quantify the completeness of the projection and choice of projection orbitals. Hence, following a good projection of 99% accuracy, the band overlap at each K-point was examined to ensure the diagonals are close to one, after which a comparison of the PDOS was done for the K and Ag atoms in the K_3Ag intermetallics. Figure 2.13 represents the PDOS of K computed using the plane wave (VASP) and the basis set (LOBSTER) methods.

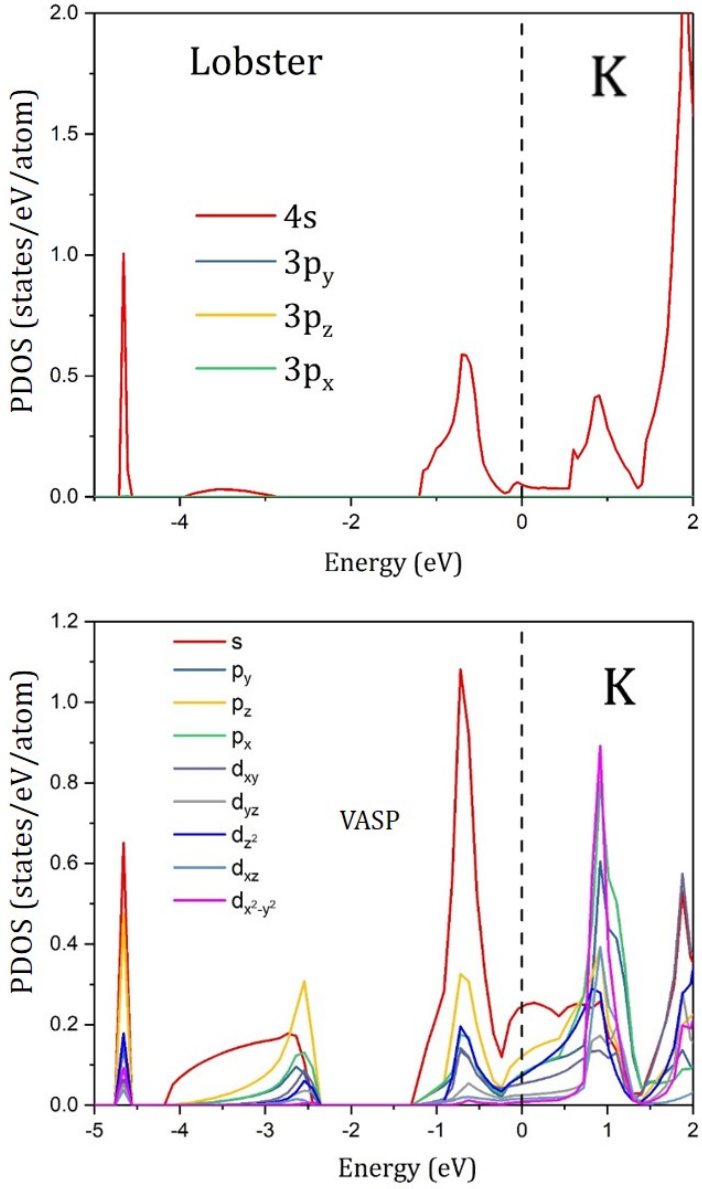

Figure 2.13: Projected density of state (PDOS) of K in the cubic Fm-3m K_3Ag using LOBSTER and VASP

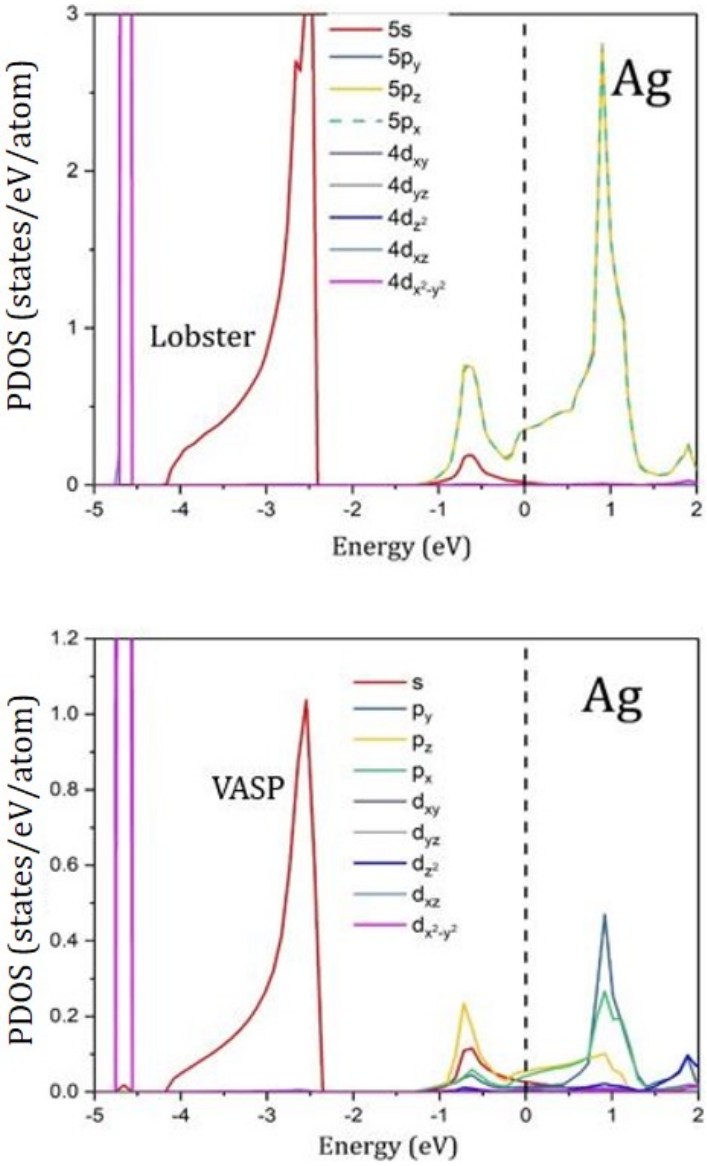

Figure 2.14: Projected density of state (PDOS) of Ag in the cubic Fm-3m K_3Ag using LOBSTER and VASP

The LOBSTER PDOS excluded the 3d orbitals of K due to the limitation in the default basis set, hence, it only reproduces the 4s orbital density of state (with that of the 3p very low when compared to the plane wave method). However, the integrated number of electrons from the LOBSTER and plane wave method PDOS agree with each other. Similarly, the Ag PDOS using both methods are very similar below the Fermi level (Figure 2.14). Irrespective

of the difference in the PDOS from LOBSTER when compared to the plane wave result, the total density of state from both methods is practically indistinguishable below the Fermi level that is responsible for chemical bonding (i.e the upper valence state from -5eV to 0eV) (Figure 2.15). The calculated COHP for the three possible bonding interactions formed in the K_3Ag is given in Figure 2.16.

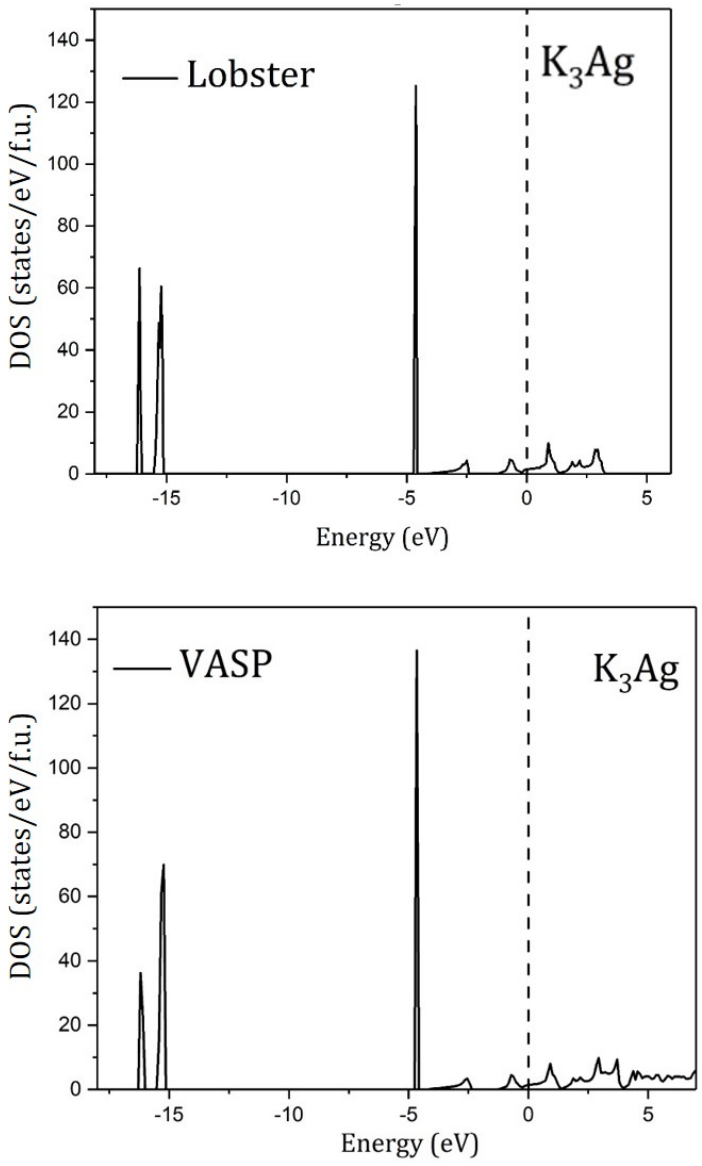

Figure 2.15: Total density of state of the cubic Fm-3m K_3Ag using LOBSTER and VASP

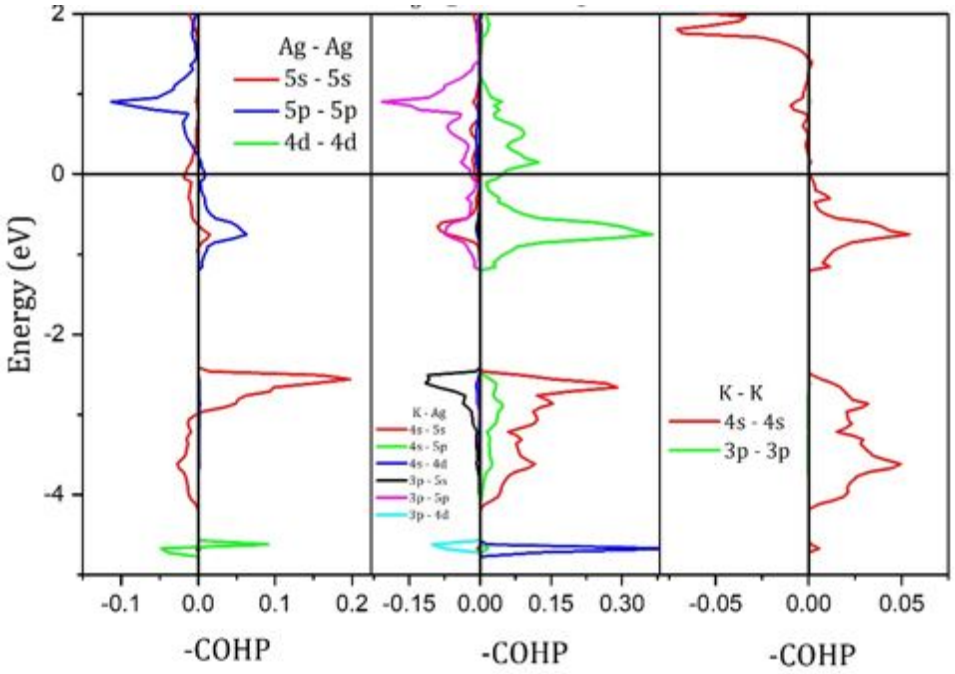

Figure 2.16: Crystal orbital Hamiltonian Population (COHP) of cubic Fm-3m K_3Ag. The positive and negative COHP axis denotes bonding and ant-bonding regions respectively.

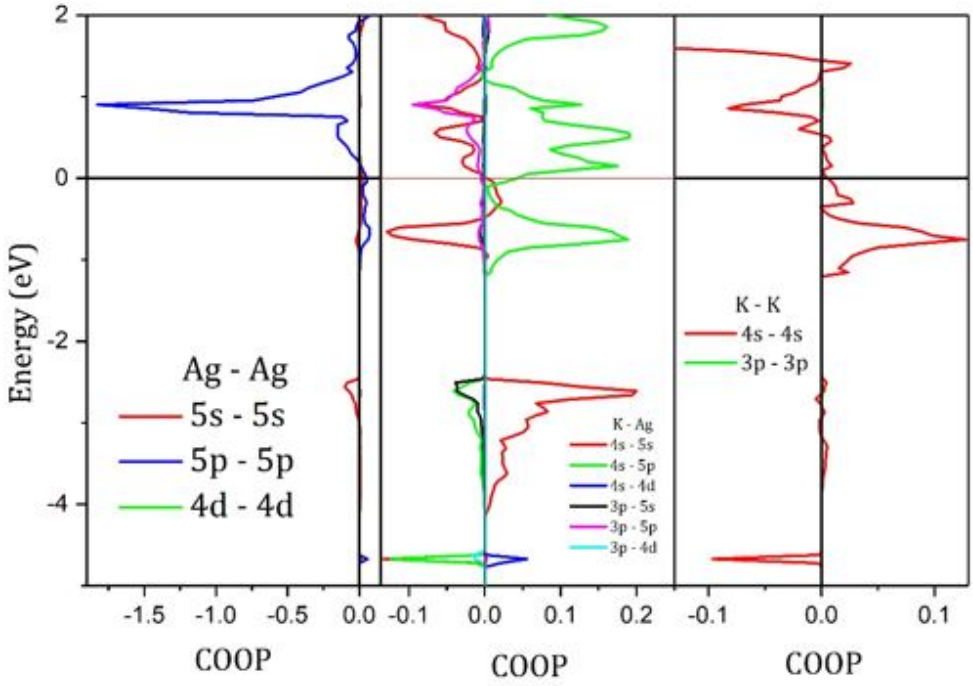

Figure 2.17: Crystal orbital overlap Population (COOP) of cubic Fm-3m K_3Ag. The positive and negative COOP axis denotes bonding and ant-bonding regions respectively.

As noted earlier, the positive and negative -COHP axis corresponds to the bonding and anti-bonding regions respectively. For the Ag-Ag interaction, we observe the 5s-5s and 4d-4d interactions show anti-bonding peak before the bonding peak which contradicts basic chemistry (i.e ideally, it should be bonding before anti-bonding), hence we liken this to an artifact in the computation of the Ag-Ag Hamiltonian population. In other to validate this reasoning, we compare COHP with the COOP of the Ag-Ag interaction shown in Figure 2.17. As can be seen from the COOP, the 5s is completely anti-bonding as expected. Surprisingly, the COOP reveals no Ag-Ag bonding interaction in the K_3Ag. However, the COHP and COOP both show that the K_3Ag forms strong K-Ag bonds through the 4s and 5p orbitals of K and Ag respectively with a relatively weak K-K bonding interaction formed by the 4s orbitals of K. This result suggest that regardless of the predominance of the Ag atoms in the valence state of the K_3Ag band structure (Figure 2.11), the structure is not entirely stabilized by the formation of covalent Ag-Ag bond interaction. Instead it is primarily stabilized through the formation of stronger K-Ag bonds. In general all the methods applied here yield consistent results and confirm that the K atoms are not spectators in the intermetallics as proposed earlier, although there is a significant electron transfer from K to Ag. As a result the K-Ag bond interaction dominate the electronic K_3Ag structure with bond order of 0.195. Hence, its reasonable to say, a 2-center-2-electron K-Ag bond is the primary bond interaction of the K_3Ag cubic structure.

2.4 Conclusion

The electronic structure and bonding nature which favours the formation and stability of unusual K_2Ag and K_3Ag intermetallic compounds under compression as reported by Atou et. al. [114] have been extensively studied here. All available plane wave and localized basis set dependent bonding analysis methods such as Wannier functions, Quantum theory of atoms in molecule (QTAIM), Natural Bond Orbitals (NBO), Solid State Adaptive natural density partitioning (SSAdNDP), Crystal Orbital Hamiltonian Population (COHP) and Crystal Orbital Overlap Population (COOP) have been employed to interprete the so called chemical bonding in the K_2Ag and K_3Ag intermetallics at 4.0GPa and 6.4GPa respectively.

The obtained wannier orbitals from the disentangled band structure of the intermetallics show that at low pressure s, p and d orbitals of Ag primarily dominate the band structure of K_2Ag. However, at higher pressure the K atom begins to significantly contribute to the valence bands of K_3Ag thereby forming some kind of s, p and d hybrid orbitals. The NBO analysis reveal the nature of the orbital hybridization in both structures and confirms the electron transfer from the K atom to the 5s orbitals of the Ag atom. Search for multi-center bonds yields three 2c-2e$^-$ bonds for the K_2Ag which includes Ag-Ag, Ag-K and K-K interactions. Surprisingly, multi-center bond search of K_3Ag yield no Ag-Ag bond interaction, only Ag-K2, Ag-K1 and K1-K2 bonds were recovered. The topological analysis using the QTAIM method of Bader recoveres similar bond interactions in the low and high pressure structures. All bonding interactions in K_2Ag and K_3Ag are closed shell, where the closed shell interactions in this case can be due to ionic interaction, like in NaCl or very weak covalency as a result of very small density at the bond critical point. In addition, the bond critical points are closer to the alkali atom in K_2Ag and K_3Ag. The COHP and COOP performed with LOBSTER code also support the Ag-K bond interactions are between 5p of Ag and 4s of K in both structures. However caution has to be taken when extracting bonding information at high pressure using the COHP and COOP methods implemented in the LOBSTER code. Following an accurate projection to the LCAO basis, hence, the recommendation from this study is that one compares the LOBSTER extracted PDOS of each atom with the PDOS computed from a plane wave calculation in other to validate the projection quality. In the past, other theorists only compare the total density of states but this can be misleading as this study have proven that, irrespective of the orbitals included in the projection, the total density of state will always agree with the plane wave total DOS. A comparison of the Bader charges obtained from the low pressure K_2Ag and higher pressure K_3Ag reveals an $\approx 13\%$ decrease in the Bader charge of each K atom and an $\approx 30\%$ increase in the Bader charge of Ag as the pressure increased from 4.0GPa in K_2Ag to 6.4GPa in the K_3Ag intermetallics. Finally, all these bonding analysis techniques must be applied with care when treating high pressure systems due to the extensive modification of the electron density on application of pressure. Hence, a naive localized description is not appropriate and may lead to erroneous interpretation.

Chapter 3

Bonding in the Three Phases of Na-Au Intermetallics

3.1 Introduction

The understanding of the structure and bonding of intermetallic phases is challenging [130]. Accurate description of the electronic structure of alkali metals by the nearly free electron (NFE) model at ambient conditions gives them the name "simple" metals [131]. The physical and chemical properties of alkali metals, such as electronic density, electronic structure, etc. are greatly altered by pressure [132, 133, 134]. Under compression, atomic orbitals of alkali metals are modified and cause s-p, s-d or p-d hybridization of the orbitals resulting in a series of pressure induced phase transitions to form complex low symmetry structures [120, 135, 136, 137, 138, 139, 140, 141, 142, 143]. Physical properties such as reduced melting temperatures [136, 138, 144], superconductivity [145, 146, 147] and metal to insulator/semiconductor transitions [120, 137, 138, 139, 148] emerge as a consequence of these pressure induced phase transitions and the NFE model fails at these extreme conditions. Binary phases of alkali metals and gold previously studied have shown unusual and intriguing electronic properties [132, 149]. In the early 20th century, Zintl et al.[103] obtained a black deposit from an ammonia solution of sodium by adding Au, which they claimed to be NaAu compound. An understanding of the orbital hybridization in these intermetallics will help explain the formation of alkali metal transition metal alloys at high pressure. There are currently several computational approach to analyze bonding in periodic solid state systems in a chemical perspective. These include, Natural Bond Orbital (NBO) analysis [23, 20, 21, 22], Solid State Adaptive Natural Density Partitioning (SSAdNDP) [24], Maximally Localized

Wannier Functions (MLWF) [25], Crystal Orbital Hamiltonian Population (COHP) analysis [128] and Atoms in Molecules [27, 28, 29, 150]. NBO analysis constructs real space representation of localized bonding and lone pair orbitals from the density matrix of an electronic structure calculation [94]. These natural orbitals are the eigen-orbitals of the first order density matrix [151]. The SSAdNDP is an extension of AdNDP to periodic systems and offers description of Lewis-like multi-center (nc-2e$^-$) bonds. SSAdNDP have been applied to different periodic systems of various structural complexities and have correctly identified the bonding motifs in them [24]. Bonding in periodic systems have also been analyzed using MLWF [152, 153, 25]. Here a unitary transformation of the band structure to a set of functions localized within a single unit cell is performed via Wannier transform. Wannier functions can thus be said to be obtained from Fourier transformation of the Bloch functions. A review on the applications and properties of MLWF can be found in ref [25]. Following Mulliken's pioneering work [30] on electron assignment to bonds and to atom centers, several methods for electron partitioning in molecules have been proposed. Within non-variational extended Huckel theory, Hughbanks and Hoffmann introduced a tight binding method with overlap which they called the Crystal Orbital Overlap Population (COOP) [44, 45]. In the COOP method, having calculated the band structure, the Mulliken's overlap population technique is then applied to a crystal measuring the bonding by $c^*_\mu c_\nu S_{\mu\nu}$ (where c^*_μ and c_ν are the coefficients and $S_{\mu\nu}$ is the overlap integral) with positive, zero and negative overlaps implying bonding, nonbonding and antibonding respectively [46, 26]. The dependence of the COOP method on the basis set makes it non-ideal for bonding description within first principle Density Functional Theory (DFT) [26]. Hence, the need for a bonding descriptor within first principles DFT led to the development of Crystal Orbital Hamiltonian Population (COHP) [26] method, which partitions the energy other than electrons but then similar to the COOP method since it also extracts information on the chemical interaction in a system from the band structure. A comprehensive review of the various applications of the COHP method can be found in ref.[47]. Baders Quantum theory of Atoms in Molecules (QTAIM) have made quantum mechanical description of molecular structures possible [27, 28, 29, 30]. QTAIM extracts bonding information from the electron density of the molecular system. Both theoretical and experimental electron densities have been shown to give information on

the chemical bonding in molecular systems [48, 49, 50, 51]. QTAIM identifies points where the gradient of the electron density vanishes i.e. $\nabla\rho(r_c) = 0$, these special points r_c are called critical points (CPs) and are characterized by their rank and signature labelled as (ω, σ). For the bond critical points reported here, the rank and signature are 3 and -1 respectively which implies the density parallel and perpendicular to a plane is a maximum and minimum respectively. The different criteria for use of other important topological parameters at the critical point such as density (ρ), Laplacian $\nabla^2\rho$, potential energy (V), kinetic energy (G), and the local energy densities (H) for bonding description have been summarized in previous reports [52, 53] and are defined in chapter one.

Recently, Takemura and Fujishisa [132] have synthesized Na-Au intermetallic compounds under high pressure at room temperature. Their study yielded four intermetallic phases up to 60GPa. The phase I (Na_2Au), with the tetragonal $CuAl_2$ type structure, phase II (Na_3Au) with trigonal Cu3As or hexagonal Cu3P-type structure, phase III (Na_3Au) with cubic BiF_3 type structure and finally phase IV which is said to be structurally disordered. Following the Miedema's rule [110, 111], the sodium and gold are unmixable due to the difference in their valence elctron density. However, they form intermetallic compounds under compression as reported by Takemura and Fujishisa [132]. Having used the Natural Bond Orbital Analysis (NBO), Solid State Adaptive Natural Density Partitioning (SSAdNDP), Quantum theory of Atoms in Molecules, Crystal Orbital Overlap Population (COOP) and the Crystal Orbital Hamiltonian population (COHP) analysis to accurately interpret the electronic structure and bonding of the K_3Ag and K_2Ag alloys reported by Atou et. al. [114], the same methods have been employed here to interpret the structure and chemical bonding in the three phases of the Na-Au intermetallics reported by Takemura and Fujishisa [132] and also search for electron localizations in non-nuclear positions in the crystal which are sometimes called electrides. The results reveal, from simple topological analysis of the electron density one can distinguish between two structures that cannot be differentiated by comparing equation of states computed with highly accurate DFT method. This chapter describes the electronic structure and bonding nature of the topologically stable sodium gold intermetallics.

3.2 Computational Details

Structural optimizations, charge densities and electronic band structures were calculated using the Vienna ab initio Simulation (VASP) code [85] and Projector Augmented plane Waves (PAW) potential [93]. The Na potential employed $2p^6$ $3s^1$ as valence states while the Au potential employed $5d^{10}$ $6s^1$ as valence states, with the Perdew-Burke-Ernzerhof (PBE) exchange correlation functional [37]. The Solid State Adaptive Natural Density Partitioning (SSAdNDP) code [24] was used to search for localized and delocalized n center 2 electron (nc-2e) bonds. A projection algorithm was used to mimic the Plane Wave Density Functional Theory (PW DFT) in a localized Atomic Orbital (AO). The wannier90 code [87] interfaced with VASP was used to obtain the band structure from a GW [88] calculation, disentangle the various bands and generate the Wannier orbitals corresponding to the disentangled bands. Further bonding information was obtained from the energy band structure by calculating the COHP as implemented in the Local Orbital Basis Suite Towards Electronic Reconstruction (LOBSTER) program [89] which projects PAW functions onto localized slater type orbitals. The topological analysis, evaluation of crystal voids with procrystal density [90] and search for non-nuclear maxima (NNM) with the Yu-Trinkle algorithm [154] were performed using the Critic2 program [91] and bond orders were obtained using the density derived electrostatic and chemical (DDEC6) method implemented in the Chargemol programs [92]. All visualizations were done using Visualization for Electronic Structure Analysis (VESTA) [122] and Visual molecular dynamics (VMD) [155] programs.

3.3 Results and Discussion

3.3.1 Na_2Au Phase I

Phase I of the sodium gold binary, denoted as Na_2Au, has a tetragonal unit cell (I4/mcm) with four formula units (Z = 4). Experimental charge density analysis of the I4/mcm Na_2Au performed at different pressures by Dr. Jianbao Zhao using the Maximum Enthropy Method (MEM) is shown in Figure 3.1. At 0.21GPa, the charge density around the Na atom can be seen to have a cylindrical shape which tends to break up at 0.83GPa with some of the electrons occupying the non-nuclear positions as can be clearly seen in the 2D plot of the charge density along the 001 plane at 0.83GPa (Figure 3.1). To quantify and understand the non-nuclear maximum (NNM), plane wave DFT calculation was first performed on the Phase I lattice structure at 0.83GPa using a large charge density grid. The charge density obtained was used to perform QTAIM topological analysis to extract the critical points. From the topological analysis, three non-equivalent bond critical points were obtained with bond orders and the topological parameters at the critical point given in table 3.1. All the Laplacian (∇^2 (r_{BCP})) at the bond critical points are positive which indicate charge depletion in the bond critical point and suggest a closed shell interaction between the atoms. The density at the bond critical point ($\rho(r_{BCP})$) is an indicator of bond strength, hence, it shows the Au-Au bond is the strongest interaction followed by the Na-Au bond interaction in agreement with the computed bond orders. Integration of the atomic basins using the Yu-Trinckle algorithm [154] yields one NNM occupying four symmetry equivalent sites shown in blue in Figure 3.2. The procrystal density plot recovers the NNM as can be seen in Figure 3.2a. Similarly, the Electron Localization Function (ELF) [156] plot of the I4/mcm Na_2Au at 0.45 isovalue indeed show electrons in the non-nuclear positions and correspond with the NNM position from the topological analysis (Figure 3.2b). Further investigation indicates the NNMs lie on a hexagonal plane formed by the first and second nearest neighbour Na atoms as can be seen in Figure 3.2c and 3.2d. In agreement with MEM analysis, the topological analysis revealed the NNMs were formed from the Na atoms. Burdett and McCormick [156] have shown that ELF values below ELF=0.5 can be interpreted as representing regions between atomic shells

or regions where the nodal contributions to ELF far outweighs the contribution of the density, therefore, the electron density is small in these regions [156]. Hence, the NNMs recovered from the topological analysis and MEM analysis are simply regions of low electron density in the Na_2Au intermetallics. A plot of the bond critical points is shown in Figure 3.3.

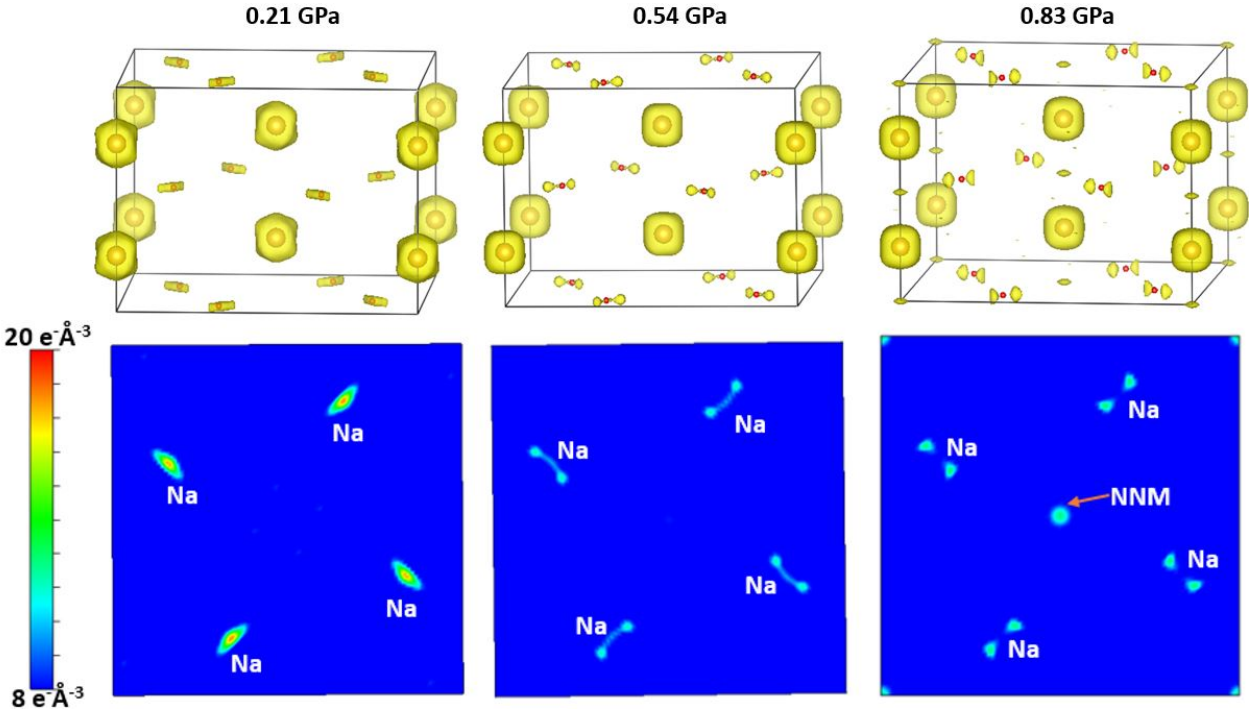

Figure 3.1: Three dimensional and corresponding two dimensional (along the 001 plane) charge density analysis of I4/mcm Na_2Au using the Maximum Enthropy Method (MEM).

Bond	d(Å)	Bond Order	$\rho(r_{BCP})$ (ea_0^{-3})	$\nabla^2(r_{BCP})$ (ea_0^{-5})	V (E_h)	G (E_h)	H (E_h)	G/ρ $(E_h e^{-1} a_0^3)$
Au-Au	2.770	0.830	0.056	0.098	-0.056	0.0413	-0.014	0.7415
Na-Au	3.010	0.190	0.013	0.049	-0.008	0.010	0.002	0.756
Na-Na	3.400	0.060	0.005	0.001	-0.001	0.001	0.000	0.156

Table 3.1: Topological properties of Na_2Au Phase I at the bond critical points from QTAIM at 0.83GPa. Where a_0 and E_h are bohr and hartree units respectively.

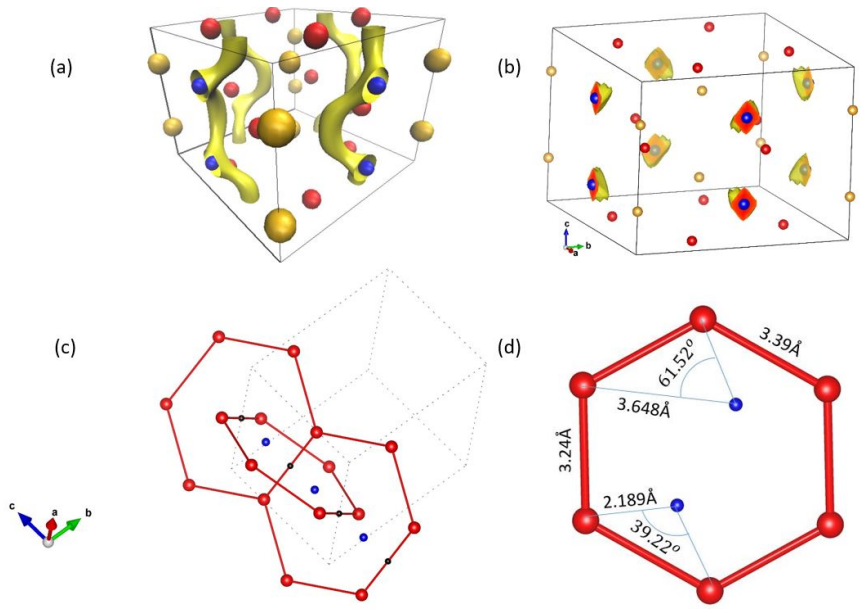

Figure 3.2: Analysis of Na_2Au phase I at 0.83GPa. (a) Procrystal density in yellow superposed with the NNMs in blue (b) ELF at 0.45 isovalue (c and d) hexagonal rings of Na. Atom colour: Na = red, Au = gold and NNM = blue

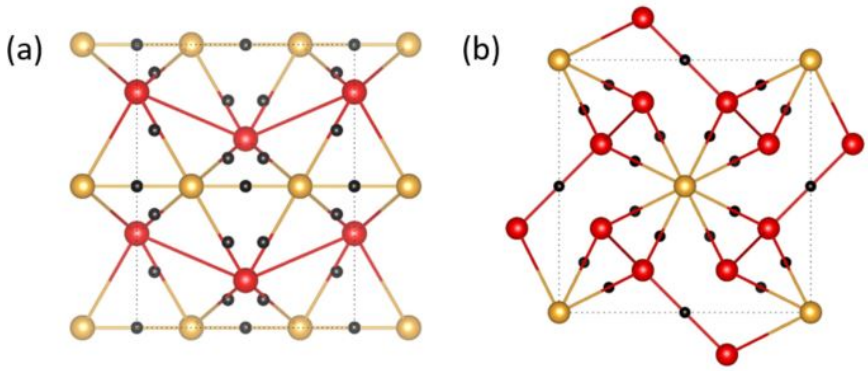

Figure 3.3: Bond critical points (BCPs) plot of the Na_2Au phase I at 0.83GPa. Atom colour: Na = red, Au = gold and BCPs = black

Having recovered the NNM from QTAIM analysis, the calculated plane wave orbitals were projected to atom center basis with the def2-QZVP [124, 125, 126, 157, 158, 159] atomic orbital basis set. The overall projection spillover is less than 10^{-2} and the NBO orbital occupancy for the Au s, p and d orbitals are 0.99, 0.79 and 9.85e^- respectively. This roughly corresponds to an atomic electron configuration of $5d^{10}$ $6s^1$ $6p^1$ for the Au atom. Meanwhile, the natural orbital population on the Na atom are 0.27, 0.86 electrons for the s and p orbitals respectively. Having obtained the orbital occupancies from the NBO analysis, SSAdNDP

was employed to analyze the density matrix for chemical bonding patterns. The SSAdNDP general search yields 44 1c-2e$^-$ bonds (lone pairs), where 24 of the lone pairs are 2p orbitals centered around the Na atoms and the other 20 are completely 5d orbitals centered around the Au atoms with occupation numbers (ON) of approximately 1.99 and 1.97 electrons on the sodium and gold atoms respectively. Further search for multi-center bonds yields two symmetry nonequivalent 2c-2e$^-$ bonds which include Au-Au and Na-Au with occupation numbers (ONs) of approximately 1.33 and 1.05 electrons respectively. No sensible Na-Na bond interaction was recovered from the localized multi-center bond search owing to the fact, the Na-Na bond from the topological analysis had an extremely low density at the critical point (table 3.1). Disentangled Wannier band structure and corresponding Wannier orbitals were obtained by disentangling the valence band as shown in blue in Figure 3.4, with inner and outer energy windows of -7.08eV and 1.92eV respectively and the frozen state at the fermi level (0eV). From the disentangled valence bands, the bond between the Au atoms was obtained and found to be similar to the 2c-2e$^-$ Au-Au bond from the SSAdNDP search (Figure 3.4). Localized 5d Wannier orbitals centered around the Au atom as shown in Figure 3.4 were recovered from the lower valence bands. These 5d Wannier orbitals of Au can be seen to correspond with the 5d lone pairs of Au from the SSAdNDP search that do not take part in the bonding.

Atom	Bader Charge	NBO Charge	DDEC6 Charge
Na	+0.664	+0.369	+0.457
Au	-1.332	-0.739	-0.914

Table 3.2: Bader, natural bond orbital (NBO) and density derived electrostatic and chemical (DDEC6) charge analysis of Na_2Au at 0.83GPa.

To describe electron sharing in Na_2Au, charge analysis calculations were performed and the corresponding Bader, NBO and DDEC6 charges on the Na and Au atoms are compared in table 3.2. Due to the higher electronegativity of gold, it is expected that the Na atoms donate electrons to the gold as in this case all the charge analysis method employed follow similar trend with each Na atom donating electrons to the Au atoms. Having identified the atomic nature at the Na and Au atoms in Na_2Au, an orbital decomposed description of the bond interaction using the COHP method, which partitions the bands structure energy in

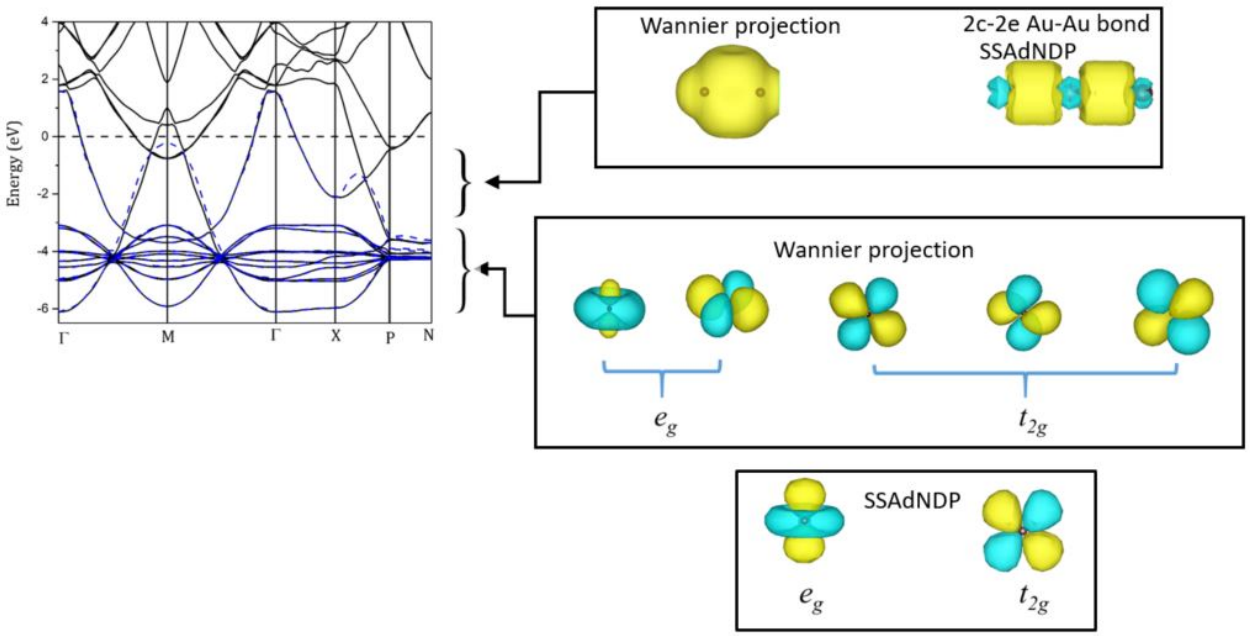

Figure 3.4: Disentangled band structure, corresponding Wannier orbitals and SSAd-NDP plots of the phase I Na_2Au centered on the Ag atom.

terms of orbital pair contribution by projecting the results from a plane wave calculation into linear combination of atomic orbitals (LCAO), was performed. As already established in chapter two, a comparison of the plane wave and LCAO orbital decomposed density of state is essential in view of the deficiency with the default basis set available in LOBSTER, to ensure that the true valence orbitals of the Na and Au atoms are completely reproduced. Figure 3.5 shows the Na and Au PDOS computed using the plane wave and LCAO methods. The comparison show the Au PDOS are qualitatively similar whereas for Na PDOS, inclusion of empty 3p orbital seems to yield erroneous result for the LOBSTER code. The reason being that a common set of Slater orbitals were used to represent the p orbitals for Na (i.e the 3p components is basically the same as the core 2p). Irrespective of the choice of projection orbitals, the total DOS qualitatively and quantitatively agree as can be seen in Figure 3.6 for the Phase I Na_2Au. Hence, comparing just the total DOS can be misleading as already established in chapter two. It is important to note that all the plane wave to localized orbital projections performed here had a projection accuracy of 99% and in addition, the band overlaps were manually examined and all the diagonals were close to one.

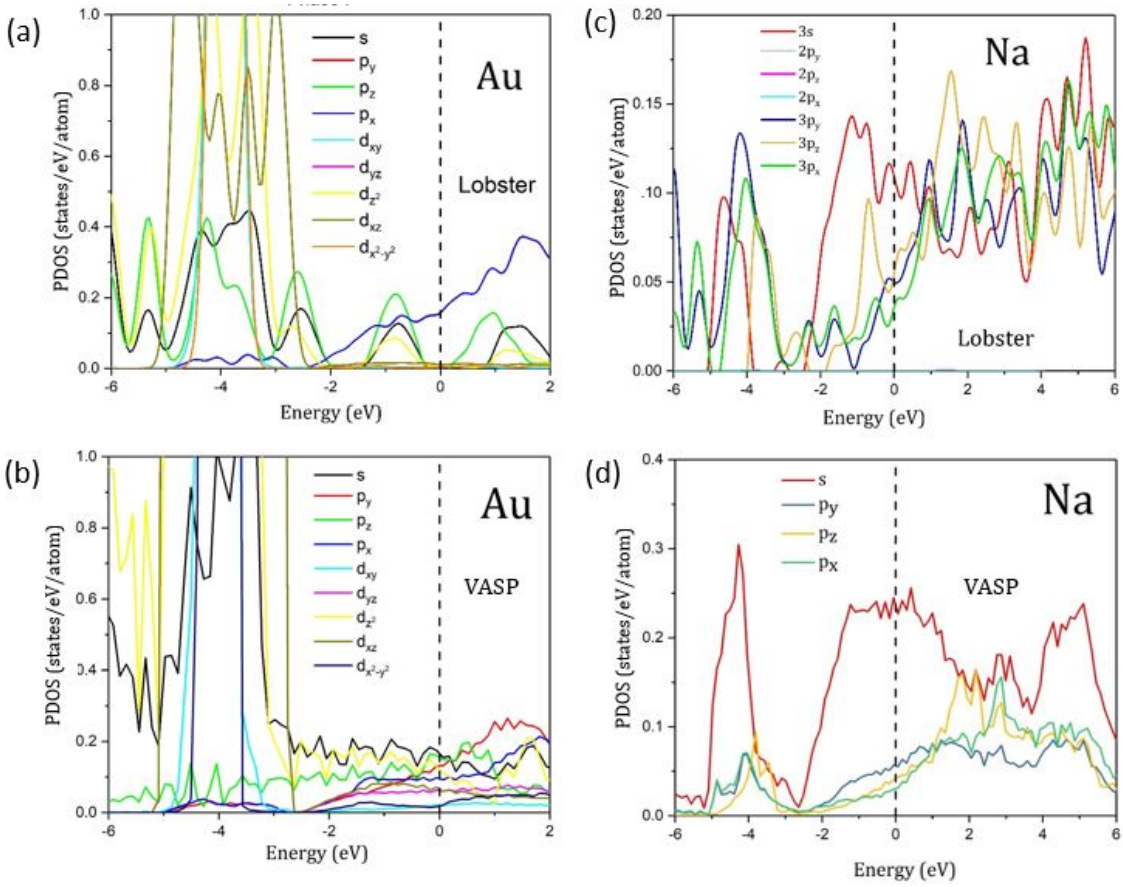

Figure 3.5: Projected density of state of Au and Na using the plane wave and local basis set methods for the Na_2Au Phase I.

The COHP analysis between the nearest neighbors Au-Au, Na-Au and Na-Na interactions with bond lengths 2.77Å, 3.01Å and 3.40Å respectively are shown in Figure3.7. The positive and negative –COHP axis represent the bonding and anti-bonding regions respectively. The Au-Au COHP show the bond interaction is primarily due to the 6p orbitals. Figure3.7 also shows some bonding between the Na-Au, since the 3p introduces an artifact, the Na-Au bond is mostly due to the 2p and 6s orbitals of Na and Au respectively. However, the Na-Na COHP show very weak bond interaction between the Na atoms in the Phase I Na_2Au which also agrees with the very low density at the Na-Na bond critical point obtained from the topological analysis. Hence, all the plane wave and localized orbital bonding analysis methods employed here accurately described the Phase I Na_2Au structure at 0.83GPa. Although the LOBSTER only provide a qualitative picture at the best. Similar methods have been applied to study the Phase II and Phase III structures in the preceding section.

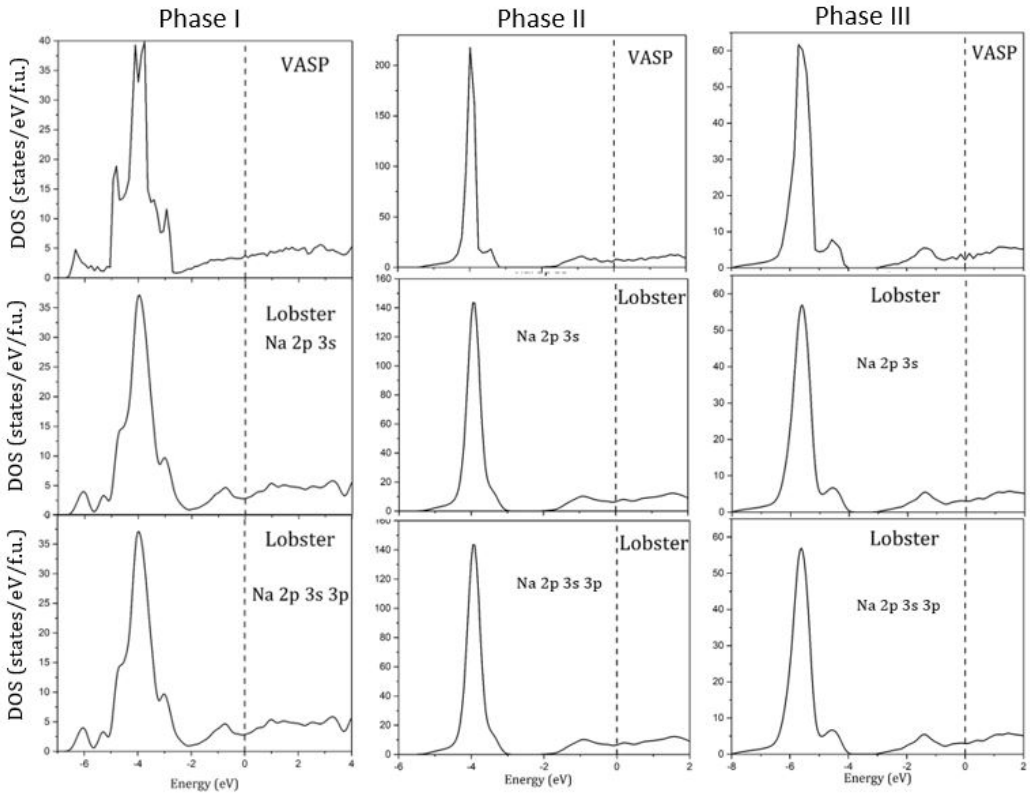

Figure 3.6: Total density of state of the phase I, phase II and phase III sodium gold intermetallics at 0.83GPa, 2GPa and 51.7GPa respectively.

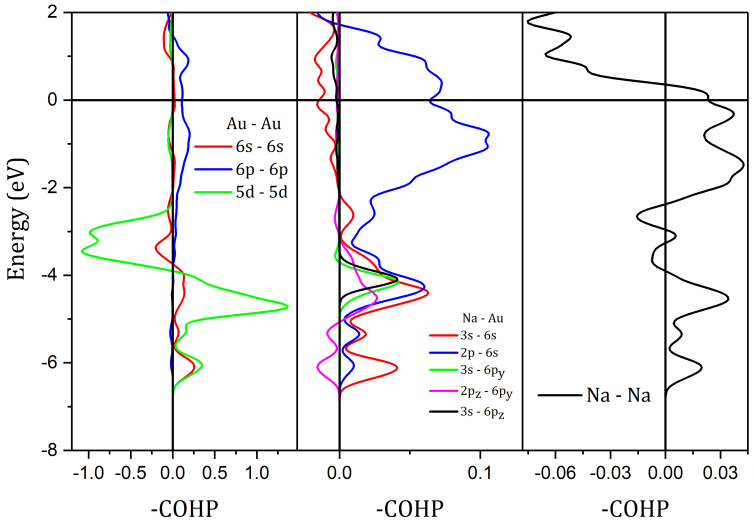

Figure 3.7: Crystal orbital Hamiltonian Population (COHP) of Na_2Au phase I at 0.83GPa. The positive and negative -COHP axis denotes bonding and ant-bonding regions respectively.

3.3.2 Na_3Au Phase II

X-ray diffraction analysis of Phase II sodium gold intermetallics (Na_3Au) found the space group could be either trigonal Cu_3As or hexagonal Cu_3P-type structure. Despite great efforts, Takemura and Fujishisa [132] could not determine which structure was correct, neither could both structures be distinguished from DFT equation of state (Figure 3.8). However, MEM analysis of the charge density by Dr. Jianbao Zhao reveal the trigonal structure (P-3c1) yield unrealistic charge density as shown in Figure 3.9a whereas that of the hexagonal structure ($P6_3cm$) yielded a more reasonable charge density given in Figure3.9b. This suggested the hexagonal $P6_3cm$ Na_3Au structure of the Phase II is the accurate structure. To validate the MEM results, topological analysis of both Cu_3As and Cu_3P-type structures were performed using a very dense charge density grid from a plane wave DFT calculation at 2GPa. Regardless of the grid dimension used, topological analysis of the trigonal (Cu_3As-type) structure failed to satisfy the Morse sum (nuclear - bond + ring - cage = 0) [127]. On the other hand the hexagonal structure satisfies the Morse sum. Hence, the trigonal structure is topologically unstable. This is in agreement with the MEM analysis and corroborates the fact that the topologically stable $P6_3cm$ structure is the accurate Phase II structure.

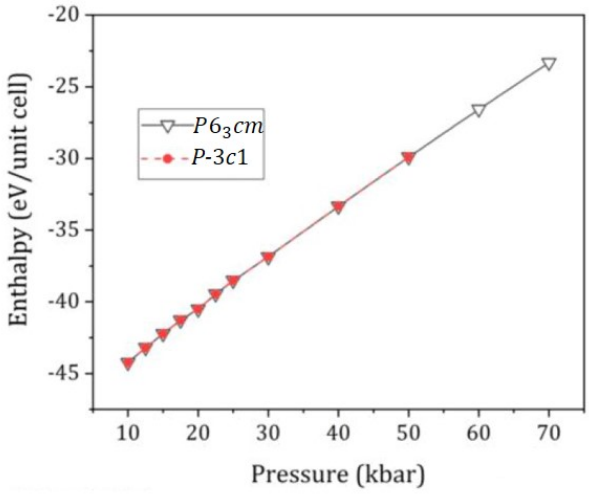

Figure 3.8: Density functional theory calculated equation of state of the experimental $P6_3cm$ and P-3c1 Na_3Au phase II structures. As can be seen from the plot, both structures are indistinguishable as their equation of state overlap.

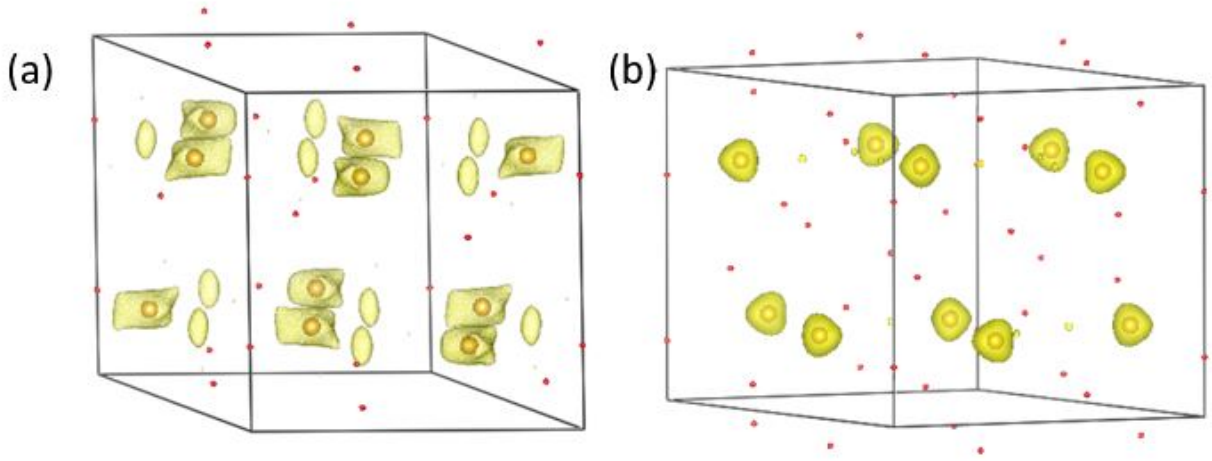

Figure 3.9: MEM analysis of the (a) trigonal Cu_3As and (b) hexagonal Cu_3P-type structure

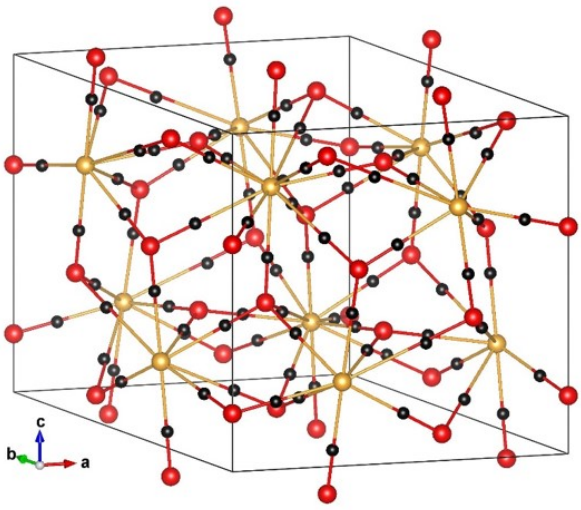

Figure 3.10: Bond critical points (BCPs) plot of the Na_3Au phase II at 2GPa. Atom colour: Na = red, Au = gold and BCPs = black

The Phase II Na_3Au structure has six formula units (Z=6) per unit cell containing four symmetry nonequivalent Na atoms with a hexagonal unit cell ($P6_3cm$) optimized to 2GPa have been used for the bonding analysis here. Bond critical points obtained from QTAIM topological analysis is given in table 3.3. Eight unique bond critical points were obtained between the Au and four different Na atoms in the structure as summarized in table 3.3. All the Laplacian (∇^2 (r_{BCP})) at the bond critical points are positive which indicate charge depletion in the bond critical point and suggest a closed shell interaction between the atoms.

A plot of the obtained critical point in the hexagonal Phase II Na_3Au unit cell is shown in Figure3.10.

Bond	d(Å)	Bond Order	$\rho(r_{BCP})$ (ea_0^{-3})	$\nabla^2(r_{BCP})$ (ea_0^{-5})	V (E_h)	G (E_h)	H (E_h)	G/ρ $(E_h e^{-1} a_0^3)$
Au-Na1	2.892	0.272	0.016	0.061	-0.011	0.013	0.002	0.0.820
Na2-Au	2.929	0.272	0.015	0.066	-0.011	0.0114	0.003	0.913
Au-Na4	2.966	0.254	0.014	0.052	-0.009	0.011	0.002	0.783
Au-Na3	2.963	0.254	0.014	0.046	-0.009	0.010	0.001	0.704
Na3-Au	2.979	0.255	0.014	0.044	-0.008	0.010	0.001	0.686
Au-Na4	3.044	0.216	0.013	0.046	-0.008	0.010	0.002	0.752
Na3-Au	3.396	0.124	0.009	0.018	-0.004	0.004	0.001	0.471
Na4-Au	3.682	0.070	0.007	0.010	-0.002	0.002	0.000	0.333

Table 3.3: Topological properties Na_3Au Phase II at the bond critical points from QTAIM at 2GPa. Where Na1, Na2, Na3 and Na4 are the four unique Na atoms occupying the 2a, 4b, 6c and 6c atomic sites respectively

DFT calculation on Phase II was followed by NBO of the hexagonal Phase II Na_3Au obtained from the projection using a def2-QZVPD basis set [124, 125, 126, 157, 158, 159]. The resulting NBO occupancy for the s, p and d orbitals of Au are 1.14, 0.86 and 9.92 electrons respectively showing Au $5d^{10}$ $6s^1$ $6p^1$ configuration. The NBO population of the Na atom are 0.31 and $0.44e^-$ for the s and p orbitals respectively, there is a small but not insignificant occupancy of the Na 3p orbital. SSAdNDP analysis yields 84 1c-$2e^-$ bonds, where 54 of the lone pairs are 2p orbitals centered around the Na atoms and the other 30 are completely 5d orbitals centered around the Au atoms with ONs of approximately 1.99 and 1.97 electrons on the sodium and gold atoms respectively. Further search for multi-center bonds recovers the Na-Au bonds with an occupation number of 1.21 electrons. The valence and lower conduction bands shown in red in Figure 3.11 were Wannierised with inner and outer energy windows of -1.679eV and 6.181eV respectively with the frozen state at the Fermi level (0eV). It has been shown by Marzari et. al. [25], that freezing the Fermi level ensure only the selected bands below the Fermi level are Wannierised. From the disentangled valence bands, we obtained 2p Wannier orbitals of the Au atoms shown in Figure 3.11. Wannierising the lower valence

band (in blue colour) yields localized 5d and 6s orbital mixing with the orbitals centered around the Au atom (Figure3.11). The Bader charges on the Na and Au atoms shown in table 3.4 is consistent with the higher electronegativity of Au since it gains electron from the Na atoms.

Atom	Bader Charge	NBO Charge	DDEC6 Charge
Na1	+0.631	+0.249	+0.492
Na2	+0.663	+0.285	+0.499
Na3	+0.671	+0.315	+0.483
Na4	+0.658	+0.302	+0.486
Au	-1.981	-0.890	-1.466

Table 3.4: Bader, natural bond orbital (NBO) and density derived electrostatic and chemical (DDEC6) charge analysis of Na_3Au Phase II at 2GPa .

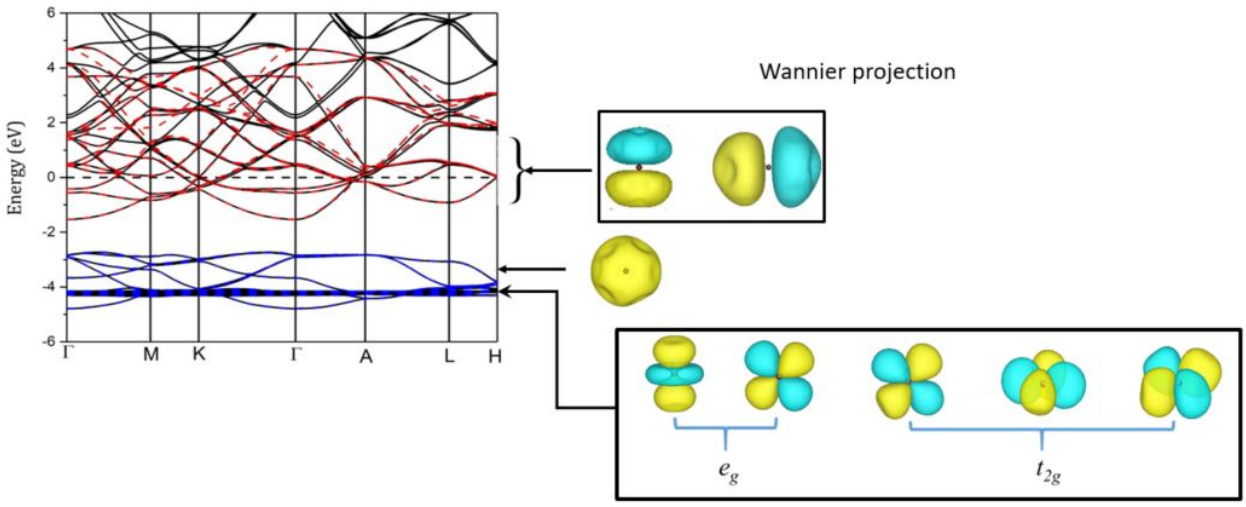

Figure 3.11: Disentangled band structure and corresponding Wannier orbitals of hexagonal $P6_3cm$ Na_3Au Phase II centered on the Au atom.

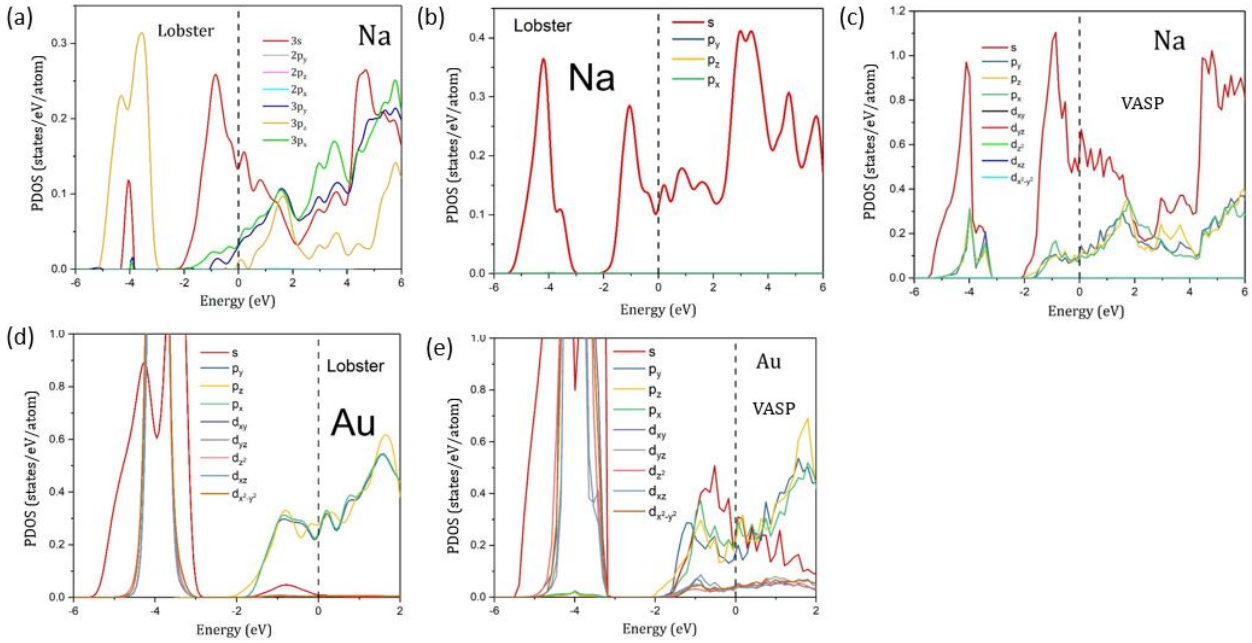

Figure 3.12: Projected density of state of Au and Na using the plane wave and local basis set methods for the Na_3Au Phase II.

The computed Na and Au PDOS using the plane wave and projected LCAO methods are compared in Figure 3.12, the computed Au PDOS qualitatively agree for both methods. Attempt to include the empty 3p orbital once again yield erroneous result for the LOBSTER. However, the choice of projection orbitals has no major effect on the total DOS as can be seen in Figure 3.6. One must be cautious to interpret the p bonding of Na. The COHP analysis between the nearest neighbor Au-Au, Na-Au and Na-Na interactions with bond lengths 5.095Å, 2.89 Å and 3.34 Å respectively is show in Figure 3.13. Contrary to the Phase I, the strong bonding character in the Phase II is observed between the Na-Au bond. The positive and negative –COHP axis represent the bonding and anti-bonding regions respectively. Au-Au COHP actually indicate no Au-Au bond interaction due to the inverted order of the bonding and anti-bonding orbitals as previously explained in chapter two. Hence, the primary bonding interaction is between the Na-Au, since the inclusion of Na 3p orbital introduces an artifact, the Na-Au bond is mostly due to the 3s and 6p orbitals of Na and Au respectively. However, there is no Na-Na bond interaction in the Phase II Na_3Au which also agrees with the topological analysis, SSAdNDP and Wannier analysis.

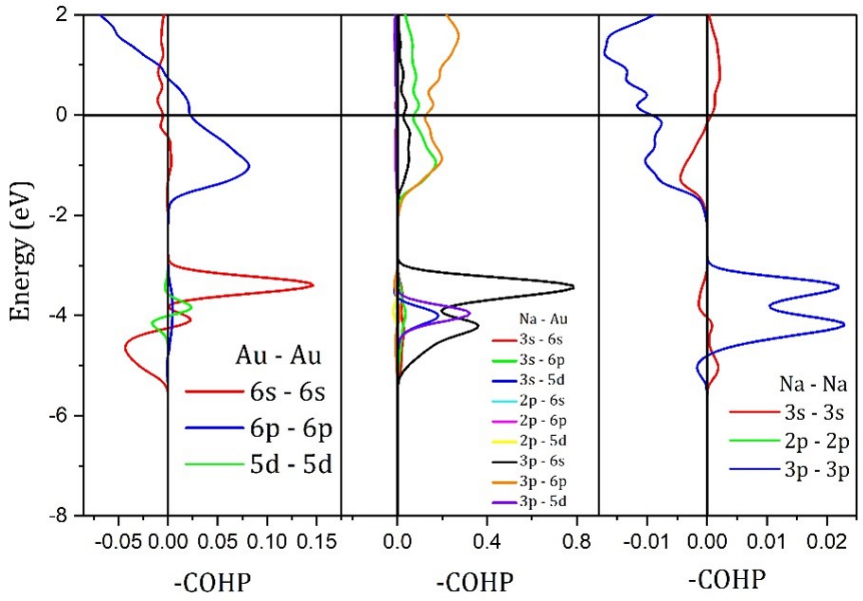

Figure 3.13: Crystal orbital Hamiltonian Population (COHP) of Na_3Au phase II at 2GPa. The positive and negative -COHP axis denotes bonding and ant-bonding regions respectively.

3.3.3 Na_3Au Phase III

The high pressure Phase III Na_3Au was formed at about 3.6GPa and remains stable up to about 54GPa. This structure has a cubic unit cell (Fm-3m) with four formula units (Z=4). The experimental electron density line profile at different pressures given in Figure3.14a reveal the electron density around the Au atom increases with increased pressure while that of the Na decreases with increased pressure. Similar trend can also be seen from Figure3.14b which show the experimental charge density plot at 51.7GPa and suggest electron transfer from the Na to the Au atom. Following the successful structural and bonding description of the lower pressure Phase I and Phase II using the plane wave and localized basis set dependent methods, the phase III structure at 51.7GPa have been used for analysis here. A def2-QZVPD atomic basis set was utilized to project the plane wave to localized atomic orbitals. The natural bond orbital occupancy for the s, p and d orbitals of Au are 1.22, 0.94 and 9.99 electrons respectively, indicating a $5d^{10}\ 6s^1\ 6p^1$ configuration. The NBO population of the Na atom are 0.41 and 0.18 e^- for the s and p orbitals respectively. Therefore there are

lesser electrons in the Na 3p orbital. SSAdNDP search for localized bonding orbitals yield 56 1c-2e$^-$ bonds with occupation numbers (ON) of approximately 1.987, 1.984 and 1.962 electrons on the 4b Na, 8c Na and Au atoms respectively. 36 of the lone pairs are 2p orbitals centered around the Na atoms and the other 20 are completely 5d orbitals centered around the Au atoms. Further search for nc-2e$^-$ bonds with n $>$ 1 yielded three unique two center two electron bond interactions which include the Au-Na1, Au-Na2 and Au-Au bonds, where Na1 and Na2 are the two unique Na atoms occupying the 4b and 8c atomic sites respectively. No Na-Na bond was found from the multi-center bond search.

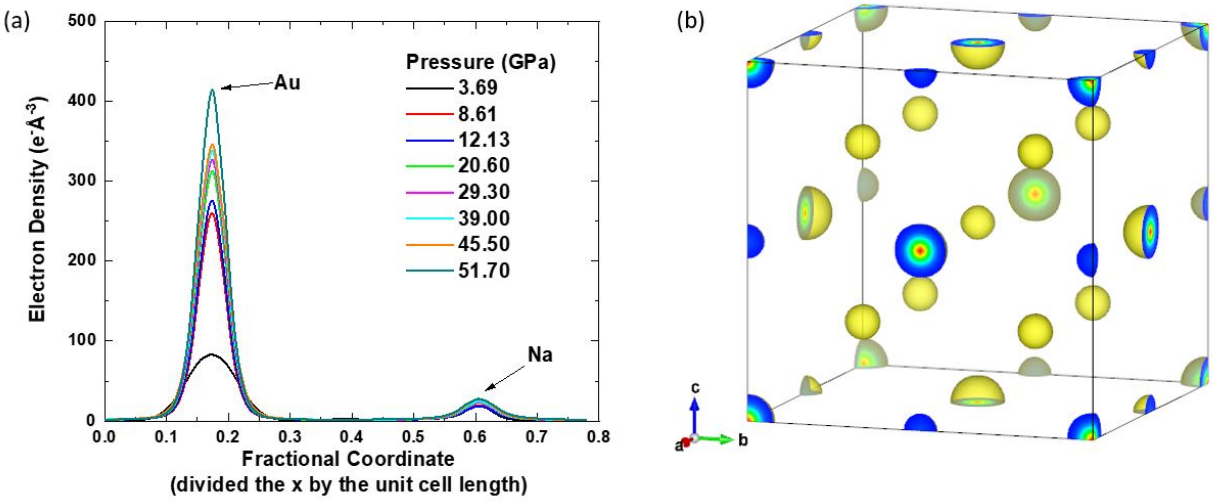

Figure 3.14: Experimental (a) Electron density line profile of phase III Na_3Au at different pressures and (b) Charge density plot of Na_3Au phase III at 51.7GPa

All the bond interactions recovered from SSAdNDP analysis have occupation numbers close to 1.8e$^-$. Topological analysis of Phase III Na_3Au found three bond critical points summarized in table 3.5. The obtained bond critical points correlates with the three unique two center two electron bonds recovered from the multi-center bond search. From the topological parameters at the bond critical point, the Phase III sodium-gold intermetallics at 51.7GPa is primarily composed of closed shell interactions evident from the positive laplacians with no Na-Na bond interaction present in the binary. The Au-Au bond length increased by 51% in the phase III when compared to the phase I. Meanwhile the first nearest neighbour Au-Na bond length in phase II decreased just by about 16% as the structure is compressed to 51.7GPa in the phase III. From the visual representation of the bond critical points (Figure3.15), each

Na atom occupying the 8c atomic site is bonded to the four Au atoms forming a tetrahedral coordination which suggest the Na-Au are bonded through a hybridization of the s and p orbitals of Na and Au respectively.

Bond	d(Å)	Bond Order	$\rho(r_{BCP})$ (ea_0^{-3})	$\nabla^2(r_{BCP})$ (ea_0^{-5})	V (E_h)	G (E_h)	H (E_h)	G/ρ $(E_h e^{-1} a_0^3)$
Au-Na1	2.980	0.130	0.019	0.057	-0.012	0.013	0.001	0.692
Au-Na2	2.580	0.266	0.031	0.137	-0.029	0.032	0.003	1.033
Au-Au	4.208	0.040	0.015	0.013	-0.006	0.005	-0.001	0.320

Table 3.5: Topological properties of Na_3Au Phase III at the bond critical points from QTAIM at 51.7GPa. Where Na1 and Na2 are the two symmetry nonequivalent Na atoms.

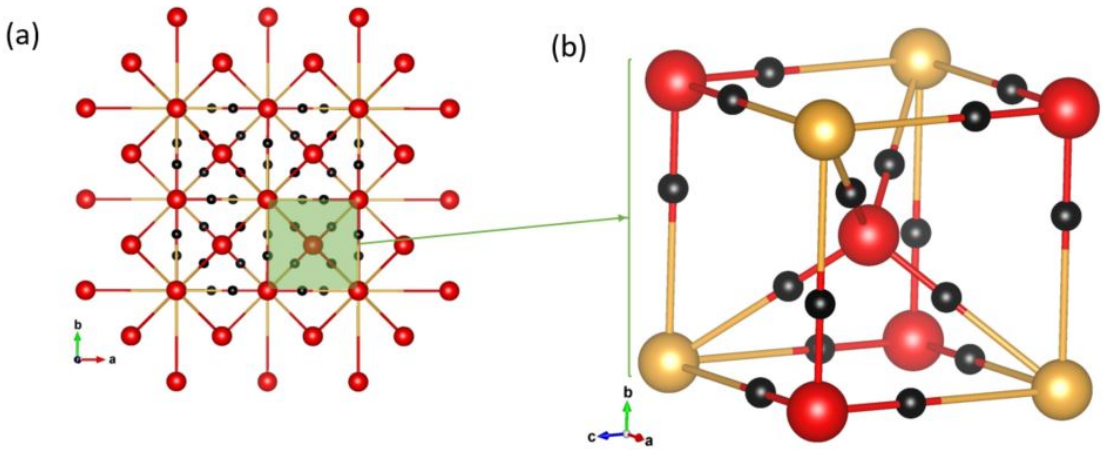

Figure 3.15: Bond critical point plot of the Na_3Au at 51.7GPa (a) 001 plane of the unit cell and (b) a subsection of the unit cell. Atom colour: Na = red, Au = gold and BCPs = black

To further interprete the bonding in phase III Na_3Au, Wannier orbitals were obtained from the disentangled valence and lowest conduction band using an inner and outer energy windows of -3.0eV and 5eV respectively with the frozen state at the fermi level (0eV). The wannierization yielded 5p orbitals centered around the Au atom as shown in red in Figure 3.16. Similarly, Wannierisation of the lower valence band yielded localized 5d and 6s orbital mixing similar to the Phase II, with the orbitals centered around the Au atom as shown in

Figure 3.16. These 5d Au Wannier orbitals correspond with the 5d Au lone pairs from the SSAdNDP search. Atomic charges of the Au and two symmetry nonequivalent Na atoms are summarized in table 3.6. The more elctronegative Au atom gains electrons from the Na atoms which supports the line profile electron density from experiment shown in Figure 3.14a. All the charge analysis methods employed show similar trend for the charge transfer between the Na and Au atoms in Phase III Na_3Au.

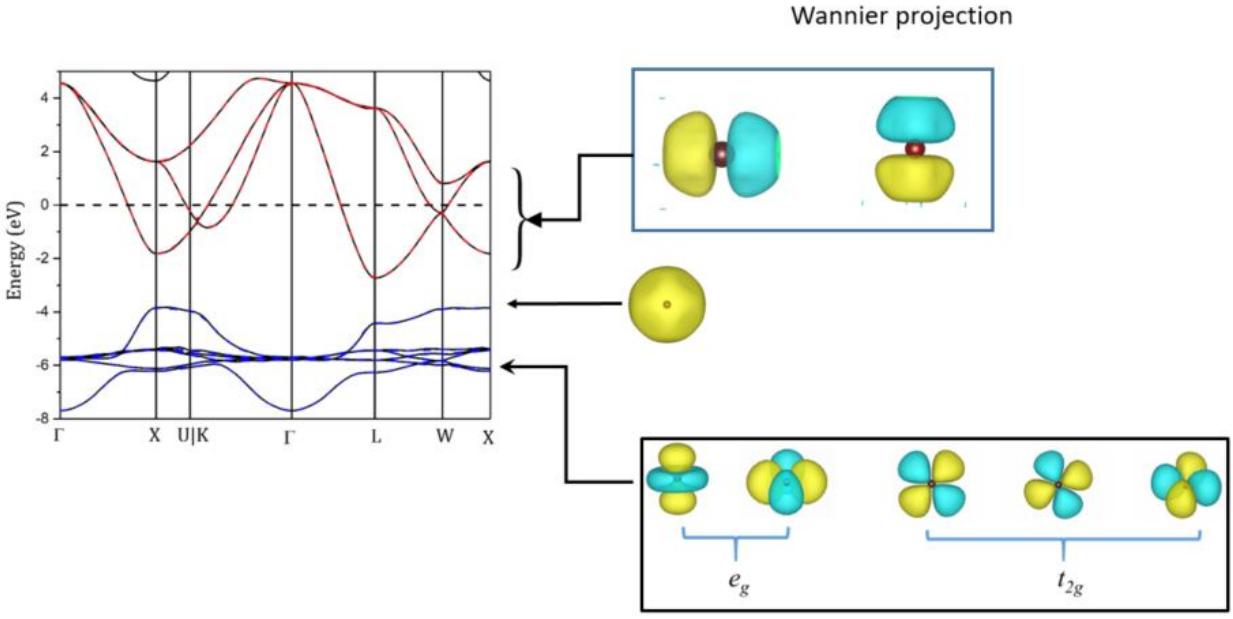

Figure 3.16: Disentangled band structure and corresponding Wannier orbitals of Fm3m Na_3Au phase III centered on the Au atom.

Atom	Bader Charge	NBO Charge	DDEC6 Charge
Na1	+0.632	+0.412	+0.526
Na2	+0.629	+0.330	+0.664
Au	-1.890	-1.073	-1.853

Table 3.6: Bader, natural bond orbital (NBO) and density derived electrostatic and chemical (DDEC6) charge analysis of Na_3Au Phase III at 51.7GPa .

Topological analysis on phase III at 51.7GPa yields no non-nuclear maximum (NNM). Hence, contrary to pure alkali metals which show increased localization of the interstitial electrons

at high pressure due to the core-valence overlap [160, 121], the sodium-gold intermetallics studied here show decrease in the localized interstitial electrons at high pressure. Similar trend was recently observed for sodium-potassium system by Frost et. al. [161], the authors attributed the reduced localization to the unusual structure of the NaK system they found. This is obviously not the case for the Na-Au system, instead the high electronegativity of gold contributes to the reduced localization of interstitial electrons at higher pressure.

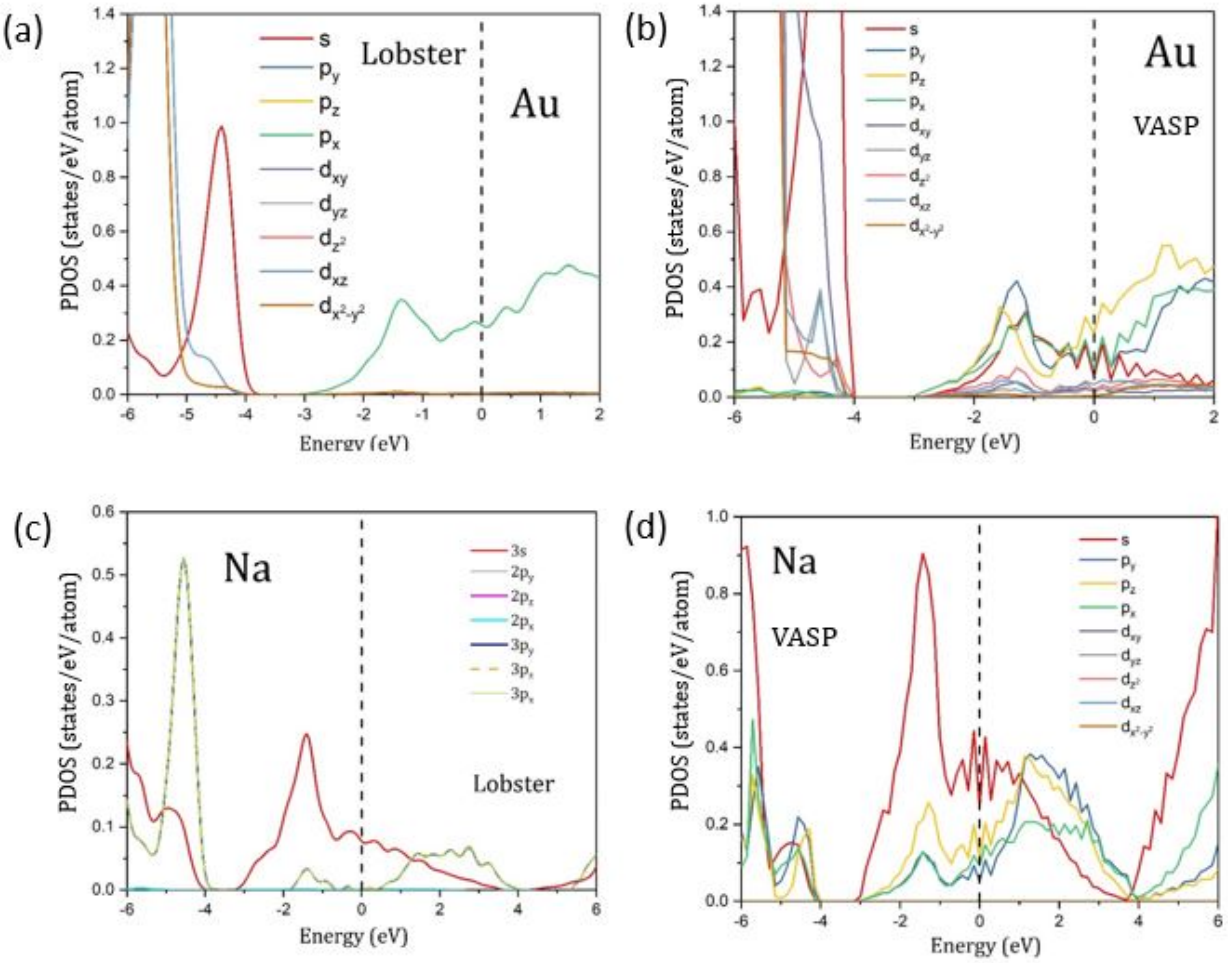

Figure 3.17: Projected density of state of Au and Na using the plane wave and local basis set methods for the Na_3Au Phase III.

By comparing the Na and Au PDOS computed using the plane wave and LCAO methods, the computed Au PDOS from LOBSTER show qualitative agreement to the plane wave result. On the other hand, although the Na PDOS for the 3s orbital profile is reproduced, the inclusion of the 3p orbital of Na simply collapsed to the 2p as found in the plane wave

PDOS. Although the agreement between the PDOS from the plane wave and localized orbital basis set method are not perfect, their total DOS greatly agree as can be seen in Figure 3.6 for the Phase III Na_3Au. As already established in chapter two, the agreement between the total DOS can be misleading and should not be a yardstick for validating projection accuracy from plane wave to localized basis. Assuming there is no Na 3p contribution to the bonding due to the small NBO population, the COHP analysis yields a qualitative description of the interaction between the neighbor Au-Au, Na-Au and Na-Na shown in Figure 3.18. The result show no Na-Na bond interaction and the Na-Au bond is formed by the 3s and 6p orbitals of Na and Au respectively. This description is consistent with the QTAIM analysis.

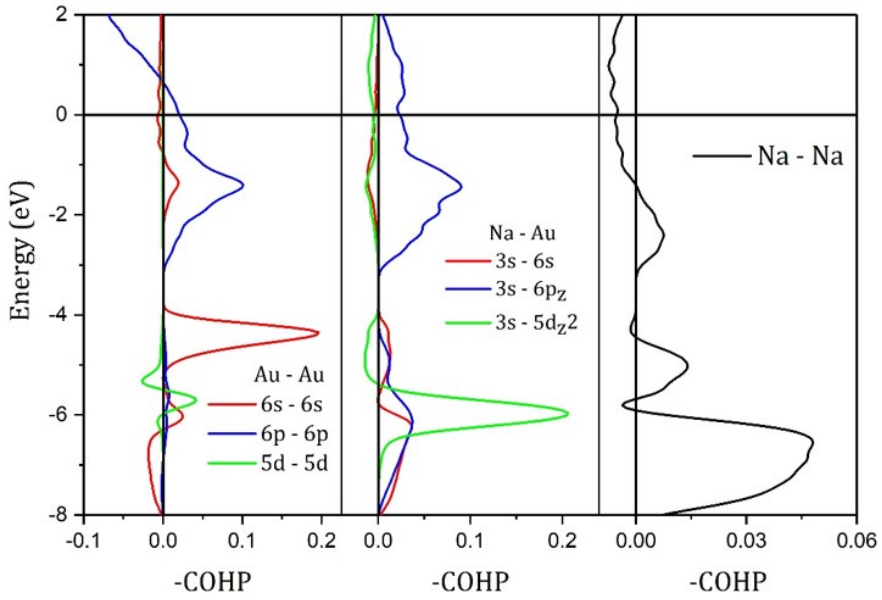

Figure 3.18: Crystal orbital Hamiltonian Population (COHP) of Na_3Au phase III at 51.7GPa. The positive and negative -COHP axis denotes bonding and ant-bonding regions respectively.

3.4 Conclusion

All the different computational approaches earlier introduced have been applied to the topologically stable phase I (Na_2Au), hexagonal phase II (Na_3Au) and cubic phase III (Na_3Au) sodium gold binaries to explore the bonding nature of these intermetallics. The trigonal Cu_3As-structure type of the phase II was found to be topologically unstable with the Morse sum not equal to zero, hence, only the hexagonal Cu_3P-type structure phase II which satisfies the Morse sum have been studied here. Maximum Enthropy Method (MEM) analysis of the experimental diffraction pattern also confirms the hexagonal phase II structure as the correct structure. Bonding nature of stable phase I, phase II and phase III sodium gold binaries at 0.83GPa, 2GPa and 51.7GPa respectively have been studied here using the conventional bonding theories to interpret the structure of these Na-Au alloys at high pressure. Topological analysis of the phase I structure found one non-nuclear maximum (NNM) and three unique bond critical points which includes Au-Au, Na-Au and Na-Na bond interactions. The positive laplacians at the obtained bond critical points indicated the bonds were typical closed shell interactions. Also, the NNM occupied four symmetry equivalent sites in the crystal structure. These NNMs were also recovered from the electron localization plot but with an isovalue of 0.45. Hence, the NNMs recovered from the topological analysis and MEM analysis are simply regions of low electron density in the Na_2Au intermetallics. NBO analysis of the Na_2Au structure revealed electron transfer from the Na to the Au atoms which is consistent with the electronegativity difference between the Na and Au atoms. Also, the SSAdNDP search for multi-center bonds in the phase I structure yields two symmetry nonequivalent 2c-2e$^-$ bonds which include Au-Au and Na-Au with occupation numbers (ONs) of approximately 1.33 and 1.05 electrons respectively. The low ON of the bonds correlates with the low densities at the bond critical points from the topological analysis. Wannierization of the valance band from the band structure also recovered the bond between the gold atoms. The COHP analysis of the bonds revealed the orbitals responsible for the individual bond interactions. The Au-Au COHP show the bond interaction is primarily due to the 6p orbitals of Au while the Na-Au bond is mostly due to the 2p and 6s orbitals of Na and Au respectively. However, transition from phase I to the phase II structure breaks the Au-Au and

Na-Na bonds evident in phase I, leaving the Na-Au bonds as the only bonding interaction stabilizing the phase II structure. Search for multi-center bonding in the phase II structure recovered the Na-Au bonds with an ON of 1.21 electrons. Topological analysis of the phase II revealed these Na-Au bonds are closed shell interactions with low densities at the bond critical point. Similar to the phase II, the lower conduction band and valence band of the Phase III structure is primarily p-orbitals centered around Au, with only Na-Au and weak Au-Au bonding interactions obtained from the topological analysis. Analysis of the densities at the bond critical points for the phase I, phase II and phase III Na-Au bonds, reveal an increase in charge concentration at the BCPs at increased pressure. In addition, the bond critical points are closer to the alkali atom in the three phases of Na-Au intermetallics. Bader charge analysis of the three phases confirms the electron transfer from Na to Au which is expected from the electronegativity difference of the atoms. Atomic basin integration of the phase II and III using the Yu-Trinkle algorithm yields no NNMs unlike the phase I. Hence, contrary to pure Alkali metals which show increased localization of the interstitial electrons at high pressure, due to the core-valence overlap [160, 121], the sodium-gold intermetallics studied here show decrease in the localized interstitial electrons at high pressure. Similar trend was recently observed for sodium-potassium system by Frost et. al. [161], the authors attributed the reduced localization to the unusual structure of the NaK system they found. This is obviously not the case for the sodium-gold system, instead the high electronegativity of gold contributes to the reduced localization of interstitial electrons at higher pressure. Hence, decreased localization of interstitial electrons at increased pressure can be said to favor the formation and stability of alkali metal transition metal alloys.

Chapter 4

Transition path, electronic structure and bonding of Cs-II to complex Cs-III and Cs-III to Cs-IV

4.1 Introduction

Under extreme conditions such as high temperature and high pressure, the chemical bonding, electronic structures and properties of materials can undergo significant changes that leads to unusual chemical species which can otherwise not be reached at ambient conditions. Cesium metal has long attracted attention due to its unusual sequence of phase transition under pressure [162]. At ambient pressure, Cs metal assumes the body-centered cubic (BCC) structure and abbreviated as Cs-I. By displacement and electrical resistance measurements at room temperature, Bridgman [163] discovered two phase transitions of Cs which are the BCC Cs-I to face-centered cubic (FCC) Cs-II at 2.37GPa with relative volume $V/V_0 = 0.63$ and the Cs-II to Cs-III at about 4.22GPa with relative volume $V/V_0 = 0.455$. Using *in situ* high-pressure X-ray diffraction, Hall et. al. [164] confirmed the FCC structure assigned to Cs-II and they also showed that the Cs-II to Cs-III transition is an isostructural transition. Hence, the Cs-III was believed to retain the same FCC structure as Cs-II but with a considerably smaller lattice constant, at the time Cs and Ce are the two elements known to undergo an isostructural phase transition under pressure [162]. Takemura et. al. [165] discovered the tetragonal Cs-IV which forms at 4.3GPa with relative volume $V/V_0 = 0.418$. The Cs-IV transforms to Cs-V at about 12GPa [166] and is said to become superconducting in this vicinity [167], which makes it the first known superconducting alkali metal. The Cs-V

remains stable up to about 70GPa where it transforms to the double hexagonal close packed Cs-VI [168].

Over the years, pressure driven electronic transition where the 6s valence electrons were transferred to the more localized 5d-like state was used to explain the unusual properties of Cs. For example, the high compressibility of cesium below 10GPa [169], apparent isostructural phase transition [164], anomalous decrease in coordination number with increasing pressure (from 12 in Cs-II and Cs-III to 8 in Cs-IV) [165], observed anomalous melting curve [170, 171], resistivity [171, 172, 173] and optical properties [174]. The possibility of the FCC to FCC transition of Cs has been a subject of discussion as several *ab initio* computational studies conclude that Cs-III cannot assume the FCC structure [175, 176] and the computed FCC Cs-III is at a density far greater than the observed [177]. Contrary to the simple FCC structure previously reported by Hall et. al. [164], single crystal x-ray diffraction study of Cs-III at room temperature by McMahon et. al. [178] revealed a complex orthorhombic (space group $C222_1$) structure with 84 atoms in the unit cell. Since after the double hexagonal close packed Cs-VI was discovered, no other new phase of the Cs metal was found at higher pressure until recently Guan et. al. [179] predicted a post double hexagonal close packed cesium structure which they found with a crystal structure searching technique. The new post Cs-VI structure of Guan et. al. [179] was predicted to form above 180 GPa with just 0.3% volume reduction associated with the transformation. The newly reported phase of the Cs metal is said to have the same crystal symmetry and atomic arrangements with the low pressure FCC Cs-II. However, the bonding in the high pressure FCC phase is through the d electrons, unlike the low pressure Cs-II. Crystalline solid - solid transitions are one of the consequence of a change in pressure or temperature of a crystalline solid causing it to transform to another crystalline solid [180]. These transitions are referred to be first-order with a discontinuity in the volume, enthalpy and entropy due to modifications to the crystal packing or arrangement. However, the magnitude of the crystal packing changes in these solid - solid transformations are very much smaller compared to those that occur in transformations from crystalline solid to liquid. Crystalline forms of water and carbon are typical examples of solids commonly known to undergo crystalline solid - solid transitions [181, 182]. There is a need for comprehensive understanding of the transformation mechanisms because they often help

determine the material properties [183]. Other transitions like amorphous to crystalline or even crystalline to amorphous which find great application in fields like the pharmaceuticals have also been reported in metals [184, 185]. Understanding of the atomistic mechanisms of solid - solid phase transitions are still lagging due to the complexity of these transitions, it is also difficult to investigate them experimentally in most cases [183]. Although, colloidal model systems [186] were used in the past to directly observe the movement of the particles through a video microscopy, this model was developed in an attempt to circumvent the limitations of an atomistic understanding of solid - solid phase transitions. However, computer simulations, such as *ab initio* molecular dynamics, could help to resolve these issues and have been previously applied to describe the transition path of solids [187, 188, 181]. Over the years, constant pressure and temperature molecular dynamics simulations have proven to be suitable for phase transition studies. Though, the realistic timescales of these transitions far exceeds the few nanosecond (ns) time scale achieved in molecular dynamics and is one of the challenges faced by such constant pressure and temperature molecular dynamics methods [187]. The use of elevated pressures and sometimes temperatures are able to circumvent this limitation by modifying the kinetics. However, excessively strong driving may affect the mechanism of the transition process, hence, over-pressurization of the system should be avoided as much as possible [189]. Recently, Zhu et. al. [190] reported a mechanism of the graphite to diamond transition at high temperature by employing a large-scale molecular dynamics (MD) simulation. These previous studies validated the applicability of molecular dynamics for studying the atomistic mechanisms of phase transition. Hence, of interest in this work is the complex orthorhombic Cs-III of 84 atoms reported by Hall et. al. [164] and is said to be stable between 4.2GPa and 4.3GPa after which it transforms to Cs-IV which has a more simpler tetragonal structure. Over the years, no detailed study have been performed to theoretically reconstruct this complex Cs-III to Cs-IV and the Cs-II to Cs-III transitions nor critically explain the electron transfer in these structures. A clear knowledge of the structure and bonding nature of Cs-II, Cs-III and Cs-IV is critical for understanding the structural formation of complex Cs-III and likely help to explain its narrow stability pressure range. Through molecular dynamics simulation, the transition paths of the Cs-II $\rightarrow$ Cs-III and Cs-III $\rightarrow$ Cs-IV have been explored here in other to define the transition mechanism. In addition,

the electron density topological property of the Cs-II, Cs-III and Cs-IV structures have been studied. The results reveal the transition in the Cs-III to Cs-IV and the Cs-II to Cs-III transitions are typical crystalline solid-solid transitions with no evidence of melting found in the transition states. From the molecular dynamics simulation snapshots, the transformation mechanism observed in the Cs metal is martensitic (i.e a transformation that occurs through a diffusionless cooperative motion of all the atoms in a transformation region) for Cs-II $\rightarrow$ Cs-III transformation whereas the Cs-III $\rightarrow$ Cs-IV transition occurs through nucleation and growth. Also the results suggest existence of rather large activation barrier for the reverse transition to Cs-II by decompression (Cs-III $\rightarrow$ Cs-II).

4.2 Computational method

Structural optimizations, charge densities, density of state and *ab initio* molecular dynamics (AIMD) were performed using the Vienna *ab initio* Simulation (VASP) code [85] and Projector Augmented plane Waves (PAW) potential [93]. The Cs potential employed 5s, 5p and 6s as valence states, with the Perdew-Burke-Ernzerhof (PBE) exchange correlation functional [191]. The optimized 84 atoms Cs-III crystal structure was used as the starting configuration for the Cs-III $\rightarrow$ Cs-IV molecular dynamics (MD). An 84 atom Cs-II cell in the FCC geometry arranged in a body-centered hexagonal axis system was also used for the compression (Cs-II $\rightarrow$ Cs-III) and decompression (Cs-III $\rightarrow$ Cs-II) MD simulations. All the simulations were performed in an isobaric-isothermal ensemble (NPT) and the Langevin thermostat was used to control the temperature [67]. Using a timestep of 2fs a run of 40ps was first performed to equilibrate the thermodynamic parameters. This was then followed by a production run of 80ps for the Cs-III to Cs-IV transition and a 160ps run for the compression (Cs-II $\rightarrow$ Cs-III) and decompression (Cs-III $\rightarrow$ Cs-II) transition paths. To analyse the electronic structures, topological analysis was performed using the Critic2 program [91]. All visualizations were done using Visualization for Electronic Structure Analysis (VESTA) [122] code.

4.3 Results and discussion

4.3.1 Cs-III → Cs-IV transition path

Pressure driven solid - solid phase transitions can be categorized into two mechanisms. A reconstructive transformation, where large changes such as breakage and formation of bonds take place at the transition. The second type is displacive transition, where only little changes to the atomic positions are observed at the transition, and is often accompanied by a small strain [192]. The Cs-III → Cs-IV have been investigated first because we believe it has a simpler pathway for transformation from a complex to much simpler structure. To reveal the type of phase transitions and the atomistic details of the transition path, *ab initio* molecular dynamics (AIMD) simulation was performed in the NPT ensemble with a Langevin thermostat [67] for temperature control.

The phase transition from the complex orthorhombic Cs-III to the tetragonal Cs-IV (Figure 4.1d) reported experimentally at 4.3 GPa have been reconstructed theoretically here using *ab initio* molecular dynamics simulation method. The experimental Cs-III shown in Figure 4.1a and 4.1c was used as the starting configuration for the MD simulation. The experimental Cs-III crystal structure [164] is composed of four alternating layers of Cs atoms (Figure 4.1a), Figure 4.1b shows one layer of the Cs-III structure projected on the (010) plane. The red arrow and question mark in Figure 4.1 present the scientific question answered in this section "how does the Cs-III transform to the Cs-IV?". Figure 4.2. shows the evolution of the thermodynamic parameters during the simulation. As can be seen from Figure 4.2a, the mean pressure was maintained at 60 kbar which is in the region where Cs-IV is stable. Also the insert in Figure 4.2a is a snapshot of the last configuration after 120 ps. It is important to note that the simulation temperature in other to recover this Cs-III → Cs-IV transition was set to 400 K which is slightly below the thermodynamic melting point of Cs at the simulated pressure. The studied system was found to remain a solid, perhaps due to the well known overheating effect in a NPT or NVT simulation. The time evolution of the temperature is also given in Figure 4.2b and it shows the fluctuations in the simulation temperature is reasonable and within the desired temperature. An obvious discontinuity is observed in the

free energy close to 30 ps as indicated by the dashed arrow in Figure 4.2c. It is important to note that the free energy in VASP is computed from the electron entropy [85]

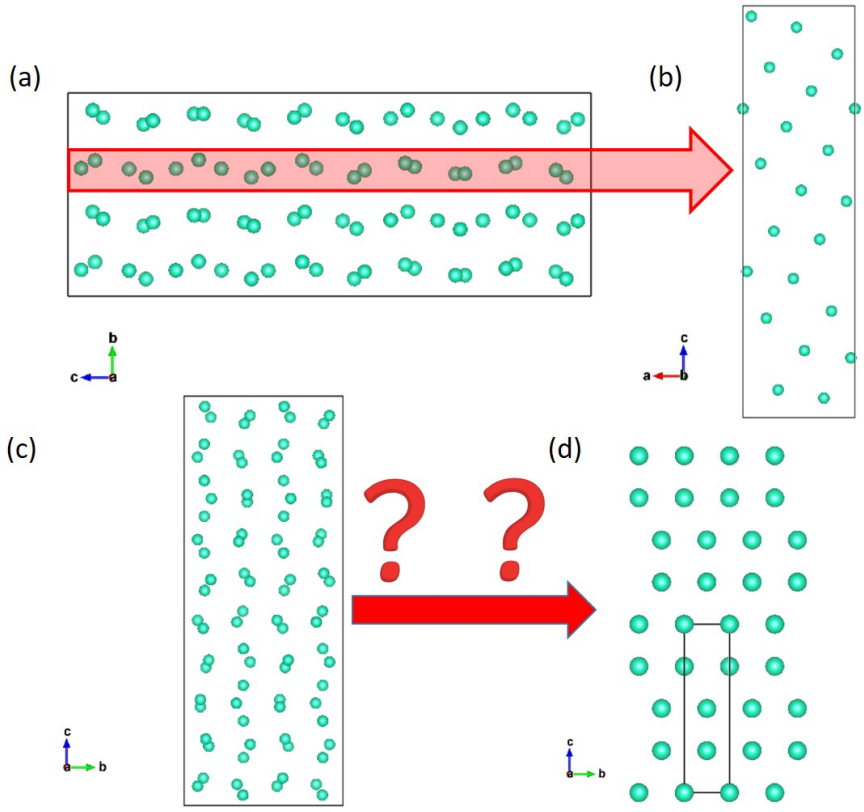

Figure 4.1: (a) (100) plane projection of experimental Cs-III structure (b) (010) plane projection of one layer of the Cs-III structure (highlighted by the pale red arrow) (c) Cs-III structure projected down the **a** axis (d) view down the **a** axis of experimental Cs-IV structure. The red question mark and arrow presents the scientific question answered in this section "how does the Cs-III transform to another crystalline Cs-IV?".

Randomly selected configurations around the discontinuity were then analyzed by quenching the structure at 0K through geometry optimization. The procedure is akin to the characterization of inherent structure of a liquid [193, 194, 195, 196, 197]. However, the optimized structures were found to still maintain the Cs-III structure but with a 9.5% reduction in volume. This slight volume decrease is also evident from the time evolution of the volume as there exist a dip in the volume around the same simulation time where the free energy is discontinuous as indicated by the arrow in Figure. 4.2d. In addition to the thermodynamic parameters, the time evolution of the lattice vectors provide information on the structural distortion and angles can provide insights on the studied transition.

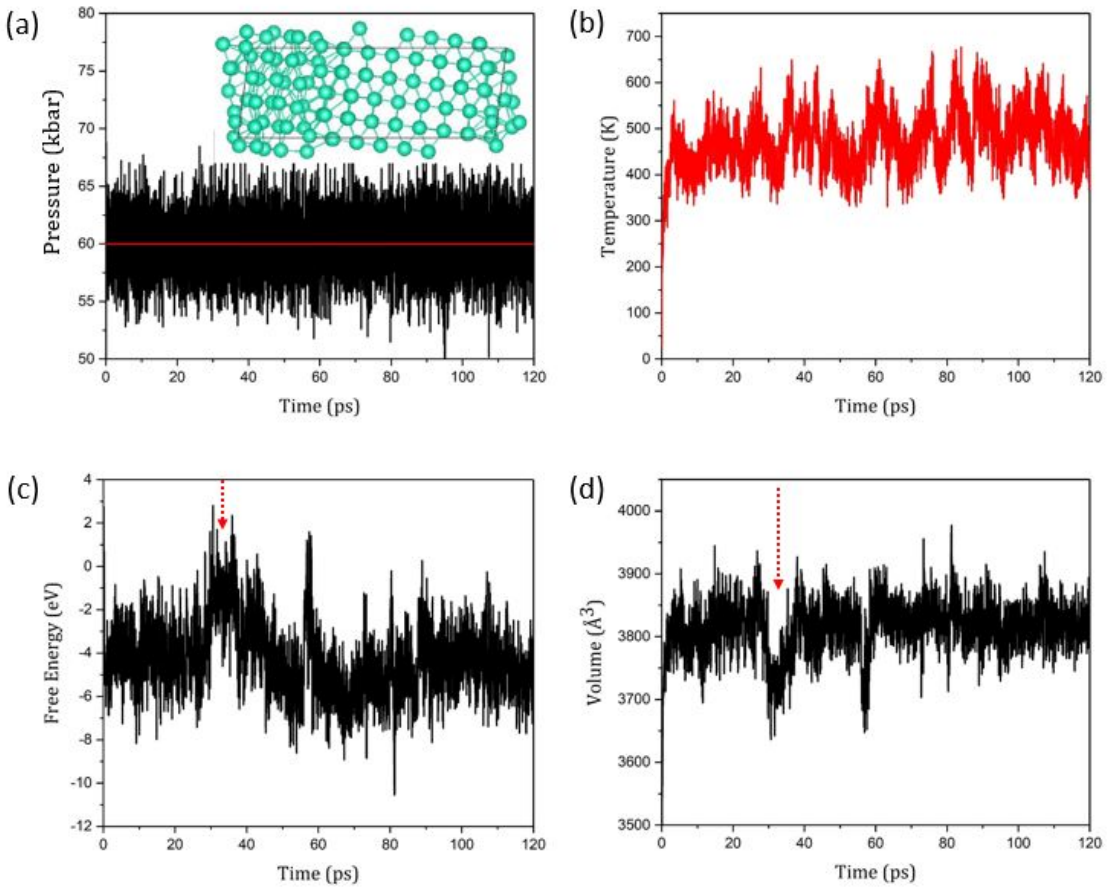

Figure 4.2: Thermodynamics parameters of Cs-III NPT simulation at 60 kbar (a) Pressure (b) Temperature (c) Free Energy (d) Volume. The insert in (a) is an optimized snapshot at 120 ps while the red arrows indicate discontinuous regions.

As can be seen in Figure 4.3a the **c** axis of the Cs-III structure increased with a slight discontinuity around 80ps after which it remained fairly constant. The **a** axis decreased at a fairly constant rate with time and becomes almost constant after 80ps. The **b** axis remains fairly constant throughout the simulation. The evolution of the cell angle given in Figure 4.3b show that the β (angle between **a** and **c**) and γ (angle between **a** and **b**) angles simultaneously decreased with time and become fairly constant after around 80ps. However, the α (i.e angle **b** and **c**) angle show an abrupt increase from 90^0 to 98^0 at around 50ps simulation time, and then remains constant. This substantial change in the α angle suggested the phase change in the crystal primarily occurred on the **bc** (100) plane. To further validate this reasoning, randomly selected snapshots throughout the simulation were extracted and examined for the evidence of a phase transition to Cs-IV.

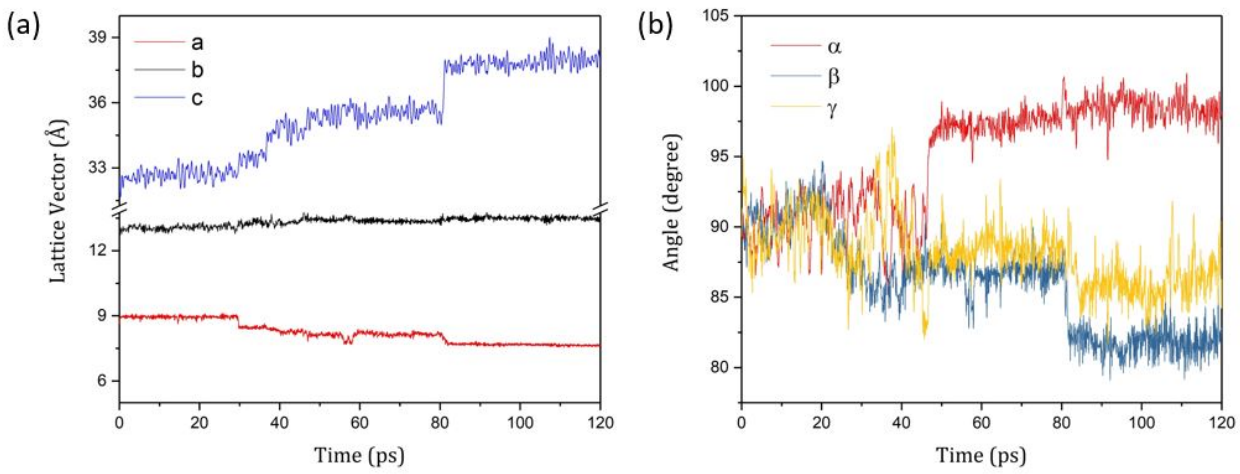

Figure 4.3: Time evolution of Cs-III NPT simulation at 60Kbar for the (a) lattice parameters (b) angles

The (100) plane of the starting Cs-III configuration is shown in Figure 4.4a. The other snapshots in Figure 4.4b, 4.4c, 4.4d, 4.4e and 4.4f are optimized configurations after 10ps, 20ps, 40ps, 80ps and 120ps respectively. The atomic motion and rearrangement of the Cs atoms with increased simulation time can be seen in Figure 4.4. Optimized configurations after 10ps and 20ps shown in Figure 4.4c and 4.4d, respectively, still retain remnant features of the starting Cs-III configuration, but the Cs atoms are slightly displaced. However, after 40ps, periodicity of the Cs-III structure seems to be lost completely and regions of disorder and some order separated by a dash line can be seen in Figure 4.4d.

As will be discussed below, longer simulation reveal a clear interface showing the nucleation and growth of Cs-IV crystal in the (100) plane as depicted by the red circle in Figure 4.4e. The nucleation was initiated at 80ps corresponding to the region where fluctuations in the free energy and volume becomes relatively stable (see Figure 4.2c and 4.2d). Also the formation of the crystalline Cs-IV on the (100) plane of the Cs-III is consistent with the observed large increase of the α angle over time (Figure 4.3b). Extended simulation run up to 120ps revealed more nucleation and growth of Cs-IV and gradually spreading through the simulation box. Also, coexistence of Cs-IV and Cs-III is evident in the quenched configuration after 120ps as can be seen in Figure 4.3f. Similar nucleation process have been previously reported for some other crystalline solids like the graphite to diamond transition reported by Khaliullin et. al. [181].

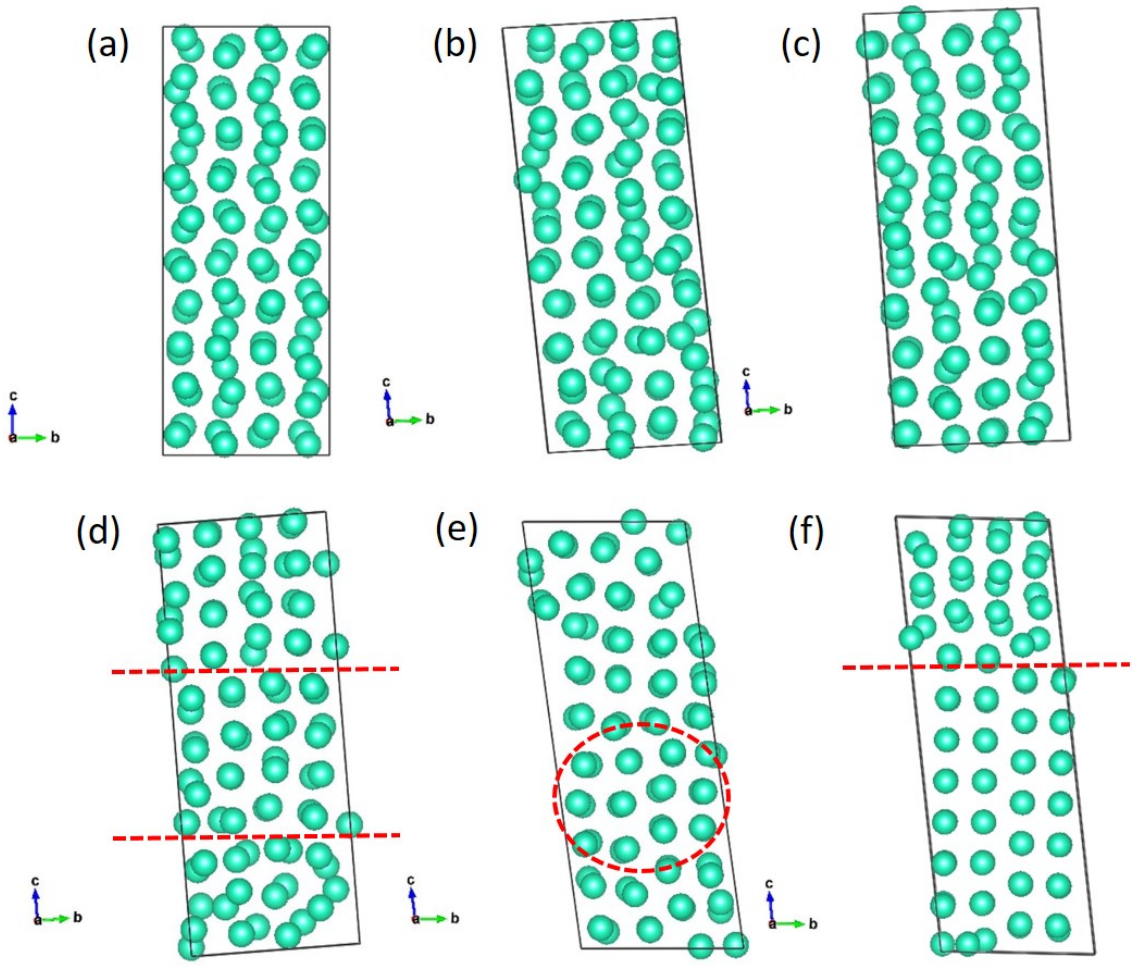

Figure 4.4: (100) plane projection of (a) the starting Cs-III Structure and Optimized Cs-III snapshots at (b) 10ps (c) 20ps (d) 40ps (e) 80ps (f) 120ps. N.B The disordered portion in (f) looks denser than the ordered portion. This is due to the illusion created by the displaced underneath atoms in the top layer of the projection. The red dash markings separate regions of order and disorder on the optimized snapshots.

To monitor the time evolution of the atomic positions, the root mean squared displacement (RMSD) of the Cs atoms throughout the simulation was computed and depicted in Figure 4.5 as a function of time. The red arrows in Figure 4.5 indicate discontinuous points after a relatively steady displacement. At 25ps, the examined snapshot still maintained the periodicity of Cs-III structure. After 45ps, the Cs atoms had a fairly constant displacement for 20ps and the optimized snapshots in this region differed from the initial structure but had not transformed to the desired Cs-IV. However, ordered Cs atom regions suspected to be Cs-IV began to appear after 80ps (Figure 4.4e). Hence, the type of phase transition that takes

place as the Cs-III transforms to Cs-IV is a reconstructive phase transition as the transition path shown in Figure 4.4 features some significant bond breaking and formation also evident from the large displacement of the Cs atoms throughout the simulation.

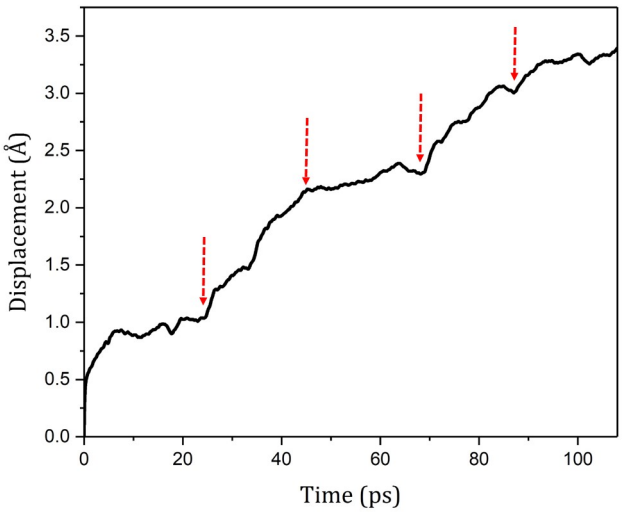

Figure 4.5: Time evolution of Cs atom displacement for the Cs-III → Cs-IV transition. The red arrows indicate discontinuous regions after a relatively steady motion.

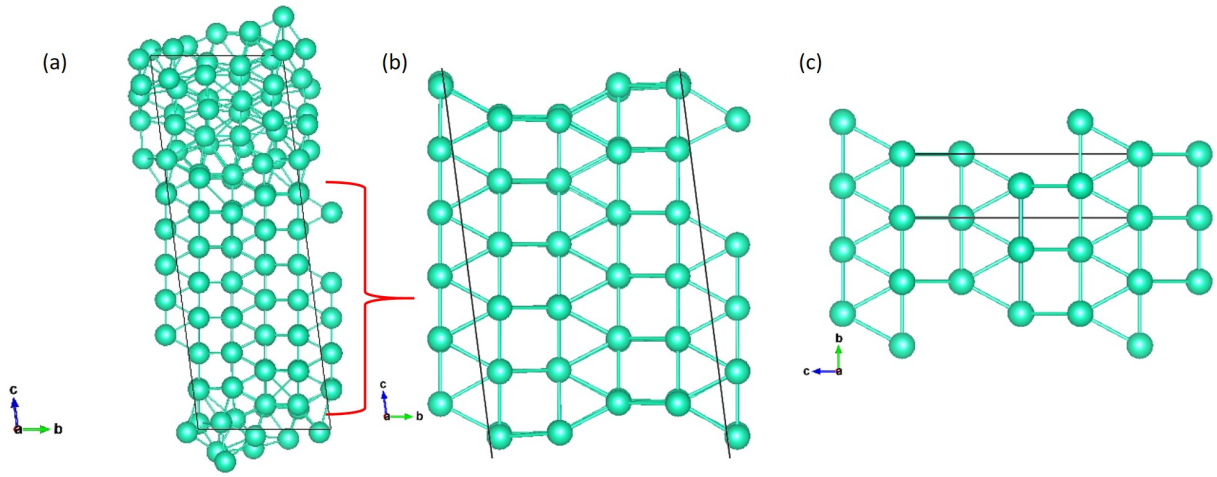

Figure 4.6: Comparison of (a and b) optimized 120ps Cs-III structure with the (c) experimental Cs-IV structure. The ordered region of the extracted Cs-III snapshot can be seen to match the Cs-IV structure.

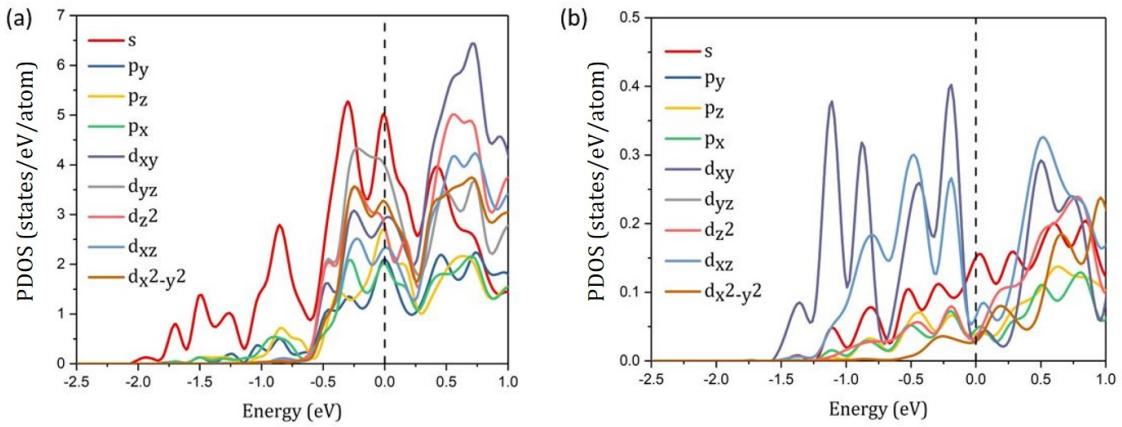

Figure 4.7: Projected density of state of (a) Cs-III and (b) Cs-IV. The s-d transition is evident as the d orbitals can be seen to dominate the valence states in Cs-IV unlike the Cs-III where s is the dominant orbital.

Figure 4.6 shows a comparison of the optimized configuration after 120ps with the (100) plane of the experimental Cs-IV structure. An enlarged periodic region of the 120ps Cs-III configuration is shown in Figure 4.6b. When compared with Figure 4.6c, which is the crystal structure of Cs-IV, a perfect agreement is observed. Thus the nucleation formed from the NPT molecular dynamics simulation on Cs-III indeed resulted in the crystalline Cs-IV. The Cs-III to Cs-IV transformation is a growth process that forms through systematic rearrangement of the Cs atoms by increasing the c-axis while uniformly reducing the a and b axis to accommodate the tetragonal Cs-IV structure. Crystal structures which have trigonal-prismatic motifs are known to show dominance of d-electrons bonding [198]. Cs-IV which has triangular and square arrangement of the Cs atoms (Figure. 4.6) is also expected to reflect the dominance of bonding via the d-electrons near the Fermi energy. The electronic structure is examined by comparing the projected densities of state (pDOS) of Cs-III to that of Cs-IV (Figure. 4.7). From the pDOS, the Cs phases are metallic. On closer examination of the orbitals near the Fermi level, it is evident in Cs-III that the valence states and lowest conduction states are dominated by the 6s orbital with low lying 5d and 6p orbitals. In comparison to the pDOS of Cs-IV shown in Figure. 4.7b, the d population are dominant in the valence state. This implies an s-d band transition has indeed occurred as the complex Cs-III transforms to simple open structured Cs-IV.

4.3.2 Compression (forward) Cs-II → Cs-III transformation

Following the study on the reconstruction of Cs-III to Cs-IV transition, NPT molecular dynamics simulation method was applied in an attempt to investigate the simple FCC Cs-II to the complex Cs-III (compression or forward) transition. The red arrow and question marks in Figure 4.8 presents the scientific question of this section "how does the FCC Cs-II transform to a complex orthorhombic Cs-III structure?". Figure 4.8a shows the crystal structures of the initial Cs-II configuration used in the NPT molecular dynamics simulation. For the forward transition, the starting configuration is an 84 atom simulation cell constructed from the FCC Cs-II structure, Figure 4.8a and commensurate with the Cs-III structure (Figure 4.8b). The shaded purple arrow highlights one layer of the Cs-III structure projected on the (010) plane.

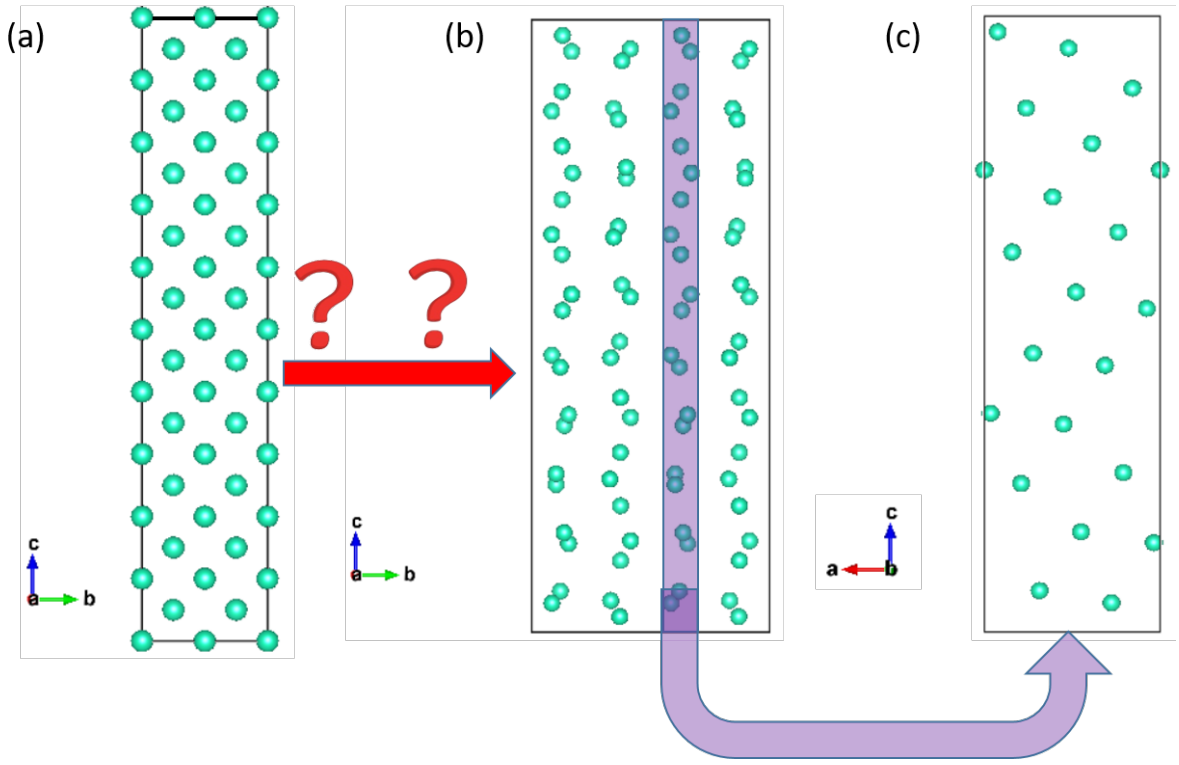

Figure 4.8: Snapshots of (a) starting Cs-II configuration for the NPT molecular dynamics simulation projected down the **a** axis (b) (100) plane of the experimental Cs-III structure (c) single layer of the Cs-III structure plotted on the **ac** plane. The purple arrow indicate the extracted layer while the red arrow and question marks present the scientific question "how does the Cs-II transform to the complex Cs-III?".

The relevant thermodynamics parameters of the NPT molecular dynamics simulation for the forward transition (i.e compression from Cs-II) is presented in Figure 4.9. The simulation pressure was set to 42kbar, which is the pressure at which the Cs-III was observed from experiment. As expected, Figure 4.9a shows the mean pressure is maintained at the desired pressure of 42kbar. The temperature was controlled using a Langevin thermostat [67], and maintained at 275K as shown in Figure 4.9b. A rise in the free energy was observed at 25ps (indicated by the red arrow in Figure 4.9c) and then dropped to an almost constant value at 60ps. This change is accompanied with a reduction in volume in the same region (Figure 4.9d).

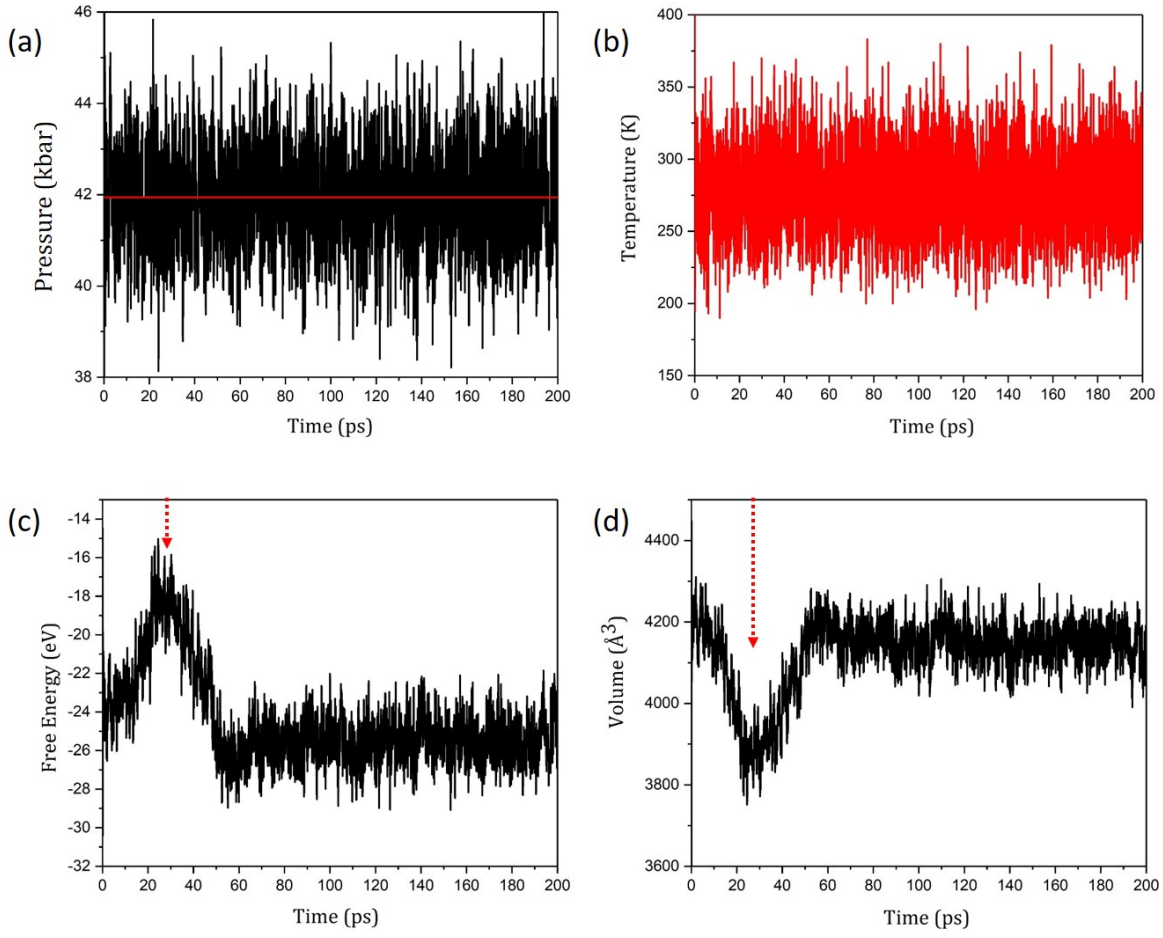

Figure 4.9: Thermodynamics parameters of the NPT molecular dynamics simulation for the forward (Cs-II → Cs-III) transition (a) Pressure (b) Temperature (c) Free Energy (d) Volume. The red arrows indicate discontinuous regions.

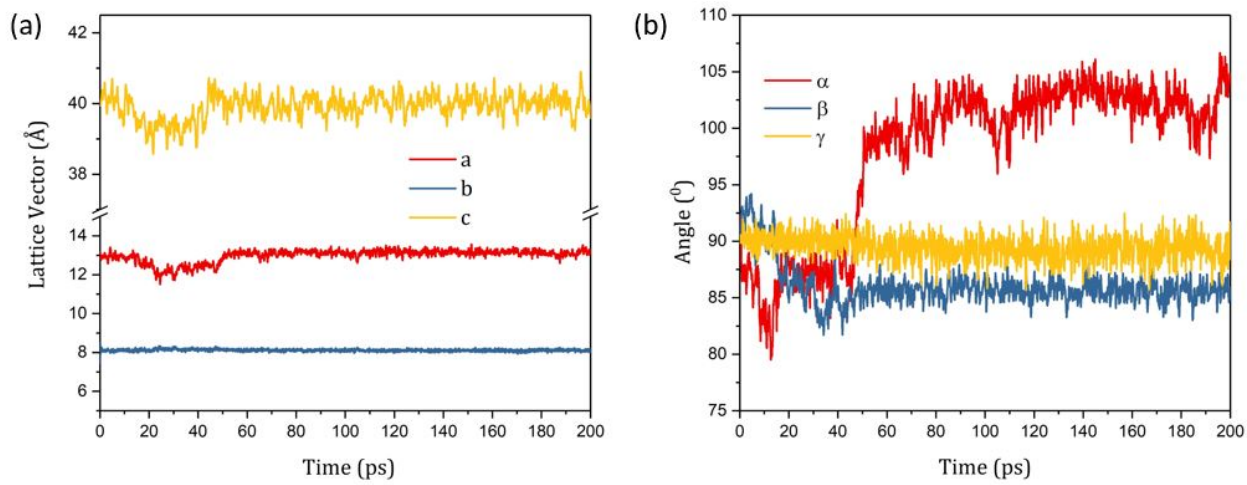

Figure 4.10: Evolution of the (a) lattice vectors and (b) angles of the NPT molecular dynamics simulation for the forward transition (i.e Cs-II - Cs-III)

Temporal variations of the lattice vector and angles for this compression (Cs-II → Cs-III) is depicted in Figure 4.10a and 4.10b respectively. The **a** and **c** lattice vectors decreased slightly near the 30ps where the free energy and volume drastically changed. However, after 35ps, the **a** and **c** lattice vectors become stabilized. In contrast to the **a** and **c** axis, no significant change is observed for the **b** lattice vector, implying that there was little variation along the **b** axis with time. The temporal evolution of the lattice angles shown in Figure 4.10b define α, β and γ angles of the lattice plane. The γ angle remained fairly constant throughout the simulation. In comparison, the β angle slightly decreased from 92^0 to 86^0 in the first 40ps and then remained almost constant. However, the α angle was found to decrease from 90^0 to 80^0 in the first 12ps, it then increased to 102^0 and becomes steady after 60ps. The root mean squared displacement was examined to evaluate how far the atoms had deviated from the original starting configuration.

First the average displacement (RMSD) of the Cs atoms were examined as a function of time (Figure 4.11). The Cs atoms moved 1.5Å from their initial position in the first 40ps and maintained a fairly constant displacement for additional 50ps after which it increased to 1.7Å and then remained constant for the remainder of the simulation. To check if the Cs atom displacements has led to the eventual Cs-II to Cs-III transformation, random configurations were selected every 20ps from the MD trajectory (i.e at 20ps, 40ps, 60ps, 80ps, 100ps, 120ps, 140ps, 160ps, 180ps and 200ps). Each extracted snapshot was quenched to 0K by

performing a geometry optimization. It is important to note that the axis system between the experimental Cs-III and the reconstructed structure from Cs-II changed (i.e Cs-II **a** corresponds to Cs-III **b** and Cs-II **b** corresponds to Cs-III **a**, the **c** axis remains unchanged). The (010) plane of the experimental Cs-III structure (one layer highlighted by the purple arrow in Figure 4.8) formed on the (100) plane of the Cs-II supercell. Hence the (010) and (100) planes of the experimental Cs-III and simulated Cs-II snapshots have been examined for phase transition here.

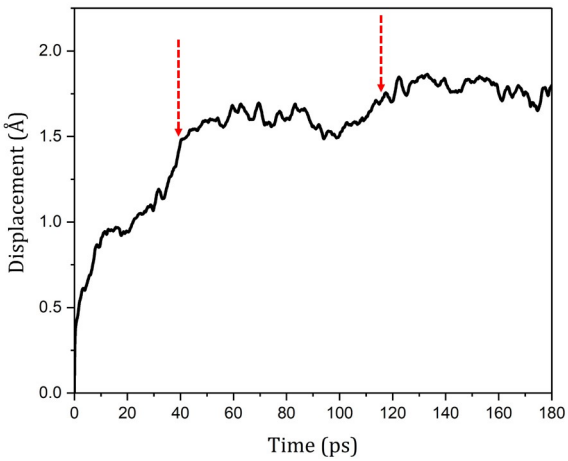

Figure 4.11: Time evolution of the Cs atom displacement for the Cs-II → Cs-III transition. The red arrows indicate regions before steady displacement of the Cs atoms.

A comparison of one layer of the Cs-III (010) plane, Figure 4.12a and (100) plane of optimized snapshots from the Cs-II → Cs-III NPT molecular dynamics is presented in Figure 4.12b-k. After 20ps, two sections of the Cs atoms distinguished by a horizontal drift of the upper section along the **b** axis is observed in the selected snapshot shown in Figure 4.12b. The atoms maintained similar arrangements at 40ps as can be seen in Figure 4.12c. From 60ps, the (100) plane of extracted snapshots begin to show similar atomic arrangement as the (010) plane of the Cs-III. These regions of similar Cs atom local environment are marked in red in Figure 4.12. Closer examination of the 200ps snapshot (Figure 4.13b) reveal the **c** axis tilts by 20^0 while the Cs atoms makes a 30^0 tilt similar to the tilt angle of the Cs atoms in the experimental Cs-III structure shown in Figure 4.13a.

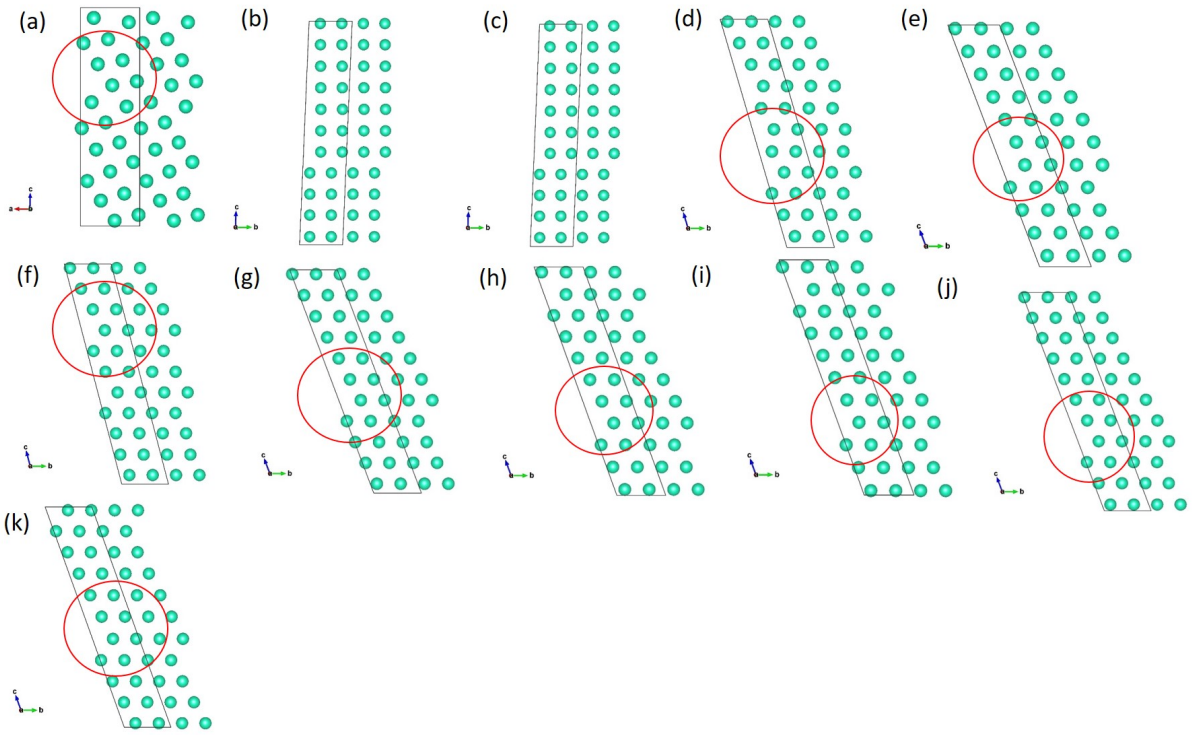

Figure 4.12: (a) One layer of Cs-III (010) plane and (100) plane of the optimized Cs-II → Cs-III NPT configurations extracted after (b) 20ps (c) 40ps (d) 60ps (e) 80ps (f) 100ps (g) 120ps (h) 140ps (i) 160ps (j) 180ps (k) 200ps. The red circles mark regions of similar Cs atom arrangements compared to the experimental Cs-III structure in (a).

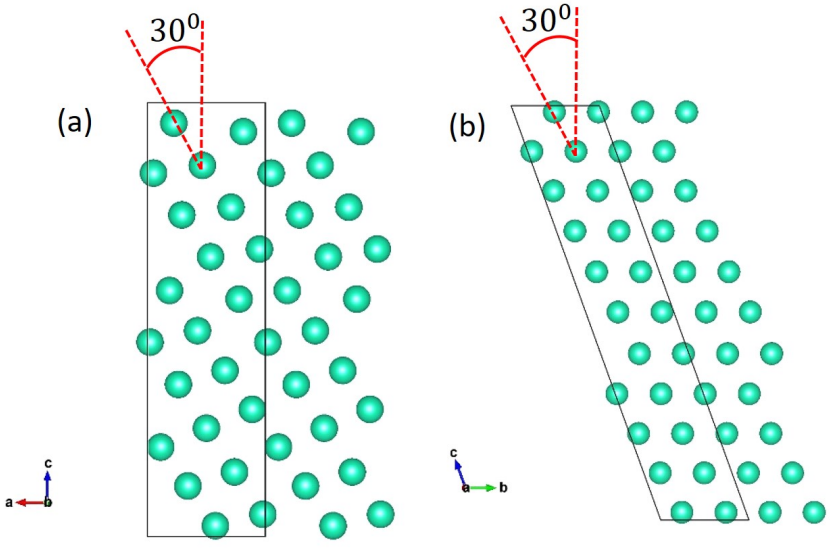

Figure 4.13: (a) One layer of experimental Cs-III (010) plane and (b) (100) plane of the optimized Cs-II → Cs-III NPT configurations extracted after 200ps. The tilt angles of the Cs atoms in both snapshot is identical which indicates the obtained structure at 200ps is the transformed Cs-III structure.

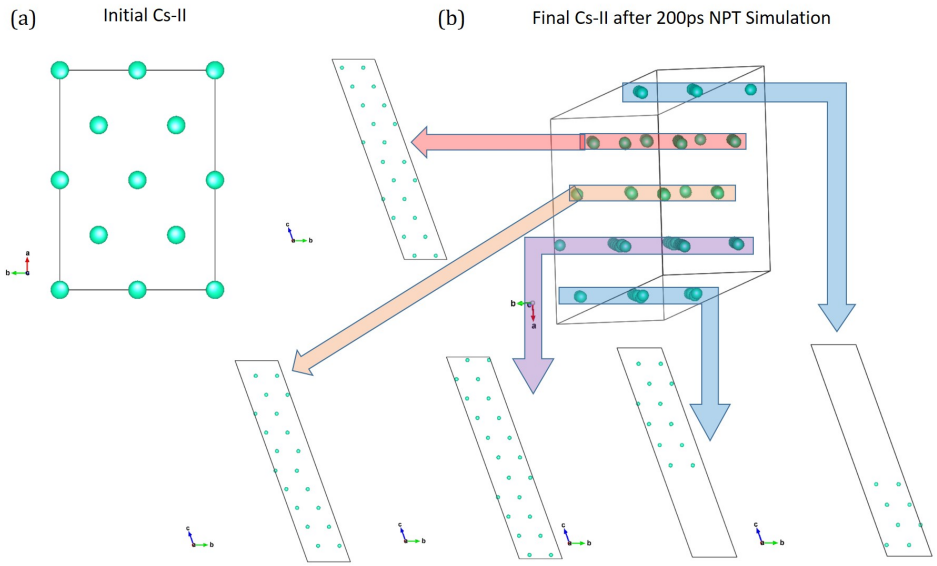

Figure 4.14: Projection down the **c** axis for (a)Initial Cs II structure used for the molecular dynamics (MD) simulation and (b) Optimized snapshot after 200ps for the Cs-II → Cs-III transformation. The arrows point to the (100) planes of the highlighted layers.

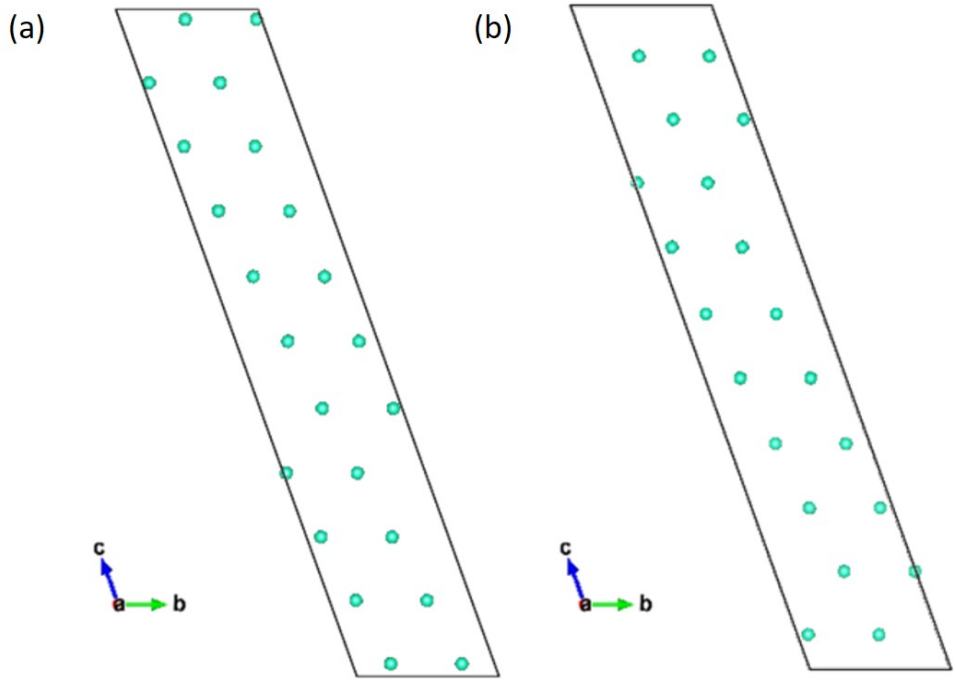

Figure 4.15: (a and b) The (100) plane of two adjacent layers of the optimized Cs-II → Cs-III NPT configuration extracted after 200ps. Note the differences in the tilted angle.

A distinct feature of the Cs-III structure is that the Cs atoms are not co-planer in the layers. After 200ps, one snapshot was extracted and quenched to 0K. Projected view of the optimized snapshot showing five layers of Cs atoms in Figure 4.14b. Note that the top and bottom layers corresponds to the same layer i.e the layers highlighted blue (Figure 4.14b). Hence, there are four layers of Cs atoms (highlighted blue, pink, yellow and purple in Figure 4.14b) in the optimized snapshot similar to the experimental Cs-III (i.e the experimental Cs-III consists of four alternating Cs atom layers). Closer examination of the (100) plane of each layer show the non-coplanar Cs atom feature i.e the Cs atoms in each layer are not co-planer. This is confirmation that the final Cs-II snapshot in Figure 4.14b is transformed Cs-III.

As already noted earlier, the unit cell of the experimental Cs-III is composed of four identical layers of alternating orientations (Figure 4.1a). Similar feature was also observed in the extracted snapshots from the NPT molecular dynamics simulation of Cs-II → Cs-III transformation (Figure 4.14). Two adjacent layers of the 200ps snapshot are compared in Figure 4.15. The tilting of the respective planes are the same as observed in the experiment [178].

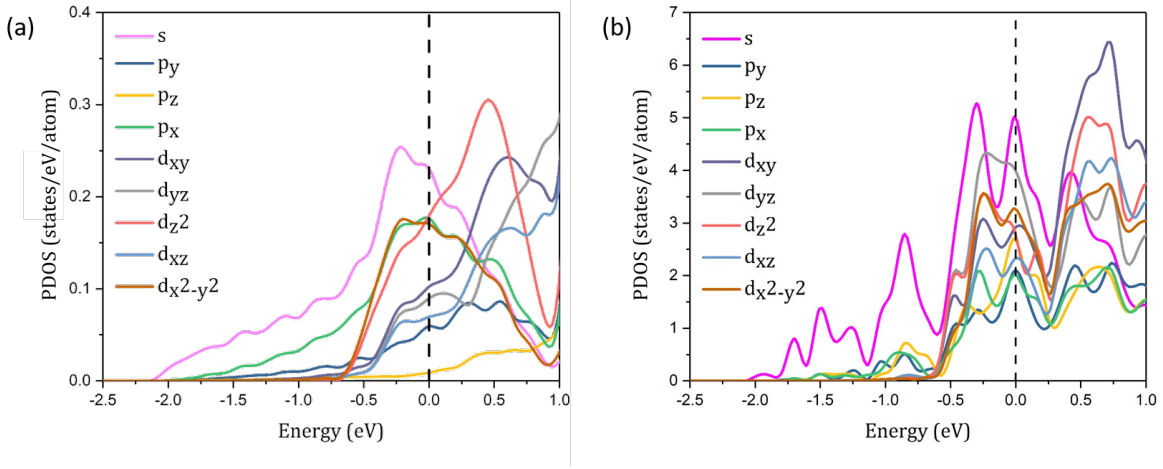

Figure 4.16: Comparison of the projected density of state of (a) Cs-II and (b) Cs-III.

A comparison of the Cs-II and Cs-III projected density of state in Figure 4.16a and 4.16b show the 6s orbital still dominates the valence states. This suggest that the s-d transition from Cs-II to Cs-III is not completed, although there are notable increase in the d-DOS near the Fermi level. Finally, the 30^0 inclination and alternating layer arrangement of the Cs atoms observed in the optimized molecular dynamics snapshot (Figure 4.13b and 4.15) confirms the Cs-II has transformed to Cs-III and the transformation does not occur through nucleation and growth (Figure 4.12). Instead this Cs-II $\rightarrow$ Cs-III transformation occurs through a cooperative motion of the Cs atoms, hence, it is a martenistic transformation. In addition, due to the 1GPa stability window of the Cs-III, the backward transformation (i.e decompression from Cs-III to Cs-II) was performed and is summarized below.

4.3.3 Decompression (backward) Cs-III → Cs-II transformation

Having recovered the Cs-III from a forward transformation (i.e compressing Cs-II → Cs-III), similar methods have been applied to reconstruct the Cs-II from a reverse transformation path (i.e decompressing Cs-III → Cs-II). From experiment [178], Cs-III is only stable within a very small pressure range from 4.2GPa to 4.3GPa. From the extrapolation of the phase boundaries, Ref. [199] shows Cs-III will disappear around 170K and the Cs-II to Cs-IV transition become direct. This observation indicates the energetics from the Cs-II to Cs-III and Cs-II → Cs-IV may be very competitive. Hence, it is relevant to investigate the possibility of the reverse transformation i.e Cs-III → Cs-II at 300K. The backward transformation was simulated using an NPT ensemble at 30Kbar in an attempt to recover the Cs-II structure from the 84 atoms Cs-III structure shown in Figure 4.8b.

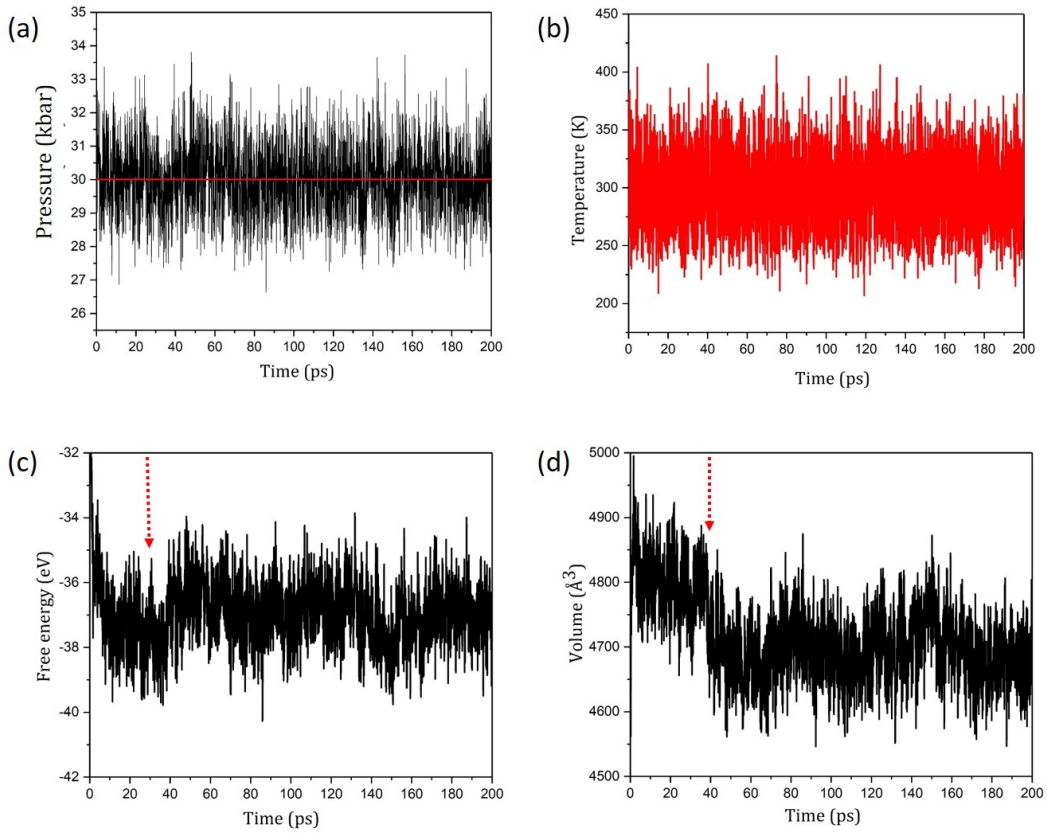

Figure 4.17: Thermodynamics parameters of the NPT molecular dynamics simulation for the backward (Cs-III → Cs-II) transition (a) Pressure (b) Temperature (c) Free Energy (d) Volume

The relevant thermodynamics parameters from the simulation of the Cs-III → Cs-II transformation are presented in Figure 4.17. The simulation temperature was controlled using a Langevin thermostat [67] with the mean temperature maintained at the desired temperature of 300K as evident in Figure 4.17b. Contrary to the Cs-III → Cs-IV and Cs-II → Cs-III transitions where a very significant change was observed in the free energy around 30ps, the Cs-III → Cs-II on the other hand does not show such spikes in the free energy. Instead, the free energy drops within the aforementioned simulation step as evident in Figure 4.17c. These aforementioned trend in the free energy is valid because the Cs-III → Cs-II transformation is from a high density Cs-III to a lower density Cs-II structure. Temporal evolution of the lattice vectors and angles from the decompression are presented in Figure 4.18a and 4.18b respectively. The **a** and **b** lattice vectors remains fairly constant throughout the simulation, only the **c** axis greatly decreased as the structure evolved with time. The angles between the lattice vectors on the other hand fluctuate throughout the simulation.

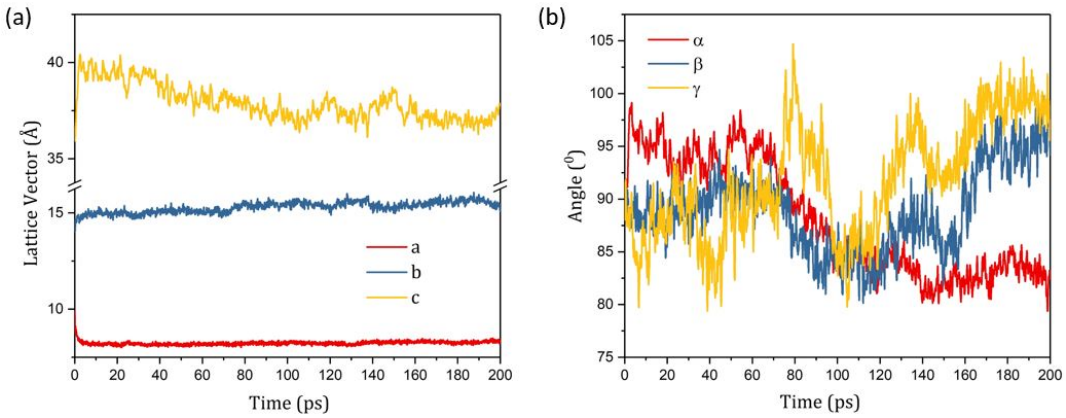

Figure 4.18: Evolution of the (a) lattice vectors and (b) angles of the NPT molecular dynamics simulation for the backward transition (i.e Cs-III → Cs-II)

The α angle (i.e angle between the **b** and **c** axis) decreased quickly to 82^0 after 150ps simulation time and remained fairly constant. The β (i.e angle between the **a** and **c** axis) and γ (i.e angle between the **a** and **b** axis) angles maintained similar trend with both angles increasing as the simulation evolved. The distortions to the lattice angles observed in the Cs-III → Cs-II transformation differ from those seen in the Cs-II → Cs-III transformation. These trend in the lattice angles for the reverse transformation are expected because the Cs-III structure is being decompressed to 30Kbar in an attempt to recover the Cs-II.

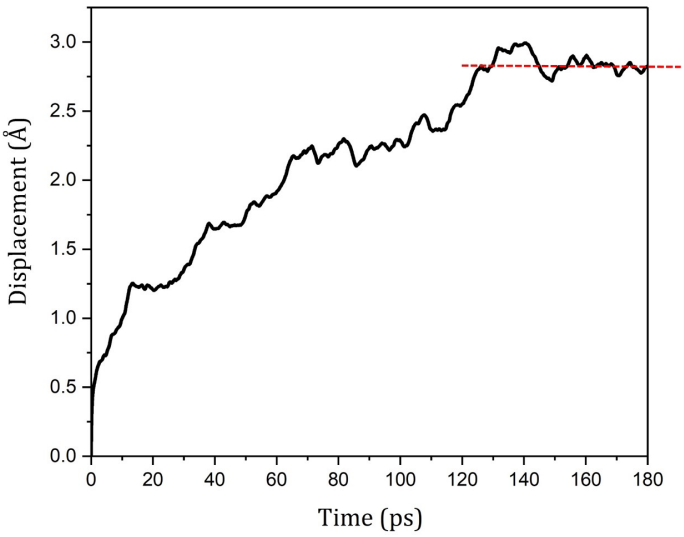

Figure 4.19: Displacement the Cs atoms in the Cs-III → Cs-II transition. The mean displacement remained fairly constant after 160ps.

The average deviation of the Cs atoms from their original positions in the decompression transition is shown in Figure 4.19. The plot shows the atomic displacement increased steadily with time until 120 - 130ps and then remained fairly constant. Random configurations were selected from the Cs-III → Cs-II transition NPT molecular dynamics trajectory at 40ps, 100ps, 140ps and 200ps and quenched to 0K. The optimized configurations at 40ps, 100ps, 140ps and 200ps are presented in Figure 4.20a, 4.20b, 4.20c and 4.20d respectively. A close examination of the structure revealed similar local environment of the Cs atom when projected down the (100) plane. The orange patches on the optimized configurations shown in Figure 4.20 highlights the local environment of the Cs which forms a hexagonal-like Cs atom ring network. However, the Cs atoms which form the ring networks are not co-planer. Close examination of the 200ps snapshot reveal three regions separated by the red dashed line in Figure 4.21a. The intermediate region in Figure 4.21a show some ordered layers of Cs atoms while the other two layers lack periodicity. Figure 4.21b show the projection of the ordered region on the (100) plane, it also show a hexagonal-like Cs atom network. However, the local environment of the Cs atoms in Figure 4.21c still differ from that of the Cs-II.

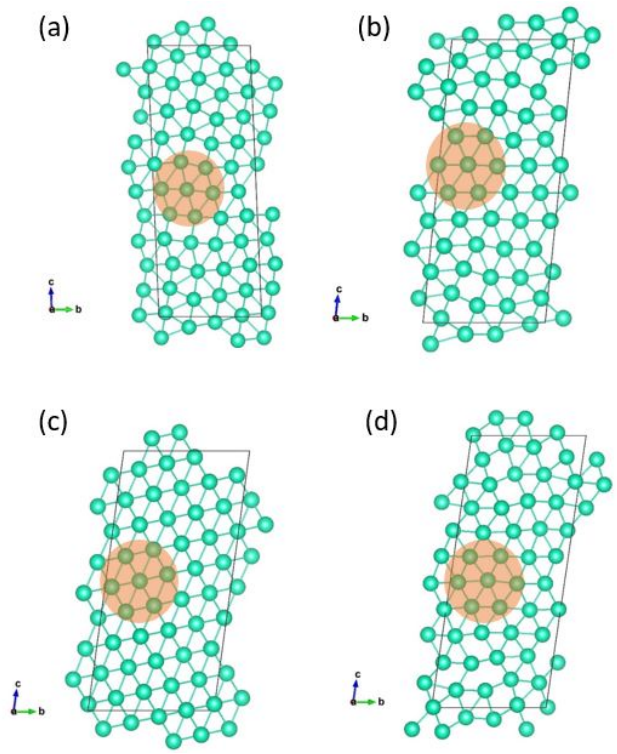

Figure 4.20: Optimized snapshots from the Cs-III → Cs-II transition after (a) 40ps (b) 100ps (c) 140ps (d) 200ps simulation time.

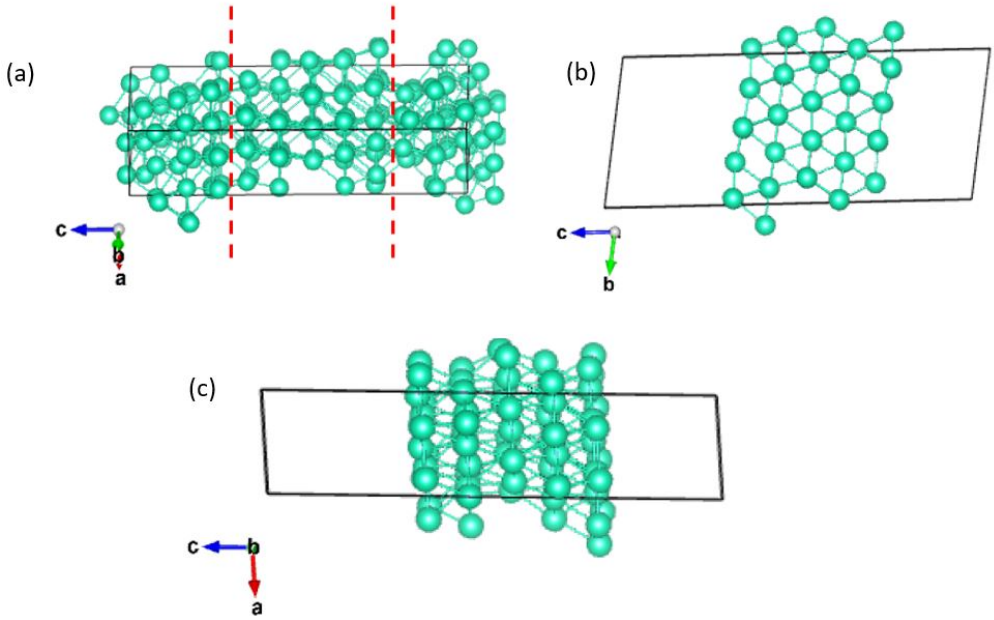

Figure 4.21: Optimized snapshot extracted from the Cs-III → Cs-II NPT molecular dynamics simulation trajectory after 200ps. (a) projection down the b axis showing three regions (b) (100) plane and (c) (010) plane of the ordered region.

Hence, the Cs-II was not recovered from the 200ps simulation. This suggests the activation barrier for the reverse (Cs-III $\rightarrow$ Cs-II) transformation is larger. This is to be expected, as the energy barrier for the reverse transition is the sum of the activation energy for the forward transition from Cs-II $\rightarrow$ Cs-III and the energy difference between Cs-III and Cs-II. Furthermore, previous reports have noted that, because DFT-based molecular dynamics (MD) simulation are restricted to systems of a few hundreds of atoms, one of it's obvious drawback is that the simulated phase transition collectively occur, with all chemical bonds reconstructed simultaneously across the simulation box thereby causing an increase in the activation barrier and makes the transition less frequent [187, 188, 189, 181, 200]. The compression (Cs-II $\rightarrow$ Cs-III) and decompression (Cs-III $\rightarrow$ Cs-II) transition paths studied here show transformations that occur through a cooperative motion of all the Cs atoms in the simulation cell, which is a typical characteristics of a martensitic transformation. Previous reports have shown that solid - solid transitions can either follow a diffusive nucleation or various diffusionless martensitic transitions that also involves breaking and formation of bonds [201]. Hence, unlike the Cs-III $\rightarrow$ Cs-IV transition which occur through nucleation and growth of the Cs atom, the Cs-II $\rightarrow$ Cs-III and Cs-III $\rightarrow$ Cs-II transitions occur through a martensitic transformation.

4.3.4 Electron Density Topological Analysis

The quantum theory of atom in molecule (QTAIM) topological analysis method developed by Bader [150, 27, 28, 29] have been used to quantify electrides in molecular and periodic systems [202, 203]. The QTAIM have also been used in Chapter two and three of this thesis to describe the bonding of high pressure intermetallic structures. Hence, similar methods have been employed in this chapter to analyze the electron density topology of the Cs-II, Cs-III and Cs-IV structures. Topological analysis of the Cs-II which has a face centered cubic structure was analyzed at 3GPa. The analysis revealed one non-nuclear maximum (NNM) present in the Cs-II structure occupying four symmetry equivalent point (Figure 4.22a). The QTAIM analysis also yielded bond critical points (BCPs) between the Cs atoms with the topological properties at the Cs - Cs bond critical point presented in table 4.1. The low density ($\rho(r_{BCP})$) and positive Laplacian ($\nabla^2\rho(r_{BCP})$) and local energy density (H) at the BCP indicates the bond is a closed shell interaction. The BCPs are represented by the black dots in the Cs-II structure while the NNMs are the blue circles shown in Figure 4.22a. By integrating the atomic basin using the Yu-trickle algorithm [154], the volume of the NNM and Cs atom are 2.53(a.u)^3 and 411.85(a.u)^3 respectively. In addition, the integrated charges are 8.99e$^-$ and 0.01e$^-$ for the Cs and NNM respectively. Though the volume at the NNM position is small compared to the Cs atom, there is some transfer of electrons to the intersticial sites. The Cs-II has never been previously reported to have an electride, hence, the results of the topological analysis presented here are new. However, this observation has been reprted in elemetal Li at ambient pressure [204]. In other to further probe the presence of the NNMs in Cs-II, the electron localization function (ELF) was plotted and superposed with the NNM positions from the QTAIM analysis as shown in Figure 4.22b. At the 0.7 isovalue plotted here, the ELF can be seen to localized in the NNM position, hence, validating the results from the topological analysis. In addition, the absence of ELF maxima along the Cs-Cs bond axis support the QTAIM analysis of a weak closed shell interaction.

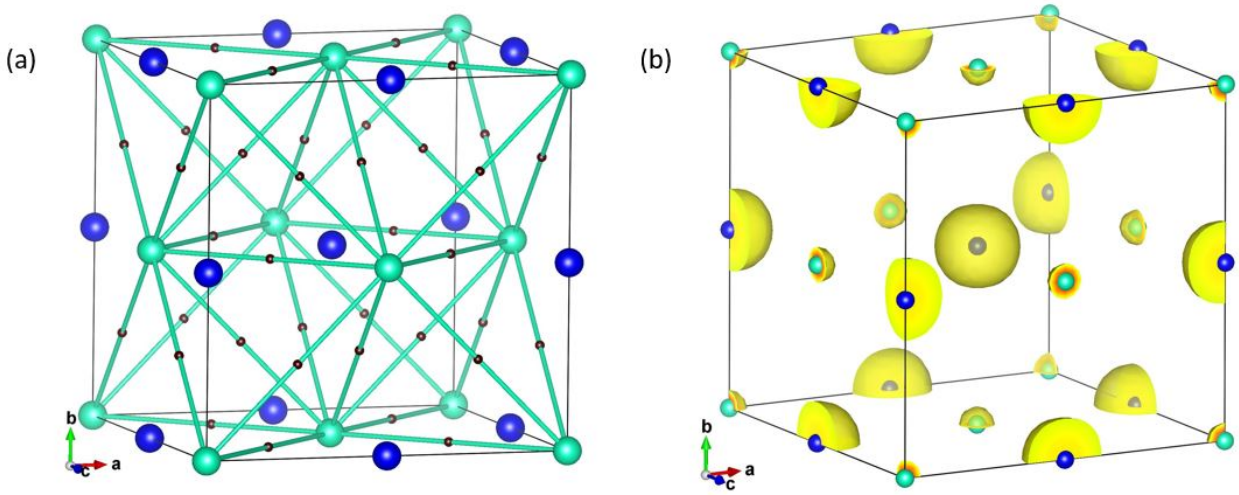

Figure 4.22: (a) Cs-II topological graph showing the bond critical points in black and NNMs in blue (b) ELF of Cs-II at 0.7 isovalue superposed with the NNMs in blue

Critical Point	d(Å)	$\rho(r_{BCP})$ (ea_0^{-3})	$\nabla^2\rho(r_{BCP})$ (ea_0^{-5})	V (E_h)	G (E_h)	H (E_h)	Int. Vol. (a_0^3)
Cs							411.85
NNM							2.53
Cs - Cs	4.428	0.004	0.006	-0.001	0.001	0.0002	

Table 4.1: Topological properties of Cs-II at the nuclear (Cs and NNM) and bond (Cs - Cs) critical points. Where only the integrated volume have been reported for Cs and the non-nuclear maximum (NNM) because the density (ρ), Laplacian ($\nabla^2\rho$), potential energy (V), kinetic energy (G), and local energy densities (H) are not important at the nuclear positions.

The complex orthorhombic Cs-III structure at 4.2GPa have been analyzed here. The ELF using an isovalue of 0.92 is plotted in Figure 4.23. The plot reveals electron localization in the interstitial sites of the Cs-III structure. The ELF projection along the 100 plane suggest that each lobe of the electrides forms from nearest neighbour Cs atoms as can be seen in Figure 4.23a. Also the projected view presented in Figure 4.23b reveal the electrides localize in the inter Cs. layers The complex nature of the Cs-III 84 atoms structure makes it difficult to perform the topological analysis. However, the ELF can be used to validate the presence of electrides. Hence, the large isovalue of the localized electrons in the Cs-III implies that

the Cs atoms transfer the electrons to the interstitial regions of the structure. As discussed above, this is due to the small participation of the Cs 5d near the Fermi level.

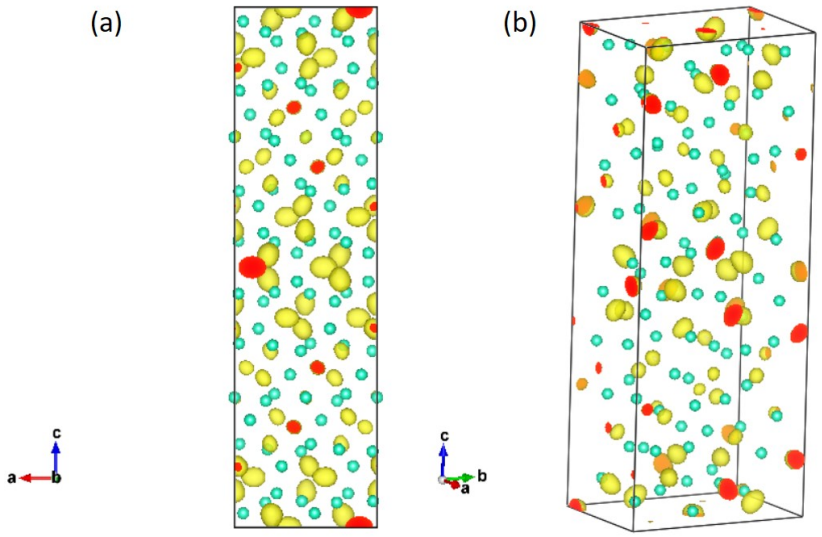

Figure 4.23: Electron localization function (ELF) of Cs-III at 0.92 isovalue for the (a) 100 plane and (b) projected view. Colour code; green = Cs atoms, yellow = ELFs.

To understand the electron distribution from the 84 atom Cs in Cs-III to the 4 atom Cs in Cs-IV, the electron density topology of Cs-IV was analyzed. The topological analysis finds three unique non nuclear maximums (NNMs) and symmetry inequivalent bond critical points between the NNMs (table 4.2). No bond critical point (BCP) was found between the Cs atoms. Analysis of ρ and $\nabla^2\rho$ at the bond criical points reveal the NNMs form a covalent bond interaction though the magnitude of ρ at the BCP is less than that of a true covalent bond. Figure 4.24 is a plot of the NNMs and bond critical points superposed with the electron localisation function (ELF) of the Cs-IV structure. The blue atoms are the NNMs (electrides) while the black atoms are the bond critical points between the NNMs (Figure 4.24) as obtained from the topological analysis. Further analysis of the ELF plotted in Figure. 4.25 reveals a wavelike localisation of electrons in the Cs-IV. The plot of the ELF is in exact agreement with the electron density distribution reported earlier [205, 206]. By superposing the electron localisation from the ELF with the NNM positions from the topological analysis shown in Figure 4.24. It is found that the NNMs occupy the vertexes of the electride wave pattern and BCPs are located between the NNMs. This observation shows unequivocally that the electrides are interacting with each other.

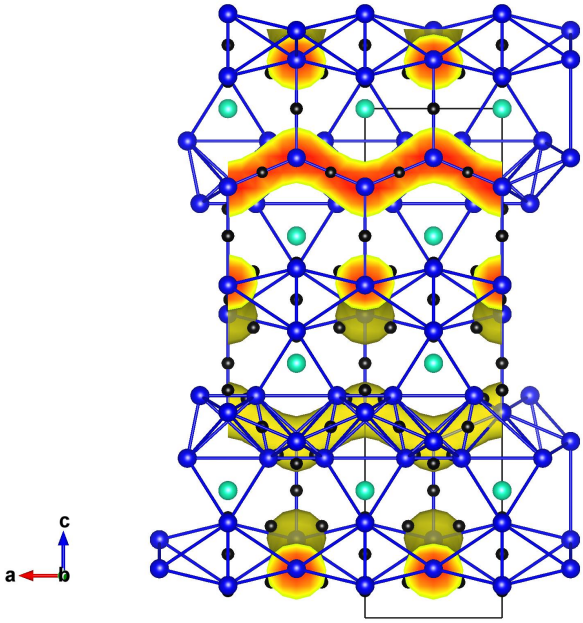

Figure 4.24: (a) Repeated structure of Cs-IV showing the NNMs in blue, BCPs in black, Cs atom in green and ELF at 0.64 isovalue in yellow

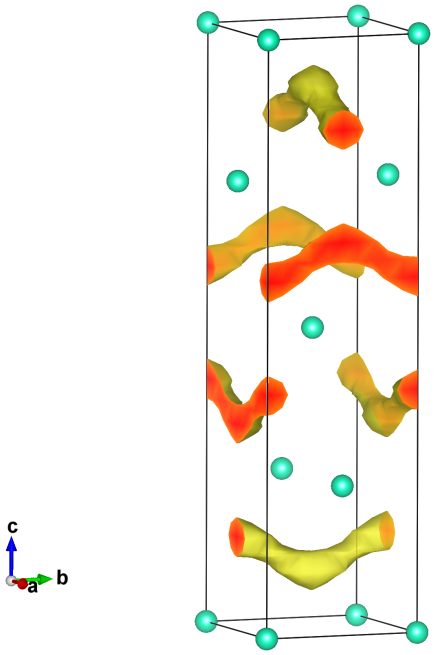

Figure 4.25: (b) 0.64 ELF plot of Cs-IV

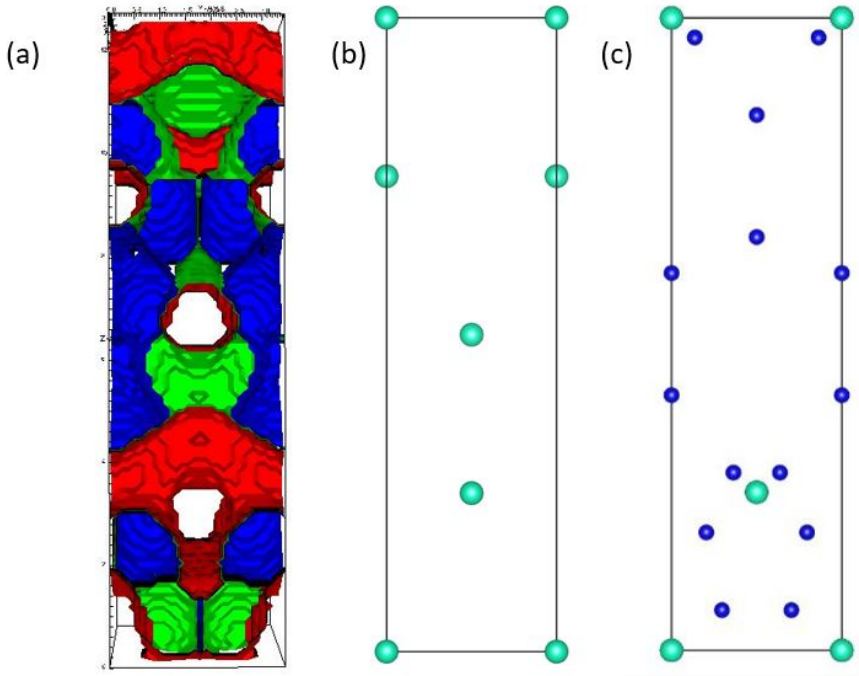

Figure 4.26: Cs-IV (a) Topological volume (colours denote different NNM's) (b) (1,0,0) projection (c) (1,0,0) plane showing the NNM's in blue

Critical Point	d(Å)	$\rho(r_{BCP})$ (ea_0^{-3})	$\nabla^2\rho(r_{BCP})$ (ea_0^{-5})	V (E_h)	G (E_h)	H (E_h)	Int. Vol. (a_0^3)
Cs							0.012
NNM1							49.87
NNM2							36.94
NNM3							1.571
NNM2 - NNM2	1.867	0.006	-0.005	-0.001	-0.0001	-0.001	
NNM1 - NNM2	1.969	0.006	-0.002	-0.001	0.0002	-0.001	
NNM3 - NNM1	1.230	0.002	-0.014	0.001	-0.0022	-0.001	

Table 4.2: Topological properties of Cs-IV at the nuclear (Cs, NNM1, NNM2 and NNM3) and bond critical points. Where only the integrated volume have been reported for Cs and the non-nuclear maximum (NNM) because the density (ρ), Laplacian ($\nabla^2\rho$), potential energy (V), kinetic energy (G), and local energy densities (H) are not important at the nuclear positions. NNM1, NNM2 and NNM3 are the three non-nuclear maximum occupying different symmetry sites.

Previous charge density analysis of Cs-IV found the wavelike interstitial electrons due to the Cs s-d hybridization [206]. The bonding between the Cs 5d localized the electrons in the void space forming the NNMs (electrides). The topological analysis of the Cs-IV reported here show no Cs-Cs bond, instead the covalent interaction is between the interstitial NNMs. The absence of Cs-Cs bond critical points in the Cs-IV implies that the structure is stabilized through the formation of covalently bonded NNMs. Hence, unlike the Cs-II and Cs-III structures where some Cs-Cs bond interactions exist, the Cs-IV primarily consists of covalently bonded NNMs with no Cs-Cs bond interaction. It is also evident from Figure 4.24 that the NNMs adopt the triangular-prismatic arrangements with the Cs atoms intercalated in the NNM triangles. Analysis of the Cs-IV topological volume defined by Bader [27] (Figure 4.26a) shows crystal voids at the Cs atom positions indicating almost total electron transfer from the Cs to the interstitial regions. The Bader volume (i.e volume enclosed by zero flux surface) is around the NNM positions represented by the colour gradients in Figure 4.26a. This is consistent with the integrated volumes from the topological analysis summarized in table 4.2 and also supports the critical point analysis which revealed no bonding between the

Cs atoms. Thus, the Cs atoms are stabilized in the Cs-IV by forming Cs^+ ions and localised the electrons as electrides formed from the overlap of the Cs d orbitals. The blue NNM positions in Figure 4.26c corresponds to the region of finite volume shown in the topological graph.

4.4 Conclusion

Density functional theory (DFT) based NPT molecular dynamics simulation method applied here succeeded to reproduce the complex Cs-II → Cs-III and Cs-III → Cs-IV transitions through a compression. The Cs-III → Cs-IV transition path was obtained from a 120ps NPT molecular dynamics simulation run with the temperature and pressure set to 400K and 60Kbar. The Cs-IV began to crystallized after about 80ps. At 120ps, over half of the Cs-III crystal structure had transformed into the tetragonal Cs-IV structure. Analysis of the quenched configuration after 120ps revealed that the Cs-IV forms off the complex Cs-III structure through nucleation and growth of the Cs atoms at high pressure without any evidence of melting in the transition state. Having examined the Cs-III → Cs-IV transition path, the same method was applied to reconstruct the forward or compression (Cs-II → Cs-III) and backward or decompression (Cs-III → Cs-II) transformations. For the forward transition, an 84 atom Cs-II simulation cell commensurate with the Cs-III cell was used as the starting configuration for the molecular dynamics run. Snapshots from the simulation trajectory were extracted and quenched through structural optimization at 0K. The optimized configurations extracted every 20ps from the 200ps simulation were examined. The Cs-III began to form on the (100) plane of the Cs-II molecular dynamics snapshots after 60ps. At 200ps the **c** lattice vector and the Cs atoms in the layers tilt by 20^0 and 30^0 respectively in other to accommodate the transformation to Cs-III. The Cs atom moved cooporatively throughout the process, with no evidence of melting in the transition state. The results show the Cs-II → Cs-III transformation is a martenistic transition. The optimized configurations from the backward transition MD simulation show similar local features i.e each of the Cs atoms formed a hexagonal ring on the (010) plane with a central Cs atom connected to the other six Cs atoms which formed the hexagonal ring. However, the Cs atom local environment

for the optimized snapshot is different from that of the expected Cs-II structure. The MD simulation did not show the Cs-III structure transform to Cs-II after 200ps. It is perhaps because the Cs-III $\rightarrow$ Cs-II reverse transition path has a high activation barrier. In addition to reconstruct the transformation paths, topological analysis of the Cs-II, Cs-III and Cs-IV structures were performed based on Bader's Quantum theory of atoms in molecules method. The results reveal that the three Cs structures studied here all possess electrides. The topological volume of the interstitial electrons increased as the structure transformed to Cs-IV. Hence, the presence of the localized electrons at non-nuclear positions in the Cs metal can be thought of as a consequence of the progressively s and d orbital mixing of the Cs atom.

Chapter 5

X-ray Absorption Spectra (XAS) and Non-Resonant Inelastic X-ray Scattering (NRIXS) of Water and Ice Ih

5.1 Introduction

Water is the most abundant liquid on Earth and is essential for supporting life. Though water have been extensively studied for many years, the basic structural and dynamical properties are still not well understood [207, 208, 209, 210, 211, 212, 213]. Under ambient condition, water molecules are believed to form tetrahedral coordination with four neighbours through hydrogen bonds [214]. Tetrahedral coordination was also observed for the solid phase ice 1h. In the liquid state, this hydrogen bond network was not destroyed but fluctuate on a picosecond to nanosecond time scale due to disruptions from thermal fluctuations [215]. The understanding of the structure of liquid water at the molecular level is elusive and remains at the centre of scientific debate. One of the primary question "is the local structure of water ring-and-chain like or tetrahedral"? [216, 217]. Hence, advances in theory and experiment are needed. Accurate description of the nature of liquid water from electronic structure measurements has been a subject of great interest for many years. Information on the electronic structure of matter has been greatly obtained from X-ray Absorption Near Edge Structure (XANES) spectroscopy also known as XAS [218]. XAS has proven to be a great technique for electronic structure studies due to the element specificity and orbital selectivity. Non-Resonant Inelastic X-ray Scattering (NRIXS) can be shown to be similar to XAS at low momentum transfer $\mathbf{q}$ from the Fermi's golden rule. Replacement of the dipole

transition operator $\mathbf{d} = \epsilon \cdot \mathbf{r}$ with the momentum translation operator $\mathbf{d} = \exp(i\mathbf{q} \cdot \mathbf{r})$ makes the XAS different from NRIXS. However, at small momentum transfer value $\mathbf{q}$, NRIXS becomes comparable to XAS because a Taylor expansion of the operator $\exp(i\mathbf{q} \cdot \mathbf{r})$ only the dipole term is retained. Through a DFT calculated X-ray absorption spectroscopy (XAS) of a model water cluster, an alternative description of water at ambient condition which was proposed to have an asymmetric hydrogen bond coordination with one donating and one accepting H-bond suggested by Wernet et. al. [214]. The water molecule in the proposed structure have a polymeric linkage which favours the formation of hydrogen bonded rings and chains [214]. However, the unusual thermodynamic properties of water can not clearly be associated to this kind of ring and chain network [219]. For example, water reaches a density maximum at 4^0C. Tetrahedrally coordinated liquids are known to exhibit a density maximum which has however not been found in liquids containing only two hydrogen bonds per molecule, hence the density maximum property of water was said to be a consequence of the open nature of its quasi-tetrahedral structure [220]. Connections have been made between the theory of ambient liquid water and regions of deeply supercooled water where two structurally distinct forms of water such as the low-density liquid (LLD) and high-density liquid (HDL) have been proposed to exist [221, 222]. The LDL was said to have a tetrahedral coordination while the HDL possessed an asymmetric local hydrogen bond coordinationn which features weakened or broken hydrogen bonds and a distorted first hydration shell [5]. Though fluctuations between the LDL and HDL structural species can explain some anomalous properties of water, the true structure of liquid water is still being debated. X-ray absorption spectroscopy (XAS) which excites core electrons to unoccupied states can serve as a structural probe since the electronic character of unoccupied states are sensitive to the local geometry of the structure. The XAS of water from both theory and experiment have shown that the spectrum can be divided into three regions; a pre-edge region at 535eV, main edge region centered at 537eV and the post edge region around 541eV. The pre-edge region is said to be a signature of distorted hydrogen bonds. The spectral features at the main edge region is suggested to reflect a collapse in the water second hydration shell and sensitive to the hydrogen bond distortions in liquid water [223, 224]. The observed pre-edge feature in the liquid water XAS is relatively strong when compared with the XAS of crystalline ice [214]. On the other hand,

X-ray Raman spectroscopy (XRS) study of condensed phases of water by Tse. et. al [225] found the pre-edge spectral feature existed in both water and crystalline ice. Hence, the local environments should be similar and led to the conclusion that the pre-edge feature of water is not a reliable indicator of the magnitude of local disorder within the hydrogen bonded network. Several theoretical approximations, such as transition-potential density functional theory (TP-DFT) [5, 226, 227], complex polarization propagator density functional theory (CPP-DFT) [5], time-dependent density functional theory (TDDFT) [228] etc. have been applied to model the XAS of liquid water. All the aforementioned theoretical methods only gave a qualitative interpretation of the pre-edge, main-edge and post-edge features of the absorption spectra but none could accurately reproduce the experimental spectrum [5]. It is obvious that accurate theoretical prediction of the water XAS spectrum is still a major challenge [229]. To understand the structural properties of liquid water, there is a need to identify the reason for the failures of the simulated spectra. Given that water coordination in the liquid state is not rigid, a reliable way to calibrate XAS calculations would be to calculate the absorption spectra of the well known hexagonal ice Ih in which the crystal structure is not disputed [230]. Surprisingly, calculations of the XAS of ice Ih has not been performed until very recently. The structure of Ice Ih is composed of a tetrahedral oxygen atom coordination, with each oxygen connected to its nearest neighbour through hydrogen bonds. Several experimental XAS spectrum of hexagonal ice have been reported for either ice grown on different substrates or the bulk ice phase [231, 225, 232, 4, 233, 234, 235]. All XAS measurements of hexagonal ice gave qualitatively similar spectral profile with slight difference in the intensities and relative ratios of the peaks at the three regions of the spectra. These slight variations are either due to the different sample preparation methods or the experimental methods employed [4]. Only recently XAS of hexagonal ice Ih was computed by Zhovtobriukh *et. al.* [5] using four different water models with increasing oxygen and proton disorder. The authors employed transition-potential half-core-hole approximation and the complex polarization propagator approaches to compute the excitations employing localized basis set based on density functional theory (TP-DFT and CPP-DFT). Results from the 32 cluster water model yield spectra in poor agreement with the experimental spectrum of ice Ih. The authors attributed the disagreement to either the cluster size or structures they

used for their calculations [5]. The Bethe-Salpeter Equation (BSE) method which takes into account core-hole and electron-electron correlation has not yet been widely applied to water is an effective way to address this challenge, though it is computationally very demanding. In this work, the BSE method have been employed to predict theoretical absorption spectra and compare with experimental results. The objective is to better understand the local structure of liquid water and provide insight on the proper modelling of water and hexagonal ice Ih from theory. For this purpose, crystalline ice Ih in which the crystal structure is well known have been used to benchmark the theoretical method in this work using advanced electron structure method. We found a reasonable agreement of the theoretical and experimental XAS on ice Ih. Consequently, the BSE was used to calculate the XAS of liquid water to shed light on the local structure of liquid water which has been debated for several years. This chapter reports the calculated absorption spectra of crystalline ice Ih, and compressed liquid water and how they compare with experiments.

5.2 Computational Methods

Core level BSE method implemented in the OCEAN code [86] was used for all XAS and NRIXS calculations. Each spectrum was averaged over 18 photon directions for the NRIXS at a chosen momentum transfer values ($\mathbf{q}$) and only three photon directions for the XAS. It is important to note that all DFT calculations in OCEAN employed the local density approximation (LDA) functional because it is the only density functional implemented. Ice Ih configuration with 96 molecules collected from an *Ab initio* Molecular Dynamics (AIMD) simulation of Ref. [7] using an opt-PBE-vdW functional was used for the initial XAS and IXS calculations. To account for nuclear quantum motion of the hydrogen atoms, the AIMD 96 molecules ice Ih configuration of Ref. [7] was used as starting configuration for a series of Path integral centroid molecular dynamics (PICMD) in the canonical (NVT) ensemble. The PICMD were performed at 200K with 16 beads to mimic the quantum particle and a 0.01fs time step. One configuration was extracted every 150ps from the 600ps PICMD simulation and used to calculate the XAS and IXS of crystalline ice Ih. For the liquid water, a 64 molecule water model was used for the XAS and IXS calculation. The PICMD calculation for the

liquid water was performed at 300K for 10 different pressure points again using 16 beads and a time step of 0.01fs. X-ray absorption spectroscopy (XAS) and Non-resonant Inelastic X-ray Scattering (NRIXS) of three randomly selected Path Integral Centroid Molecular Dynamics (PICMD) configurations at each pressure were calculated. For each pressure, average XAS over the three different configurations were computed. Additional analysis was performed on the PICMD trajectories at each of the pressure points to interpret the local structure of compressed liquid water. An efficient way to execute the OCEAN code is provided in Appendix C.

5.3 Results and Discussion

The objective of the present study is to probe the structure of compressed water at room temperature and to compare with the known structures of high pressure ices. It is known that in dense ice starting from ice-VI, interpenetrating hydrogen bond networks are formed from the second nearest neighbour water molecules [11, 7, 236].

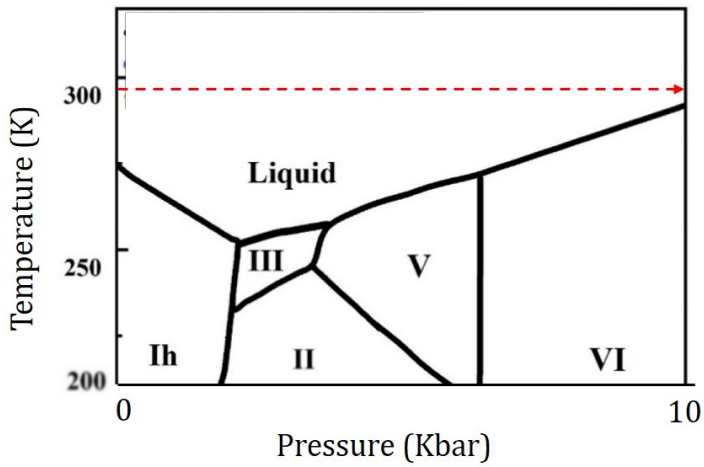

Figure 5.1: Phase diagram of water adapted from Ref. [3]. The red dotted line shows the direction of compression.

A phase diagram of water under pressure is shown in Figure 5.1. It shows that when ice is compressed at 250K, it undergoes a sequence of crystal-crystal transformation Ih $\rightarrow$ III

$\rightarrow$ V $\rightarrow$ VI [3]. Each crystalline phase has their own unique structure. However, when ice V transformed to ice VI, the hydrogen bond network of water changed from a single to an interpenetrating network. Therefore the scientific question to be answered in this work is "does the structure of compressed water follow a similar structural transformation as compressed ice?". The compression condition of the liquid water calculations follows the experimental work performed by our collaborators. A water model was been compressed up to 10Kbar as water crystallize into ice VI above 10Kbar at room temperature. As already noted in the introduction, it is essential to validate the theoretical procedure from the calculation of the XAS of the well established hexagonal ice Ih structure [230]. This was followed by the calculations of the XAS and NRIXS of compressed water.

5.3.1 Ice Ih

Figure 5.2a show the (001) plane of the crystalline ice Ih structure optimized from an AIMD calculation [7]. The calculated XAS and IXS spectra performed using this crystal structure is presented in Figure 5.2b. The IXS was performed at three different momentum transfer values (i.e, 2.5Å^{-1}, 4.5Å^{-1} and 6.5Å^{-1}). The computed spectrum reproduced the three regions of ice Ih XAS. Namely, a pre-edge region at 535eV, main edge region centered at around 537eV and a post edge region around 541eV. The $\mathbf{q}$ dependence of the absorption edge at the pre-edge region is evident in Figure 5.2b. As $\mathbf{q}$ increased, the intensity of the pre-edge region also increased with the intensity at $\mathbf{q}$=2.5Å^{-1} very similar to the XAS. This similarity to the XAS spectrum is verified as IXS is comparable to XAS at a small momentum transfer values because the Taylor expansion of the momentum translation operator $\mathbf{d} = \exp(i\mathbf{q} \cdot \mathbf{r})$ can be approximated to a dipole operator similar to XAS.

Comparison of the ice Ih XAS based on the AIMD optimized structure together with other theoretical and experimental [4] results are shown in Figure.5.3a. The BSE calculated XAS spectra compares well with the theoretical results of Zhovtobriukh *et. al.* [5]. Even though both theoretical spectra agree with each other, the predicted spectra is still not consistent with experiment as both show sharp peaks not observed in the experiment. Zhovtobriukh *et. al.* [5] attributed the inability of the transition-potential density functional theory (TP-DFT) [5, 226, 227], nor the complex polarization propagator density functional theory (CPP-

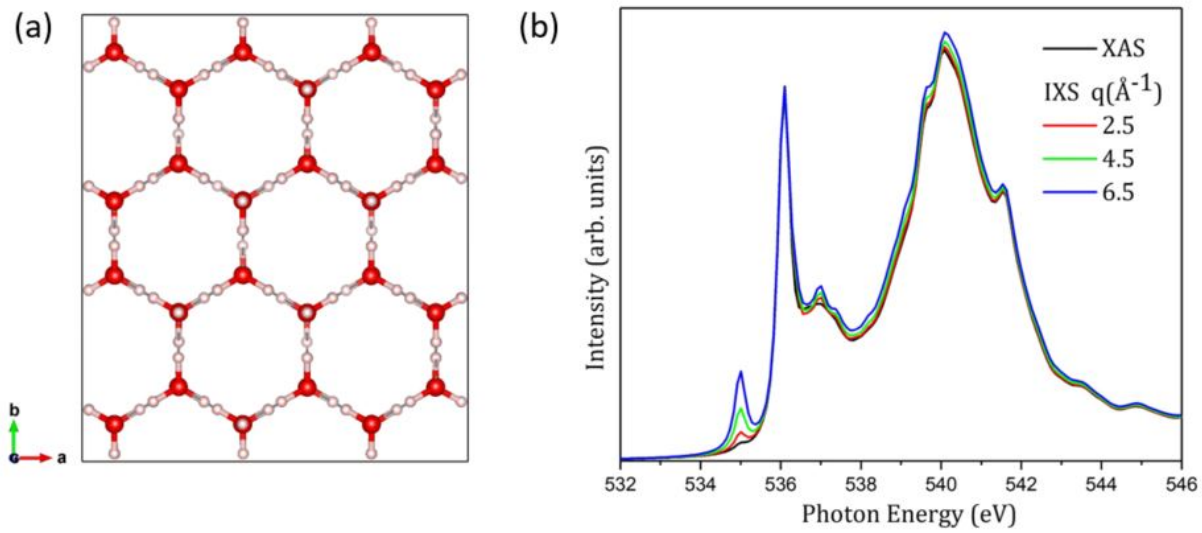

Figure 5.2: (a) Crystal structure of AIMD ice Ih structure and (b) corresponding XAS and IXS theoretical spectra of the AIMD ice Ih structure computed from BSE (OCEAN).

DFT) [5] method, to reproduce the experimental spectrum to the limited size of the water cluster models. Another factor is that the CPP and TP density functional methods used are dependent on the choice of localized basis sets. In the previous study, the authors tested several basis sets before settling for the individual gauge for localised orbitals (IGLO-III) [237] basis to describe core relaxation and the 19s19p19d [238] even-tempered basis which they used for the calculations of the absorption spectra. In comparison, the BSE method employed in this study used a plane wave expansion which is almost close to a complete basis set. Furthermore, periodicity of crystalline ice Ih is properly accounted in our calculation.

However, as shown in Figure 5.3 the BSE calculation still obviously failed to reproduce the experimental XAS spectrum. Having validated the BSE method from comparison with previous results, we sought to explain the discrepancy with experiment. One possibility is whether the inclusion of local distortions by considering the dynamics of the atoms in the ice Ih model would improve the agreement. For this purpose, a Path Integral Centroid Molecular Dynamics (PICMD) simulation was carried out. A constant temperature PICMD was performed at 200K with 16 beads for both the hydrogen and oxygen atom using a time step of 0.01fs. The simulation temperature was controlled using a Nose Hover thermostat. The volume was adjusted manually until the stress on the model is isotropic and close to 0GPa.

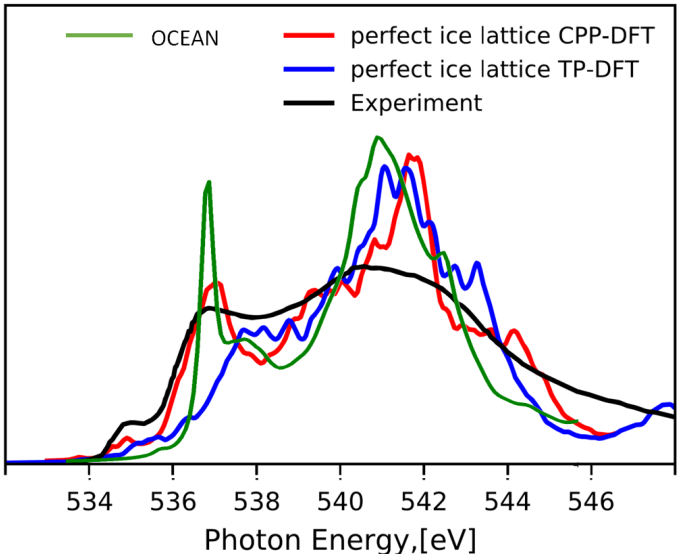

Figure 5.3: Comparison of XAS of ice Ih from BSE (OCEAN) with experimental results of ref.[4] and theoretical data of ref.[5].

The resulting density of 0.916g/cc is in remarkable agreement with experiment. Figure 5.4 shows the relevant thermodynamic parameters extracted from the simulation. The relatively large fluctuations in the pressure is due to the lack of a barosat. The inset in Figure 5.4a is a plot of the position of the instantaneous beads in the (001) plane at 150ps. The O-O, O-H and H-H radial distribution functions shown in Figure 5.5 were computed from the PICMD trajectories to examine the structural properties of ice Ih. A comparison of the O-O RDF with results of ref. [6] computed from the classical MD with a similar Thole-type model potential (TTM3-F model) on crystalline ice Ih is given in Figure 5.6. Both RDFs from the PICMD and TTM3-F model agree well with each other and the slight difference in the intensities of the RDF at the peak positions are perhaps due to the temperature difference (i.e the PICMD was performed at 200K and the TTM3-F model was performed at 230K). This temperature dependence of the crystalline ice Ih RDF peak intensities at the first and second coordination shells have been previously reported by Lindberg and Wang [239]. They introduced an electrostatic switching procedure to systematically generate ice configurations at various temperatures and the calculated RDFs of the ice structures at the different temperatures indeed revealed the peak intensities decreases with increase in temperature [239]. However, the authors also identified a hydrogen bond defect at temperatures above 200K which they could not classify as either a D defect (i.e two protons present in the hydrogen

bond) or an L defect (i.e no proton present in the hydrogen bond). Similar analysis were not performed. Nevertheless, the trend of the 200K ice Ih RDF reported here is also consistent with previous reports [239]. Therefore, the ice structures from the PICMD simulation preserves the crystalline ice Ih local structural properties.

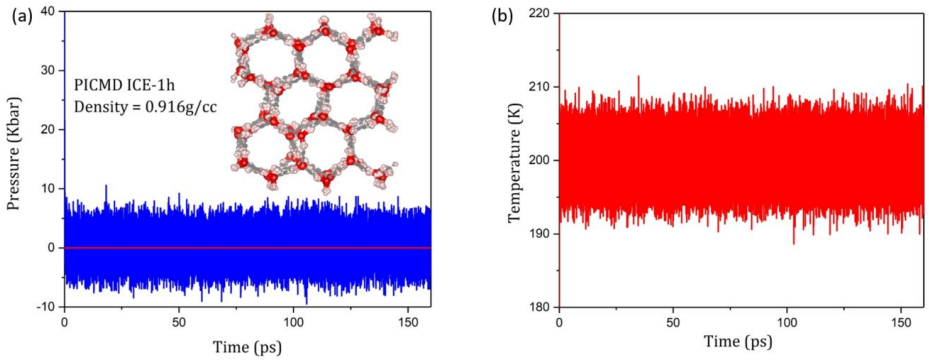

Figure 5.4: Thermodynamic parameters from the PICMD simulation of crystalline ice Ih.

The XAS spectrum computed from the optimized static AIMD configuration (Figure5.7a) is compared to the present PICMD simulation in Figure5.7b, 5.7c, 5.7d and 5.7e at 150ps, 300ps, 450ps and 600ps respectively. Close examination of each configuration reveal the reorientation of the hydrogen atoms are slightly different for each structure. The calculated XAS and IXS spectra corresponding to the snapshots of the ice Ih structures are presented in Figure 5.8. At 150ps, the computed XAS and IXS of the PICMD configuration shown in Figure 5.8b also show the sharp peaks that were present in the absorption spectrum calculated using the AIMD configuration (Figure 5.8a) have been broadened significantly. Hence, including temporal local distortions in the model through an MD simulation brings the spectra in closer agreement with experiment (Figure 5.8). The peak intensity between 537eV and 539eV increased in the PICMD configurations as shown in Figure 5.8b, 5.8c, 5.8d and 5.8e when compared to that of the static structure optimized by AIMD shown in Figure5.8a. Moreover, the X-ray absorption spectra computed by BSE using PICMD snapshots reproduce the prominent pre-edge feature. Furthermore, the intensity in the region between 536eV to 541eV increased substantially and bring the theory in better agreement with experiment.

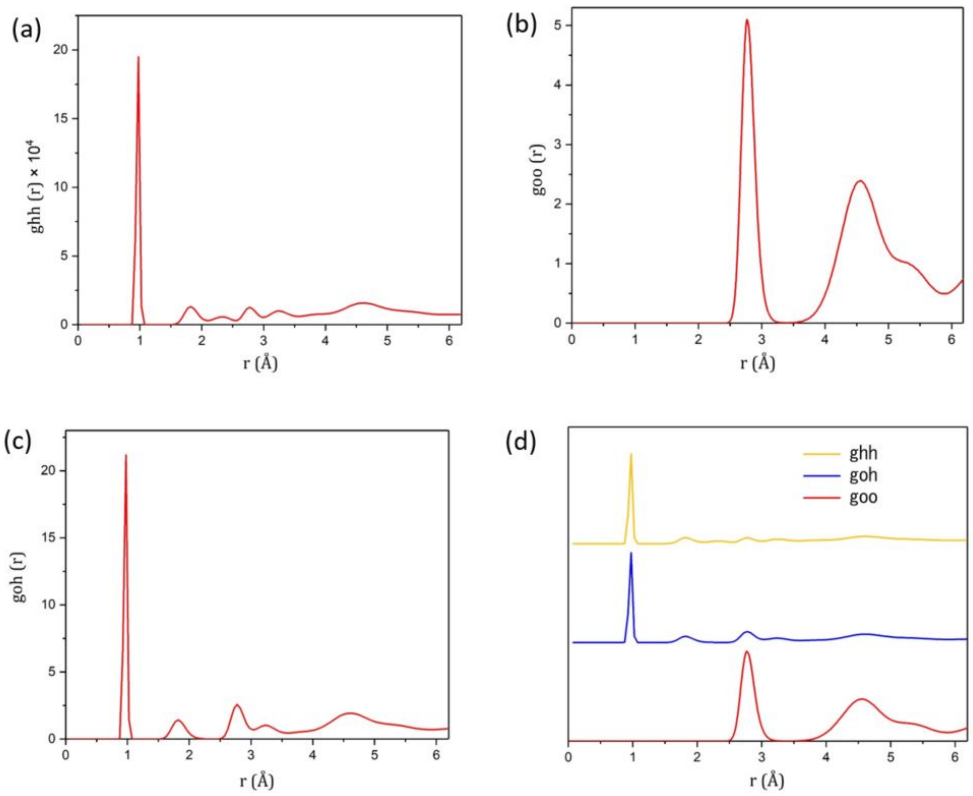

Figure 5.5: Radial Distribution Functions (RDF) of crystalline ice Ih computed from PICMD at 200K (a) Hydrogen - Hydrogen (b) Oxygen - Oxygen (C) Oxygen - Hydrogen and (d) stacked plot of the three RDFs.

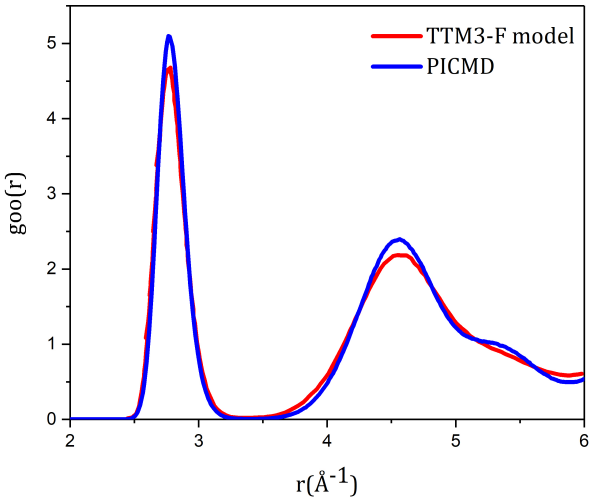

Figure 5.6: Comparison of oxygen - oxygen radial distribution function ($g_{OO}(r)$) of ice Ih PICMD and TTM3-F model [6].

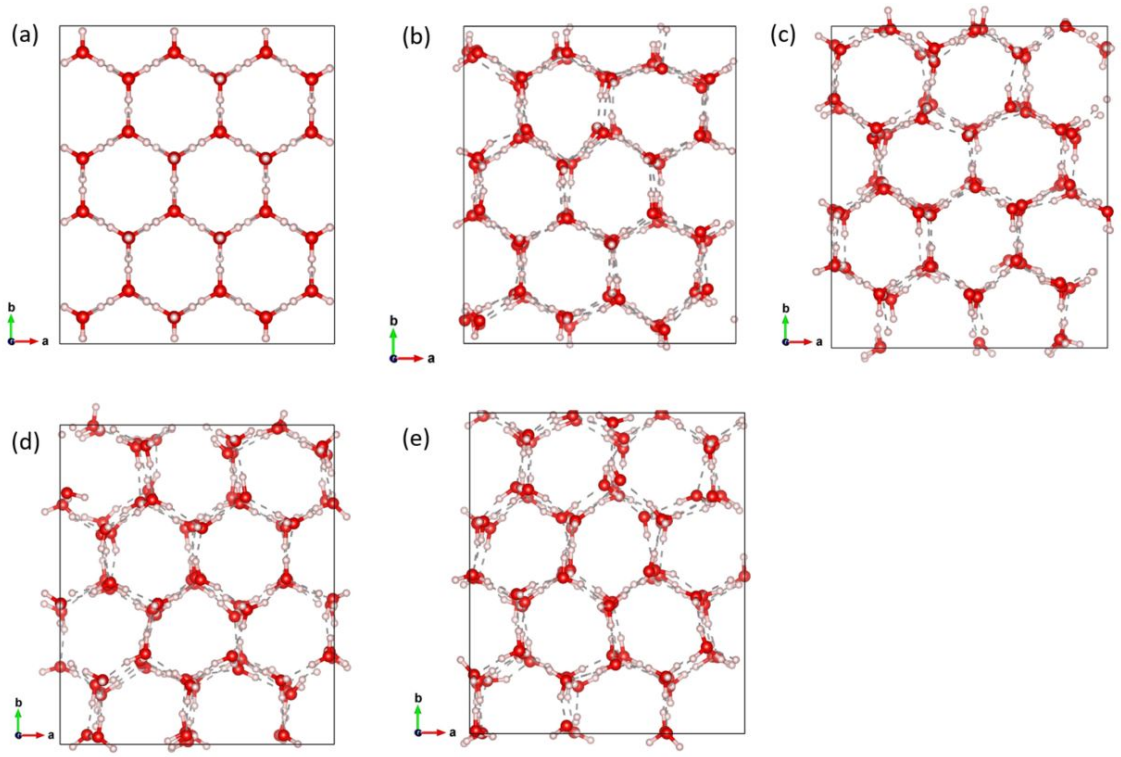

Figure 5.7: 001 plane of the ice Ih crystal structures (a) from AIMD and from PICMD simulation after (b) 150ps (c) 300ps (d) 450ps and (e) 600ps.

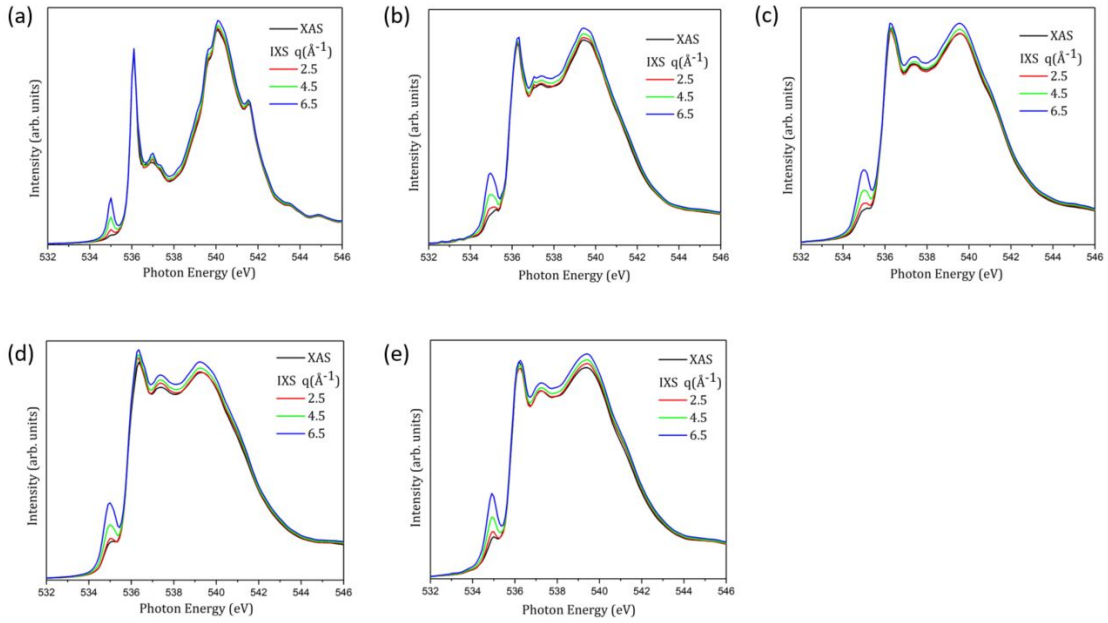

Figure 5.8: Corresponding XAS and IXS of the ice Ih structures in Figure5.7.

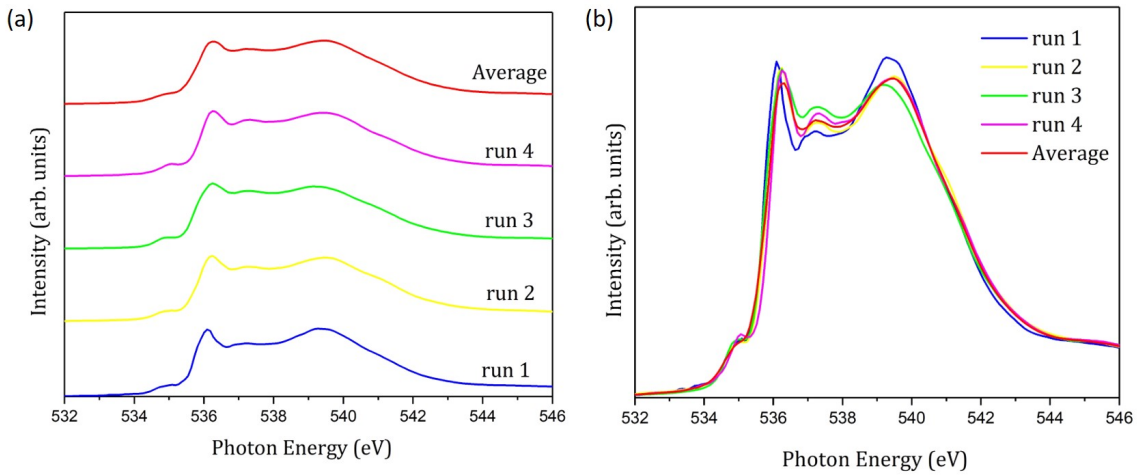

Figure 5.9: Comparison of the ice Ih XAS from individual snapshot of the PICMD configurations and the average (a) waterfall plots (b) overlaid plots.

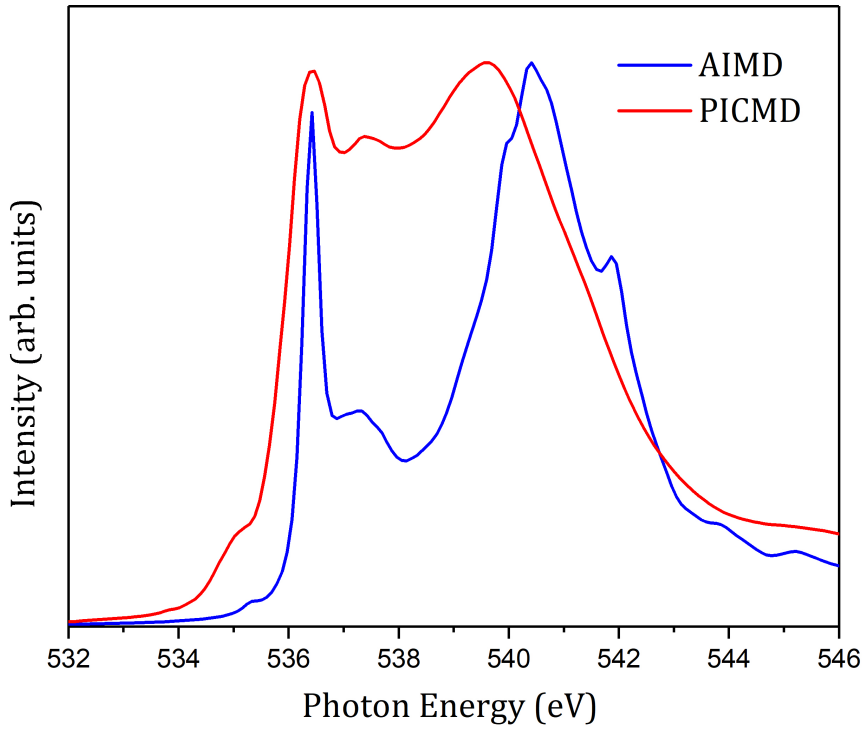

Figure 5.10: BSE calculated XAS of ice Ih computed from the AIMD optimized structure and compared with the average BSE calculated XAS of the ice Ih PICMD snapshots (see text).

To closely examine the spectral changes due to the PICMD configurations, the XAS of individual snapshot of the PICMD configuration and the averaged XAS were compared in Figure 5.9. Where run 1, run 2, run 3 and run 4 corresponds to the XAS computed using extracted PICMD configurations shown in Figure5.7b, 5.7c, 5.7d and 5.7e respectively. The spectral features around 537eV and 539eV can be seen to vary slightly for each of the configurations. This small change is due to the difference in the slight core-hole correlation introduced by the different configurations. A comparison of the ice Ih XAS computed using the static (AIMD) configuration and the average XAS of the four different PICMD configurations is shown in Figure 5.10. Apart from the obvious broadening of the peak, the average PICMD XAS spectrum can be seen to shift slightly to lower energy near the post-edge region. It should be noted that some of the difference may be attributed to the different densities, the optimized density of the AIMD (0K) static structure using PBE functional is 1.156g/cc as compared to the PICMD (200K) structure of 0.916g/cc. To understand the difference between the structures from static and dynamic simulations, extracted snapshots of local structure of the same oxygen from the two calculations are shown in Figure 5.14. As can be seen in Figure5.14, the central oxygen atom O4 is tetrahedrally coordinated to four first nearest neighbour oxygen atoms through two donating and two accepting hydrogen bonds which is the generally accepted structure of crystalline ice Ih [214, 230]. By comparing the bond angle the central oxygen (O4) makes with the oxygen of the acceptor hydrogen atoms i.e O3-O4-O7, the PICMD angle 109.24^0 is just 1% less than that of the static structure. However, the bond angle the reference oxygen of the donating hydrogen atoms make with O2 and O19 is 108.31^0 and 104.74^0 for the AIMD and PICMD structures respectively and the angle of the PICMD configuration is 3.3% less than that of the AIMD and approximately 4.4% less than the angle of a perfect tetraheral. In addition, from Figure 5.14 the measured bond length between the acceptor hydrogen and the central oxygen atoms (i.e $H_{acceptor}$ - O4) for the static (AIMD) and dynamic (PICMD) structures are 1.539Å and 1.757Å respectively; similarly that of the donor hydrogen of the central oxygen atom and O19 (i.e H_{donor} - O19) for AIMD and PICMD structures are 1.533Å and 1.727Å respectively. The difference in the hydrogen bond lengths are consistent with the density difference between the structures i.e the static AIMD structure is denser than the dynamic (PICMD) structure. Probability of

the O-O-O angular distribution in the modeled PICMD ice Ih trajectory was computed and is shown in Figure 5.13a. The O-O-O angles spread between 100^0 and 130^0 with the highest probability at around 109^0 which is the expected tetrahedral angle for ice Ih.

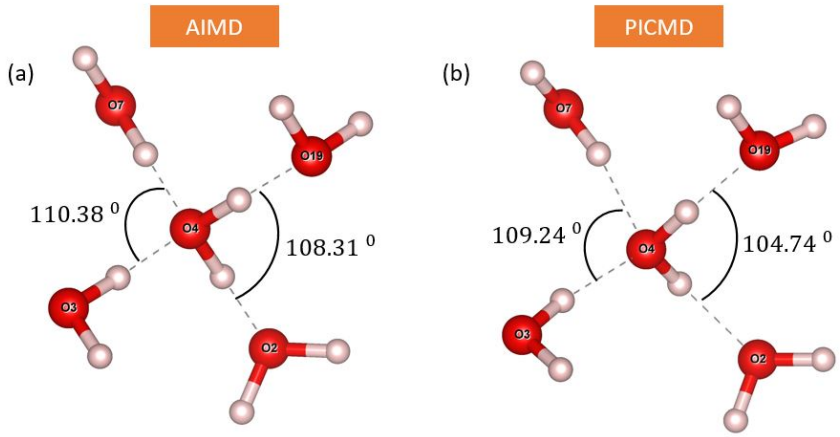

Figure 5.11: Local structure of the ice Ih AIMD configuration compared to that of the PICMD. The angles indicate the O-O-O bond angle.

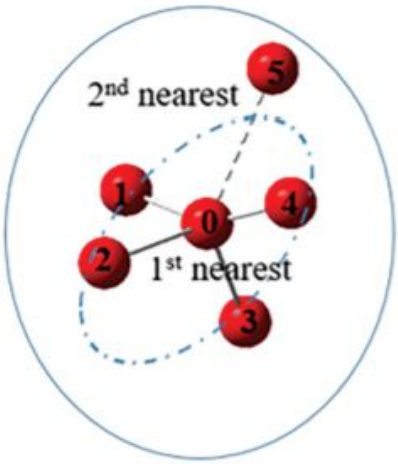

Figure 5.12: Schematic illustration of the hydrogen bond local environment of a water molecule with oxygen 0 as the central atom. Where the four hydrogen bonded molecules (1–4) to 0 are the first nearest neighbours of 0 and oxygen 5 forms the second nearest neighbour of 0 which can be both hydrogen bonded and non-hydrogen bonded to 0. Adapted from ref. [7].

A schematic representation of the nearest neighbour water is shown in Figure 5.12. The oxygen one to four (O1, O2, O3 and O4) are the first nearest neighbour oxygen atoms of oxygen

zero, while oxygen five (O5) is the second nearest neighbour that forms interpenetrating hydrogen bonds. The probability of hydrogen bonded (phb) and probability of non-hydrogen bonded (pnhb) second nearest neighbour water molecule in the ice Ih was computed and is presented in Figure 5.13b. The almost negligible pnhb compared to phb shows the second nearest neighbour water molecules form no interpenetrating H-bond network in ice Ih. This observation agrees with a previous report [7].

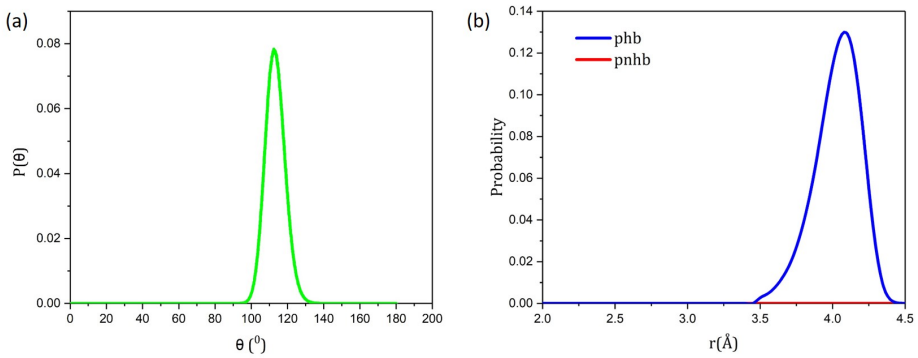

Figure 5.13: (a) Probability of the angular distribution of the O-O-O angle in ice Ih and (b) probability of hydrogen bonded (phb) and non hydrogen bonded (pnhb) second nearest neighbour water molecule in the ice Ih.

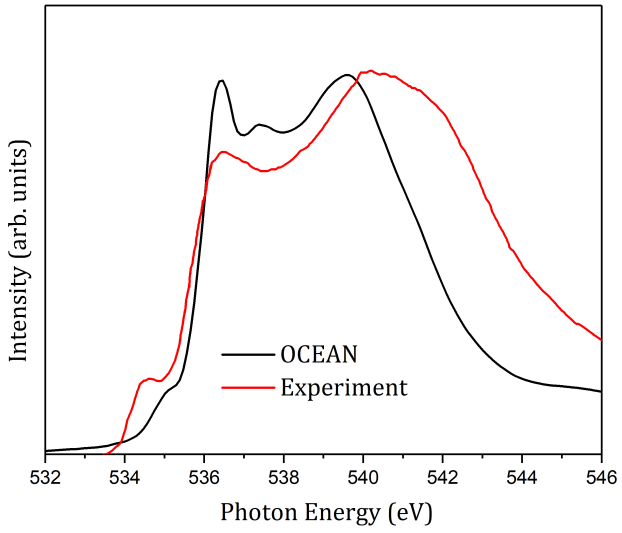

Figure 5.14: Comparison of the averaged ice Ih XAS computed from BSE (OCEAN) with the experimental data of Sellberg et. al.[4].

The XAS averaged over the four PICMD configurations using BSE method was plotted together with the experimental results of Sellberg et. al.[4] recorded at T = 232K on a thin ice film embedded between two Si_3N_4 windows in Scanning Transmission X-ray Microscopy (STXM) mode. The BSE calculated XAS presented here show better agreement with the experimental result compared to previous theoretical studies [5]. However, the calculated XAS here still fails to completely reproduce the entire observed spectrum. The post-edge maximum in the BSE spectrum is shifted to a lower energy and the bandwidth is narrow. The discrepancy is likely related to the lack of high energy continuum orbitals in the calculation and perhaps the LDA approximation. To the best of our knowledge, the BSE calculated XAS of ice-Ih reported here is the best available theoretical spectrum on ice-Ih. Having obtained XAS specta of ice-Ih in better agreement with experiment using the BSE implemented in the OCEAN code, similar method have been applied to model the liquid water in the preceding section.

5.3.2 Water

The calculation of accurate theoretical XAS spectrum is dependent on the underlying method employed and has posed a major challenge [229]. This project is initiated in order to help interpret the local structure of high pressure water from comparison to the XRS spectra measured by our group and collaborators. To optimize computational resources, the use of optimum parameters for the calculation is paramount. Hence, using one of the configurations from previous AIMD on water [240], we tested the convergence of some essential parameters. The test for the number of band convergence is shown in Figure 5.15a. As can be seen from the normalized plots with the axis shifted to align with the pre-edge peaks, the number of empty states included in the calculation changes the spectral features hence there is need to select an appropriate number of empty bands. Since the pre-edge region is the primary interest here i.e region between 534eV and 536eV, the 1024 bands appeared to be sufficient and was used for preceding calculations. After the computation of the ground state with DFT, the OCEAN BSE code performs a core-hole potential screening calculation. Therefore, we tested the convergence of the k-points used for the core-hole screening. Figure 5.15b, shows the XAS of the water model using a $2 \times 2 \times 2$ and $3 \times 3 \times 3$ k-point grids. No significant difference can be seen from the plot, hence a $2 \times 2 \times 2$ mesh is sufficient. Test on the convergence of the k-points used for the BSE calculation was also performed (Figure 5.15c). Again, there is no significant difference between the $12 \times 12 \times 12$ and $16 \times 16 \times 16$ k-point set. Therefore, a $12 \times 12 \times 12$ is sufficient for this system. Having completed the convergence test, the oxygen K-edge XAS and NRIXS at 0 kbar averaged over three water configurations at different momentum transfer values (q = 2.5Å^{-1}, 4.5Å^{-1} and 6.5Å^{-1}) were calculated. The results are presented in Figure 5.16a. It shows that intensity of the pre-edge peak increases as **q** increases which reflects the **q** dependence of the pre-edge peak. The intensity of the high energy region is underestimated, as mentioned above, this is as a result of the neglected continuum states due to core ionization. To improve the agreement with experiment at the high energy region, a correction in the form of an arctan step function was added to account for the transition of the ejected photoelectron to the continuum [241]. As shown in Figure 5.16b, the post-edge becomes broader and in better agreement with experiment.

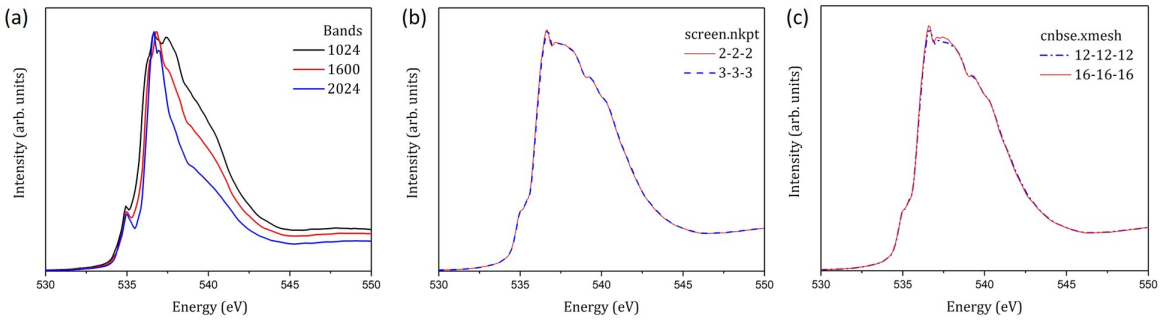

Figure 5.15: XAS of water (a) using different bands. (b) with different screening k-point grid (c) with different BSE mesh sizes.

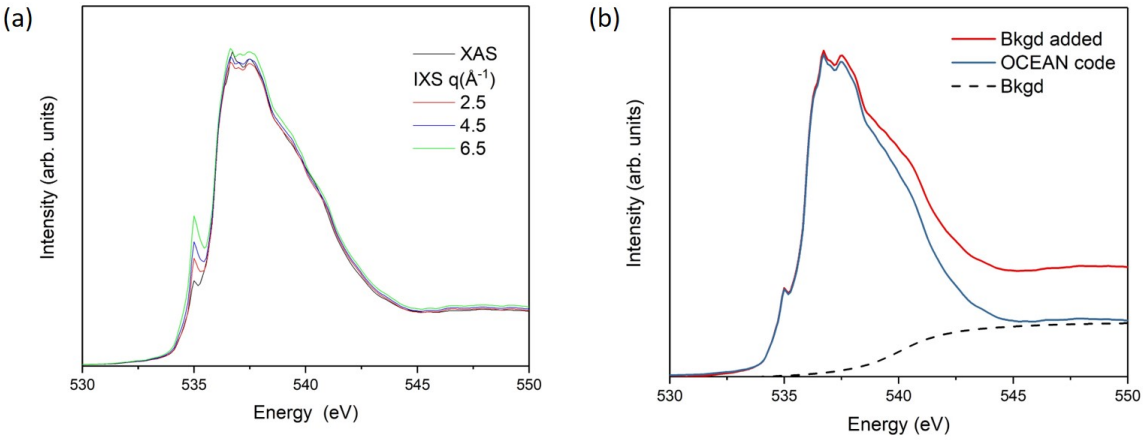

Figure 5.16: (a) XAS and NRIXS of water at 0kbar (b) Background corrected XAS at 0kbar.

For comparison, the non-resonant inelastic X-ray spectra (NRIXS) of water were computed at different momentum transfer (**q**) with snapshots extracted from the earlier AIMD simulation at 300K [240]. They are compared with experimental spectra in Figure 5.17 (the solid and dotted spectral lines are theory and experiment respectively). The theoretical spectra can be seen to reproduce the major spectral features in the pre-edge, main-edge and post edge regions in agreement with the experimental spectra. Intensity of the pre-edge region can be seen to increase with increased momentum transfer value (**q**) as observed in the ice Ih presented in the previous section. XAS of water have been computed from several theoretical methods which also yielded spectras in agreement with experiment [225, 242, 243, 244]. However,

there is limited studies on the effect of nuclear motion on the local structure of compressed water. Only recently did Zhaoru et. al. [245] investigate the role of nuclear quantum effect on the spectral features of water using a 128 water molecule supercell at different pressures. Their results revealed that the inclusion of the nuclear quantum effect introduced important effects to the spectra on both the energies and line shape [245].

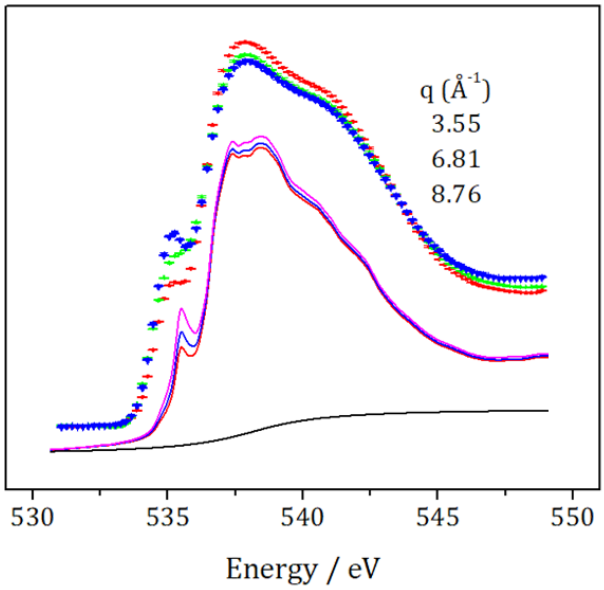

Figure 5.17: Comparison of the Experimental (doted lines) and BSE based (solid lines) inelastic X-ray scattering (IXS) spectra of water at different momentum transfer values.

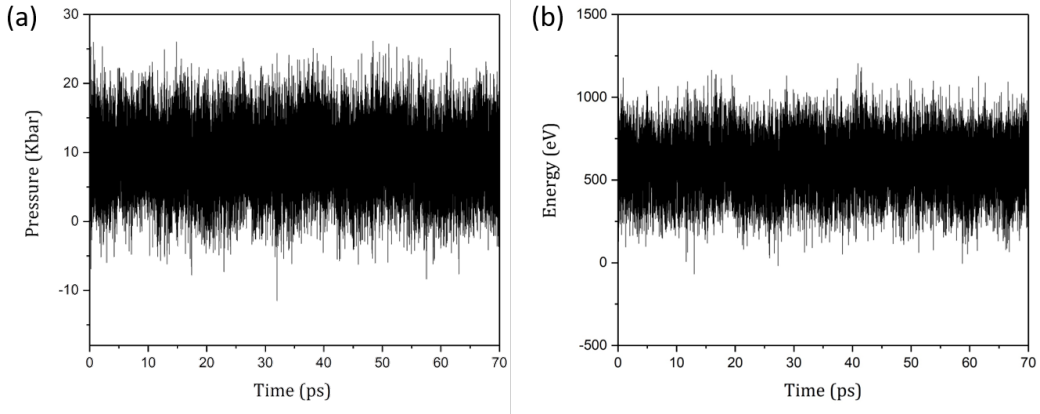

Figure 5.18: Time evolution of thermodynamic parameters from the PICMD simulation of water. (a) Pressure (b) Energy

Previous reports of the role of nuclear quantum effect on hydrogen bond fluctuations can be found in Ref. [246, 247, 248, 249]. In the present study, the nuclear quantum effects at different pressures were accounted for by performing a path integral centroid molecular dynamics (PICMD) simulation using a 64 water molecule model. Figure 5.18 shows the relevant thermodynamic parameters extracted from the PICMD simulation at 9.874Kbar. As discussed earlier, the large pressure fluctuation is due to the absence of a barostat. However, the pressure and energy fluctuate within a mean value.

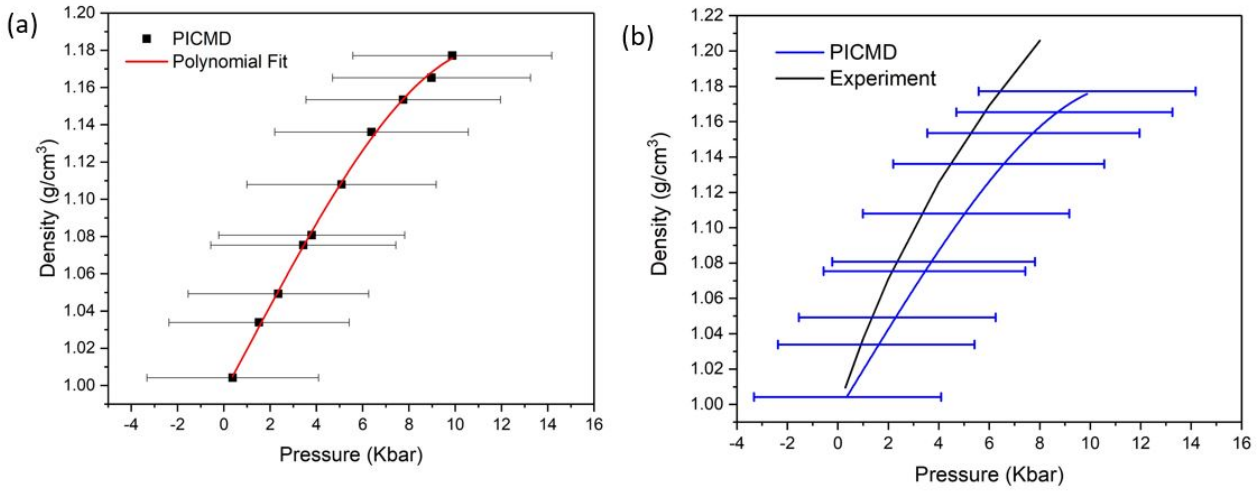

Figure 5.19: Density pressure plot (a) 3rd order polynomial fit of obtained PICMD pressure (b) comparison with experiment [8].

The theoretically optimized densities of the PICMD water model at different pressures were compared with the experimental densities in Figure 5.19b. The results show good agreement within the error estimates. The error bars were estimated by averaging over the density of the entire trajectory after equilibration. The deviation of the calculated density at high pressure from experiment is suspected to be due to the fact that the TTM2.1-F model used was only parameterized for water at ambient condition [97]. Nonetheless, the theoretical density of water reported here are within the experimental errors and, to the best of our knowledge, the best available theoretical densities of water at high pressure. Another way to validate the accuracy of the modeled water structure is by computing the radial distribution function (RDF). Hence, the radial distribution function of the PICMD water at different pressure was computed and is shown in Figure 5.20.

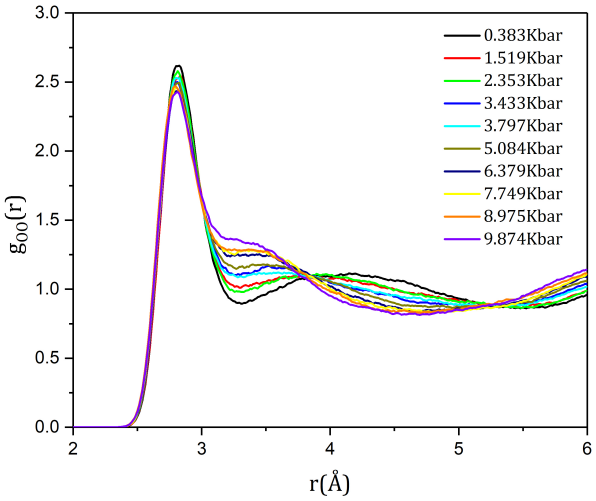

Figure 5.20: Pressure dependence of the oxygen - oxygen radial distribution function of obtained PICMD water.

Previous reports have shown that the O-O radial distribution function of water at around 3.3Å and 4.5Å increases and decreases respectively with respect to pressure [250, 251]. Similar features were observed in the RDF computed from the trajectories of the PICMD water model at different pressure shown in Figure 5.20. Also the two crossing (isobetic) points at 3.8Å and 5.2Å were also observed in the experimental RDF measured up to 7.7kbar [250, 251]. This is due to compression of the second coordination shell into the first shell. At 9.874Kbar, the highest pressure studied here, the water is so dense that the RDF at the second coordination shell water merged with the first coordination sphere. This decrease of correlation at 4.5Å is due to the presence of interpenetration of hydrogen bond network. Previous report have shown the decrease to apparently indicate weakening of the tetrahedral nearest ordering in the water molecule due to compression [251]. Having verified the quality of the simulated structures of high pressure water, BSE calculations were employed to calculate the X-ray absorption spectroscopy (XAS) and Non-resonant Inelastic X-ray Scattering (NRIXS). At each pressure three randomly selected PICMD configurations were used. Moreover, for NRIXS, three different momentum transfer values ($\mathbf{q}$ = 2.5Å^{-1}, 4.5Å^{-1} and 6.5Å^{-1}) were computed for each configuration and averaged over 16 photon directions for each $\mathbf{q}$.

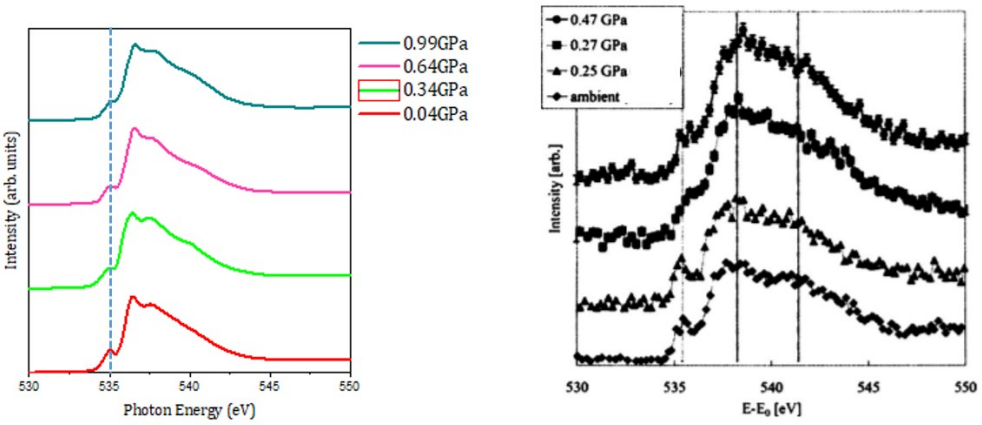

Figure 5.21: (a) BSE based XAS of water at selected pressure studied here (b) Experimental near-edge spectra of water modified from Ref. [9]. Note the ambient and 0.25GPa data are experimental results of Ref. [10].

The XAS spectrum is the average of three different snapshots (Figure 5.21a). The experimental XRS of compressed water in 5.21b showed the pre-edge peak intensity slightly increased as the pressure increased from 0.27 to 0.47GPa (Figure 5.21b) [9]. The authors compared their results with an earlier XRS results reported in Ref. [10] which showed no significant change in the pre-edge feature of the spectra as the pressure increased from ambient to 0.25GPa (Figure 5.21b). Fukui et. al. [9] attributed the discrepancy between their results and that of Ref. [10] to be due to the error of pressure determination or difference in experimental details. However, XAS calculation of water performed here from 0.04GPa to 0.99GPa (Figure 5.21a) show that the spectral features at the pre-edge region (noted by the blue dashed lines in Figure 5.21a) as well as the features at the post-edge region only change slightly with pressure. Similar to the XAS, the NRIXS spectra averaged over the same configurations at each $\mathbf{q}$ (i.e 2.5Å^{-1} and 6.5Å^{-1}) was computed (Figure 5.22a and Figure 5.23a). It can be seen that high pressure water show the intensity of the pre-edge peak is dependent on the momentum transfer and the pressure.

Figure 5.22 show a comparison of the low $\mathbf{q}$ inelastic X-ray scattering (IXS) spectra of water with the experimental low $\mathbf{q}$ (where $\mathbf{q}$=3.1Å^{-1} for ice Ih and $\mathbf{q}$=4.2Å^{-1} for ice VI, VII and VIII) IXS of ice at different pressures. It is pertinent to note that "there is a large density difference" between ice Ih (at 0Kbar) and high pressure ice VI (at 17Kbar) [11] is 0.45g/cc (Figure 5.22b and Figure 5.23b).

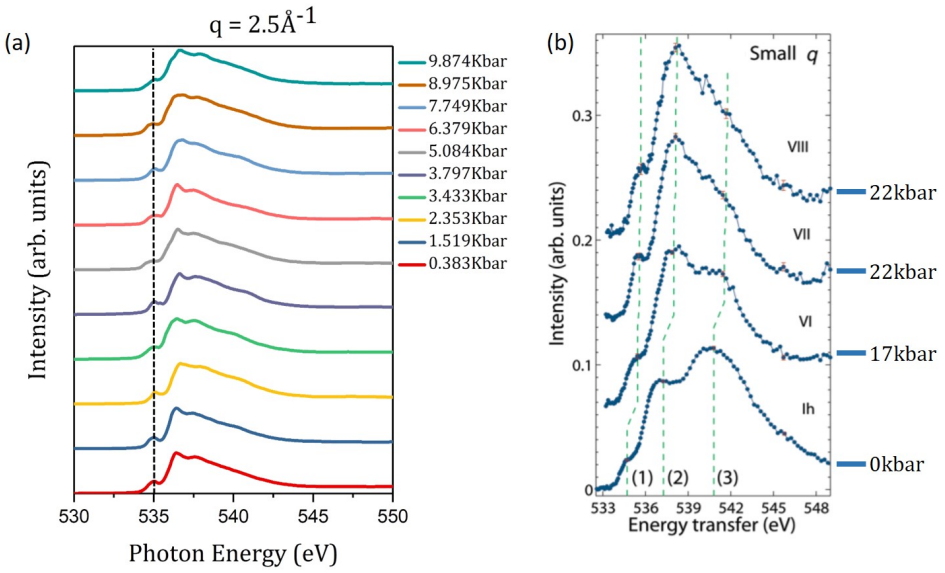

Figure 5.22: Comparison of (a) BSE based inelastic X-ray scattering (IXS) spectra of water at different pressures computed at low momentum transfer value ($\mathbf{q} = 2.5\text{Å}^{-1}$) and (b) Experimental IXS spectra of ice adapted from ref. [11] computed at $\mathbf{q}$=3.1Å^{-1} for ice Ih and $\mathbf{q}$=4.2Å^{-1} for ice VI, VII and VIII.

This large density difference is reflected in the shift of the spectra to higher energy as ice Ih is compressed to ice VI. On the other hand, further compression from VI → VII → VIII, the positions of the respective absorption edges remain unchanged. However, the spectral shape and features changed slightly with pressure as can be seen in Figure 5.22b. The density difference between ice VI (at 17Kbar) and ice VIII (at 22Kbar) is 0.25g/cc [11]. For the compressed water (Figure 5.22a), the calculated density difference between the 0.383Kbar and 9.874Kbar structures is 0.18g/cc which is 33% less than the density difference between ice VI and VIII. In addition, the peak positions in the calculated IXS spectra of high pressure water remain largely unchanged as observed in the ice when compressed from ice VI to ice VIII (Figure 5.22b). The IXS spectra of water (5.22a and 5.23a) and ice (5.22b and 5.23b) at small and large $\mathbf{q}$ only differ at the pre-edge region i.e the peak intensities become stronger. The observed changes in the spectral features of the ice was attributed to the increased coordination via an approaching second coordination shell [11] and have been shown to form interpenetrating hydrogen bonds [236]. The most significant difference in the spectral profile is the gradual increase of the intensity in the post-edge region relative to the edge region. In high pressure ice VI and ice VII, the XAS spectra is similar to that of compressed water.

The BSE calculated spectra also show relative increase of the post-edge peak intensities. Since there is a large difference in the densities of experimental high pressure ices with the compressed water studied here, we cannot draw a conclusion on the similarities or differences. We have to wait for the analysis of the NRIXS spectra recently measured in the same pressure range.

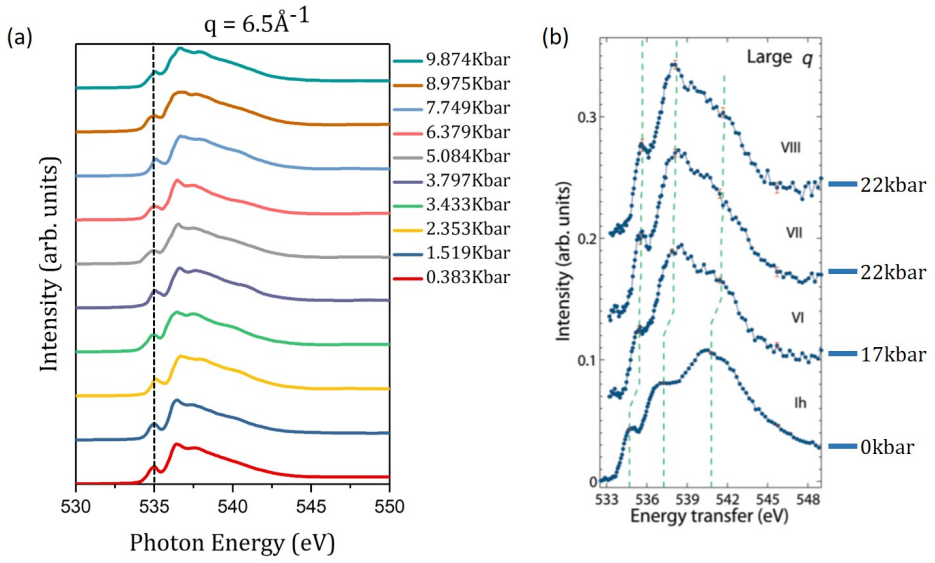

Figure 5.23: Comparison of (a) BSE based inelastic X-ray scattering (IXS) spectra of water at different pressures computed at high momentum transfer value ($\mathbf{q} = 6.5\text{Å}^{-1}$) and (b) Experimental IXS spectra of ice adapted from ref. [11] computed at $\mathbf{q}$=9.4Å^{-1} for ice Ih, ice VI, VII and VIII.

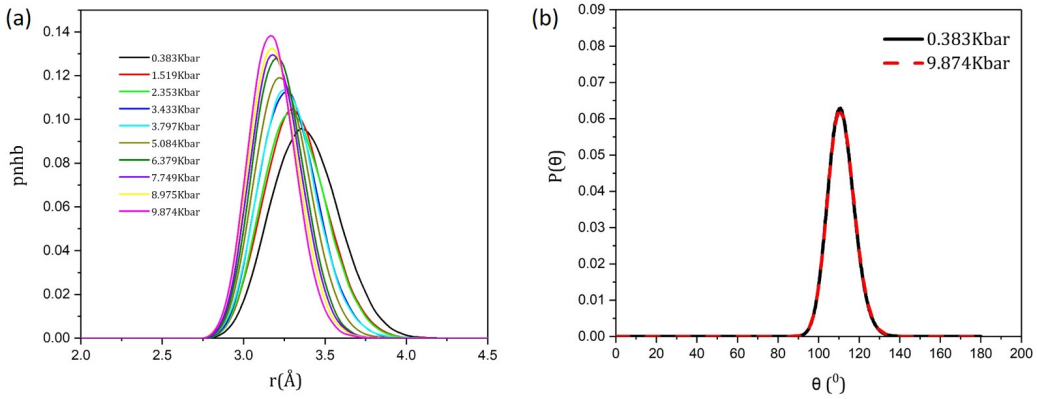

Figure 5.24: (a) probability of non hydrogen bonded (pnhb) second nearest neighbour water molecule in the PICMD water at different pressures and (b) Probability of the angular distribution of the O-O-O angle in the low pressure and high pressure water.

To understand how the change in the water spectra relates to the local structure and hydrogen bond network, the probabilities of hydrogen bonded (phb) and non-hydrogen bonded (pnhb) second nearest neighbour water were computed. The O-O-O angular distribution of the low pressure and high pressure PICMD water shown in Figure 5.24b reveal the local water environment is tetrahedral coordinated at low pressure and the local structure is maintained (Figure 5.24b). The pressure dependence of the pnhb second nearest neighbour water molecule is given in Figure 5.24a. The bond at the peak maximum is shifted to shorter distance in response to the compression. For example, the $O\cdots O$ distance at the maximum shifted by 0.3Å from 0.383Kbar to 9.874kbar. Finally, the probability of non-hydrogen bond second nearest neighbour water molecule also increased with pressure (Figure 5.24a). This indicates the crowding into the coordination shell by the second nearest neighbour water. The approaching second nearest neighbour water form interpenetrating hydrogen bond networks similar to compressed ice [7, 11, 236].

5.4 Conclusion

The X-ray absorption spectra (XAS) and Non-Resonant Inelastic X-ray scattering (NRIXS) of crystalline ice Ih and water have been studied using the Bethe-Salpeter Equation (BSE) method implemented in the OCEAN code. The calculated XAS on an AIMD optimized crystalline ice Ih structure gave absorption spectra similar to previously calculated theoretical spectra of Zhovtobriukh et. al [5]. The calculated spectra consist of sharp spikes that are not present in the experimental XAS spectra of crystalline ice Ih and failed to reproduce the true experimental spectra of ice Ih. However, accounting for the nuclear quantum effect by a path integral centroid molecular dynamics (PICMD) simulation, the BSE XAS spectrum improved substantially and became comparable to experiment. The local structure of the PICMD configurations employed in the calculation were then examined. The hydrogen bond analysis revealed that the PICMD ice Ih configurations consist of continuous hydrogen bond network with no interpenetrating H-bonds formed by the second nearest neighbour water molecules. For liquid water, PICMD simulation was performed on a 64 water model at ten different pressure points. The calculated XAS using both previous AIMD and the present PICMD trajectories are comparable and agree with experiment apparently. The atomic motions masked the difference for the classical (AIMD) and quantum (PICMD) structures. In one sense, this observation is similar to the crystalline ice Ih calculations in which reasonable agreement with experiment are obtained if the atomic dynamics are considered. Also, the probability of hydrogen bonded and non hydrogen bonded second nearest neighbour analysis revealed the compressed water structures behave like high density crystalline ice with interpenetrating hydrogen bond network from the compression of the second coordination shell into the first nearest neighbour shell. Hence, the spectral fingerprints of compressed water i.e features of the calculated spectra support the suggestion that there is an increased coordination by approaching second nearest neighbour water molecules.

Chapter 6

CONCLUDING REMARKS

The central aim of this work is to benchmark the applicability of all available bonding analysis methods to interpret the structure, electronic structure and electronic spectra of simple materials at high pressure. In addition, the reconstructive phase transition of elemental Cs around the complex Cs-III to interpret the electronic structure and nature of transformation, and finally the last part of this work focused on the study of the local structure of compressed water and crystalline ice-Ih. The theoretical methods employed are based on first principles density functional theory (DFT), molecular dynamics (MD) and path integral centroid molecular dynamics (PICMD).

Chapter 1 gave a brief introduction to the thesis subject, followed by a discussion of the fundamental theories behind the computational tools employed for all the calculations.

Chapter 2 benchmarked the applicability of all available bonding analysis methods to describe the unusual potassium silver intermetallics formed under compression with stoichiometries K_2Ag and K_3Ag. Analysis of the K_2Ag revealed that the K atom transfers electrons to the Ag atom and forms K-K, K-Ag and Ag-Ag bond interactions with the K-Ag being the strongest bond present in the compound. Contrary to the K_2Ag, bond analysis of the K_3Ag yielded no Ag-Ag bond interaction. This is due to the very large separation of the first nearest neighbour Ag-Ag. All plane wave and localized basis set dependent bond analysis methods employed yielded consistent results, however, the projected density of state (PDOS) computed using the LOBSTER code should always be checked against the PDOS from the plane wave method before trusting the crystal orbital overlap population (COOP) and crystal orbital Hamiltonian population (COHP) results from the LOBSTER code. In summary, all the

bonding analysis techniques should be carefully applied when treating high pressure systems, due to the extensive modification of the electron density on application of pressure. Hence, a naive localized description is not appropriate and may lead to erroneous interpretation.

Chapter 3 reported the description of the electronic structure and bonding of the three phases of sodium gold intermetallics following the benchmark established in chapter two. Analysis of the phase I Na_2Au structure revealed the presence of electrons in non-nuclear positions of the structure commonly known as electrides. These NNMs were found to form from the Na atoms in agreement with the experimental maximum entropy method (MEM) analysis. The experimental structure of the Phase II Na_3Au sodium gold intermetallics was said to have trigonal Cu_3As or hexagonal Cu_3P-type structure. The two structures could not be distinguished from DFT calculated equations of state. However, the topological analysis results presented here revealed the trigonal structure failed to satisfy the Morse sum whereas the tetragonal structure does satisfy the Morse sum and is thus said to be topologically stable and as well the accurate phase II structure. Further analysis of the topologically stable Na_3Au phase II and phase III structures yielded no NNMs. Finally, Bader's quantum theory of atoms in molecule (QTAIM) revealed all the bond interactions present in the structures are closed shell interactions.

Chapter 4 reported the reconstruction of the transformation paths from Cs-II $\rightarrow$ Cs-III and Cs-III $\rightarrow$ Cs-IV to define the transition mechanism. In addition, the topological properties of the Cs-II, Cs-III and Cs-IV structures were reported. The results reveal the transition in the Cs-III to Cs-IV and the Cs-II to Cs-III transitions are typical crystalline solid-solid transitions with no evidence of melting in the transition states. From the molecular dynamics simulation snapshots, the transformation mechanism observed in the Cs-III - Cs-IV is not martensitic (i.e a transformation that occurs through a diffusionless cooperative motion of all the atoms in a transformation region) rather it occurs through some kind of nucleation and growth. The Cs-II - Cs-III transformation on the other hand was found to occur through some kind of cooperative motion of all the atoms in the super cell. Also the results suggest existence of a very large activation barrier for the reverse transformation to Cs-II from a backward (i.e Cs-III $\rightarrow$ Cs-II) transition.

Chapter 5 employed the Beth-Salpeter Equation (BSE) method to calculate the X-ray absorption spectra (XAS) and Nuclear Resonant inelastic X-ray scattering (NRIXS) of ice Ih and compressed water at different momentum transfer values. Theoretical spectra computed using snapshots from the PICMD simulation performed here yielded results in good agreement with experiment for both water and ice Ih. Further analysis of the trajectories revealed the water maintain approximate tetrahedral coordination and not dramatically different from crystalline ice. Also the results showed that compressed water form interpenetrating hydrogen bonds by compressing the second nearest neighbour water molecules into the first coordination shell similar to the behaviour of high density ices.

6.1 Outlook

Based on the research results of this thesis, there are several interesting future works that can be explored. For instance chapter two and three highlighted the limitation of the localized basis set dependent method employed in the LOBSTER code. Future work can be done to incorporate a more flexible basis set that can allow user modifications of the choice of projection orbitals. Also, the structure and bonding nature of intermetallic phases can be described following the benchmark results from chapter two and three of this thesis.

In chapter four, the inability of the standard DFT molecular dynamics to fully reconstruct the reverse (Cs-III $\rightarrow$ Cs-II) transformation path is as a result of the large activation barrier of the transformation. Also the limited simulation box size attainable in standard DFT molecular dynamics have been previously noted to be one of the limitations of reconstructing phase transitions. However, these limitations can be circumvented through machine learning metadynmics simulation which can accommodate thousands of atoms in the simulation cell [252, 253, 200]. Hence, more work can be done using machine learning metadynamics method to reconstruct the backward (Cs-III $\rightarrow$ Cs-II) transformation.

Finally, since the OCEAN BSE code uses the local density approximation (LDA) as the functional for DFT, more work can be done to include a better functional like the generalized gradient approximation (GGA). In addition, a machine learning based method can also be

employed to overcome the system size limitation of standard DFT. Taking into account the aforementioned future works will greatly improve the theoretical XAS spectra agreement with experiment.

References

[1] X. Leng, F. Jin, M. Wei, and Y. Ma. *WIREs Comput Mol Sci.*, 6:532–550, 2016.

[2] S. Motoyuki. Path integral simulations. In *Reference Module in Chemistry, Molecular Sciences and Chemical Engineering*. Elsevier, 2018.

[3] J. Xu, J. Liu, J. Liu, W. Hu, X. He, and J. Li. Phase transition of ice at high pressures and low temperatures. *Molecules*, 25, 2020.

[4] J. A. Sellberg, S. Kaya, V. H. Segtnan, C. Chen, T. Tyliszczak, H. Ogasawara, D. Nordlund, L. G. M. Pettersson, and A. Nilsson. Comparison of x-ray absorption spectra between water and ice: New ice data with low pre-edge absorption cross-section. *The Journal of Chemical Physics*, 141, 2014.

[5] I. Zhovtobriukh, P. Norman, and L. G. M. Pettersson. X-ray absorption spectrum simulations of hexagonal ice. *The Journal of Chemical Physics*, 150:034501, 2019.

[6] S. Imoto, S. S. Xantheas, and S. Saito. Molecular origin of the difference in the hoh bend of the ir spectra between liquid water and ice. *The Journal of Chemical Physics*, 138, 2013.

[7] X. Yong, J. S. Tse, and N. J. English. optpbe-vdw density functional theory study of liquid water and pressure-induced structural evolution in ice ih. *Canadian Journal of Chemistry*, 95:1205–1211, 2017.

[8] W. Wagner and A. Pruay. The iapws formulation 1995 for the thermodynamic properties of ordinary water substance for general and scientific use. *Journal of Physical and Chemical Reference Data*, 31:387–535, 2002.

[9] H. Fukui, S. Huotari, D. Andrault, and T. Kawamoto. Oxygen k-edge fine structures of water by x-ray raman scattering spectroscopy under pressure conditions. *The Journal of Chemical Physics*, 127:134502, 2007.

[10] Y. Q. Cai, H.K. Mao, P. C. Chow, J. S. Tse, Y. Ma, S. Patchkovskii, J. F. Shu, V. Struzhkin, R. J. Hemley, H. Ishii, C. C. Chen, I. Jarrige, C. T. Chen, S. R. Shieh, E. P. Huang, and C. C. Kao. Ordering of hydrogen bonds in high-pressure low-temperature H_2O. *Phys. Rev. Lett.*, 94:025502, 2005.

[11] T. Pylkkanen, V. M. Giordano, J. Chervin, A. Sakko, M. Hakala, J. A. Soininen, K. Hamalainen, G. Monaco, and S. Huotari. Role of non-hydrogen-bonded molecules in the oxygen k-edge spectrum of ice. *The Journal of Physical Chemistry B*, 114:3804–3808, 2010.

[12] D. Natalia, D. Leonid, A. S. Natalia, A. Artem, T. Stuart, H. Michael, B. Elena, B. Maxim, P. Clemens, B. P. Vitali, P. Sylvain, C. Irina, G. Biliana, M. Yves-Laurent, E. Petr, S. Irina, and S. Anatoly. Terapascal static pressure generation with ultrahigh yield strength nanodiamond. *Science Advances*, 2:e1600341, 2016.

[13] M. Miao, Y. Sun, E. Zurek, and H. Lin. Chemistry under high pressure. *Nat Rev Chem*, 4:508–527, 2020.

[14] P. F. McMillan. Pressing on: the legacy of percy w. bridgman. *Nat. Mater*, 4:715–718, 2005.

[15] R. J. Hemley and W. Percy. Bridgman's second century. *High Press. Res.*, 30:581–619, 2010.

[16] L. Dubrovinsky, N. Dubrovinskaia, V. B. Prakapenka, and A. M. Abakumov. Implementation of micro-ball nano-diamond anvils for high- pressure studies above 6mbar. *Nat. Commun.*, 3:1163, 2012.

[17] L. Dubrovinsky, N. Dubrovinskaia, E. Bykova, M. Bykov, V. Prakapenka, C. Prescher, K. Glazyrin, H. P. Liermann, M. Hanfland, M. Ekholm, Q. Feng, L. V. Pourovskii, M. I. Katsnelson, J. M. Wills, and I. A. Abrikosov. The most incompressible metal osmium at static pressures above 750 gigapascals. *Nature*, 525:1476–4687, 2015.

[18] I. Fleming. *Molecular Orbital Theory*, chapter 1, pages 1–67. John Wiley Sons, Ltd, 2010.

[19] J. P. Foster and F. Weinhold. Natural hybrid orbitals. *Journal of the American Chemical Society*, 102:7211–7218, 1980.

[20] A. E. Reed, R. B. Weinstock, and F. Weinhold. Valency and bonding: A natural bond orbital donor-acceptor perspective. *J. Chem. Phys.*, 83:735–746, 1985.

[21] A. E. Reed, L. A. Curtiss, and F. Weinhold. Valency and bonding: A natural bond orbital donor-acceptor perspective. *J. , Chem. Rev.*, 88:899–926, 1988.

[22] F. Weinhold. Chemical bonding as a superposition phenomenon. *J. , Chem. Educ.*, 76:1141–1146, 1999.

[23] F. Weinhold and C. R. Landis. Valency and bonding: A natural bond orbital donor-acceptor perspective. *Cambridge University Press, Cambridge, U.K*, 3, 2005.

[24] T. R. Galeev, B. D. Dunnington, J. R. Schmidt, and A. I. Boldyrev. Solid state adaptive natural density partitioning: a tool for deciphering multi-center bonding in periodic systems. *Phys. Chem. Chem. Phys.*, 15:5022–5029, 2013.

[25] N. Marzari, A. A. Mostofi, J. R. Yates, I. Souza, and D. Vanderbilt. Maximally localized wannier functions: Theory and applications. *Rev. Mod. Phys.*, 84:1419–1475, 2012.

[26] R. Dronskoski and P. E. Blochl. *J. Phys. Chem. Soc.*, page 8617, 1993.

[27] R. F. W. Bader. Atoms in molecules: A quantum theory. *Oxford: Clarendon Press*, 1990.

[28] R. F. W. Bader. *Acc. Chem. Res.*, (18):9, 1985.

[29] R. F. W. Bader. *Chem. Rev.*, (91):893, 1991.

[30] H. J. Bohorquez, R. J. Boyd, and C. F. Matta. *J. Phys. Chem. A*, page 12991, 2011.

[31] M. Born and R. Oppenheimer. High pressure electrides: A predictive chemical and physical theory. *Annalen der physik*, 389(457), 1927.

[32] P. Hohenberg and W. Kohn. *Phys. Rev.*, 136:B864–B871, (1964).

[33] W. Kohn and L. J. Sham. *Phys. Rev.*, 140:A1133–A1138, (1965).

[34] D. M. Ceperley and B. J. Alder. Ground state of the electron gas by a stochastic method. *Phys. Rev. Lett.*, 45:566–569, 1980.

[35] J. P. Perdew, K. Burke, and M. Ernzerhof. Generalized gradient approximation made simple. *Phys. Rev. Lett.*, 77:3865–3868, 1996.

[36] J. P. Perdew and W. Yue. Accurate and simple density functional for the electronic exchange energy: Generalized gradient approximation. *Phys. Rev. B*, 33:8800–8802, 1986.

[37] K. Burke, J. P. Perdew, and M. Ernzerhof. *Phys. Rev. Lett*, 77:3865, 1996.

[38] D. Yu. Zubarev and A. I. Boldyrev. Developing paradigms of chemical bonding: adaptive natural density partitioning. *Phys. Chem. Chem. Phys.*, 10:5207–5217, 2008.

[39] A. I. Boldyrev. Natural hybrid orbitals. *Chemical Reviews*, 105:3716–3757, 2005.

[40] D. Yu. Zubarev, B. B. Averkiev, H. Zhai, L. Wang, and A. I. Boldyrev. Aromaticity and antiaromaticity in transition-metal systems. *Phys. Chem. Chem. Phys.*, pages 257–267, 2008.

[41] H. J. Zhai A. N. Alexandrova, A. I. Boldyrev and L. S. Wang. *Coord. Chem. Rev.*, 250:2811, 2006.

[42] D. Yu. Zubarev and A. I. Boldyrev. Comprehensive analysis of chemical bonding in boron clusters. *Journal of Computational Chemistry*, 28:251–268, 2007.

[43] I. Souza, N. Marzari, and D. Vanderbilt. Maximally localized wannier functions for entangled energy bands. *Phys. Rev. B*, 65:035109, 2001.

[44] T. Hughbanks and W. N. Lipscomb. *J. Chem Phys.*, page 2179, 1962.

[45] R. Hoffmann. *J. Chem. Phys.*, page 1397, 1963.

[46] T. Hughbanks and R. Hoffmann. *J. Am. Chem. Soc.*, page 3528, 1983.

[47] S. Steinberg and R. Dronskowski. *Crystal*, page 225, 2018.

[48] R. Parthasarthi, V. Subramania, and N. Sathyamurthy. *J. Phys. Chem. A*, page 843, 2005.

[49] D. S. Arputharaj, V. R. Harthwar, T. N. G. Row, and P. Kumaradhas. *Cryst. Growth. Des*, page 4357, 2012.

[50] V. R. Hathwar, A. V. Paul, S. Natarajan, and T. N. G. Row. *J. Chem. A*, page 12818, 2011.

[51] M. S Pavan, R. Pal, K. Nagarajan, and T. N. G Row. *Cryst. Growth Des.*, page 5477, 2014.

[52] S. J. Grebowski. *Chem. Rev.*, page 2597, 2011.

[53] S. J. Grebowski. *J. Phys. Chem. A*, page 1838, 2012.

[54] V. Garbuio, M. Cascella, and O. Pulci. Excited state properties of liquid water. *J. Phys. Condens. Matter*, page 33101, 2009.

[55] L. Reining. The gw approximation: content, successes and limitations. *WIREs Computational Molecular Science*, 8:e1344.

[56] L. Hedin. *Phys. Rev. A*, (139):796, 1965.

[57] L. Hedin and S. Lundquist. *Solid State Phys.*, 1969.

[58] G. Onida, L. Reining, and A. Rubio. *Rev. Mod. Phys.*, page 601, 2002.

[59] P. Zimmermann, S. Peredkov, P. M. Abdala, S. DeBeer, M. Tromp, C. Muller, and J. A. van Bokhoven. Modern x-ray spectroscopy: Xas and xes in the laboratory. *Coordination Chemistry Reviews*, 423:213466, 2020.

[60] G. S. Henderson, F. M. F. de Groot, and B. J. A. Moulton. *Reviews in Mineralogy Geochemistry*, 79pp:75–138, 2014.

[61] B. J. Alder and T. E. J. Wainwright. Phase transition for a hard sphere system. *J. Chem. Phys.*, pages 1208–1209, 1957.

[62] B. J. Alder and T. E. J. Wainwright. Studies in molecular dynamics. i. general method. *J. Chem. Phys.*, pages 459–466, 1959.

[63] A. Rahman. *Phys.Rev.*, (136):A405–A411, 1964.

[64] H. C. Andersen. Molecular dynamics simulations at constant pressure and/or temperature. *The Journal of Chemical Physics*, 72:2384–2393, 1980.

[65] L.V. Woodcock. Isothermal molecular dynamics calculations for liquid salts. *Chemical Physics Letters*, 10:257 – 261, 1971.

[66] J. Q. Broughton, G. H. Gilmer, and J. D. Weeks. Constant pressure molecular dynamics simulations of the 2d râ^'12 system: Comparison with isochores and isotherms. *The Journal of Chemical Physics*, 75:5128–5132, 1981.

[67] T. Schneider and E. Stoll. Molecular-dynamics study of a three-dimensional one-component model for distortive phase transitions. *Phys. Rev. B*, 17:1302–1322, 1978.

[68] A. J. Page, T. Isomoto, J. M. Knaup, S. Irle, and K. Morokuma. Effects of molecular dynamics thermostats on descriptions of chemical nonequilibrium. *Journal of Chemical Theory and Computation*, 8:4019–4028, 2012.

[69] H. J. C. Berendsen, J. P. M. Postma, W. F. van Gunsteren, A. Dinola, and J. R. Haak. Molecular dynamics with coupling to an external bath. *The Journal of Chemical Physics*, 81:3684–3690, 1984.

[70] S. C. Harvey, R. K. Z. Tan, and T. E. Cheatham III. The flying ice cube: Velocity rescaling in molecular dynamics leads to violation of energy equipartition. *Journal of Computational Chemistry*, 19:726–740, 1999.

[71] S. Nose. A unified formulation of the constant temperature molecular dynamics methods. *The Journal of Chemical Physics*, 81:511–519, 1984.

[72] W. G. Hoover. Canonical dynamics: Equilibrium phase-space distributions. *Phys. Rev. A*, 31:1695–1697, 1985.

[73] G. J. Martyna, M. L. Klein, and M. Tuckerman. Nosé hoover chains: The canonical ensemble via continuous dynamics. *The Journal of Chemical Physics*, 97:2635–2643, 1992.

[74] W. F. Van Gunsteren and H. J. C. Berendsen. A leap-frog algorithm for stochastic dynamics. *Molecular Simulation*, 1:173–185, 1988.

[75] S. Nose. Constant Temperature Molecular Dynamics Methods. *Progress of Theoretical Physics Supplement*, 103:1–46, 1991.

[76] M. Parrinello and A. Rahman. Crystal structure and pair potentials: A molecular-dynamics study. *Phys. Rev. Lett.*, 45:1196–1199, 1980.

[77] M. Parrinello and A Rahman. Polymorphic transitions in single crystals: A new molecular dynamics method. *Journal of Applied Physics*, 52:7182–7190, 1981.

[78] E. Braun, J. Gilmer, H. B. Mayes, D. L. Mobley, J. I. Monroe, S. Prasad, and D. M. Zuckerman. Best Practices for Foundations in Molecular Simulations [Article v1.0]. *Living journal of computational molecular science*, 1, 2019.

[79] D. J. Evans and B. L. Holian. The nosé hoover thermostat. *The Journal of Chemical Physics*, 83:4069–4074, 1985.

[80] C. P. Herrero and R. Ramírez. Path-integral simulation of solids. *Journal of Physics: Condensed Matter*, 26:233201, 2014.

[81] J. Cao and G. A. Voth. The formulation of quantum statistical mechanics based on the feynman path centroid density. i. equilibrium properties. *The Journal of Chemical Physics*, 100:5093–5105, 1994.

[82] R. P. Feynman and A. R. Hibbs. *Molecular Orbital Theory*, pages 279–286. McGraw-Hill Book Company, 1965.

[83] J. Cao and G. A. Voth. The formulation of quantum statistical mechanics based on the feynman path centroid density. ii. dynamical properties. *The Journal of Chemical Physics*, 100:5106–5117, 1994.

[84] S. Jang and G. A. Voth. A derivation of centroid molecular dynamics and other approximate time evolution methods for path integral centroid variables. *The Journal of Chemical Physics*, 111:2371–2384, 1999.

[85] G. Kresse and J. Hafner. *Phys. Rev. B*, 47:558, 1993.

[86] J. Vinson, J. J. Rehr, J. J. Kas, and E. L. Shirley. Bethe-salpeter equation calculations of core excitation spectra. *Phys. Rev. B*, 83:115106, 2011.

[87] A. A. Mostofi, J. R. Yates, G Pizzi, Y. S. Lee, I. Souza, D. Vanderbilt, and N. Marzari. An updated version of wannier90: A tool for obtaining maximally-localised wannier functions. *Comput. Phys. Commun.*, (185), 2014.

[88] M. S. Hybertsen and S. G. Louie. *Phys. Ref. B*, 34:5390, 1986.

[89] S. Maintz, V. L. Deringer, A. L. Techougreff, and R. Dronskowski. *J. of Comp. Chem.*, pages 1030–1035, 2016.

[90] M. A. Spackman and E. N. Maslen. *J. Phys. Chem.*, 90, 1986.

[91] A. Otero de-la Roza, M. A. Blanco, M. Pandas, and V. Luana. *Compt. Phys. Commun.*, pages 157–166, 2009.

[92] A. M. Thomas. Introducing ddec6 atomic population analysis: part 3.comprehensive method to compute bond orders. *RSC Adv.*, 7:45552, 2017.

[93] G. Kresse and D. Joubert. *Phys. Rev. B*, 59:1758, 1999.

[94] F. Weinhold. Chemical bonding as a superposition phenomenon. *J. Chem. Educ.*, 76:1141–1146, 1999.

[95] N. W. Ashcroft and N. D. Mermin. *Solid State Physics*, 47:14251–14269, 1996.

[96] J. M. Foster and S. F. Boys. *Rev. Mod. Phys.*, 32:300–302, 1960.

[97] X. Yong, C. J. Burnham, N. J. English, and J. S. Tse. Classical and path-integral molecular-dynamics study on liquid water and ice melting using non-empirical ttm2.1-f model. *Molecular Physics*, 117:3241–3253, 2019.

[98] R. Hoffmann. Solids and surfaces , a chemist's view of bonding in extended structures. *Wiehiem: VCH*, 1988.

[99] J. S. Tse. A chemical perspective on high pressure crystal structures and properties. *National Science Review*, 7:149–169, 2020.

[100] Y. Li, J. Hao, H. Liu, Y. Li, and Y. Ma. The metallization and superconductivity of dense hydrogen sulfide. *The Journal of Chemical Physics*, 140:174712, 2014.

[101] A. Drozdov, M. Eremets, I. Troyan, V. Ksenofontov, and S. I. Shylin. Conventional superconductivity at 203 kelvin at high pressures in the sulfur hydride system. *Nature*, 525:73–76, 2015.

[102] G. Yuri. Crystal structure and bonding in intermetallic compoundsâ˜†. In *Reference Module in Chemistry, Molecular Sciences and Chemical Engineering*. Elsevier, 2019.

[103] E. Zintl, J. Goubeau, and Z. W. Dullenkopf. *Phys. Chem.*, 154A, 1931.

[104] F. Laves. *Naturwissenschaften.*, 29:241–255, 1941.

[105] R. Kniep and S. Kauzlarich. In chemistry, structure and bonding of zintl phases and ions. *VCH Publishers*, 1996.

[106] W. Klemm and E. Z. Bussman. *Anorg. Allg. Chem.*, 319:297–311, 1963.

[107] W. B Pearson. *Acta Crystallogr.*, 17:1–15, 1964.

[108] F. Stein and A. Leineweber. Laves phases: a review of their functional and structural applications and an improved fundamental understanding of stability and properties. *J Mater Sci*, 56:5321–5427, 2021.

[109] V. F. Degtyareva. Potassium under pressure: Electronic origin of complex structures. *Solid State Sciences*, 36:62–72, 2014.

[110] A. P. Miedema, P. F. de Chatel, and F. R. de Boer. *Physica B+C*, 100:1–28, 1980.

[111] D. G. Pettifor. *Solid State Phys.*, 40(43), 1987.

[112] R. M. Sternheimer. *Phys. Rev.*, 78, 1950.

[113] K. Takaemura and K. Syassen. *Phys. Rev. B*, 32, 1985.

[114] T. Atou, M. Hasegawa, L. J. Parker, and J. V. Badding. Unusual chemical behavior for potassium under pressure: Potassium - silver compounds. *J. Am. Chem. Soc.*, 118:12104–12108, 1996.

[115] C. T. Prewitt and R. T. Downs. in ultrahigh pressure mineralogy. *ed. Hemley, R. J.*, pages 283–318, 1998.

[116] W. Grochala, R. Hoffmann, J. Feng, and N. W. Ashcroft. The chemical imagination at work in very tight places. *Angew. Chem. Int. Ed.*, 46:3620–3642, 2007.

[117] L. Zhang, Y. Wang, J. Lv, and Y. Ma. Materials discovery at high pressures. *Nat. Rev. Mater.*, 2:17005, 2017.

[118] M. Hanfland, K. Syassen, N. E. Christensen, and D. L. Novikov. New high- pressure phases of lithium. *Nature*, 408:174–178, 2000.

[119] M. I. McMahon and R. J. Nelmes. High- pressure structures and phase transformations in elemental metals. *Chem. Soc. Rev.*, 35:943–963, 2006.

[120] Y. Ma, M. Eremets, A. Oganov, Y. Xie, I. Trojan, S. Medvedev, A. O. Lyakhov, M. Valle, and V. Prakapenka. Transparent dense sodium. *Nature*, 458:182–185, 2009.

[121] M. S. Miao and R. Hoffmann. High pressure electrides: a predictive chemical and physical theory. *Acc. Chem. Res.*, 47:1311–1317, 2014.

[122] K. Momma and F. Izumi. *VESTA3* for three-dimensional visualization of crystal, volumetric and morphology data. *Journal of Applied Crystallography*, 44:1272–1276, 2011.

[123] J. S. Tse, G. Frapper, A. Ker, R. Rousseau, and D. D. Klug. Phase stability and electronic structure of k-ag intermetallics at high pressure. *Phys. Rev. Lett.*, 82:4472–4475, 1999.

[124] D. Andrae, U. Häuermann, M. Dolg, H. Stoll, and H. Preu. Energy-adjusted ab initio pseudopotentials for the second and third row transition elements. *Theor. Chim. Acta*, 77:123–141, 1990.

[125] F. Weigend, F. Furche, and R. Ahlrichs. Gaussian basis sets of quadruple zeta valence quality for atoms h-kr. *J. Chem. Phys.*, 119:12753–12762, 2003.

[126] F. Weigend and R. Ahlrichs. Balanced basis sets of split valence, triple zeta valence and quadruple zeta valence quality for h to rn: Design and assessment of accuracy. *Phys. Chem. Chem. Phys.*, 7:3297, 2005.

[127] M. Morse. The critical points of functions and the calculus of variations in the large. *Bulletin of the American Mathematical Society*, 35:38–54.

[128] V. L. Deringer, A. L. Tchougreeff., and R. Dronskowski. Crystal orbital hamilton population (cohp) analysis as projected from plane-wave basis sets. *The Journal of Physical Chemistry A*, 115:1089–5639, 2011.

[129] I. I. Naumov and R. J. Hemley. Origin of transitions between metallic and insulating states in simple metals. *Phys. Rev. Lett.*, 114:156403, 2015.

[130] R. Rousseau and J. S. Tse. Rationalization of Structures of Binary Alloys in a Real Space Atomic Level Perspective. *Progress of Theoretical Physics Supplement*, 138:47–59, 2000.

[131] L. Yang, X. Qu, X. Zhong, D. Wang, Y. Chen, J. Yang, J. Lv, and H. Liu. Decomposition and recombination of binary interalkali Na_2K at high pressures. *The Journal of Physical Chemistry Letters*, 10:3006–3012, 2019.

[132] K. Takemura and H. Fujihisa. Na-Au intermetallic compounds formed under high pressure at room temperature. *Phys. Rev. B*, 84:014117, 2011.

[133] N. E. Christensen and D. L. Novikov. High-pressure phases of the light alkali metals. *Solid State Communications*, 119(8):477–490, 2001.

[134] M. Ross and A. K. McMahan. Systematics of the $s \to d$ and $p \to d$ electronic transition at high pressure for the elements i through la. *Phys. Rev. B*, 26:4088–4093, 1982.

[135] Y. Ma, A. R. Oganov, and Y. Xie. High-pressure structures of lithium, potassium, and rubidium predicted by an ab initio evolutionary algorithm. *Phys. Rev. B: Condens. Matter Mater. Phys.*, 78:014102, 2008.

[136] E. Gregoryanz, L. F. Lundegaard, M. I. McMahon, C. Guillaume, R. J. Nelmes, and M. Mezouar. Structural diversity of sodium. *Science*, 320:1054–1057, 2008.

[137] M. Marqués, M. I. McMahon, E. Gregoryanz, M. Hanfland, C. L. Guillaume, C. J. Pickard, G. J. Ackland, and R. J. Nelmes. Crystal structures of dense lithium: A metal-semiconductor-metal transition. *Phys. Rev. Lett.*, 106:095502, 2011.

[138] C. L. Guillaume, E. Gregoryanz, O. Degtyareva, M. I. McMahon, M. Hanfland, S. Evans, M. Guthrie, S. V. Sinogeikin, and H. K. Mao. Cold melting and solid structures of dense lithium. *Nat. Phys.*, 7:211–214, 2011.

[139] J. Lv, Y. Wang, L. Zhu, and Y. Ma. Predicted novel high-pressure phases of lithium. *Phys. Rev. Lett.*, 106:015503, 2011.

[140] C. J. Pickard and R. J. Needs. Dense low-coordination phases of lithium. *Phys. Rev. Lett.*, 102:146401, 2009.

[141] M. Marqués, G. J. Ackland, L. F. Lundegaard, G. Stinton, R. J. Nelmes, M. I. McMahon, and J. Contreras-García. Potassium under pressure: A pseudobinary ionic compound. *Phys. Rev. Lett.*, 103:115501, 2009.

[142] M. Winzenick, V. Vijayakumar, and W. B. Holzapfel. High-pressure x-ray diffraction on potassium and rubidium up to 50 gpa. *Phys. Rev. B*, 50:12381–12385, 1994.

[143] Y. Yao, J. S. Tse, and D. D. Klug. Structures of insulating phases of dense lithium. *Phys. Rev. Lett.*, 102:115503, 2009.

[144] Y. Feng, J. Chen, D. Alfè, X. Z. Li, and E. Wang. Nuclear quantum effects on the high pressure melting of dense lithium. *The Journal of chemical physics*, 142:064506, 2015.

[145] K. Shimizu, H. Ishikawa, D. Takao, T. Yagi, and K. Amaya. Superconductivity in compressed lithium at 20 k. *Nature*, 419:597–599, 2002.

[146] V. V. Struzhkin, M. I. Eremets, W. Gan, H. K. Mao, and R. J. Hemley. Superconductivity in dense lithium. *Science*, 298:1213–1215, 2002.

[147] A. M. Schaeffer, S. R. Temple, J. K. Bishop, and S. Deemyad. High-pressure superconducting phase diagram of 6 li: Isotope effects in dense lithium. *Proc. Natl. Acad. Sci. U. S. A.*, 112:60–64, 2015.

[148] T. Matsuoka and K. Shimizu. Direct observation of a pressure-induced metal-to-semiconductor transition in lithium. *Nature*, 458:186–189, 2009.

[149] J. S. Kouvel. Unusual nature of the abrupt magnetic transition in ferh and its pseudobinary variants. *Journal of Applied Physics*, 37:1257–1258, 1966.

[150] G. Henkelman, A. Arnaldsson, and H. Jonsson. A fast and robust algorithm for bader decomposition of charge density. *Comput. Mater. Sci.*, 36:354–360, 2006.

[151] P. Löwdin and H. Shull. Natural orbitals in the quantum theory of two-electron systems. *Phys. Rev.*, 101:1730–1739, 1956.

[152] F. Zipoli, M. Bernasconi, and A. Laio. Ab initio simulations of lewis-acid-catalyzed hydrosilylation of alkynes. *ChemPhysChem*, 6:1772–1775, 2005.

[153] J. Handgraaf and E. J. Meijer. Realistic modeling of ruthenium-catalyzed transfer hydrogenation. *Journal of the American Chemical Society*, 129:3099–3103, 2007.

[154] M. Yu and D. R. Trinkle. *J. Chem. Phys*, (134), 2011.

[155] W. Humphrey, A. Dalke, and K. Schulten. Vmd-visual molecular dynamics. *J.Molec. Graphics*, 14:33–38, 1996.

[156] J. K. Burdett and T. A. McCormick. Electron localization in molecules and solids: The meaning of elf. *The Journal of Physical Chemistry A*, 102(31):6366–6372, 1998.

[157] B. P. Pritchard, D. Altarawy, B. Didier, T. D. Gibsom, and T. L. Windus. A new basis set exchange: An open, up-to-date resource for the molecular sciences community. *J. Chem. Inf. Model.*, 59:4814–4820, 2019.

[158] D. Feller. The role of databases in support of computational chemistry calculations. *J. Comput. Chem.*, 17:1571–1586, 1996.

[159] K. L. Schuchardt, B. T. Didier, T. Elsethagen, L. Sun, V. Gurumoorthi, J. Chase, J. Li, and T. L. Windus. Basis set exchange: A community database for computational sciences. *J. Chem. Inf. Model.*, 47:1045–1052, 2007.

[160] B. Rousseau and N. W. Ashcroft. Interstitial electronic localization. *Phys. Rev. Lett.*, 101:046407, 2008.

[161] M. Frost, E. E. McBride, M. Schörner, R. Redmer, and S. H. Glenzer. Sodium-potassium system at high pressure. *Phys. Rev. B*, 101:224108, 2020.

[162] D. A. Young. *Phase Diagrams of the Elements Young University of California Press, Berkeley, CA (USA)*, pages 135–135. Angewandte Chemie, 1993.

[163] P. W. Bridgman. Compressions and polymorphic transitions of seventeen elements to 100,000 kg/cm^2. *Phys. Rev.*, 60:351–354, 1941.

[164] H. T. Hall, L. Merrill, and J. D. Barnett. High pressure polymorphism in cesium. *Science*, pages 1297–1299, 1964.

[165] K. Takemura, S. Minomura, and O. Shimomura. X-ray diffraction study of electronic transitions in cesium under high pressure. *Phys. Rev. Lett.*, 49:1772–1775, 1982.

[166] U. Schwarz, K. Takemura, M. Hanfland, and K. Syassen. Crystal structure of cesium-v. *Phys. Rev. Lett.*, 81:2711–2714, 1998.

[167] J. Wittig. Pressure-induced superconductivity in cesium and yttrium. *Phys. Rev. Lett.*, 24:812–815, 1970.

[168] K. Takemura, N. E. Christensen, D. L. Novikov, K. Syassen, U. Schwarz, and M. Hanfland. Phase stability of highly compressed cesium. *Phys. Rev. B*, 61:14399–14404, 2000.

[169] D. B. McWhan, G. Parisot, and D. Bloch. Evidence for a continuous s-d transition in FCC caesium at high pressure. *Journal of Physics F: Metal Physics*, 4:L69–L75, 1974.

[170] G. C. Kennedy, A. Jayaraman, and R. C. Newton. Fusion curve and polymorphic transitions of cesium at high pressures. *Phys. Rev.*, 126:1363–1366, 1962.

[171] A. Jayaraman, R. C. Newton, and J. M. McDonough. Phase relations, resistivity, and electronic structure of cesium at high pressures. *Phys. Rev.*, 159:527–533, 1967.

[172] R. A. Stager and H. G. Drickamer. Effect of pressure on the resistance of cesium. *Phys. Rev. Lett.*, 12:19–20, 1964.

[173] D. B. McWhan and A. L. Stevens. Anomalous temperature dependence of Cs resistivity at high pressure. *Solid State Communications*, 7:301–304, 1969.

[174] H. Tups, K. Takemura, and K. Syassen. Interband optical absorption and electronic $s - d$ transition in rb and cs at high pressures. *Phys. Rev. Lett.*, 49:1776–1779, 1982.

[175] N. E. Christensen, D. J. Boers, J. L. van Velsen, and D. L. Novikov. Negative thermal expansion coefficient and isostructural transition in fcc cesium. *Phys. Rev. B*, 61:R3764–R3767, 2000.

[176] N. E. Christensen, D. J. Boers, J. L. van Velsen, and D. L. Novikov. Ab initio thermodynamics of body-centred cubic and face-centred cubic cs. *Journal of Physics: Condensed Matter*, 12(14):3293–3312, 2000.

[177] Y. Xie, Y. M. Ma, T. Cui, Y. Li, J. Qiu, and G. T. Zou. Origin of bcc to fcc phase transition under pressure in alkali metals. *New Journal of Physics*, 10:063022, 2008.

[178] M. I. McMahon, R. J. Nelmes, and S. Rekhi. Complex crystal structure of cesium-iii. *Phys. Rev. Lett.*, 87:255502, 2001.

[179] L. Guan, L. Zhu, and S. Xie. The recurrence of dense face-centered cubic cesium. *Journal of Physics: Condensed Matter*, 33:035404, 2020.

[180] Z. D. C. Stephen. Chapter 2 - thermodynamics and kinetics of phase transitions. In S. Z. D. Cheng, editor, *Phase Transitions in Polymers*, pages 17–59. Elsevier, Amsterdam, 2008.

[181] R. Z. Khaliullin, H. Eshet, and T. D. Kühne J. Behler M. Parrinello. Nucleation mechanism for the direct graphite-to-diamond phase transition. *Nature materials*, 10:693–697, 2011.

[182] P. W. Atkins. *Physical Chemistry*, 4th edn. Freeman and Company, San Francisco., 1990.

[183] S. Pogatscher, D. Leutenegger, J. E. Schawe, P. J. Uggowitzer, and J. F. Löffler. Solid-solid phase transitions via melting in metals. *Nature communications*, 7:11113, 2016.

[184] R. B. Schwarz and W. L. Johnson. Formation of an amorphous alloy by solid-state reaction of the pure polycrystalline metals. *Phys. Rev. Lett.*, 51:415–418, 1983.

[185] A. Blatter and A. M. Von. Reversible amorphization in laser-quenched titanium alloys. *Phys. Rev. Lett.*, 54:2103–2106, 1985.

[186] V. J. Anderson and H. N. Lekkerkerker. Insights into phase transition kinetics from colloid science. *Nature*, 416:811–815, 2002.

[187] S. Scandolo, M. Bernasconi, G. L. Chiarotti, P. Focher, and E. Tosatti. Pressure-induced transformation path of graphite to diamond. *Phys. Rev. Lett.*, 74:4015–4018, 1995.

[188] F. Zipoli, M. Bernasconi, and R. Martonak. Constant pressure reactive molecular dynamics simulations of phase transitions under pressure: The graphite to diamond conversion revisited. *Eur. Phys. J. B*, 39:41–47, 2004.

[189] D. Zahn and S. Leoni. Nucleation and growth in pressure-induced phase transitions from molecular dynamics simulations: Mechanism of the reconstructive transformation of NaCl to the CsCl-type structure. *Phys. Rev. Lett.*, 92:250201, 2004.

[190] S. Zhu, X. Yan, J. Liu, A. R. Oganov, and Q. Zhu. A revisited mechanism of the graphite-to-diamond transition at high temperature. *Matter*, 3:864–878, 2020.

[191] K. Burke J. P. Perdew and M. Ernzerhof. *Phys. Rev. Lett*, 77:3865, 1996.

[192] A. Mujica, A. Rubio, A. Mu noz, and R. J. Needs. High-pressure phases of group-iv, iii–v, and ii–vi compounds. *Rev. Mod. Phys.*, 75:863–912, 2003.

[193] F. Bresme, E. Chacan, and P. Tarazona. Molecular dynamics investigation of the intrinsic structure of water at fluid interfaces via the intrinsic sampling method. *Phys. Chem. Chem. Phys.*, 10:4704–4715, 2008.

[194] F. H. Stillinger and T. A. Weber. Inherent structure theory of liquids in the hard sphere limit. *The Journal of Chemical Physics*, 83:4767–4775, 1985.

[195] C. Chakravarty, P. G. Debenedetti, and F. H. Stillinger. Generating inherent structures of liquids: Comparison of local minimization algorithms. *The Journal of Chemical Physics*, 123:206101, 2005.

[196] B. Bagchi. *Inherent structures of liquid water*, page 61–70. Cambridge Molecular Science. Cambridge University Press, 2013.

[197] E. Chacan, P. Tarazona, and J. Alejandre. The intrinsic structure of the water surface. *The Journal of Chemical Physics*, 125:014709, 2006.

[198] H. G. von Schnering and R. Nesper. How nature adapts chemical structure to curved space. *Angew. Chem. Int. Ed. Engl*, pages 1059–1080, 1987.

[199] E. Y. Tonkov and E. G. Ponyatovsky. Phase transformations of elements under high pressure. *CRC Press.*, 2004.

[200] Q. Tong, X. Luo, A. A. Adeleke, P. Gao, Y. Xie, H. Liu, Q. Li, Y. Wang, J. Lv, Y. Yao, and Y. Ma. Machine learning metadynamics simulation of reconstructive phase transition. *Phys. Rev. B*, 103:054107, 2021.

[201] Y. Peng, W. Li, F. Wang, T. Still, A. G. Yodh, and Y. Han. Diffusive and martensitic nucleation kinetics in solid-solid transitions of colloidal crystals. *Nat Commun*, 8:14978, 2017.

[202] S. P. Sitkiewicz, E. Ramos-Cordoba, J. M. Luis, and E. Matito. How many electrons does a molecular electride hold? *The Journal of Physical Chemistry A*, 125:4819–4835, 2021.

[203] S. G. Dale, A. Otero de-la Roza, and E. R. Johnson. Density-functional description of electrides. *Phys. Chem. Chem. Phys.*, 16:14584–14593, 2014.

[204] R. Rousseau, K. Uehara, D. D. Klug, and J. S. Tse. Phase stability and broken-symmetry transition of elemental lithium up to 140 GPa. *ChemPhysChem*, 6:1703–1706, 2005.

[205] S. von G. Hans and R. Nesper. How nature adapts chemical structures to curved surfaces. *Angewandte Chemie International Edition in English*, 26:1059–1080, 1987.

[206] J. S. Tse and E. V. Boldyreva. *Electron Density Topology of Crystalline Solids at High Pressure*, pages 573–623. Springer Netherlands, 2012.

[207] P. Ball. Water is an active matrix of life for cell and molecular biology. *Proceedings of the National Academy of Sciences*, 114:13327–13335, 2017.

[208] Y. Marcus. The effect of complex anions on the structure of water. *Journal of Solution Chemistry*, 44:2258–2265, 2015.

[209] A. S. Yamada, H. W. Thompson, and D. M. Fayer. Water-anion hydrogen bonding dynamics: Ultrafast ir experiments and simulations. *The Journal of Chemical Physics*, 146:234501, 2017.

[210] J. Liu, X. He, and J. Z. H. Zhang. Structure of liquid water a dynamical mixture of tetrahedral and ring-and-chain like structures. *Phys. Chem. Chem. Phys.*, 19:11931–11936, 2017.

[211] Y. Ding, A. A. Hassanali, and M. Parrinello. Anomalous water diffusion in salt solutions. 111:3310–3315, 2014.

[212] J. R. Errington and P. G. Debenedetti. Relationship between structural order and the anomalies of liquid water. *Nature*, 409:318–321, 2001.

[213] A. Hassanali, F. Giberti, J. Cuny, T. D. Kühne, and M. Parrinello. Deep into the water: Exploring the hydro-electromagnetic and quantum-electrodynamic properties of interfacial water in living systems. *Proton Transfer Through the Water Grossamer. Proceedings of the National Academy of Sciences of the United States of America*, 409:318–321, 2013.

[214] P. Wernet, D. Nordlund, U. Bergmann, M. Cavalleri, M. Odelius, H. Ogasawara, L. Å. Näslund, T. K. Hirsch, L. Ojamäe, and P. Glatzel et al. The structure of the first coordination shell in liquid water. *Science*, 304:995–999, 2004.

[215] M. Chen, H. Ko, R. C. Remsing, A. M. F. Calegari, B. Santra, Z. Sun, A. Selloni, R. Car, M. L. Klein, J. P. Perdew, and X. Wu. Ab initio theory and modeling of water. *Proceedings of the National Academy of Sciences*, 114:10846–10851, 2017.

[216] T. Head-Gordon and M. E. Johnson. Tetrahedral structure or chains for liquid water. *Proceedings of the National Academy of Sciences*, 103:7973–7977, 2006.

[217] L. B. Skinner, J. C. Benmore, J. C. Neuefeind, and J. B. Parise. The structure of water around the compressibility minimum. *The Journal of Chemical Physics*, 141:214507, 2014.

[218] L. A Naslund, J. Luning, Y. Ufuktepe, H. Ogasawara, Ph. Wernet, U. Bergmann, L. G. M. Pettersson, and A. Nilsson. *J. Phys. Chem. B*, pages 13835–13839, 2005.

[219] J. D. Smith, C. D. Cappa, B. M. Messer, W. S. Drisdell, R. C. Cohen, and R. J. Saykally. Probing the local structure of liquid water by x-ray absorption spectroscopy. *The journal of physical chemistry. B*, 110:20038–20045, 2006.

[220] C. A. Angell, R. D. Bressel, M. Hemmati, E. J. Sare, and J. C. Tucker. Water and its anomalies in perspective: tetrahedral liquids with and without liquid-liquid phase transitions. invited lecture. *Phys. Chem. Chem. Phys.*, 2:1559–1566, 2000.

[221] P. H. Poole, F. Sciortino, U. Essmann, and H. E. Stanley. Phase behaviour of metastable water. *Nature*, 360:324–328, 1992.

[222] M. Osamu and E. S. Harry. The relationship between liquid, supercooled and glassy water. *Nature*, 396:329–335, 1998.

[223] A. Nilsson and L. Gunnar M. Pettersson. The structural origin of anomalous properties of liquid water. *Nature Communications*, 6, 2015.

[224] C. J Sahle, C. Sternemann, C. Schmidt, S. Lehtola, S. Jahn, L. Simonelli, S. Huotari, M. Hakala, T. PylkkÃ¤nen, A. Nyrow, K. Mende, M. Tolan, K. HÃmÃlÃinen, and M. Wilke. Microscopic structure of water at elevated pressures and temperatures. *Proceedings of the National Academy of Sciences of the United States of America*, 110:6301–6306, 2013.

[225] J. S. Tse, D. M. Shaw, D. D. Klug, S. Patchkovskii, G. Vankó, G. Monaco, and M. Krisch. X-ray raman spectroscopic study of water in the condensed phases. *Physical review letters*, 100, 2008.

[226] M. Odelius, M. Cavalleri, A. Nilsson, and L. G. M. Pettersson. X-ray absorption spectrum of liquid water from molecular dynamics simulations: Asymmetric model. *Phys. Rev. B*, 73, 2006.

[227] M. Leetmaa, M.P. Ljungberg, A. Lyubartsev, A. Nilsson, and L.G.M. Pettersson. Theoretical approximations to x-ray absorption spectroscopy of liquid water and ice. *Journal of Electron Spectroscopy and Related Phenomena*, 177:135–157, 2010.

[228] G. Brancato, N. Rega, and V. Barone. Accurate density functional calculations of near-edge x-ray and optical absorption spectra of liquid water using nonperiodic boundary conditions: The role of self-interaction and long-range effects. *Phys. Rev. Lett.*, 100, 2008.

[229] Z. Sun, L. Zheng, M. Chen, M. L. Klein, F. Paesani, and X. Wu. Electron-hole theory of the effect of quantum nuclei on the x-ray absorption spectra of liquid water. *Phys. Rev. Lett.*, 121:137401, 2018.

[230] V. F. Petrenko and R. W. Whitworth. Physics of ice. *Oxford University Press*, 2002.

[231] D. Nordlund, H. Ogasawara, K. J. Andersson, M. Tatarkhanov, M. Salmerón, L. G. M. Pettersson, and A. Nilsson. Sensitivity of x-ray absorption spectroscopy to hydrogen bond topology. *Phys. Rev. B*, 80:233404, 2009.

[232] Y. Zubavichus, Y. Yang, M. Zharnikov, O. Fuchs, T. Schmidt, C. Heske, E. Umbach, G. Tzvetkov, F. P. Netzer, and M. Grunze. Local structure of amorphous ice as revealed by o k-edge exafs. *ChemPhysChem*, 5:509–514, 2004.

[233] D. Nordlund, H. Ogasawara, Ph. Wernet, M. Nyberg, M. Odelius, L.G.M. Pettersson, and A. Nilsson. Surface structure of thin ice films. *Chemical Physics Letters*, 395:161–165, 2004.

[234] A. Nilsson, H. Ogasawara, M. Cavalleri, D. Nordlund, M. Nyberg, Ph. Wernet, and L. G. M. Pettersson. The hydrogen bond in ice probed by soft x-ray spectroscopy and density functional theory. *The Journal of Chemical Physics*, 122, 2005.

[235] Ph. Parent, C. Laffon, C. Mangeney, F. Bournel, and M. Tronc. Structure of the water ice surface studied by x-ray absorption spectroscopy at the o k-edge. *The Journal of Chemical Physics*, 117:10842–10851, 2002.

[236] C. Lin, X. Liu, X. Yong, J. S. Tse, J. S. Smith, J. N. English, B. Wang, M. Li, W. Yang, and H. Mao. Temperature-dependent kinetic pathways featuring distinctive thermal-activation mechanisms in structural evolution of ice vii. *Proceedings of the National Academy of Sciences*, 117:15437–15442, 2020.

[237] B. Andreas, D. Michael, K. Wolfgang, S. Hermann, and P. Heinzwerner. Ab initio energy-adjusted pseudopotentials for elements of groups 13-17. *Molecular Physics*, 80:1431–1441, 1993.

[238] L. Triguero, L. G. M. Pettersson, and H. Ågren. Calculations of near-edge x-ray-absorption spectra of gas-phase and chemisorbed molecules by means of density-functional and transition-potential theory. *Phys. Rev. B*, 58:8097–8110, 1998.

[239] G. E. Lindberg and F. Wang. Efficient sampling of ice structures by electrostatic switching. *The journal of physical chemistry. B*, 20:6436–6441, 2008.

[240] X. Yong. Theoretical study on phase transitions and chemical reactions of selected materials under high pressure. *University of Saskatchewan*, 2016.

[241] M. Wilke, F. Farges, P. Petit, G. E. Brown, and F. Martin. Oxidation state and coordination of fe in minerals: An fe k-xanes spectroscopic study. *American Mineralogist*, 86:714–730, 2001.

[242] P. David and G. Giulia. X-ray absorption spectra of water from first principles calculations. *Phys. Rev. Lett.*, 96:215502, 2006.

[243] L. A. Naslund, J. LÃning, Y. Ufuktepe, H. Ogasawara, Ph. Wernet, U. Bergmann, L. G. M. Pettersson, and A. Nilsson. X-ray absorption spectroscopy measurements of liquid water. *The Journal of Physical Chemistry B*, 109:13835–13839, 2005.

[244] M. Chen, H. Ko, R. C. Remsing, A. M. F. Calegari, B. Santra, Z. Sunc, A. Selloni, R. Car, M.. L. Klein, J. P. Perdew, and X. Wu. Ab initio theory and modeling of water. *Proceedings of the National Academy of Sciences*, 114:10846–10851, 2017.

[245] S. Zhaoru, Z. Lixin, C. Mohan, K. Michael L., P. Francesco, and W. Xifan. Electron-hole theory of the effect of quantum nuclei on the x-ray absorption spectra of liquid water. *Phys. Rev. Lett.*, 121:137401, 2018.

[246] X. Li, B. Walker, and A. Michaelides. Quantum nature of the hydrogen bond. *Proceedings of the National Academy of Sciences*, 108(16):6369–6373, 2011.

[247] M. Ceriotti, J. Cuny, M. Parrinello, and D. E. Manolopoulos. Nuclear quantum effects and hydrogen bond fluctuations in water. *Proceedings of the National Academy of Sciences*, 110:15591–15596, 2013.

[248] B. Chen, I. Ivanov, M. L. Klein, and M. Parrinello. Hydrogen bonding in water. *Phys. Rev. Lett.*, 91:215503, 2003.

[249] J. A. Morrone and R. Car. Nuclear quantum effects in water. *Phys. Rev. Lett.*, 101:017801, 2008.

[250] J. Urquidi, S. Singh, C. H. Cho, and G. W. Robinson. Origin of temperature and pressure effects on the radial distribution function of water. *Phys. Rev. Lett.*, 83:2348–2350, 1999.

[251] A. V. Okhulkov, Yu. N. Demianets, and Yu. E. Gorbaty. X-ray scattering in liquid water at pressures of up to 7.7 kbar: Test of a fluctuation model. *The Journal of Chemical Physics*, 100:1578–1588, 1994.

[252] A. Laio and M. Parrinello. Escaping free-energy minima. *Proceedings of the National Academy of Sciences*, 99:12562–12566, 2002.

[253] G. Bussi and A. Laio. Using metadynamics to explore complex free-energy landscapes. *Nat. Rev. Phys.*, 2:200–212, 2020.

Appendix A

Supporting information for Chapter two

Presented here in Figure A.1 and A.2 are the total and projected density of states of the K_2Ag and K_3Ag respectively, to further establish the importance of using the projected density of state to validate the LOBSTER projections instead of the total density of state. As can be seen from the figures, the total density of states always agree but plotting the PDOS reveal that inclusion of the 4p yields negative DOS which implies the projection orbitals used is not correct. Hence it's necessary to correlate the PDOS from LOBSTER with the PDOS from a plane wave calculation before using the COHP and COOP results.

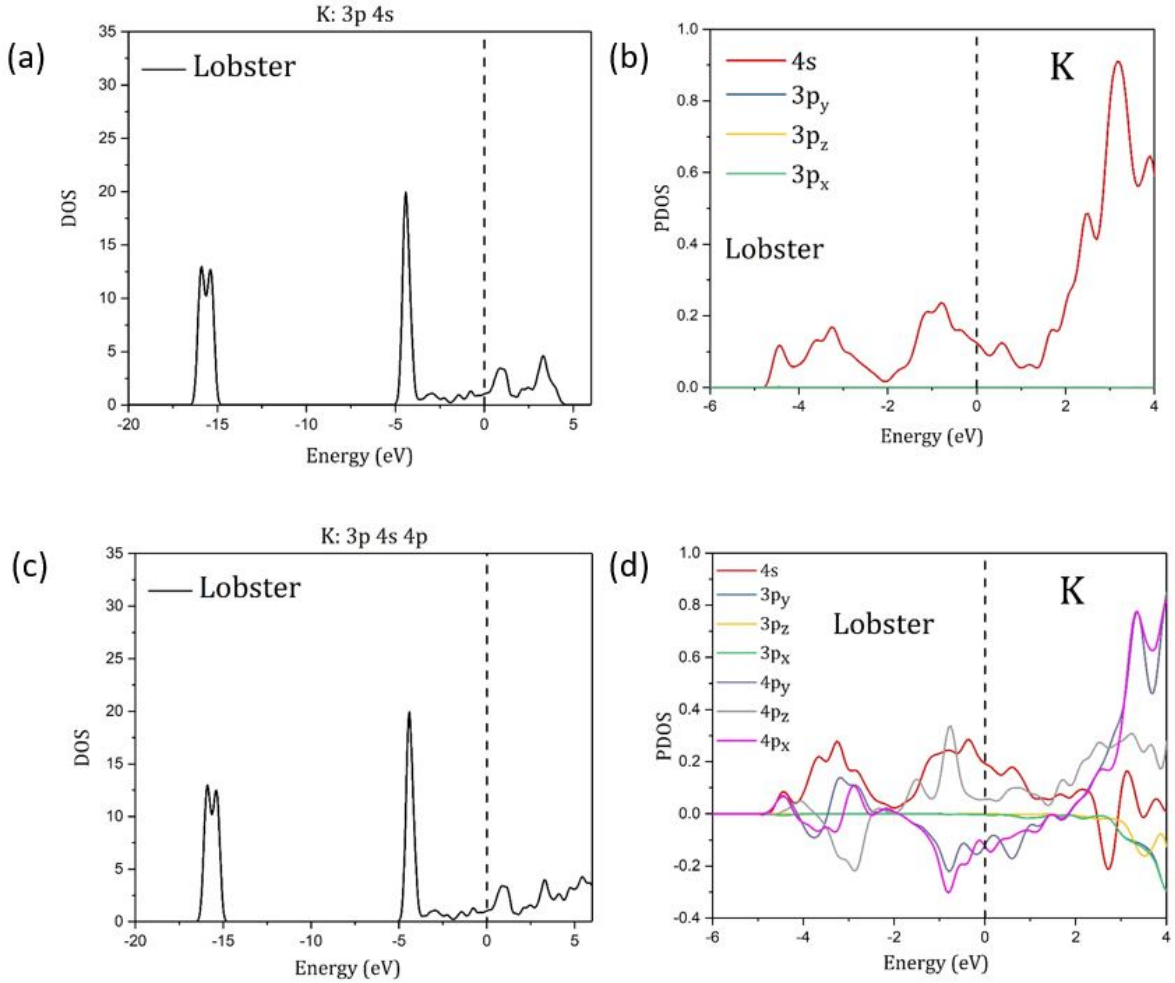

Figure A.1: (a and b) Total and Projected density of state (PDOS) of K in the hexagonal P6/mmm K_2Ag using LOBSTER with 3p 4s projection orbitals for K and (b and c) Total and Projected density of state (PDOS) of K in the hexagonal P6/mmm K_2Ag using LOBSTER with 3p 4s 4p projection orbitals for K

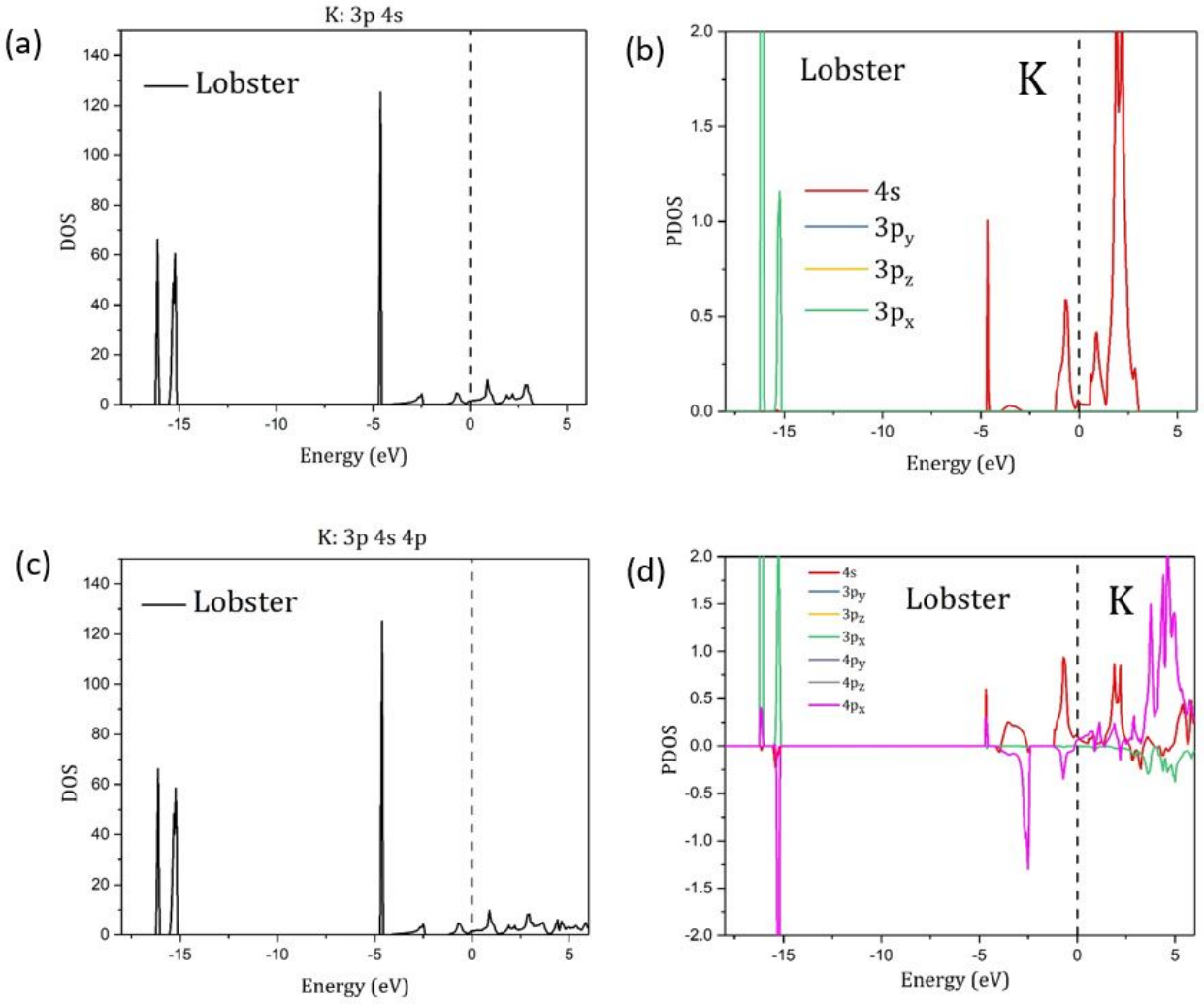

Figure A.2: (a and b) Total and Projected density of state (PDOS) of K in the cubic K_3Ag using LOBSTER with 3p 4s projection orbitals for K and (b and c) Total and Projected density of state (PDOS) of K in the cubic K_3Ag using LOBSTER with 3p 4s 4p projection orbitals for K

Appendix B

Supplementary Information for Chapter Three

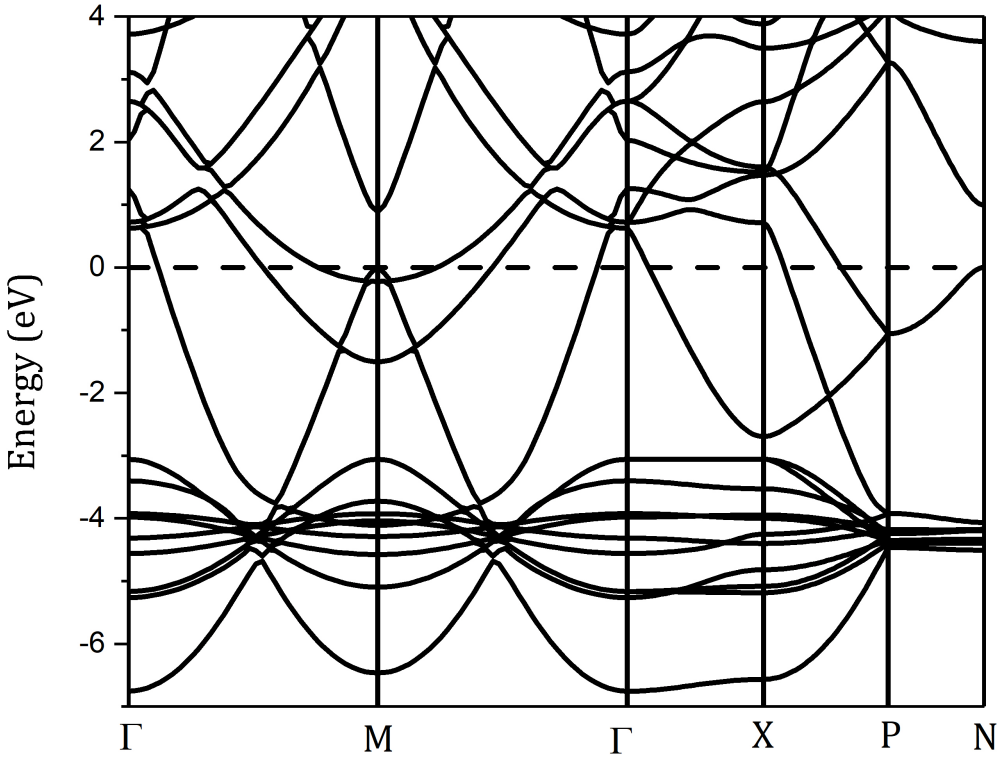

Figure B.1: DFT band structure of the tetragonal I4/mcm Na_2Au Phase I.

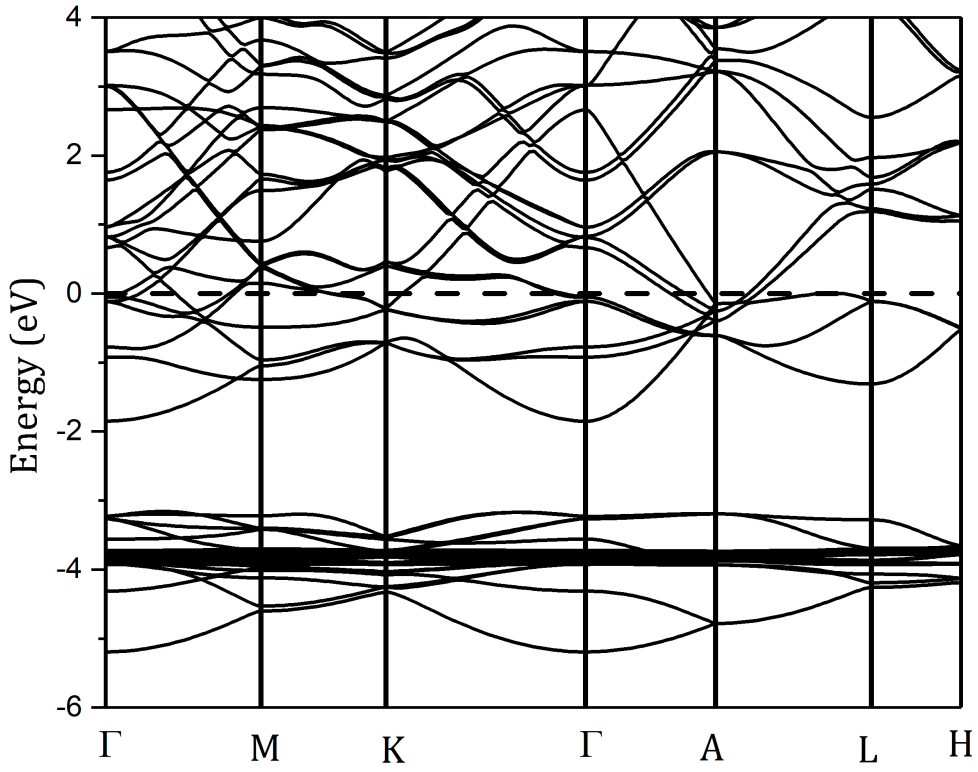

Figure B.2: DFT band structure of the hexagonal $P6_3cm$ Na_3Au Phase II.

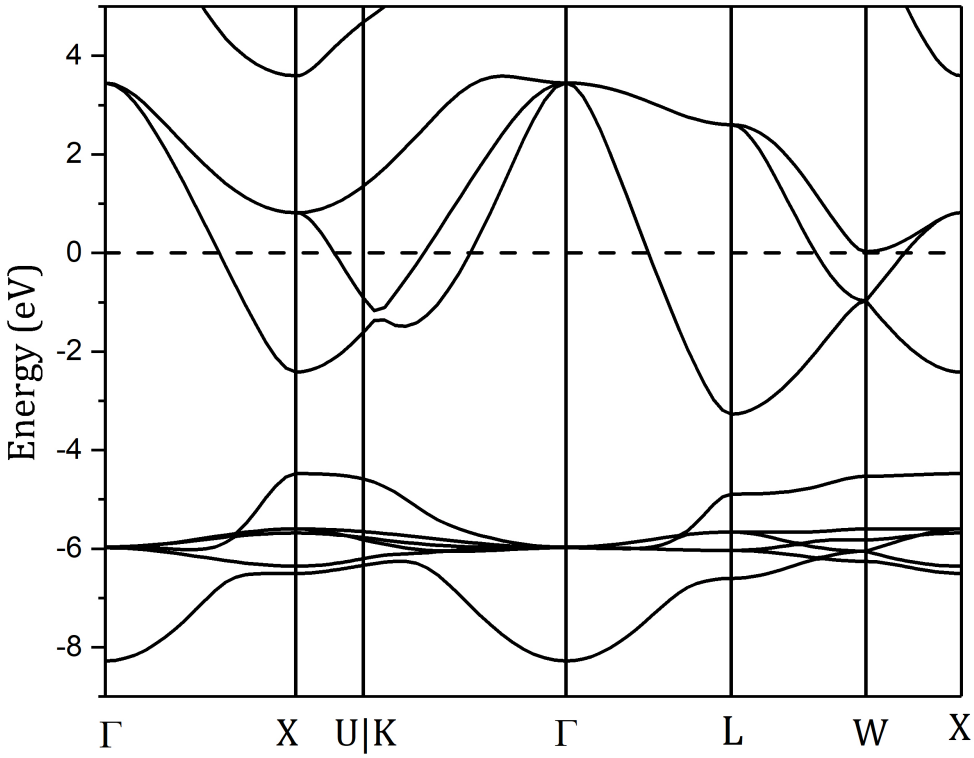

Figure B.3: DFT band structure of the cubic Fm-3m Na_3Au Phase III.

Appendix C

Additional information for Chapter Four

C.1 Effective way to run the OCEAN code

The ocean is an *ab initio* Density Functional Theory (DFT) based code that numerically solve the Bethe-Salpeter Equation (BSE) for calculations of core-level spectra [86]. There are several steps involved in the process of running the ocean code as the code uses a variety of compiled programs and scripts. However, the entire processes is primarily driven by simply running the main script ocean.pl. Due to the fact that most of the ocean code stages require only a single processor, running the parent ocean.pl script can be very inefficient for a system of many atoms. Hence, from my experience using the code, I will highlight some tips on how to run all the stages independently and more efficiently. For a system of very large number of atoms, the calculation requires a large number of bands, hence the DFT stage is one of the most expensive stages to run. The first tip is to run the ocean.pl with the desired number of processors (usually very large) and track the calculation until the DFT stage is completed. After the DFT stage, stop the calculation because most of the stages from this point require fewer or single processors. Having completed the DFT stage, navigate to the "Common" directory and edit the para_prefix file by reducing the number of processors to around 32CPUs or less. Then change to the SCREENING directory and run the screen.pl in this directory. Once the screening stage is completed, change to the "CNBSE" directory. This stage of the calculation requires only one CPU and is also one of the most time consuming stage. Hence, run the cnbse_mpi.pl with only one core in the CNBSE directory. The process can take over 5 days depending on the number of atoms the spectra has to be computed for. Following the aforementioned steps reduces the risk of wasting computer resources and failed calculations.

Permission

Inbox ×

nnanna ukoji <nnannaceci1@gmail.com>
to zhaojianbao.bjwj

Dear Jianbao,

Please, I need your permission to include your MEM analysis of the Na-Au in my thesis, to my support my theoretical results.

A reply to this email is good enough.

Thank you.
Nnanna.
--
N.

Jianbao Zhao
to me

Dear Nnanna,

As we are planning to publish these results soon, for now that's fine to cite the MEM analysis and results of the Na-Au as unpublished work.

Cheers,
Jianbao

Jianbao Zhao Ph.D.
Associate Scientist, Far-Infrared Beamline

Canadian Light Source Inc.
44 Innovation Boulevard
Saskatoon, SK
S7N 2V3